

# **On the Synthesis, Properties, and Applications of Metal Dithiocarbamate Complexes**

---

A dissertation submitted for the degree of Doctor of Philosophy

at

University of Technology Sydney

Faculty of Science

School of Mathematical and Physical Sciences

by

**Alexander Angeloski**

June 2019

---

## Certificate of Original Authorship

I, Alexander Angeloski declare that this thesis by publication, is submitted in fulfilment of the requirements for the award of Doctor of Philosophy, in the School of Mathematical and Physical Sciences at the University of Technology Sydney.

This thesis by publication is wholly my own work unless otherwise referenced or acknowledged. In addition, I certify that all information sources and literature used are indicated in the thesis.

This document has not been submitted for qualifications at any other academic institution.

This research is supported by the Australian Government Research Training Program.

Signature of Candidate:

Production Note:

Signature removed prior to publication.

---

Date: 17-6-2019



## Acknowledgements

This PhD project and resultant dissertation are a testament to the rigorous nature of science. In my quest to uncover a new understanding, and my personal growth, I have not walked alone. Undoubtedly this work would not be possible without the assistance and guidance from many individuals. The list of supporters is endless, and regrettably I cannot list them all, for fear I will accidentally overlook some key supporter and bring endless shame to myself. With this in mind, I sincerely thank all of you who have provided assistance to me over the years, from the faceless figures to the omnipresent ones.

First and foremost I express my endless gratitude towards my supervisory panel; Assoc. Prof. Andrew McDonagh, Prof. Michael Cortie, and Dr. Tristan Rawling, who have each in their own way provided the gift of knowledge to me. As a whole, my three supervisors have guided me through the darkness and into the light, as my guides in the Divine Comedy. Next, I would like to thank my family, who have always supported me throughout my life and studies.

Of equal importance are my close friends and collaborators within UNSW; Dr. James Hook, and Dr. Mohan Bhadbhade. Indeed, my entire research project would not have been possible without the assistance of UNSW due to access to instruments and expertise that are not endemic to UTS. These two great minds not only provided access, but also continued support, guidance and intellectual stimulation.

I also thank one of my closest of friends and supporters, Dr. Ronald Shimmon. He has been the most supportive of managers (indeed this research was performed whilst simultaneously managing the materials science research laboratory spaces 3 days a week!). Last but not least, I wish to thank the ANSTO for access to its wonderful instruments, both at the Australian Synchrotron in Melbourne and the OPAL nuclear reactor at Lucas Heights.

## Publications arising from this work

1. A. Angeloski, A.T. Baker, M. Bhadbhade, A.M. McDonagh, "Bis( $\kappa^2$ S,S'-di(isopropyl)dithiocarbamato)nickel(II): Anagostic C-H $\cdots$ Ni interactions and physical properties", *Journal of Molecular Structure*, 2016, 1113, 127-132
2. A. Angeloski, J.M. Hook, M. Bhadbhade, A.T. Baker, A.M. McDonagh, "Intramolecular H $\cdots$ S interactions in metal di(isopropyl) dithiocarbamate complexes", *CrystEngComm*, 2016, 18, 7070-7077
3. A. Angeloski, A.R. Gentle, J.A. Scott, M.B. Cortie, J.M. Hook, M.T. Westerhausen, M. Bhadbhade, A.T. Baker, A.M. McDonagh, "From Lead(II) Dithiocarbamate Precursors to a Fast Response PbS Positive Temperature Coefficient Thermistor", *Inorganic Chemistry*, 2018, 57, 2132-2140
4. J.A. Scott, A. Angeloski, I. Aharonovich, C.J. Lobo, A.M. McDonagh, M. Toth, "In situ study of the precursor conversion reactions during solventless synthesis of Co<sub>9</sub>S<sub>8</sub>, Ni<sub>3</sub>S<sub>2</sub>, Co and Ni nanowires", *Nanoscale*, 2018, 10, 15669-15676
5. A. Angeloski, M.B. Cortie, J.A. Scott, D.M. Bordin, A.M. McDonagh, "Conversion of single-crystals of a nickel(II) dithiocarbamate complex to nickel sulfide crystals", *Inorganica Chimica Acta*, 2019, 487, 228-233
6. A. Angeloski, A. Rawal, M. Bhadbhade, J.M. Hook, R.W. Schurko, A.M. McDonagh, "An Unusual Mercury(II) Diisopropyldithiocarbamate Coordination Polymer", *Crystal Growth and Design*, 2019, 19, 1125-1133



## Table of Contents

Certificate of Original Authorship .....	i
Acknowledgements.....	ii
Publications arising from this work.....	iii
Abstract.....	v
Chapter 1: Introduction; A Research Overview .....	1
Synthesis of dithiocarbamate anions.....	1
Coordination to metals .....	3
Applications of dithiocarbamate complexes .....	4
Aims and Objectives.....	6
Thesis Overview .....	7
Chapter 2: Bis( $k^2S,S'$ -di(isopropyl)dithiocarbamato)nickel(II): Anagostic C-H $\cdots$ Ni interactions and physical properties.....	10
Chapter 3: Conversion of single-crystals of a nickel(II) dithiocarbamate complex to nickel sulfide crystals.....	18
Chapter 4: From Lead(II) Dithiocarbamate Precursors to a Fast Response PbS Positive Temperature Coefficient Thermistor .....	26
Chapter 5: Intramolecular H $\cdots$ S interactions in metal di-(isopropyl)dithiocarbamate complexes .....	37
Chapter 6: An Unusual Mercury(II) Diisopropyldithiocarbamate Coordination Polymer .....	47
Chapter 7: Discussion.....	58
Chapter 8: Conclusions and Future Directions .....	63
Conclusions .....	63
Future Directions .....	63
Appendices:.....	65
A1: Supporting information associated with Chapter 3 .....	65
A2: Supporting information associated with Chapter 4 .....	67
A3: Supporting information associated with Chapter 5 .....	82
A4: Supporting information associated with Chapter 6 .....	95
References: .....	106

## Abstract

Metal dithiocarbamate complexes possess many interesting and useful properties which has made them ubiquitous in the literature. Their discovery was early in the field of sulfur chemistry, with their applications as vulcanisation accelerators and fungicides being explored not long after. Nowadays, most published reports focus on their molecular structures, and their use as single source precursors to metal sulfide materials. Much of the research in those fields omits the relationship between their structure and properties, or their mechanism of decomposition to metal sulfide materials. This dissertation presents an investigation into the synthesis of metal dithiocarbamate complexes, with an emphasis on the relationship between their structure and properties, and how these properties affect their use as potential single source precursors to metal sulfide materials. Firstly, investigations into subtle intermolecular interactions were conducted using a nickel(II) dithiocarbamate complex. The complex was subsequently used as a single source precursor to NiS, and provided insight into the mechanisms behind its decomposition. The use of lead(II) dithiocarbamate complexes as precursors to PbS materials was investigated in a study that highlighted the relationship between the structure of the complex, and the resultant PbS material. Along the way, important insights relating to the structure and spectroscopic properties of dithiocarbamate complexes were also gained, leading to an uncovering of the mechanisms behind restricted rotation in di(isopropyl)dithiocarbamate complexes. The dissertation concludes with a study evaluating the mechanisms behind molecular isomerisation in mercury(II) dithiocarbamate complexes.

# **Chapter 1:**

## **Introduction: A Research Overview**

## Chapter 1: Introduction; A Research Overview

In the realms of materials science and inorganic chemistry, there is a perpetual exploration of new materials to solve existing and emerging problems. In this regard, dithiocarbamate-based compounds have emerged as interesting and useful materials. Dithiocarbamate (DTC) compounds are sulfur analogues of carbamate compounds (Figure 1), being first described in 1850, which was quite early in the history of organo-sulfur chemistry.<sup>1</sup>

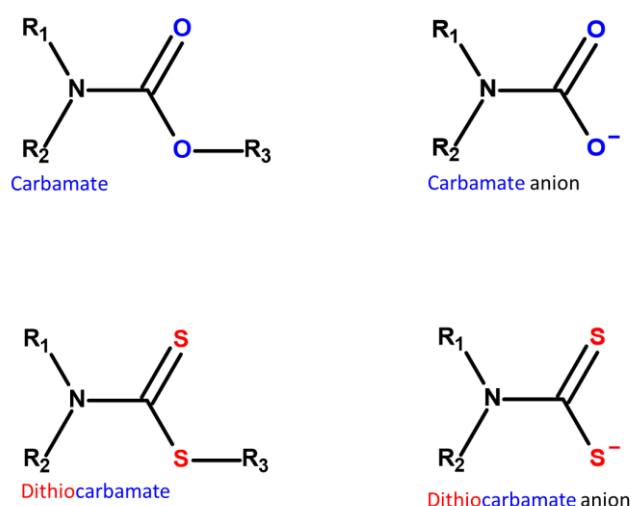
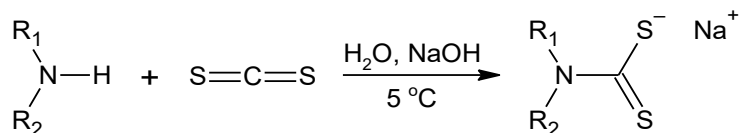


**Figure 1:** General representation of the dithiocarbamate core structure.

Interest in DTC compounds initially focused on their use as vulcanisation accelerators, being patented as early as 1859 for that purpose.<sup>2</sup> Thus, much of the early knowledge concerning DTC complexes was provided by chemists studying their application in the rubber industry between the late 1800's to early 1900's. During this time, the ability of DTC compounds to form coordination complexes by reaction with various transition metal salts was discovered, pioneered by Delépine *ca.* 1907.<sup>3</sup> Research then shifted towards the biological activity of DTC complexes and especially their insecticidal and antifungal activities.<sup>4-10</sup> DTC complexes have since become ubiquitous within the scientific literature.

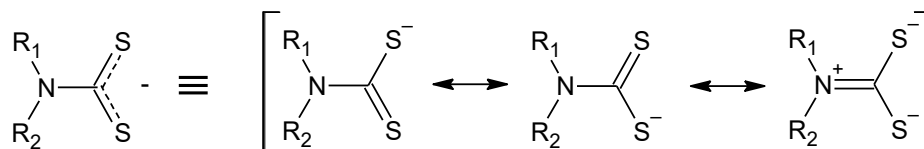
### Synthesis of dithiocarbamate anions

DTC compounds are generally synthesized by reactions between primary or secondary amines with carbon disulfide to produce intermediate dithiocarbamic acids. Dithiocarbamic acids are unstable at room temperature and were observed to decompose upon standing. This inherent instability is avoided by converting the dithiocarbamic acid to a stable salt, usually by addition of an alkali metal hydroxide (Scheme 1).



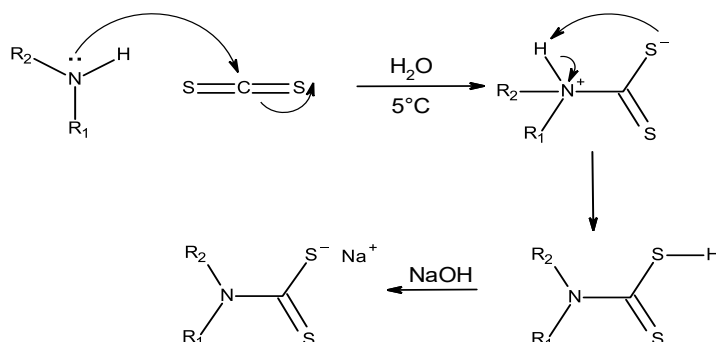
**Scheme 1:** General synthesis for *N*-alkyl dithiocarbamates

The increase in stability is achieved due to electron delocalisation within the resultant DTC anion (Scheme 2).



**Scheme 2:** Resonance stabilisation of the dithiocarbamate anion.

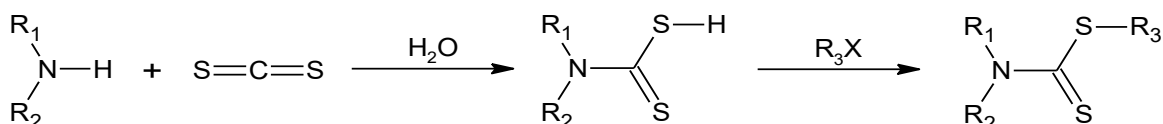
The synthesis shown in Scheme 1 proceeds if  $\text{R}_1$  and  $\text{R}_2$  are alkyl or electron donating groups, as the underlying mechanism is nucleophilic attack by nitrogen at the electron poor carbon in carbon disulfide (Scheme 3).



**Scheme 3:** Mechanism for the formation of alkyl dithiocarbamates.

In cases where  $\text{R}_1$  or  $\text{R}_2$  are electron withdrawing groups or groups that can stabilise a positive charge (on the nitrogen atom) through delocalisation (e.g. aryl groups), the reaction does not proceed to completion. Resonance effects make the synthesis of DTCs containing aromatic amines difficult but they can be overcome with the use of strong bases such as *n*-butyllithium. The reaction of the amine with alkyllithium produces lithium amide intermediates, which are more reactive towards  $\text{CS}_2$ .<sup>11</sup>

There are instances where *S,N*-substituted DTCs may be required (which are outside of the scope of this dissertation, as their ability to act as ligands is poor). In such cases, the *N*-substituted DTC anion is utilised as a nucleophile, which can react with an alkyl halide (Scheme 4).



**Scheme 4:** A general method for the synthesis of *S,N*-substituted dithiocarbamates.

Purification of *N*-substituted dithiocarbamates is achieved predominately *via* recrystallization. In practice, performing the reaction (between amine, carbon disulfide and alkali metal hydroxide) in a minimum volume of appropriate solvent results in the DTC salt precipitating from the reaction mixture. From there, filtration followed by recrystallization is often sufficient to produce *N*-dithiocarbamates of high purity.<sup>12</sup>

In some cases, e.g. in the realms of biological testing, a higher purity DTC (~99.0 % purity) is required. This is achieved by derivatisation of the intermediate dithiocarbamic acid, followed by chromatographic purification, and subsequent deprotection. This has been demonstrated by Giboreau and Morin, who substituted the metal hydroxide with tributyltin oxide producing an intermediate stannyl DTC which was purified by column chromatography, followed by deprotection.<sup>13</sup> For the purposes of this dissertation, the typical recrystallization method was found to be sufficient for the DTC salts to be used in subsequent reactions without further purification (e.g. chromatographic separation) being necessary.

### Coordination to metals

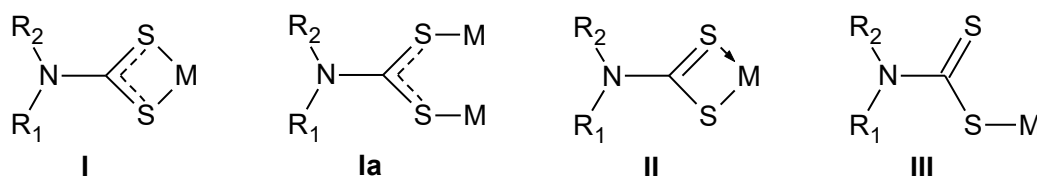


**Figure 2:** Four commonly observed *N*-dithiocarbamate coordination modes.

DTC anions possess strong metal binding properties and generally behave as chelating ligands producing coordination complexes as shown in Modes **I** and **II** in Figure 2. In Mode **I**, the DTC anion behaves as a symmetric bidentate ligand with an equal charge distribution across the  $RR'-NCS_2^-$  moiety. Mode **Ia** is a bridging variation of mode **I** resulting in dimeric, trimeric, oligomeric and polymeric structures. Mode **II** is characterized by an unsymmetrical charge distribution and thus unequal M-S bond lengths but still with bidentate coordination. In contrast, Mode **III** shows the formal negative charge localized on one of the sulfur atoms leading to a monodentate coordination geometry.

Examples of complexes containing these bonding modes will be found in Chapters 2-6, but generally the coordination modes shown in Figure 2 are independent on  $R^1$  and  $R^2$ , which have very little influence on the M-S bond nature.<sup>14</sup> There are exceptions, where steric effects of  $R^1$

and  $R^2$  affect the geometry of the resultant complex, and thus exert influence on the coordination modes.<sup>15</sup> The propensity to favour one form (over another) appears to be linked to a combination of the aforementioned steric effects, the nature of the central metal atom, and the nature of secondary interactions within the crystal structure.<sup>16, 17</sup> Where the metal has an affinity for sulfur (e.g. Hg(II)), modes I or II are favoured,<sup>18</sup> in contrast to cases where the metal has less preference (e.g. Na(I)), where mode III is dominant.<sup>19</sup> Beyond these generalisations, prediction of the coordination modes is exceptionally difficult,<sup>17</sup> for example octahedral Sn(IV) DTC complexes can contain forms III and I simultaneously.<sup>20</sup>

### Applications of dithiocarbamate complexes

DTC complexes have attracted significant attention due to their interesting and useful properties.<sup>21-23</sup> The combination of various metal centres and the ability to readily alter the DTC ligand structure has yielded complexes with biological applications<sup>24-32</sup> such as anti-neoplastic agents,<sup>33</sup> rescue agents in cisplatin therapy<sup>34</sup> and bioanalytical agents.<sup>35</sup> Another useful application of metal DTCs is their use as precursors for the synthesis of metal sulfide materials.<sup>19, 30, 36-53</sup> These materials, prepared *via* thermolysis of metal DTC complexes, have been widely investigated due to their use in the development of new sensors, IR detectors and solar cell technologies.<sup>54</sup> One of these materials is lead sulfide (PbS),<sup>55, 56</sup> which is an important IV-VI semiconductor (direct bandgap  $\sim 0.41$  eV at RT).<sup>57</sup> The exciton Bohr radius of PbS<sup>58</sup> is  $\sim 18$  nm and reducing the size of crystals to less than half of this distance results in nanocrystalline PbS with size dependant optoelectronic properties.<sup>59, 60</sup> Another class of materials that have stimulated a great deal of attention in areas such as catalytic water splitting,<sup>61-68</sup> heterogeneous catalysis,<sup>69</sup> supercapacitors,<sup>70-73</sup> batteries<sup>74-80</sup> and solar cells<sup>81-87</sup> are the nickel sulfides. Unfortunately, nickel sulfides have a propensity to exist in a range of phases, and stoichiometries, such as NiS, NiS<sub>2</sub>, Ni<sub>3</sub>S<sub>2</sub>, Ni<sub>3</sub>S<sub>4</sub>, Ni<sub>6</sub>S<sub>5</sub>, Ni<sub>7</sub>S<sub>6</sub>, Ni<sub>9</sub>S<sub>8</sub>.<sup>88-93</sup> From a synthetic standpoint, these issues provide challenges when attempting to isolate individual, targeted compounds,<sup>88, 94</sup> which is of fundamental importance as each phase possesses somewhat distinct properties. These cutting-edge applications, and experimental difficulties have aroused an impressive level of attention towards manipulation of the morphology and phase of metal sulfide materials.<sup>68, 95-106</sup> Techniques such as solvo- and hydrothermal,<sup>80, 107-112</sup> solid-state,<sup>113-115</sup> microwave-assisted,<sup>71, 77</sup> spray pyrolysis<sup>116, 117</sup> and solution-based<sup>118</sup> exist. In these, separate reactants are utilized, and the phase and morphology of the resultant metal sulfide materials is adjusted by varying the solvent, capping ligand, precursors, reaction temperature and time.

An alternative approach for the synthesis of metal sulfides employs single-source precursors (SSPs) that provide control of reactant stoichiometry and the potential to tune their thermal

properties through ligand design. An ability to adjust both the stoichiometry and thermal properties by manipulation of the SSP structure can at times allow for control of the phase and morphology of the resultant materials. Typically, the precursors are designed to have a  $MS_4$  geometry. Of the most applicable types are the xanthates<sup>89, 114, 119-122 123-125</sup> and dithiocarbamates.<sup>25-27, 126, 127 88, 126, 128-138</sup> In the case of DTC complexes, modification of the substituents in the ligand structure gives rise to a range of electronic and steric effects across associated complexes, which influences the thermal properties of the resultant metal complex, thus ultimately affect the formation of nanoparticles from these SSPs.<sup>139</sup> Therefore, by adjusting the structure of the DTC ligands the phase and morphology of resultant metal sulfide materials can be easily tuned, whilst avoiding complexities associated with systems containing separate reactants. In the context of the thermal synthesis of PbS crystals, the influence of DTC ligands bearing aliphatic and aromatic substituents has been examined, whilst for nickel sulfides, the role of amines in the solution-state thermolysis of nickel DTC complexes has been investigated.<sup>129, 131, 134</sup>



## Aims and Objectives

The aims of this dissertation are to:

- 1. Synthesise a library of metal dithiocarbamate complexes**

A library of metal dithiocarbamate complexes are to be synthesised to investigate their properties and determine their possible applications.

- 2. Investigate the properties of metal dithiocarbamate complexes**

Dithiocarbamate complexes which are synthesised will be thoroughly characterised, to investigate their spectroscopic and crystallographic properties, and how they relate to the structure.

- 3. Examine applications of metal dithiocarbamate complexes**

Dithiocarbamate complexes will be investigated in the context of possible applications. These investigations will focus specifically on their use as precursors to metal sulfide materials, or the use of dithiocarbamate structures as models for complex electronic interactions.

## Thesis Overview

The articles within this dissertation are best described as discrete sub-studies focussing on different DTC complexes, with the distinction being the nature of the metal centre. The publications are further divided on the basis of article themes, namely the use of DTCs as single source precursors to metal sulfide materials, or the investigation of the structures of the DTC complexes. Thus, each of the project aims and objectives are addressed within each publication. The articles are presented in chronological order (with respect to the sequence of experimental studies) as findings within each publication generally form the basis of investigations in subsequent publications.

The data presented in Chapters 2, 3 and 4 show that metal DTC complexes are useful as single source precursors to the synthesis of metal sulfide microstructures. Chapter 2 addresses the molecular structure of bis( $\kappa^2$ S,S'-di(isopropyl)dithiocarbamato)nickel(II) examined by single-crystal X-ray diffraction to reveal an unusual anagostic C-H  $\cdots$  Ni interaction. Thermal analysis data provided a preliminary indication that the nickel(II) DTC complex is useful as a single source precursor to nickel sulfide materials.

Chapter 3 expands on the findings presented in Chapter 2. *In situ* synchrotron powder diffraction was used to investigate the transformation of bis( $\kappa^2$ S,S'-di(isopropyl)-dithiocarbamato) nickel(II) into a novel nickel sulfide (NiS) nanostructure containing exclusively the high temperature  $\alpha$ -NiS phase. Insights into the mechanisms of decomposition were obtained.

Chapter 4 examines the formation of PbS by thermolysis of two different lead(II) DTC complexes. The data show how manipulation of the DTC ligand structure influences the resultant morphology of PbS crystals. Selected PbS crystals were used to create a novel PbS based thermistor with excellent sensitivity and an ultrarapid thermal response time.

Not only do DTC complexes possess intrinsic properties that make them useful as precursors to metal sulfide materials, they also possess a rich range of coordination geometries. The ability to produce an almost limitless range of structures by varying the central metal atom in addition to the ligand substituents provides a convenient substrate for investigation of coordination chemistry and subtle crystallographic phenomena. Thus, not only are the complexes useful as single source precursors to metal sulfide materials, the structures they form are also important for the observation of unique coordination geometries in the solid state.

The latter is best manifested in the realm of noncovalent interactions in the solid state, which are of importance as they can exert significant influence on the geometry of molecules and their associated crystal structures.<sup>140</sup> Hydrogen bonding is one such important noncovalent

interaction where the focus has traditionally been on strong acceptors such as O and N.<sup>141-146</sup> In contrast, sulfur is considered a weak acceptor, and the influence of H...S hydrogen bonds on molecular structure has received considerably less attention.<sup>147-150</sup> Such interactions are important as they influence side chain geometries and secondary structure in biological systems (such as those involving the amino acid cysteine).<sup>151-155</sup> Thus, an understanding of the nature of H...S interactions is of fundamental importance.

In Chapter 5 the crystal structure of sodium di(isopropyl)dithiocarbamate pentahydrate was redetermined<sup>156</sup> for the examination of networks of C-H...S interactions. These interactions were shown to affect the symmetry of electron density within the ligand in the solid state. The asymmetry of the electron density was manifested as temperature dependent restricted rotation of the isopropyl groups in the solution and the solid state. We also show that these C-H...S interactions are ubiquitous throughout metal dipdtdc complexes for which structural determinations have been deposited.

Another example of coordination effects studied using DTC complexes is the ability of DTC complexes to be present as a range of unique complexes, including coordination polymers. For example, the reaction of HgCl<sub>2</sub> with diethyldithiocarbamate will produce three distinct molecular complexes.<sup>157-160</sup> This is unsurprising, as reactions of HgCl<sub>2</sub> with S-donor ligands have a propensity to form coordination polymers by interaction with sulfur-containing species,<sup>161-163</sup> although detailed studies of the formation of mercury coordination polymers are scarce, especially in the case of DTC complexes.<sup>159,164,165-169</sup> In Chapter 6, a new polymeric mercury(II) di(isopropyl)dithiocarbamate complex was synthesised, and used to investigate the causation of the large range of molecular architectures and isomers within mercury(II) DTCs.<sup>37</sup> Solid- and solution-state techniques were employed to track the formation of monomeric, dimeric and polymeric mercury(II) di(isopropyl)dithiocarbamate complexes. These studies provided insights into the mechanism for isomerisation within mercury(II) DTC's.

## **Chapter 2:**

Bis( $k^2S,S'$ -di(isopropyl)  
dithiocarbamato)nickel(II): Anagostic  
C-H $\cdots$ Ni interactions and physical  
properties

## Chapter 2: Bis( $\kappa^2$ S,S'-di(isopropyl)dithiocarbamato)nickel(II): Anagostic C-H $\cdots$ Ni interactions and physical properties

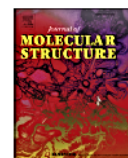
Journal of Molecular Structure 1113 (2016) 127–132



Contents lists available at ScienceDirect

Journal of Molecular Structure

journal homepage: <http://www.elsevier.com/locate/molstruc>



### Bis( $\kappa^2$ S,S'-di(isopropyl)dithiocarbamato)nickel(II): Anagostic C–H $\cdots$ Ni interactions and physical properties



Alexander Angeloski<sup>a</sup>, Anthony Thomas Baker<sup>b</sup>, Mohan Bhadbhade<sup>c</sup>,  
Andrew Michael McDonagh<sup>a,\*</sup>

<sup>a</sup> School of Mathematical and Physical Sciences, University of Technology Sydney, Ultimo, 2007, Australia

<sup>b</sup> College of Science, Health and Engineering, La Trobe University, Melbourne, 3086, Australia

<sup>c</sup> School of Chemistry, The University of New South Wales, Sydney, 2052, Australia

#### ARTICLE INFO

##### Article history:

Received 14 December 2015

Received in revised form

8 February 2016

Accepted 8 February 2016

Available online 9 February 2016

##### Keywords:

Dithiocarbamate

Anagostic

Square-planar nickel(II)

FTIR

NMR

XRD

#### ABSTRACT

The molecular structure of bis( $\kappa^2$ S,S'-di(isopropyl)dithiocarbamato)nickel(II) has been examined by single crystal X-ray diffraction. The data reveal a C–H $\cdots$ Ni anagostic interaction arising from the interaction of two non-equivalent molecules within the crystal. Thermal analysis data show that the complex decomposes at  $\sim 330^\circ\text{C}$ . The structure of the resultant NiS material was examined using scanning electron microscopy and energy dispersive X-ray spectroscopy which revealed NiS nanowires.

© 2016 Elsevier B.V. All rights reserved.

#### 1. Introduction

Dithiocarbamate complexes have attracted a significant amount of attention due to their ease of synthesis, their ability to coordinate to a range of transition and main block elements, and their interesting and useful properties [1–3]. The combination of various metal centres with the sizeable range of substituted dithiocarbamate ligands has yielded complexes with applications such as anti-neoplastic agents [4], rescue agents in cisplatin therapy [5], bio-analytical agents [6] as well as single source precursors of metal sulfide nanoparticles [7]. Dithiocarbamate complexes have also been investigated for the development of new sensors, IR detectors and solar cell technologies [8]. Substitution of the dithiocarbamate ligand gives rise to a range of electronic and steric effects across associated complexes. Some synthetic efforts have focused on optimising ligand design to allow for altered thermal properties required for nanoparticle synthesis [9]. Thus, dithiocarbamate complexes containing heterocyclic [10], alkyl [11] and phenyl [12] ligands have been pursued as single source nanoparticle

precursors.

In the context of structural interactions and possible applications of metal dithiocarbamate complexes, we have revisited the synthesis and spectroscopic characterisation of bis( $\kappa^2$ S,S'-di(isopropyl)dithiocarbamato)nickel(II) and herein report a packing polymorph of the title compound showing anagostic interactions. There are few reported structural determinations for di(isopropyl)dithiocarbamato (i-PrDTC) complexes with the only examples being Au(i-Pr<sub>2</sub>DTC)<sub>2</sub>, Pb(i-Pr<sub>2</sub>DTC)<sub>2</sub>, Hg(i-Pr<sub>2</sub>DTC)<sub>2</sub> and Ni(i-Pr<sub>2</sub>DTC)<sub>2</sub> [13–16].

#### 2. Experimental

##### 2.1. Reagents and instruments

Chemicals and solvents used in synthetic procedures were analytical or reagent grade and purchased from Sigma Aldrich and used as received. Millipore water (18.4 M $\Omega$  cm<sup>−1</sup>) was used in synthetic procedures. FT-IR spectra of single crystals were recorded using an Agilent Cary 630 FTIR spectrometer fitted with a ZnSe ATR accessory. Each spectrum was collected using 16 scans, with a resolution of 4 cm<sup>−1</sup> over the range of 4000–700 cm<sup>−1</sup>.

\* Corresponding author.

E-mail address: [Andrew.McDonagh@uts.edu.au](mailto:Andrew.McDonagh@uts.edu.au) (A.M. McDonagh).

<http://dx.doi.org/10.1016/j.molstruc.2016.02.028>

0022-2860/© 2016 Elsevier B.V. All rights reserved.

Proton and carbon nuclear magnetic resonance spectroscopy was performed using an Agilent Technologies NMR instrument operating at 500.3 MHz (for  $^1\text{H}$  experiments) and 125.7 MHz (for  $^{13}\text{C}$  experiments) at 25 °C.  $^1\text{H}$  experiments were acquired using 16 scans with a 0.01 s relaxation delay and a pulse angle of 60°. For  $^{13}\text{C}$  experiments, 300 scans with a 1.00 s relaxation delay and a pulse angle of 45° were used. The title compound was dissolved in deuterated chloroform and the solvent residual chemical shifts of 7.26 ppm (for  $^1\text{H}$  experiments) and 77.0 ppm (for  $^{13}\text{C}$  experiments) were used to calibrate the spectra. Compound **1** was dissolved in deuterated methanol and the solvent residual chemical shifts of 3.31 ppm (for  $^1\text{H}$  experiments) and 49.0 ppm (for  $^{13}\text{C}$  experiments) were used to calibrate the spectra. High resolution mass spectra were acquired using an Agilent 6510 Q-TOF with a mobile phase of 65% acetonitrile, 35% water.

UV–Vis spectra of  $\text{CHCl}_3$  solutions ( $8.3 \times 10^{-5} \text{ mol L}^{-1}$ ) were recorded using an Agilent 8453 spectrometer. The spectra were collected from 190 to 1100 nm using a resolution of 1 nm. A Thermal Advantage SDT-Q600 thermal analyser was used to obtain TG, DTG and DSC data simultaneously using alumina crucibles. Experiments were conducted using a flow of nitrogen gas ( $150 \text{ ml min}^{-1}$ ) and a heating rate of  $10 \text{ °C min}^{-1}$  over a temperature range of 25–500 °C. Residues from TGA experiments were imaged using a Zeiss Supra 55VP SEM and a Zeiss EVO LS15 SEM fitted with a Bruker Nano EDX detector was used for EDX microanalysis.

## 2.2. Crystallographic analysis

Suitable single crystals of **2** (Scheme 1) were selected under a polarizing microscope (Leica M165Z), mounted on a MicroMount (MiTeGen, USA) consisting of a thin polymer tip with a wicking aperture. The X-ray diffraction measurements were carried out on a Bruker Kappa-II CCD diffractometer at 150 K using an I $\mu$ S Incoatec Microfocus Source with Mo-K $\alpha$  radiation ( $\lambda = 0.710723 \text{ Å}$ ). The single crystal, mounted on the goniometer using cryo loops for intensity measurements, was coated with paraffin oil and then quickly transferred to the cold stream using an Oxford Cryo stream attachment. Symmetry related absorption corrections using the program SADABS [17] were applied and the data were corrected for Lorentz and polarisation effects using Bruker APEX2 software [18]. The structure was solved by direct methods and the full-matrix least-squares refinement was carried out using Shelxl [19] in Olex2 [20]. The non-hydrogen atoms were refined anisotropically. The molecular graphic was generated using Olex2 [20]. Packing diagrams were generated using the program Mercury [21].

## 2.3. Synthesis

**Synthesis of sodium di(isopropyl)dithiocarbamate (1):** Compound **1** (Scheme 1) was prepared using an adaptation of the method of Shinobu et al. [22] An aqueous solution of sodium hydroxide (4.00 g in 10 mL) was cooled with stirring to 0 °C. Diisopropylamine (10 mL) was added followed by diethyl ether (120 mL). The solution was maintained at 5 °C whilst carbon disulfide (10 mL in 5 mL of ethanol) was added dropwise. A precipitate formed immediately

upon addition and the resultant mixture was stirred for 30 min. The crude product was collected by filtration and purified by recrystallisation of a saturated methanolic solution by slow diffusion of diethyl ether. The colourless crystals were collected by filtration, washed with cold diethyl ether, and dried over  $\text{P}_2\text{O}_5$  *in vacuo*. The ligand crystallises with two waters of hydration as shown by TGA. HRMS ( $\text{M} + \text{H}^+$ ) for  $\text{NaNS}_2\text{C}_7\text{H}_{14}$  Calculated: 200.0538; Found: 200.0549.  $^1\text{H}$  NMR (500.3 MHz,  $\text{CD}_3\text{OD}$ ):  $\delta$  6.24 (br.s, 1H,  $\text{CH}(\text{CH}_3)_2$ ), 3.88 (br.s, 1H,  $\text{CH}(\text{CH}_3)_2$ ), 1.68 (br.s, 6H,  $\text{CH}(\text{CH}_3)_2$ ), 1.17 (br.s, 6H,  $\text{CH}(\text{CH}_3)_2$ ).  $^{13}\text{C}$  NMR (125.7 MHz,  $\text{CD}_3\text{OD}$ ):  $\delta$  211.2 ( $\text{NC}_2\text{S}_2$ ), 57.5 ( $\text{NC}(\text{CH}_3)_2$ ), 51.0 ( $\text{NC}(\text{CH}_3)_2$ ), 21.3 ( $\text{C}(\text{CH}_3)_2$ ), 19.8 ( $\text{C}(\text{CH}_3)_2$ ).

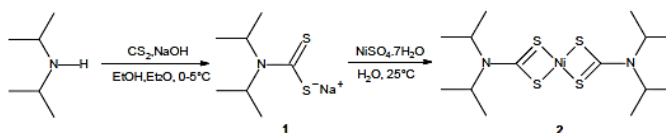
**Synthesis of bis( $\kappa^2\text{S,S}'$ -di(isopropyl)dithiocarbamate)nickel(II) (2):** An aqueous solution of compound **1** (3.00 g, 13 mmol, in 10 mL of water) was added to an aqueous solution of nickel sulfate heptahydrate (1.46 g, 5 mmol in 8 mL of water). A dark green precipitate formed immediately upon addition. The precipitate was filtered, washed with ice cold water and then diethyl ether, and dried over  $\text{P}_2\text{O}_5$  *in vacuo* to yield 1.77 g of **2** (86%). Crystals suitable for X-ray analysis were obtained as dark green blocks from solvent counter diffusion of diethyl ether into a chloroform solution of **2** over two days. HRMS ( $\text{M} + \text{H}^+$ ) for  $\text{NiN}_2\text{S}_4\text{C}_{14}\text{H}_{28}$  Calculated: 411.0562; Found: 411.0566.  $^1\text{H}$  NMR (500.3 MHz,  $\text{CDCl}_3$ ):  $\delta$  4.56 (br.s, 2H,  $\text{CH}(\text{CH}_3)_2$ ), 1.38 (br.s, 12H,  $\text{CH}(\text{CH}_3)_2$ ).  $^{13}\text{C}$  NMR (125.7 MHz,  $\text{CDCl}_3$ ):  $\delta$  205.8 ( $\text{NC}_2\text{S}_2$ ), 50.9 ( $\text{NC}(\text{CH}_3)_2$ ), 19.7 ( $\text{C}(\text{CH}_3)_2$ ) UV-vis. ( $\text{CHCl}_3$ ,  $\epsilon$  ( $\text{L mol}^{-1} \text{ cm}^{-1}$ ):  $\lambda$  618 (76), 490 (268), 435 (1581), 400 (5840), 330 (32100).

## 3. Results and discussion

### 3.1. X-ray crystal structure determination

Relevant crystal data, selected bond lengths and angles are given in Tables 1 and 2. Analysis of the X-ray crystal structure reveals some interesting differences compared to previously reported data for this compound [13,23]. In the current study, there are two independent molecules in the asymmetric unit (Fig. 1). There are no significant differences in bond lengths, angles or intermolecular interactions between the current and previous structural determinations. The nickel atoms, Ni1A (molecule A) and Ni1B (molecule B) are located at centrosymmetric special positions at (0,0,0.5) and (0,0.5,0.5), respectively. There are no significant differences between corresponding bond lengths and bond angles in the two independent molecules. Both  $\text{NiS}_4$  environments are approximately square planar, however there is a significant difference in the torsion angles about the Ni–S–C–S coordination centre;  $1.69 (6)^\circ$  for Ni1A–S1A–C1A–S2A and  $0.23 (7)^\circ$  for Ni1B–S1B–C1B–S2B. The geometry about N1A is close to planar ( $\text{C5A–N1A–C1A–S2A} = 0.2 (2)^\circ$ ) while the geometry about N1B deviates somewhat from planarity ( $\text{C5B–N1B–C1B–S2B} = -3.7 (2)^\circ$ ).

The unit cell parameters of **2** determined in the current work are summarized in Table 3 together with previously reported data for comparison [13,23]. The unit cells are different with cell volumes, c axis lengths and  $\beta$  significantly smaller in the current study compared to the previous determinations. The differences between



Scheme 1. Synthesis of **1** and **2**.



**Table 1**  
Crystal data and structure refinement parameters for 2.

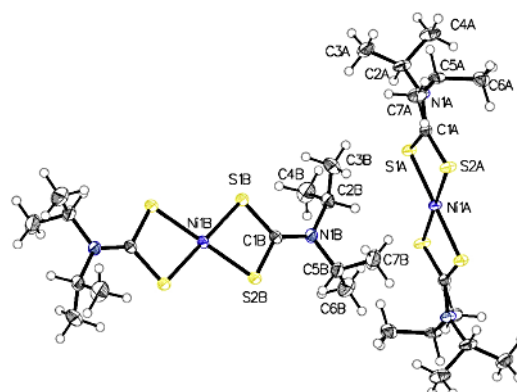
Chemical formula	2(C <sub>7</sub> H <sub>14</sub> NNi <sub>0.5</sub> S <sub>2</sub> )
<i>M<sub>r</sub></i>	411.33
Crystal system, space group	Monoclinic, <i>P</i> 2 <sub>1</sub> /c
Temperature (K)	150
<i>a</i> , <i>b</i> , <i>c</i> (Å)	8.1195 (4), 17.6976 (8), 14.6740 (8)
$\beta$ (°)	102.631 (3)
<i>V</i> (Å <sup>3</sup> )	2057.56 (18)
<i>Z</i>	4
Radiation type	Mo K $\alpha$
$\mu$ (mm <sup>−1</sup> )	1.34
Crystal size (mm)	0.27 × 0.17 × 0.06
Absorption correction	Multi-scan <i>SADABS</i> 2014/5 [17] was used for absorption correction. <i>wR</i> 2(int) was 0.1124 before and 0.0506 after correction. The Ratio of minimum to maximum transmission is 0.8221. The $\lambda/2$ correction factor is 0.00150.
<i>T</i> <sub>min</sub> , <i>T</i> <sub>max</sub>	0.613, 0.746
No. of measured, independent and observed [ <i>I</i> > 2 $\sigma$ ( <i>I</i> )] reflections	17808, 4534, 3879
<i>R</i> <sub>int</sub>	0.037
( $\sin \theta/\lambda$ ) <sub>max</sub> (Å <sup>−1</sup> )	0.643
<i>R</i> [ <i>F</i> <sup>2</sup> > 2 $\sigma$ ( <i>F</i> <sup>2</sup> )], <i>wR</i> [ <i>F</i> <sup>2</sup> ], <i>S</i>	0.027, 0.070, 1.03
No. of reflections	4534
No. of parameters	201
H-atom treatment	H-atom parameters constrained
$\Delta$ <sub>max</sub> , $\Delta$ <sub>min</sub> (e Å <sup>−3</sup> )	0.46, −0.26

**Table 2**  
Selected bond lengths (Å) and angles (°) for 2.

Bond Lengths			
Ni1B–S1B	2.1892 (4)	Ni1A–S1A	2.1965 (4)
Ni1B–S1B <sup>i</sup>	2.1891 (4)	Ni1A–S1A <sup>ii</sup>	2.1965 (4)
Ni1B–S2B <sup>i</sup>	2.1870 (4)	Ni1A–S2A <sup>ii</sup>	2.1912 (4)
Ni1B–S2B	2.1870 (4)	Ni1A–S2A	2.1912 (4)
S1B–C1B	1.7241 (16)	S1A–C1A	1.7267 (17)
S2B–C1B	1.7263 (15)	S2A–C1A	1.7294 (16)
N1B–C1B	1.314 (2)	N1A–C1A	1.316 (2)
N1B–C2B	1.493 (2)	N1A–C2A	1.4933 (19)
N1B–C5B	1.490 (2)	N1A–C5A	1.490 (2)
C2B–C3B	1.512 (3)	C2A–C3A	1.519 (2)
C2B–C4B	1.517 (3)	C2A–C4A	1.520 (3)
C5B–C6B	1.517 (3)	C5A–C6A	1.524 (2)
C5B–C7B	1.521 (3)	C5A–C7A	1.521 (2)
Bond Angles			
S1B <sup>i</sup> –Ni1B–S1B	180.000 (18)	S1A <sup>ii</sup> –Ni1A–S1A	180.0
S2B–Ni1B–S1B <sup>i</sup>	100.693 (15)	S2A–Ni1A–S1A <sup>ii</sup>	100.834 (16)
S2B <sup>i</sup> –Ni1B–S1B	100.692 (15)	S2A <sup>ii</sup> –Ni1A–S1A	100.833 (15)
S2B–Ni1B–S1B	79.307 (15)	S2A–Ni1A–S1A	79.166 (15)
S2B <sup>i</sup> –Ni1B–S1B <sup>i</sup>	79.308 (15)	S2A <sup>ii</sup> –Ni1A–S1A <sup>ii</sup>	79.167 (15)
S2B <sup>i</sup> –Ni1B–S2B	180.0	S2A <sup>ii</sup> –Ni1A–S2A	180.0
C1B–S1B–Ni1B	86.30 (5)	C1A–S1A–Ni1A	86.35 (5)
C1B–S2B–Ni1B	86.32 (5)	C1A–S2A–Ni1A	86.46 (6)
C1B–N1B–C2B	123.67 (14)	C1A–N1A–C2A	119.68 (14)
C1B–N1B–C5B	119.73 (13)	C1A–N1A–C5A	123.66 (13)
C5B–N1B–C2B	116.59 (13)	C5A–N1A–C2A	116.65 (12)
S1B–C1B–S2B	108.07 (9)	S1A–C1A–S2A	107.99 (9)
N1B–C1B–S1B	127.36 (12)	N1A–C1A–S1A	125.09 (12)
N1B–C1B–S2B	124.57 (12)	N1A–C1A–S2A	126.92 (13)
N1B–C2B–C3B	112.38 (16)	N1A–C2A–C3A	110.40 (14)
N1B–C2B–C4B	111.17 (16)	N1A–C2A–C4A	110.51 (14)
C3B–C2B–C4B	114.13 (17)	C3A–C2A–C4A	113.02 (14)
N1B–C5B–C6B	110.59 (16)	N1A–C5A–C6A	112.38 (14)
N1B–C5B–C7B	110.19 (16)	N1A–C5A–C7A	112.14 (13)
C6B–C5B–C7B	113.79 (16)	C7A–C5A–C6A	113.45 (15)

Symmetry codes: (i)  $-x, -y, -z+1$ ; (ii)  $-x, -y+1, -z+1$ .

the current crystal structure and those previously reported are most apparent when viewed along the *b* axis (Fig. 2). It is apparent that the differences in unit cells are the result of a difference in the relative rotation of molecules A and B. We propose that the differences in the current structure arise from different solvent mixtures and methods used during the crystallisation process

**Fig. 1.** ORTEP of 2 with atom labeling scheme and 50% thermal ellipsoids.**Table 3**  
Summary of previous and current unit cell parameters.

Cell volume (Å <sup>3</sup> )	<i>a</i> (Å)	<i>b</i> (Å)	<i>c</i> (Å)	$\beta$ (°)	Reference
2127	8.160 (2)	17.830 (3)	15.620 (3)	110.50 (2)	[23]
2127.94	8.147 (2)	17.820 (2)	15.630 (2)	110.32 (3)	[13]
2057.56	8.119 (4)	17.698 (8)	14.674 (8)	102.63 (3)	This work

(chloroform/ethanol evaporation vs diffusion of diethyl ether into chloroform solution in the current report).

In the current study, molecule A is oriented in a perpendicular fashion to molecule B allowing for intermolecular H···S contacts, with H6BB (on C6B) approximately 3.09 Å from S2A. There is also an intermolecular H···S contact of approximately 2.90 Å between H5A (on C5A), and S2B. These intermolecular contacts are highlighted in Fig. 3. In addition to the H···S contacts, there is a C–H···Ni contact of approximately 3.00 Å between H2B and Ni1A. Agostic and agostic interactions [24] have been described for C–H···M interactions (where M is often a d<sup>6</sup> or d<sup>8</sup> metal) [25]. Agostic interactions are 3-centre-2-electron interactions characterised by

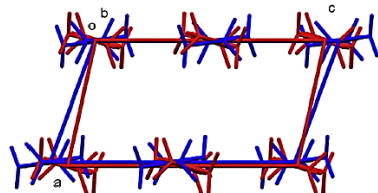


Fig. 2. Packing diagram showing a unit cell from previously determined structure [13] (blue) and unit cell (red) from the current structure viewed along the *b* axis (hydrogens and molecule A removed for clarity). (For interpretation of the references to colour in this figure legend, the reader is referred to the web version of this article.)

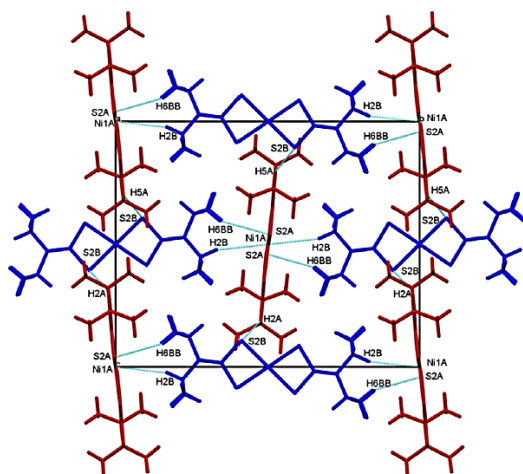


Fig. 3. Packing diagram depicting the Ni...H and S...H interactions along the *a* axis between molecule A (red) and molecule B (blue). (For interpretation of the references to colour in this figure legend, the reader is referred to the web version of this article.)

short H...M distances ( $\approx 1.8\text{--}2.2$  Å) and C–H...M angles of  $90\text{--}130^\circ$  [26]. Anagostic interactions are characterised by longer H...M distances ( $\approx 2.3\text{--}3.0$  Å) and C–H...M angles of  $110\text{--}170^\circ$  [27]. In the present case, the H...M distance of approximately 3.00 Å and C–H...Ni bond angle of ca.  $160^\circ$  is characteristic of an anagostic interaction between molecules A and B. Although such interactions have generally been reported as structural curiosities, they may play an important role in reactivity and involved in catalytic activity [28].

### 3.2. FT-IR and UV-VIS spectroscopy

IR data for **1** and **2** are presented in Fig. 4, and relevant band assignments are summarized in Table 4. There are several notable differences between the spectra. The C...N stretch moves to higher energy by  $\sim 15\text{ cm}^{-1}$  upon coordination, which indicates an increase in the carbon–nitrogen bond order [29]. A single  $\nu(\text{C}\cdots\text{S})$  band for each compound (936 and at  $938\text{ cm}^{-1}$ , respectively) indicates that the two C...S bonds (within the  $\text{NCS}_2$  moiety) are similar in nature [30]. The similar frequencies of the C...S bands for **1** and **2** suggest that the C...S bond lengths change little upon coordination of the ligand to the nickel(II) metal centre. There are two N–C stretching bands (C1–N1 and C2/C5–N1) in **1** and **2**. Upon coordination to

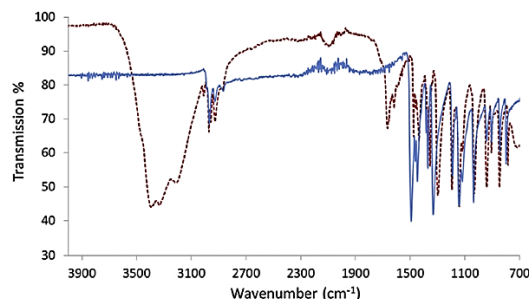


Fig. 4. FTIR spectra of **1** (red) and **2** (blue). (For interpretation of the references to colour in this figure legend, the reader is referred to the web version of this article.)

Table 4  
Selected IR spectral data for **1** and **2** ( $\text{cm}^{-1}$ ).<sup>a</sup>

Assignment	1	2
$\nu(\text{O}=\text{H})$	3300	N/A
$\nu(\text{C}=\text{H})$	2965	2963
$\delta(\text{O}=\text{H})$	1665	N/A
$\nu_s(\text{C}\cdots\text{N})$	1472	1487
$\nu_{as}(\text{CH}_3)$	1429	1437
$\nu_{sy}(\text{CH}_3)$	1352	1364
$\nu(\text{N}=\text{C})$	1296	1327
$\rho(\text{CH}_3)$	1139	1139
$\nu_s(\text{C}\cdots\text{S})$	936	938

<sup>a</sup>  $\nu$  = stretching mode,  $\delta$  = bending mode,  $\rho$  = rocking mode.

nickel(II), both bands increase in frequency indicating shortened N–C bond lengths within the delocalised electron environment about the planar nitrogen. Bands at  $\sim 1430$ ,  $1350$  and  $1140\text{ cm}^{-1}$  are assigned to the asymmetric, symmetric and rocking vibrations of the methyl groups, respectively [31]. We assign the increase in the energies of the vibrations associated the  $\text{CH}_3$  groups when moving from **1** to **2** to reduced molecular flexibility arising from Ni...H and S...H interactions. Bands below  $900\text{ cm}^{-1}$  were not able to be unambiguously assigned due to vibrational mode coupling, most probably involving C–S stretches [31]. Another notable difference is the presence of O–H stretches and bends in **1**, which are attributed to water within the ligand matrix (as indicated by TGA data) but absent in the complex (as revealed by X-ray crystal data).

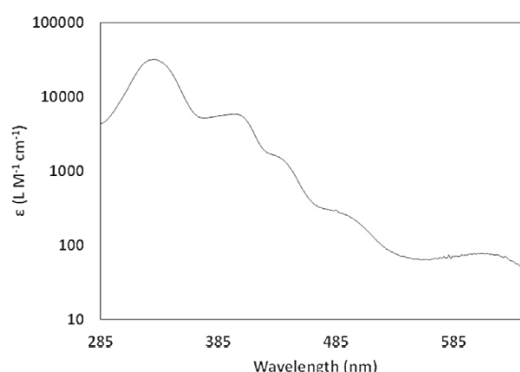


Fig. 5. Electronic spectrum of **2** in chloroform.



The electronic spectrum of **2** in chloroform (Fig. 5) shows three broad d–d absorption transitions at 618 ( $\epsilon = 76 \text{ L M}^{-1} \text{ cm}^{-1}$ ), 490 ( $\epsilon = 268 \text{ L M}^{-1} \text{ cm}^{-1}$ ) and 435 nm ( $\epsilon = 1581 \text{ L M}^{-1} \text{ cm}^{-1}$ ). These bands are assigned to the  $^1A_{1g} \rightarrow ^1A_{2g}$ ,  $^1A_{1g} \rightarrow ^1B_{1g}$  and  $^1A_{1g} \rightarrow ^1E_g$  transitions respectively [32–34]. The presence of three d–d transition bands is characteristic for square planar  $d^8$  nickel(II) complexes, and in agreement with the crystal structure of **2** [33]. The spectrum also shows an intense ligand to metal charge-transfer band at 330 nm ( $\epsilon = 32124 \text{ L M}^{-1} \text{ cm}^{-1}$ ) [33,35,36] as well as an intense band at 400 nm ( $\epsilon = 5844 \text{ L M}^{-1} \text{ cm}^{-1}$ ) which is assigned to  $\pi \rightarrow \pi^*$  transitions within the ligand N–C=S moiety [35].

### 3.3. $^1\text{H}$ and $^{13}\text{C}$ NMR studies

$^1\text{H}$  NMR spectra of **1** and **2** are shown in Fig. 6. The spectrum of **1** shows two sets of peaks arising from the ligand protons, suggesting that the two isopropyl groups are inequivalent. A signal at 6.24 ppm is assigned to one of the methine protons while a signal at 3.88 ppm is assigned to the other. The different environments may arise due to C–H $\cdots$ S interactions [27]. Similarly, two resonances at 1.68 and 1.17 ppm are assigned to the methyl groups in two inequivalent environments. Similar observations have been observed in di(isopropyl)dithiocarbamate complexes [37,38] and arise due to hindered rotation about an N–C bond (as a result the aforementioned C–H $\cdots$ S interaction) creating two magnetically inequivalent environments [37–39]. The  $^1\text{H}$  NMR spectrum of **2** contains only one signal arising from the methine protons and one signal for the methyl groups. This suggests that coordination to the metal centre diminishes the effect of C–H $\cdots$ S interactions. However, in the spectra of both **1** and **2**, the signals are broad, characteristic of underlying dynamic processes in solution. Signals assigned to  $\text{CH}(\text{CH}_3)_2$  in the spectrum of **2** appear as a broad singlet at 4.56 ppm, which is characteristic of protons associated with the H $\cdots$ Ni anagostic interaction [27,40,41]. Signals assigned to  $\text{CH}(\text{CH}_3)_2$  protons appear at 1.38 ppm, which has previously been suggested as an indicator of interactions with the  $\text{CS}_2$  moiety [42]. The change in the number of signals in the spectrum of **2** compared to that of **1** is attributed to a change in the intermolecular attractions in the solution state that occur upon coordination.

The  $^{13}\text{C}$  NMR spectra show signals arising from each of the carbon atoms of **1** and **2** (Fig. 7). The signals at  $\delta$  211.2 and  $\delta$  205.7 for **1** and **2**, respectively, are attributed to the  $\text{NCS}_2$  moiety. An upfield shift of  $\sim 5.5$  ppm upon moving from **1** to **2** is the result of increased electron density within the  $\text{NCS}_2$  moiety [43–45], which correlates with decreased C–N bond lengths indicated by FTIR spectroscopy. Two signals assigned to the methyl groups of **1**, as

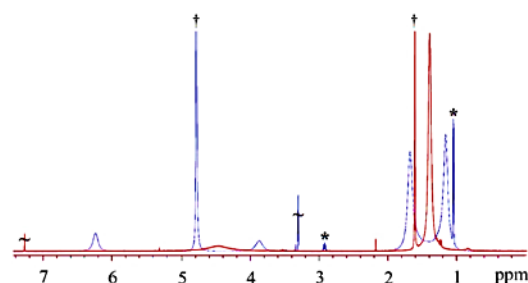


Fig. 6.  $^1\text{H}$  NMR spectra for **1** (blue, solvent =  $\text{CD}_3\text{OD}$ ) and **2** (red, solvent =  $\text{CDCl}_3$ ), at  $25^\circ\text{C}$ . † denotes solvent signal, \* denotes residual diisopropylamine, † denotes residual  $\text{H}_2\text{O}$ . (For interpretation of the references to colour in this figure legend, the reader is referred to the web version of this article.)

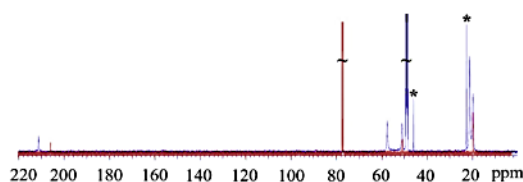


Fig. 7.  $^{13}\text{C}$  NMR spectra for **1** (blue, solvent =  $\text{CD}_3\text{OD}$ ) and **2** (red, solvent =  $\text{CDCl}_3$ ), at  $25^\circ\text{C}$ . † denotes solvent signal, \* denotes residual diisopropylamine. The 90–190 ppm region has been omitted for clarity. (For interpretation of the references to colour in this figure legend, the reader is referred to the web version of this article.)

well as two signals for the methine carbon atoms are consistent with the assignments made for the  $^1\text{H}$  NMR spectra. Similarly, fewer signals are observed in the spectrum of **2**.

### 3.4. Thermal and microstructural analysis

Thermogravimetric analysis (TGA) and differential scanning calorimetry (DSC) data for **2** are shown in Fig. 8. There was insignificant mass loss in the region  $25$ – $120^\circ\text{C}$ , which indicates a lack of water (bound or otherwise) and is in agreement with the crystallographic data. Decomposition of **2** occurs in a single event between  $298^\circ\text{C}$  and  $340^\circ\text{C}$  with an endothermic peak at  $333^\circ\text{C}$  corresponding to the loss of both ligands to produce the final decomposition product, NiS. The calculated mass loss for this event (78.1%) agrees with that observed (78.0%). The correlation between  $\text{DTG}_{\text{max}}$  and  $\text{DSC}_{\text{max}}$  suggests that thermal mass loss occurs at the onset of a solid–liquid phase change. This correlation has been commented on previously [46].

Scanning electron microscopy analysis of the TGA residue from **2** was performed and a representative micrograph is shown in Fig. 9. The material contains globular particles as well as rods with dimensions of  $\sim 0.15 \times \sim 2 \mu\text{m}$ . Energy dispersive X-ray (EDX) analysis, Fig. 9, shows that the residue contains nickel and sulfur only. This finding is in agreement with the assignment of the formula NiS for the thermolysis product. NiS nanowires obtained from the solid phase thermal decomposition of a dithiocarbamate precursor molecule have not been reported before.

## 4. Conclusions

The molecular structure of single crystals of bis( $\kappa^2\text{SS}'$ -di(isopropyl)dithiocarbamate)nickel(II) (**2**) reveal C–H $\cdots$ Ni anagostic interactions arising from the interaction of two non-equivalent molecules.

FTIR and NMR spectroscopy data show how electron density

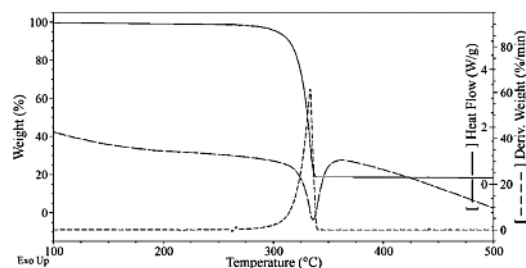


Fig. 8. TGA and DSC data for **2**. The  $25$ – $100^\circ\text{C}$  region has been omitted for clarity.

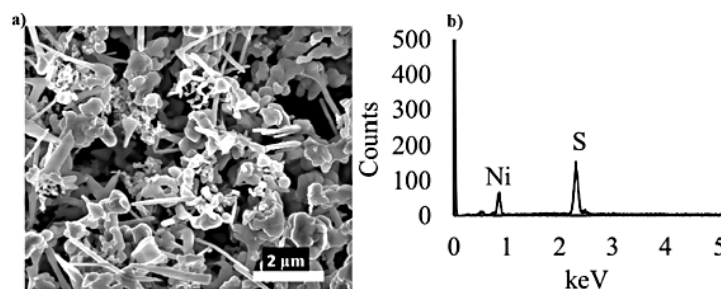


Fig. 9. SEM micrograph (a) and EDX plot (b) of the TGA residue from 2.

about the NCS<sub>2</sub> moiety is modified upon coordination of the ligand to the nickel metal centre. The nickel complex decomposes at ~330 °C in a single step, as shown by the TGA data. Upon heating, nickel(II) sulfide is produced, which upon examination using SEM and EDX spectroscopy revealed NiS nanowires.

#### Acknowledgements

We thank Dr. Ronald Shimon for laboratory assistance, Mr Jean-Pierre Guerbois for assistance with TGA, and Dr Katie McBean for assistance with SEM.

#### Supplementary data

CCDC 1440730 contains the supplementary crystallographic data for this paper. These data can be obtained free of charge via <http://www.ccdc.cam.ac.uk/conts/retrieving.html> (or from the Cambridge Crystallographic Data Centre, 12, Union Road, Cambridge CB2 1EZ, UK; fax: +44 1223 336033).



#### References

- [1] A.A. Aly, A.B. Brown, T.M.L. Bedair, E.A. Ishak, *J. Sulfur Chem.* 33 (2012) 605–617.
- [2] T. Yoshimura, Y. Kotake, *Antioxid. Redox Sign.* 6 (2004) 639–647.
- [3] J.J. Steggerda, J.A. Cras, J. Willemse, *Recl. Trav. Chim. Pays-B.* 100 (1981) 41–48.
- [4] M.N. Kouodom, G. Boscutti, M. Celegato, M. Crisma, S. Siran, D. Aldinucci, F. Formaggio, L. Ronconi, D. Fregona, *J. Inorg. Biochem.* 117 (2012) 248–260.
- [5] R.F. Borch, J.C. Katz, P.H. Lieder, M.E. Pleasants, *Proc. Natl. Acad. Sci. U. S. A.* 77 (1980) 5441–5444.
- [6] K. Saito, M.K. Ohno, *Anal. Biochem.* 349 (2006) 16–24.
- [7] G.S. Sivagurunathan, K. Ramalingam, C. Rizzoli, *Polyhedron* 65 (2013) 316–321.
- [8] R.S. Mane, C.D. Lockhande, *Mater. Chem. Phys.* 65 (2000) 1–31.
- [9] D.C. Onwudiwe, C.A. Strydom, O.S. Oluwafemi, E. Hosten, A. Jordaan, *Dalton Trans.* 43 (2014) 8703–8712.
- [10] T. Mthethwa, V.S.R.R. Pullabhotla, P.S. Mdluli, J.W. Smith, N. Revaprasadu, *Polyhedron* 28 (2009) 2977–2982.
- [11] M. Lazell, S.K. Norager, P. O'Brien, N. Revaprasadu, *Mater. Sci. Eng. C-Mater. Biol. Appl.* 16 (2001) 129–133.
- [12] D.C. Onwudiwe, P.A. Ajibade, B. Omondi, *J. Mol. Struct.* 987 (2011) 58–66.
- [13] P.C. Healy, J.W. Connor, B.W. Skelton, A.H. White, *Aust. J. Chem.* 1990 (1990) 1083–1095.
- [14] M. Ito, H. Iwasaki, *Acta Crystallogr. B* 36 (1980) 443–444.
- [15] H. Iwasaki, M. Ito, *Acta Crystallogr. B* 35 (1979) 2720–2721.
- [16] T.A. Rodina, A.V. Ivanov, A.V. Gerasimenko, O.V. Loseva, O.N. Antzutkin, V.I. Sergienko, *Polyhedron* 40 (2012) 53–64.
- [17] Bruker, SADABS, in: Madison (Ed.), Bruker AXS Inc., Wisconsin, USA, 2001.
- [18] Bruker, Apex2 and Saint, in: Madison (Ed.), Bruker AXS Inc., Wisconsin, USA, 2007.
- [19] G.M. Sheldrick, *Acta Crystallogr. A* 64 (2008) 112–122.
- [20] O.V. Dolomanov, L.J. Bourhis, R.J. Gildea, J.A.K. Howard, H. Puschmann, *J. Appl. Crystallogr.* 42 (2009) 339–341.
- [21] C.F. Macrae, P.R. Edgington, P. McCabe, E. Pidcock, G.P. Shields, R. Taylor, M. Towler, J. van de Streek, *J. Appl. Crystallogr.* 39 (2006) 453–457.
- [22] L.A. Shinobu, S.G. Jones, M.M. Jones, *Acta Pharmacol. Toxicol.* 54 (1984) 189–194.
- [23] P.W.G. Newman, A.H. White, *J. Chem. Soc. Dalton* (1972) 2239–2243.
- [24] M. Brookheart, M.L.H. Green, G. Parkin, *Proc. Nat. Acad. Sci. U. S. A.* 104 (2007) 6908–6914.
- [25] J. Ruiz, J. Lorenzo, C. Vicente, G. Lopez, J.M.L. de Luzuriaga, M. Monge, F.X. Aviles, D. Bautista, V. Moreno, A. Laguna, *Inorg. Chem.* 47 (2008) 6990–7001.
- [26] M. Brookheart, M.L.H. Green, G. Parkin, *J. Organomet. Chem.* 250 (1983) 395–408.
- [27] A. Husain, S.A.A. Nami, S.P. Singh, M. Oves, K.S. Siddiqi, *Polyhedron* 30 (2011) 33–40.
- [28] N. Ding, J. Zhang, T.S. Andy-Hor, *Dalton Trans.* (2009) 1853–1858.
- [29] B.A. Prakasham, M. Lahtinen, A. Peuronen, M. Muruganandham, E. Kolehmainen, E. Haapaniemi, M. Sillanpää, *Inorg. Chim. Acta* 425 (2015) 239–246.
- [30] F. Bonati, R. Ugo, *J. Organomet. Chem.* 10 (1967) 257–268.
- [31] K. Nakamoto, J. Fujita, R.A. Condrate, Y. Morimoto, *J. Chem. Phys.* 39 (1963) 423.
- [32] A.B.P. Lever, *Inorganic Electronic Spectroscopy*, Elsevier, 1984.
- [33] R. Dingle, *Inorg. Chem.* 10 (1971) 1141–1144.
- [34] S.C. Bajja, A. Mishra, *J. Coord. Chem.* 64 (2011) 2727–2734.
- [35] W.W.H. Wong, D.E. Phipps, P.D. Beer, *Polyhedron* 23 (2004) 2821–2829.
- [36] V.T. Yilmaz, T.K. Yazıcılar, H. Cesur, R. Ozkanca, F.Z. Maras, *Synth. React. Inorg. Met.-Org. Chem.* 33 (2003) 589–605.
- [37] A.N. Bhat, R.C. Fay, D.F. Lewis, A.F. Lindmark, S.H. Strauss, *Inorg. Chem.* 13 (1974) 886–892.
- [38] S. Bhattacharya, B.K. Kanungo, S. Sahoo, *J. Coord. Chem.* 59 (2006) 371–378.
- [39] R.M. Golding, P.C. Healy, P.W.G. Newman, E. Sinn, A.H. White, *Inorg. Chem.* 11 (1972) 2435–2440.
- [40] H.V. Huynh, L.R. Wong, P.S. Ng, *Organometallics* 27 (2008) 2231–2237.
- [41] Y. Han, H.V. Huynh, G.K. Tan, *Organometallics* 26 (2007) 6447–6452.
- [42] R. Taylor, O. Kennard, *J. Am. Chem. Soc.* 104 (1982) 5063–5070.
- [43] L. Ronconi, L. Giovagnini, C. Marzano, F. Bettio, R. Graziani, G. Pilloni, D. Fregona, *Inorg. Chem.* 44 (2005) 1867–1881.
- [44] H.L.M. Van Gaal, J.W. Diesveld, F.W. Pijpers, J.G.M. Van Der Linden, *Inorg. Chem.* 16 (1979) 3251–3260.
- [45] R. Nomura, A. Takabe, H. Matsuda, *Polyhedron* 6 (1987) 411–416.
- [46] I. Jen-La Plante, T.W. Zeid, P. Yang, T. Mokari, *J. Mater. Chem.* 20 (2010) 6612.

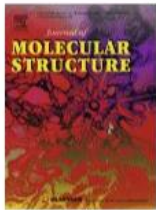
### Author Contributions and Copyright Information:

#### Bis( $\kappa^2$ S,S'-di(isopropyl)dithiocarbamato) nickel(II): Anagostic C-H $\cdots$ Ni interactions and physical properties

- A. Angeloski performed the synthesis, isolation, all measurements (excluding single-crystal X-ray diffraction), data analysis, and wrote the manuscript.
- M. Bhadbhade performed the single-crystal X-ray diffraction
- A.T. Baker revised the manuscript
- A.M. McDonagh provided conceptual advice and revised the manuscript
- All authors have reviewed the manuscript, and all persons providing assistance have been acknowledged within the manuscript.



[Home](#) [Create Account](#) [Help](#)



**Title:** Bis( $\kappa^2$ S,S'-di(isopropyl)dithiocarbamato)nickel(II): Anagostic C-H $\cdots$ Ni interactions and physical properties  
**Author:** Alexander Angeloski, Anthony Thomas Baker, Mohan Bhadbhade, Andrew Michael McDonagh  
**Publication:** Journal of Molecular Structure  
**Publisher:** Elsevier  
**Date:** 5 June 2016  
Copyright © 2016 Elsevier B.V. All rights reserved.

**LOGIN**

If you're a copyright.com user, you can login to RightsLink using your copyright.com credentials.  
Already a RightsLink user or want to [learn more?](#)

Please note that, as the author of this Elsevier article, you retain the right to include it in a thesis or dissertation, provided it is not published commercially. Permission is not required, but please ensure that you reference the journal as the original source. For more information on this and on your other retained rights, please visit: <https://www.elsevier.com/about/our-business/policies/copyright#Author-rights>

Permission for reuse of the article within this dissertation has been obtained.

## **Chapter 3:**

Conversion of single-crystals of a  
nickel(II) dithiocarbamate complex to  
nickel sulfide crystals



## Chapter 3: Conversion of single-crystals of a nickel(II) dithiocarbamate complex to nickel sulfide crystals

Inorganica Chimica Acta 487 (2019) 228–233



Contents lists available at ScienceDirect

Inorganica Chimica Acta

journal homepage: [www.elsevier.com/locate/ica](http://www.elsevier.com/locate/ica)



Research paper

### Conversion of single crystals of a nickel(II) dithiocarbamate complex to nickel sulfide crystals



Alexander Angeloski<sup>a</sup>, Michael B. Cortie<sup>a</sup>, John A. Scott<sup>a</sup>, Dayanne M. Bordin<sup>a</sup>, Andrew M. McDonagh<sup>a,\*</sup>

<sup>a</sup> School of Mathematical and Physical Sciences, University of Technology Sydney, Ultimo 2007, Australia

#### ARTICLE INFO

**Keywords:**  
Dithiocarbamate  
Nickel  
Thermolysis

#### ABSTRACT

Single crystals of bis( $\kappa^2$ S,S'-di(isopropyl)dithiocarbamato) nickel(II) were utilized as a single source precursor for the formation of NiS via thermolysis. The complex decomposed at  $-250^\circ\text{C}$  to form  $\alpha$ -NiS exclusively with no  $\beta$ -NiS detected. Analysis of the thermolysis regime using *in situ* techniques showed that the thermolysis occurs in a single step with the major volatile side-products being isopropyl-isothiocyanate and carbon disulfide. The resultant NiS was examined using SEM and TEM to reveal a retention of precursor crystal edge-length and angle relationships.

#### 1. Introduction

Nickel sulfides are renowned for their superb chemical and physical properties, which have stimulated a great deal of attention in areas such as, but not limited to, catalytic water splitting [1–8], heterogeneous catalysis [9], supercapacitors [10–13], batteries [14–20] and solar cells [21–27]. These cutting-edge applications have aroused an impressive level of attention towards manipulation of the morphology of nickel sulfide materials [8,28–33]. Unfortunately, these efforts are complicated by the propensity of nickel sulfides to exist in a range of phases, and stoichiometries, such as NiS, NiS<sub>2</sub>, Ni<sub>3</sub>S<sub>2</sub>, Ni<sub>3</sub>S<sub>4</sub>, Ni<sub>6</sub>S<sub>5</sub>, Ni<sub>7</sub>S<sub>6</sub>, Ni<sub>9</sub>S<sub>8</sub> [34–39]. From a synthetic standpoint, these issues provide challenges when attempting to isolate individual, targeted compounds [34,40], which is of fundamental importance as each phase possesses somewhat distinct properties.

Techniques utilizing separate reactants have been applied to the synthesis of Ni<sub>x</sub>S<sub>y</sub> compounds, with varying degrees of success. Synthetic methods include solvo- and hydrothermal [20,41–46], solid-state [47–49], microwave-assisted [11,17], spray pyrolysis [50,51] and solution-based [52] techniques. In these cases, the phase and morphology of the resultant Ni<sub>x</sub>S<sub>y</sub> material is adjusted by varying the solvent, capping ligand, precursors, reaction temperature and time.

An alternative approach employs single-source precursors (SSPs) that provide control of reactant stoichiometry and the potential to tune their thermal properties through ligand design. An ability to adjust both the stoichiometry and thermal properties by manipulation of the SSP structure can at times allow for control of the phase and morphology of

the resultant materials.

There has been considerable interest in the development of SSPs for the synthesis of nickel sulfides, with a focus on SSPs with NiS<sub>4</sub> geometry such as dithiocarbamates [34,53–61] and xanthates [35,48,62–65]. Furthermore, insight into the processes involved during the thermal conversion of SSPs is important to allow for manipulation of the SSP structure to achieve suitable properties such as low reaction temperature and/or selective nanostructures as shown in recent studies utilizing low-temperature melts of xanthates [66]. The role of amines in the solution-state thermolysis of nickel dithiocarbamates has been investigated [54,56,59] although no studies focusing on the processes involved in the solid state decomposition of nickel dithiocarbamates into nickel sulfide nanostructures are extant.

Nickel(II) sulfide (NiS), of relevance to this work, has two polymorphic phases, with a thermodynamically stable low temperature rhombohedral phase ( $\beta$ ,  $R_3 m$ ) and a metastable high temperature hexagonal phase ( $\alpha$ ,  $P6_3/mmc$ ). In the  $\beta$  form, Ni<sup>II</sup> atoms are surrounded by five sulfur atoms forming a tetragonal bipyramidal geometry, whilst in the  $\alpha$  form Ni<sup>II</sup> atoms are octahedrally coordinated to six sulfur atoms. The transformation between  $\alpha$  to  $\beta$  occurs between 280 and 380 °C with a volume change of  $\sim 4\%$  [35,36,67,68].

Whilst examining an unusual C–H...Ni anagostic interaction within crystals of the title compound [61], we also observed that the complex decomposed to produce NiS at elevated temperatures. Here we investigate the transformation of the nickel bis-diisopropyl dithiocarbamate SSP, bis( $\kappa^2$ S,S'-di(isopropyl)dithiocarbamato) nickel(II), Ni(DIPDC)<sub>2</sub>, (Fig. 1) which yields a novel nickel sulfide (NiS)

\* Corresponding author.

E-mail address: [Andrew.McDonagh@uts.edu.au](mailto:Andrew.McDonagh@uts.edu.au) (A.M. McDonagh).

<https://doi.org/10.1016/j.ica.2018.12.014>

Received 19 October 2018; Received in revised form 7 December 2018; Accepted 7 December 2018

Available online 10 December 2018

0020-1693/ © 2018 Elsevier B.V. All rights reserved.

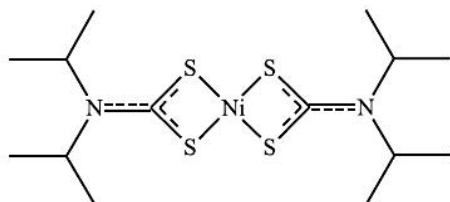


Fig. 1. Chemical structure of bis( $\kappa^2$ S,S'-di(isopropyl)dithiocarbamato)nickel (II).

nanostructure, and show that the high temperature  $\alpha$  phase can be prepared at relatively low temperatures using this method.

## 2. Results and discussion

Single crystals of  $\text{Ni}(\text{DIPDTC})_2$  in the size range 200–400  $\mu\text{m}$  were obtained by slow evaporation of a chloroform solution. Decomposition upon heating was monitored using variable temperature isotropic light microscopy (Video S1). Photomicrographs were acquired in the temperature range 30–500  $^\circ\text{C}$  whilst heating at  $3^\circ\text{C min}^{-1}$  under a flow of  $25 \text{ mL min}^{-1}$  of nitrogen. The images reveal a transition from  $\text{Ni}(\text{DIPDTC})_2$  to a solid material (Fig. 2), which we show to be  $\alpha$ -NiS (see below). Cracks in the crystal surface appear at 210  $^\circ\text{C}$  and the crystals begin to decompose at 219  $^\circ\text{C}$ , evidenced by the formation of gas bubbles within the crystals. Upon completion of the decomposition process, the crystal edge lengths have contracted significantly.

SEM images of NiS obtained from the variable temperature optical microscopy experiment show that the residue maintained the overall cuboidal morphology of  $\text{Ni}(\text{DIPDTC})_2$  crystals (Fig. 3). That is, the ratios of the edge lengths are in agreement with those of the crystals measured using optical microscopy prior to decomposition (Fig. 3). Higher magnification images of the pseudo-facet edges (Fig. 4b–e) reveal highly porous and textured NiS, with somewhat acicular crystallites extending from the surface. The individual crystallites do not show a preferred orientation with respect to the pseudo-facets and are present

as randomly orientated aciculae. This complex 3D structure was not observed in previous thermolyses of  $\text{Ni}(\text{DIPDTC})_2$  that utilized faster heating rates ( $10^\circ\text{C min}^{-1}$ ) although the aciculae were present in the current and previous work [61]. SEM-EDX mapping revealed that the structure contained an even distribution of Ni and S within the sample (Fig. 4e).

TEM micrographs of the resultant structure reveal a mixture of filamentous and globular NiS crystallites. SAED of the assembled structure produced a polycrystalline diffraction pattern indicating an overlap of many orientated NiS crystallites, with no preferred orientation relative to the edges of the three dimensional structures (Fig. 5a). Many of the observed filamentous crystallites are attached directly to the globular structures (Fig. 5b).

*In situ* real time synchrotron powder XRD experiments were performed to investigate the transformation of the SSP. Diffraction patterns were collected whilst  $\text{Ni}(\text{DIPDTC})_2$  was heated under an atmosphere of helium at a rate of  $3^\circ\text{C min}^{-1}$  (Fig. 6). The onset of decomposition is marked by a sudden decrease in the peak area of  $\text{Ni}(\text{DIPDTC})_2$  at 303  $^\circ\text{C}$  (Fig. 6) with an associated increase in the peak area for NiS. The subsequent 35  $^\circ\text{C}$  is characterized by the simultaneous decomposition of  $\text{Ni}(\text{DIPDTC})_2$  and the formation of NiS, as indicated by the overlapping diffraction patterns.

All of the  $\text{Ni}(\text{DIPDTC})_2$  decomposed by 340  $^\circ\text{C}$  yielding NiS in the high temperature  $\alpha$ -phase (indexed using COD 9009240, Fig. S1). There was no change in the peak areas assigned to NiS until 460  $^\circ\text{C}$ , whereupon the areas decreased and peaks assigned to NiO (COD 4320499) appeared (Fig. 6) due to partial oxidation of NiS (attributed to minute concentrations of oxygen in the protective helium flow). Oxidation halted as heating was discontinued and upon cooling to room temperature, the NiS retained the high-temperature  $\alpha$ -phase [69]. The expected low temperature  $\beta$ -NiS phase (COD 1538656) was not detected at any stage during the experiments (Fig. 6). Previous studies of the Ni-S binary phase system [70] showed both the  $\alpha$  and  $\beta$  polymorphs of NiS are stable in the temperature range 282  $^\circ\text{C}$  to 379  $^\circ\text{C}$ , with their relative proportions dependent on the sulfur content of the binary system. Specifically,  $\beta$ -NiS has Ni:S ratios in the range of 64:36–67:33 wt% and  $\alpha$ -NiS has Ni:S ratios in the range of 63:37–64:34 wt%. Above  $\sim 380^\circ\text{C}$  only the  $\alpha$ -phase is stable. In the current work, where  $\alpha$ -NiS formed

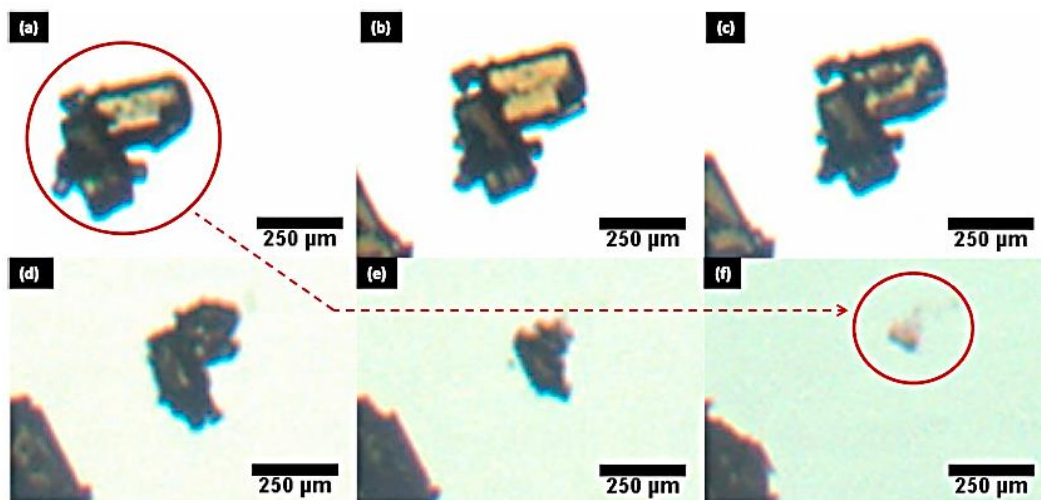


Fig. 2. Variable-temperature optical image sequence extracts from Video S1 showing the decomposition of  $\text{Ni}(\text{DIPDTC})_2$  at 30, 189, 219, 243, 246 and 255  $^\circ\text{C}$  (a–f). Conversion of the precursor crystals to NiS is indicated in red. (For interpretation of the references to colour in this figure legend, the reader is referred to the web version of this article.)



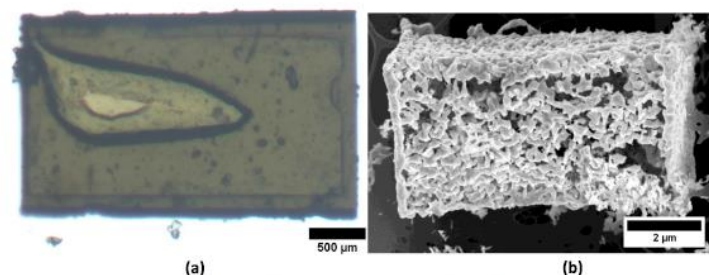


Fig. 3. (a) Optical micrograph of a typical single crystal of  $\text{Ni}(\text{DIPDTC})_2$  before thermolysis, and (b) SEM micrograph of a block of material generated by thermolysis of a single crystal of  $\text{Ni}(\text{DIPDTC})_2$ .

between  $\sim 310$  and  $350^\circ\text{C}$ , the SSP contains Ni and S in the ratio 1:4, which may favour formation of the  $\alpha$ -phase over the  $\beta$ -phase. Inductively coupled plasma-mass spectrometry analysis of the NiS prepared in this work revealed a Ni content of 63 wt%, consistent with the  $\alpha$ -phase stoichiometry. Furthermore, no  $\text{Ni}_3\text{S}_4$  or  $\text{NiS}_2$  were detected in the X-ray diffraction patterns of the decomposition product, which we attribute to the considerable proportion of the S content of the precursor that was volatilized (see below).

Thermogravimetric and gas chromatography data are shown in Fig. 7. There was no mass loss between 30 and  $200^\circ\text{C}$  indicating an absence of water. Mass loss occurred in a single event beginning at  $\sim 250^\circ\text{C}$ , with the maximum rate of mass loss at  $320^\circ\text{C}$ . The mass loss of this event (84%) corresponds to the loss of the DIPDTC ligand material, with the exception of one S per Ni, leading to the formation of NiS (calc. 78%). The discrepancy between the calculated and observed mass loss ( $\sim 6\%$ ) of this thermolysis event is attributed to a combination of instrument baseline drift, and partial oxidation of the resultant NiS (evidenced by the formation of  $\text{SO}_2$  during, and extending slightly beyond, the maximum rate of mass change). A second mass loss event of  $\sim 1.5\%$  was observed between  $430$  and  $500^\circ\text{C}$ . These results are consistent with previous work [61] although the onset of mass loss occurred  $\sim 50^\circ\text{C}$  lower than previously reported due to the slower heating rate employed in the current study. Differences in the onset of mass loss between these *in situ* techniques is attributed to differing thermal

environments in sample environment geometries in synchrotron, microscope hot-stage and thermogravimetric furnaces.

*In-situ* gas chromatography mass spectrometry was used to analyse the decomposition products produced during thermolysis (Fig. 7b). The volatile species were identified by comparison of their mass fragmentation patterns to a NIST database and are: isopropyl isothiocyanate ( $m/z = 101.2$ ), isopropyl amine ( $m/z = 101.2$ ), carbon disulfide ( $m/z = 76.2$ ), isopropyl disulfide ( $m/z = 150.1$ ), sulfur dioxide ( $m/z = 64.1$ ) and propene ( $m/z = 42.1$ ). Evolved-gas experiments where the furnace atmosphere was continuously monitored by MS provided data describing the temporal evolution of volatile species. Extracted ion chromatographs (Fig. 7c) show that volatile species evolve within the same temperature range as the decomposition event and increase in abundance as the rate of mass loss approaches the maximum. Ions arising from isopropyl isothiocyanate and di-isopropyl amine overlap at  $m/z = 101.2$ , and thus their evolution during the main mass loss event is convoluted. The co-existence of these species in the gas phase suggests that cleavage of the di-isopropyl N–C bond and the dithiocarbamate C=N bond occur nearly simultaneously during decomposition. There were no evolved volatile species following the formation of NiS until  $\sim 430^\circ\text{C}$  where sulfur dioxide was evolved with a corresponding mass loss of 1.5% (by TGA). The observation of  $\text{SO}_2$  during the main mass loss event ( $245$ – $345^\circ\text{C}$ ), and the secondary mass loss at  $\sim 430^\circ\text{C}$  indicates that the NiS was oxidized by trace levels of elemental oxygen

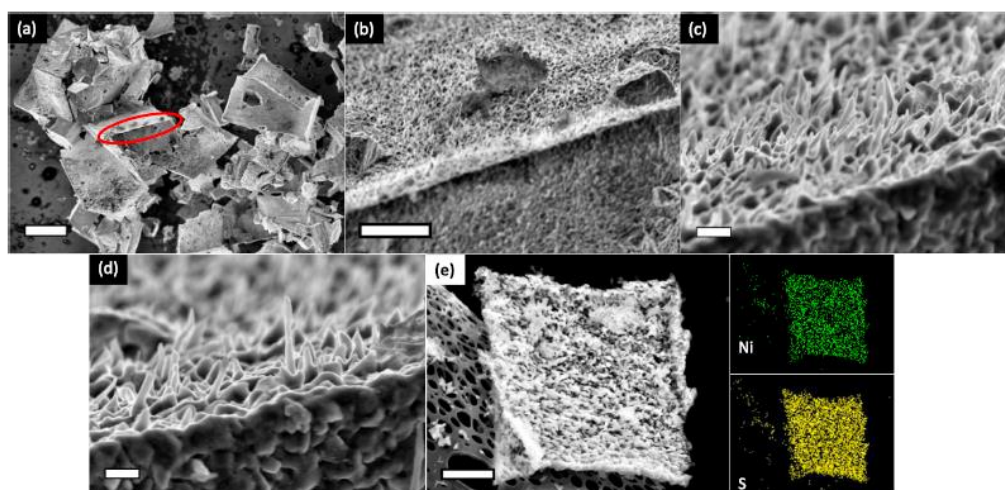


Fig. 4. SE-SEM micrographs of  $\text{Ni}(\text{DIPDTC})_2$  thermolysis residue (a–d) with EDX mapping (e) (scale bars: 40, 5, 0.5, 0.4,  $0.2\ \mu\text{m}$  respectively).

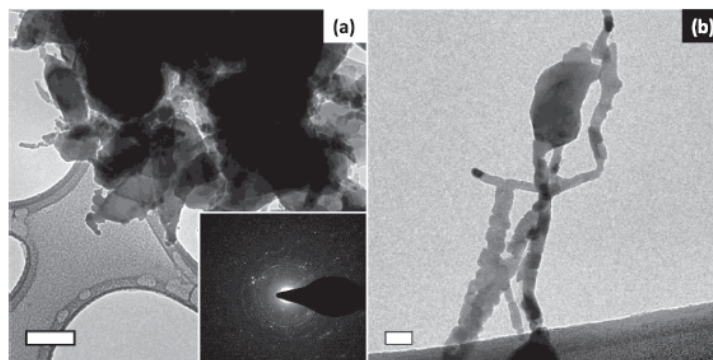


Fig. 5. (a) TEM micrograph of NiS with SAED inset, scale bar: 100 nm. (b) A NiS filament, scale bar: 20 nm.

within the experimental system to NiO, which was also observed in the powder XRD pattern of the final residue in synchrotron experiments (Fig. S2).

### 3. Conclusions

Single crystals of Ni(DIPDTC)<sub>2</sub> formed NiS upon thermolysis in a single event beginning at ~250 °C. The decomposition of the Ni(DIPDTC)<sub>2</sub> crystals resulted in the formation of α-NiS crystals with a structure that retained the approximate shape of the precursor crystals. Analysis of the thermolysis regime using *in situ* techniques showed that the thermolysis produced no intermediate species and the major volatile by-products were isopropyl-isothiocyanate and carbon disulfide. Thus, our method can be used to synthesize a single phase of nickel sulfide without the need for solvents. The process uses a readily accessible SSP that generates only volatile by-products with no intermediate liquid phase. The resultant nanostructure is highly textured and may provide promising applications in the realms of catalysis and catalytic water splitting.

### 4. Experimental section

#### 4.1. General

Bis(κ<sup>2</sup>S,S'-di(isopropyl)dithiocarbamato) nickel(II) (Ni(DIPDTC)<sub>2</sub>) was synthesized using a published procedure [61]. The complex (3.0 g) was dissolved in chloroform (60 mL) and washed several times with ultrapure water. The chloroform layer was dried over anhydrous magnesium sulfate and the volume reduced to ~5 mL, using a rotary evaporator. The concentrated solution was cooled slowly to yield crystals of Ni(DIPDTC)<sub>2</sub> suitable for X-ray diffraction experiments.

#### 4.2. Optical microscopy

Variable temperature (30–500 °C) isotropic light microscopy was performed using an Olympus BH–2 microscope fitted with a Linkam THMS600 stage in transmission configuration. Single crystals were placed atop a sapphire wafer and entombed by a silver cover of 3 mm thickness with 1 mm aperture. The stage environment was maintained under a flow of nitrogen at 25 mL min<sup>−1</sup>. A heating rate of 3.0 °C min<sup>−1</sup> was used and photomicrographs were taken at 100× magnification at 3 °C intervals using a Q-Imaging MicroPublisher 3.3RTV CCD camera.

#### 4.3. In situ X-ray diffraction

Measurements were performed on the Powder Diffraction beamline

at the Australian Synchrotron. The X-ray wavelength was 0.5893 Å (confirmed by refinement against a LaB<sub>6</sub> standard). Crystals suitable for single crystal X-ray analysis were ground in an agate pestle and mortar to produce a free flowing green powder, which was loaded into an open-ended 0.3 mm (internal diameter) quartz capillary. A positive flow of 99.999% helium through the capillary was used in conjunction with a hot-air blower heating at 3 °C min<sup>−1</sup> to produce 147 diffraction files in the temperature range 25 to 500 °C. Scans were performed in two blocks of 30 s exposure, offset by 0.5° in the 2θ range between 2.5 and 60°. The diffraction results were merged and automated peak analysis was performed using software developed in-house. All graphs were generated using MATLAB version 9.2.

#### 4.4. Thermogravimetric analysis

Simultaneous thermogravimetric and calorimetric analysis was performed using a Netzsch STA 449 F5 Jupiter thermal analyser. Samples were placed in a 90 µL alumina crucible and experiments were conducted using an atmosphere of 99.9995% helium, with a residual oxygen concentration of ~50 ppm due to diffusion through instrument orifices. A heating rate of 3 °C min<sup>−1</sup> was employed between 30 and 500 °C. Simultaneous Gas Chromatography-Mass Spectrometry was performed using a heated transfer line from the furnace to an Agilent 7890/5977 Gas Chromatography-Mass Spectrometer. A ~60 µL aliquot of furnace atmosphere was automatically sampled in 30 °C increments and diluted 1:5 with 99.9995% helium prior to injection through an Agilent HP-5MS column. Separation of volatiles was achieved with a temperature ramp of 50 to 200 °C with a heating rate of 20 °C min<sup>−1</sup>. Mass spectra were obtained with a *m/z* range of 50 to 400 amu, and referenced to known fragmentation patterns using a NIST 2014 database (NIST 14).

#### 4.5. Inductively coupled plasma-mass spectrometry (ICP-MS)

An ICP-MS spectrometer with quadrupole analyser 7500cx (Agilent Technologies, Australia) was used to measure the Ni content in the sample after acidic digestion. System optimization and method tuning were performed using a 1% nitric acid solution containing 50 ng mL<sup>−1</sup> of Li, Y and Tl. Operating conditions were RF power 1550 W, RF matching 1.58 V, sample depth 8.0 mm, carrier gas flow 1.0 L/min, nebulizer pump 0.10 rps, and S/C temperature 2.0 °C. Samples were introduced using a micromist concentric nebuliser (Glass Expansion, Agilent Technologies, Australia) and a quartz Scott type double pass spray chamber. Argon was used as a plasma gas. Calibration was carried out using single element solutions containing <sup>60</sup>Ni (High-Purity Standards). Calibration solutions were prepared at concentrations



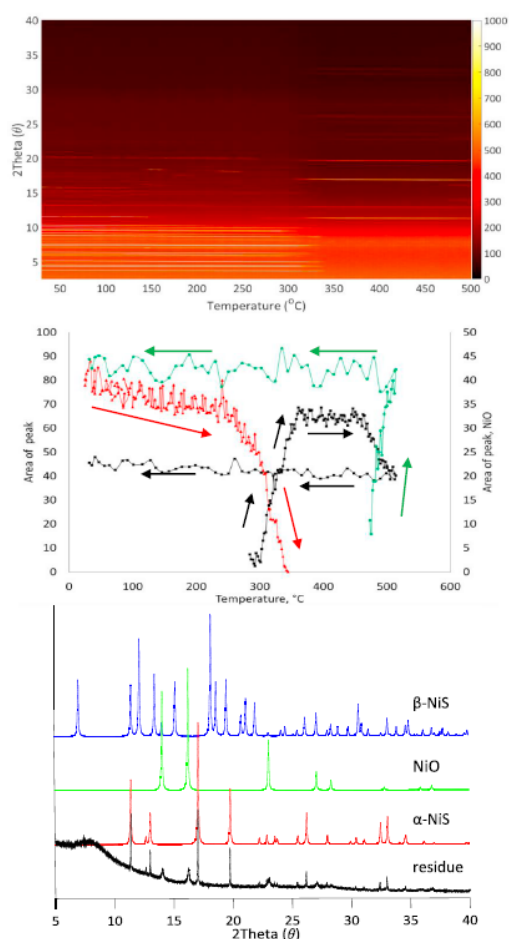


**Fig. 6.** Powder-diffraction heatmap showing changes in diffraction peak location and intensity at temperatures between 40 and 500 °C (upper) with peak area analysis for selected X-ray diffraction peaks (middle): Ni(DIPDTC)<sub>2</sub> (3.7°, red trace), NiS (11.3°, black trace) and NiO (13.9° & 16.1°, green trace). The residue after heating, with simulated patterns of expected phases is shown in the lower panel. (For interpretation of the references to colour in this figure legend, the reader is referred to the web version of this article.)

ranging from 1 to 1000 ng mL<sup>-1</sup>. A 100 ng mL<sup>-1</sup> solution of <sup>103</sup>Rh (High-Purity Standards) was used as internal standard. The calibration curve showed linearity over the range of concentrations with a correlation factor ( $r^2$ ) of 0.99.  $\alpha$ -NiS (1.17 mg) was digested using 3 mL of 69% HNO<sub>3</sub> (Ultra High Purity, Seastar) at 35 °C. The sample was then diluted with ultra-pure water (1:1000) and analysed by ICP-MS within 24 h. Analytical precision (for three injections) had RSD < 5% and accuracy was in the range 98–100%.

#### 4.6. Electron microscopy

Thermolysis products were imaged using a Zeiss Supra 55VP scanning electron microscope (operating in High-Vacuum mode) with an Oxford Instruments INCA X-Sight 7558 for energy dispersive X-ray

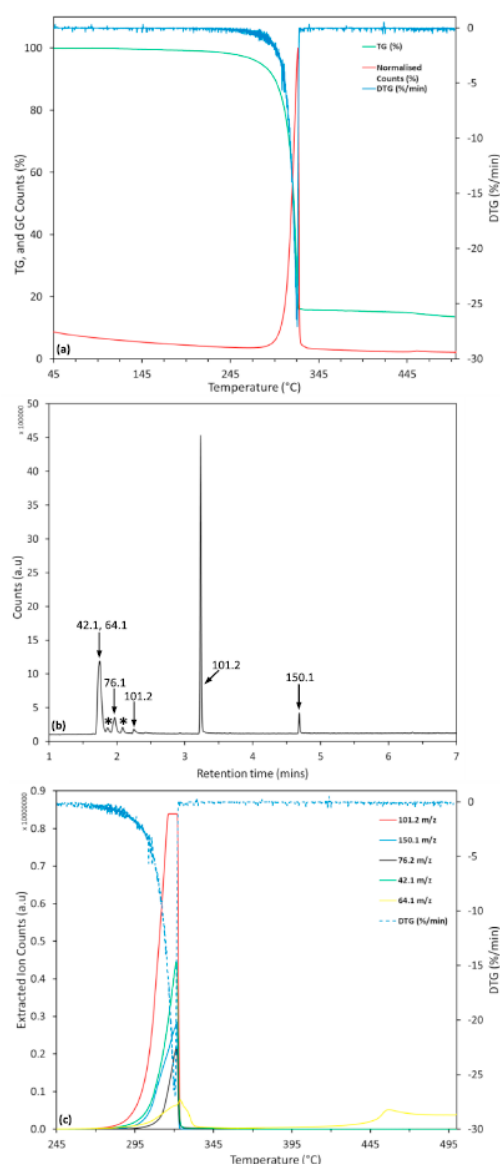


**Fig. 7.** TGA with overlaid MS TIC (a), GC-MS data of furnace atmosphere prior to DTG<sub>max</sub> = partial oxidized species (b) and temporal evolution of main decomposition products (c).

spectroscopy. Transmission electron microscope imaging was performed using a FEI Tecnai T20 TWIN microscope (LaB<sub>6</sub>) and an accelerating voltage of 200 kV.

#### Acknowledgments

We acknowledge Dr Ronald Shimmom for laboratory assistance. We

are in gratitude to the Mark Wainwright Analytical Centre, UNSW, for access to a single crystal X-ray diffractometer. This research was undertaken on the power diffraction beamline at the Australian Synchrotron, part of ANSTO. We thank technical staff at the Australian Synchrotron for their assistance. This research is supported by an Australian Government Research Training Program Scholarship.

#### Appendix A. Supplementary data



Supplementary data to this article can be found online at <https://doi.org/10.1016/j.ica.2018.12.014>.

#### References


- [1] L.-L. Feng, G. Yu, Y. Wu, G.-D. Li, H. Li, Y. Sun, T. Asefa, W. Chen, X. Zou, *J. Am. Chem. Soc.* 137 (2015) 14023–14026.
- [2] P. Luo, H. Zhang, L. Liu, Y. Zhang, J. Deng, C. Xu, N. Hu, Y. Wang, *A.C.S. Appl. Mater. Interfaces* 9 (2017) 2500–2508.
- [3] W. Zhang, Y. Wang, Z. Wang, Z. Zhong, R. Xu, *Chem. Commun.* 46 (2010) 7631–7633.
- [4] L. Zhang, B. Tian, F. Chen, J. Zhang, *Int. J. Hydrogen Energy* 37 (2012) 17060–17067.
- [5] Y. Pan, Y. Chen, X. Li, Y. Liu, C. Liu, *RSC Adv.* 5 (2015) 104740–104749.
- [6] X.L. Wu, B. Yang, Z.J. Li, L.C. Lei, X.W. Zhang, *RSC Adv.* 5 (2015) 32976.
- [7] C. Kong, S. Min, G. Lu, *ACS Catal.* 4 (2014) 2763–2769.
- [8] T. Zhu, H.B. Wu, Y. Wang, R. Xu, X.W.D. Lou, *Adv. Energy Mater.* 2 (2012) 1497–1502.
- [9] A. Olivas, J. Cruz-Reyes, V. Petranovskii, M. Avalos, S. Fuentes, *J. Vac. Sci. Technol. A* 16 (1998) 3515–3520.
- [10] J. Yang, X. Duan, Q. Qin, W. Zheng, *J. Mater. Chem. A* 1 (2013) 7880–7884.
- [11] H. Pang, C. Wei, X. Li, G. Li, Y. Ma, S. Li, J. Chen, J. Zhang, *Sci. Rep.* 4 (2014) 3577.
- [12] Y. Zhang, W. Sun, X. Rui, B. Li, H.T. Tan, G. Guo, S. Madhavi, Y. Zong, Q. Yan, *Small* 11 (2015) 3694–3702.
- [13] W. Zhou, X. Cao, Z. Zeng, W. Shi, Y. Zhu, Q. Yan, H. Liu, J. Wang, H. Zhang, *Energy Environ. Sci.* 6 (2013) 2216–2221.
- [14] S.B. Ni, X.L. Yang, T. Li, *J. Mater. Chem.* 22 (2012) 2395–2397.
- [15] S. Ji, L. Zhang, L. Yu, X. Xu, J. Liu, *RSC Adv.* 6 (2016) 101752–101759.
- [16] S.-C. Han, K.-W. Kim, H.-J. Ahn, J.-H. Ahn, J.-Y. Lee, *J. Alloys Compd.* 361 (2003) 247–251.
- [17] N.H. Idris, M.M. Rahman, S.-L. Chou, J.-Z. Wang, D. Wexler, H.-K. Liu, *Electrochim. Acta* 58 (2011) 456–462.
- [18] Z. Liu, X. Zheng, S.-L. Luo, S.-Q. Xu, N.-Y. Yuan, J.-N. Ding, *J. Mater. Chem. A* 4 (2016) 13395–13399.
- [19] N. Mahmood, C. Zhang, Y. Hou, *Small* 9 (2013) 1321–1328.
- [20] K. Aso, A. Hayashi, M. Tatsumisago, *Electrochim. Acta* 83 (2012) 448–453.
- [21] X. Sun, J. Dou, F.Y. Xie, Y.F. Li, M.D. Wei, *Chem. Commun.* 50 (2014) 9869–9871.
- [22] J. Yang, C. Bao, K. Zhu, T. Yu, F. Li, J. Liu, Z. Li, Z. Zou, *Chem. Commun.* 50 (2014) 4824–4826.
- [23] H.K. Mulmudi, S.K. Batabyal, M. Rao, R.R. Prabhakar, N. Mathews, Y.M. Lam, S.G. Mhaisalkar, *PCCP* 13 (2011) 19307–19309.
- [24] X. Wang, B. Batter, Y. Xie, K. Pan, Y. Liao, C. Lv, M. Li, S. Sul, H. Fu, *J. Mater. Chem. A* 3 (2015) 15905–15912.
- [25] S. Peng, L. Li, H. Tan, R. Cai, W. Shi, C. Li, S.G. Mhaisalkar, M. Srinivasan, S. Ramakrishna, Q. Yan, *Adv. Funct. Mater.* 24 (2014) 2155–2162.
- [26] Y. Liao, K. Pan, Q. Pan, G. Wang, W. Zhou, H. Fu, *Nanoscale* 7 (2015) 1623–1626.
- [27] H. Sun, D. Qin, S. Huang, X. Guo, D. Li, Y. Luo, Q. Meng, *Energy Environ. Sci.* 4 (2011) 2630–2637.
- [28] Y. Zhou, D. Yan, H. Xu, J. Feng, X. Jiang, J. Yue, J. Yang, Y. Qian, *Nano Energy* 12 (2015) 528–537.
- [29] Q. Liu, A. Diaz, A. Prosvirnin, Z. Luo, J.D. Batteas, *Nanoscale* 6 (2014) 8935–8942.
- [30] L. Shen, J. Wang, G. Xu, H. Li, H. Dou, X. Zhang, *Adv. Energy Mater.* 5 (2015) 1400977.
- [31] J. Xiao, L. Wan, S. Yang, F. Xiao, S. Wang, *Nano Lett.* 14 (2014) 831–838.
- [32] X.Y. Yu, L. Yu, L. Shen, X. Song, H. Chen, X.W.D. Lou, *Adv. Funct. Mater.* 24 (2014) 7440–7446.
- [33] H. Li, Y. Shao, Y. Su, Y. Gao, X. Wang, *Chem. Mater.* 28 (2016) 1155–1164.
- [34] C. Gervas, S. Mlowe, M.P. Akerman, I. Ezekiel, T. Moyo, N. Revaprasadu, *Polyhedron* 122 (2017) 16–24.
- [35] C. Buchmaier, M. Glänzer, A. Torvisco, P. Poelt, K. Wewerka, B. Kunert, K. Gatterer, G. Trimmel, T. Rath, *J. Mater. Sci.* 52 (2017) 10898–10914.
- [36] G. Kullerud, R.A. Yund, *Journal of Petrology* 3 (1962) 126–175.
- [37] J.C. Barry, S. Ford, *J. Mater. Sci.* 36 (2001) 3721–3730.
- [38] K. Ramasamy, M.A. Malik, P. O'Brien, J. Raftery, M. Hellwell, *Chem. Mater.* 22 (2010) 6328–6340.
- [39] M.V. Swain, *J. Mater. Sci.* 16 (1981) 151–158.
- [40] A. Ghezalbash, B.A. Korgel, *Langmuir* 21 (2005) 9451–9456.
- [41] M. Liu, G. Lv, G. Chen, Y. Qin, P. Sun, K. Zhou, X. Xing, C. He, *RSC Adv.* 6 (2016) 102472–102481.
- [42] P. Galkar, S.P. Pawar, R.S. Mane, M. Nuashad, D. Shinde, *RSC Adv.* 6 (2016) 112589–112593.
- [43] A. Molla, M. Sahu, S. Hussain, *Sci. Rep.* 6 (2016) 26034.
- [44] C. Wei, C. Cheng, J. Zhao, Y. Wang, Y. Cheng, Y. Xu, W. Du, H. Pang, *Chem-Asian J.* 10 (2015) 679–686.
- [45] S. He, C. Lu, G.-S. Wang, J.-W. Wang, H.-Y. Guo, L. Guo, *ChemPlusChem* 79 (2014) 569–576.
- [46] X. Jiang, Y. Xie, J. Lu, L. Zhu, W. He, Y. Qian, *Adv. Mater.* 13 (2001) 1278–1281.
- [47] J. Wang, D. Cao, G. Yang, Y. Yang, H. Wang, *J. Solid State Electrochem.* 21 (2017) 3047–3055.
- [48] N. Alam, M.S. Hill, G. Kociok-Köhne, M. Zeller, M. Mazhar, K.C. Molloy, *Chem. Mater.* 20 (2008) 6157–6162.
- [49] P.R. Bonneau, R.K. Shihao, R.B. Kaner, *Inorg. Chem.* 29 (1990) 2511–2514.
- [50] D. Mondal, G. Villemure, G. Li, C. Song, J. Zhang, R. Hui, J. Chen, C. Fairbridge, *Appl. Catal., A* 450 (2013) 230–236.
- [51] R. Boughalmi, R. Rahmani, A. Boukhachem, B. Amrani, K. Driss-Khodja, M. Amlouk, *Mater. Chem. Phys.* 163 (2015) 99–106.
- [52] Y. Fazli, S. Pourmortazavi, I. Kohsari, M. Karimi, M. Tajdari, *J. Mater. Sci. - Mater. Electron.* 27 (2016) 7192–7199.
- [53] P. O'Brien, J.H. Park, J. Waters, *Thin Solid Films* 431–432 (2003) 502–505.
- [54] A. Roffey, N. Hollingsworth, H.U. Islam, M. Mercy, G. Sankar, C.R. Catlow, G. Hogarth, N.H. de Leeuw, *Nanoscale* 8 (2016) 11067–11075.
- [55] C. Xiangying, W. Zhenghua, W. Xiong, W. Junxi, L. Jianwei, Q. Yitai, *Chem. Lett.* 33 (2004) 1294–1295.
- [56] N. Hollingsworth, A. Roffey, H.-U. Islam, M. Mercy, A. Roldan, W. Bras, M. Wolthers, C.R.A. Catlow, G. Sankar, G. Hogarth, N.H. de Leeuw, *Chem. Mater.* 26 (2014) 6281–6292.
- [57] B. Arul Prakasam, M. Lahtinen, A. Peuronen, M. Muruganandham, E. Kolehmainen, E. Haapaniemi, M. Sillanpää, *Inorg. Chim. Acta* 425 (2015) 239–246.
- [58] E. Sathiyaraj, G. Gurumoorthy, S. Thirumaran, *New J. Chem.* 39 (2015) 5336–5349.
- [59] J.I.K. Yun Ku Jung, Jin-Kyu Lee, *J. Am. Chem. Soc.* 132 2010 178 184.
- [60] B.F. Ali, W.S. Al-Akramawi, K.H. Al-Obaidi, A.H. Al-Karbolli, *Thermochim. Acta* 419 (2004) 39–43.
- [61] A. Angeloski, A.T. Baker, M. Bhadbhade, A.M. McDonagh, *J. Mol. Struct.* 1113 (2016) 127–132.
- [62] J. Cheon, D.S. Talaga, J.I. Zink, *Chem. Mater.* 9 (1997) 1208–1212.
- [63] N. Pradhan, B. Katz, S. Efrima, *J. Phys. Chem. B* 107 (2003) 13843–13854.
- [64] L. Barry, J.D. Holmes, D.J. Otway, M.P. Copley, O. Kazakova, M.A. Morris, *J. Phys.: Condens. Matter* 22 (2010) 076001.
- [65] L.K. Macreadle, H.E. Maynard-Casely, S.R. Batten, D.R. Turner, A.S.R. Chesman, *ChemPlusChem* 80 (2015) 107–118.
- [66] M.D. Khan, G. Murtaza, N. Revaprasadu, P. O'Brien, *Dalton Trans.* 47 (2018) 8870–8873.
- [67] P.P. Nash, A. International, *Phase diagrams of binary nickel alloys*, ASM, International (1991).
- [68] D.W. Bishop, P.S. Thomas, A.S. Ray, P. Simon, *J. Therm. Anal. Cal.* 64 (2001) 201–210.
- [69] C.I. Pearce, R.A.D. Patrick, D.J. Vaughan, *Rev. Mineral. Geochem.* 61 (2006) 127–180.
- [70] R.C. Sharma, Y.A. Chang, *Metall. Trans.* 11B (1980) 139–146.

## Author Contributions and Copyright Information: Conversion of single-crystals of a nickel(II) dithiocarbamate complex to nickel sulfide crystals

- A. Angeloski performed synthesis, isolation, all measurements and microscopies (excluding electron microscopies and ICP-MS), Thermogravimetric analysis, data analysis, and wrote the manuscript
- M.B. Cortie provided assistance with X-ray powder diffraction, and conceptual advice
- J. Scott performed and analysed the electron microscopies
- D. Bordin performed and analysed the ICP-MS
- All authors have reviewed the manuscript, and all persons providing assistance have been acknowledged within the manuscript.



[Home](#) [Create Account](#) [Help](#)



**Title:** Conversion of single crystals of a nickel(II) dithiocarbamate complex to nickel sulfide crystals

**Author:** Alexander Angeloski, Michael B. Cortie, John A. Scott, Dayanne M. Bordin, Andrew M. McDonagh

**Publication:** Inorganica Chimica Acta

**Publisher:** Elsevier

**Date:** 1 March 2019

© 2018 Elsevier B.V. All rights reserved.

**LOGIN**

If you're a [copyright.com](#) user, you can login to RightsLink using your [copyright.com](#) credentials. Already a **RightsLink** user or want to [learn more?](#)

Please note that, as the author of this Elsevier article, you retain the right to include it in a thesis or dissertation, provided it is not published commercially. Permission is not required, but please ensure that you reference the journal as the original source. For more information on this and on your other retained rights, please visit: <https://www.elsevier.com/about/our-business/policies/copyright#Author-rights>

Permission for reuse of the article within this dissertation has been obtained.

## **Chapter 4:**

From Lead(II) Dithiocarbamate  
Precursors to a Fast Response PbS  
Positive Temperature Coefficient  
Thermistor

## Chapter 4: From Lead(II) Dithiocarbamate Precursors to a Fast Response PbS Positive Temperature Coefficient Thermistor

### From Lead(II) Dithiocarbamate Precursors to a Fast Response PbS Positive Temperature Coefficient Thermistor

Alexander Angeloski,<sup>†</sup> Angus R. Gentle,<sup>†,‡</sup> John A. Scott,<sup>†</sup> Michael B. Cortie,<sup>†,§</sup> James M. Hook,<sup>‡</sup> Mika T. Westerhausen,<sup>†</sup> Mohan Bhadbhade,<sup>§</sup> Anthony T. Baker,<sup>||</sup> and Andrew M. McDonagh<sup>\*,†,§</sup>

<sup>†</sup>School of Mathematical and Physical Sciences, University of Technology Sydney, Ultimo 2007, Australia

<sup>‡</sup>NMR Facility, Mark Wainwright Analytical Centre and <sup>§</sup>School of Chemistry, The University of New South Wales, Sydney 2052, Australia

<sup>||</sup>College of Science, Health and Engineering, La Trobe University, Melbourne 3086, Australia

#### Supporting Information

**ABSTRACT:** PbS submicron crystals were formed by thermolysis of two different lead dithiocarbamate complexes. These precursors were readily synthesized and fully characterized, and in situ synchrotron powder diffraction experiments were performed to characterize their decomposition. The structure and purity of resultant PbS was examined using scanning electron and transmission electron microscopies, powder X-ray diffraction, and infrared spectroscopy. Submicron crystalline PbS was used to create a new PbS thermistor with excellent sensitivity and an ultrarapid thermal response time.



#### INTRODUCTION

Crystalline lead sulfide (PbS) is an important IV–VI semiconductor (direct bandgap  $\sim 0.41$  eV at room temperature (RT))<sup>1</sup> with applications in photovoltaic and photoconductive devices.<sup>2</sup> The exciton Bohr radius of PbS<sup>3</sup> is  $\sim 18$  nm, and reducing the size of crystals to less than half of this distance results in nanocrystalline PbS with size-dependent optoelectronic properties.<sup>4,5</sup> With these properties in mind, efforts have been directed toward cost-effective and scalable syntheses of bulk and nanocrystalline PbS for applications in photovoltaic cells and thermal imaging devices.<sup>6</sup>

Bulk and nanocrystalline PbS can be synthesized using solvothermal techniques employing single-source precursors (SSPs),<sup>7,8</sup> and much work has been devoted to the investigation of solution-based methods to favor stable size-tunable nanocrystalline PbS.<sup>9–14</sup> The morphology and purity of the crystalline PbS can be manipulated by altering the nature of the SSPs. In some syntheses, the byproducts generated during thermolysis of these SSPs act as capping agents that stabilize the PbS formed.<sup>15</sup> Alternatively, capping agents (e.g., octylamine) can be added to provide stability or morphological control. In addition to solvothermal techniques, PbS has been synthesized from melt reactions,<sup>15,16</sup> which occur in a solution of the molten SSPs. PbS forms as the melt is heated beyond the decomposition temperature of the SSP.<sup>17</sup> Melt reactions require no solvent and are therefore attractive for large-scale syntheses. SSPs that have been shown to be useful to prepare PbS include xanthate complexes<sup>15,18,19</sup> and, of particular relevance to the current work, dithiocarbamate (DTC) complexes.<sup>20–22</sup>

Metal DTC complexes have been extensively studied for their ability to coordinate a range of transition and main-block elements and for their interesting and useful properties.<sup>23,24</sup> The ability to readily alter the DTC ligand structure allows a range of functionality to be imparted upon the resultant complexes.<sup>25–33</sup> In particular, modification of the substituents in the ligand structure ( $S_2CNRR'^{-}$ ) influences the thermal properties of the resultant metal complex, which in turn affects the formation of nanoparticles from these SSPs.<sup>34</sup> DTC complexes containing heterocyclic,<sup>27</sup> alkyl,<sup>26</sup> and aryl<sup>28</sup> ligands have been investigated as SSPs for nanoparticle synthesis.<sup>35–38</sup> In the context of the thermal synthesis of PbS crystals, the influence of DTC ligands bearing aliphatic and aromatic substituents has been examined.<sup>22,26–28,39</sup>

In this work, a new Pb(II) DTC complex with oxygen-rich ligands, **2** (Figure 1), is examined as an SSP for PbS submicron single-crystal formation. The polyhydroxylated complex was compared to the alkyl DTC complex, **1** (Figure 1), to examine the influence of intramolecular oxygen on the thermal decomposition and formation of PbS. The thermolysis mechanisms were investigated using in situ synchrotron powder X-ray diffraction experiments. Experimental conditions were adjusted to evaluate the influence of reaction temperature and heating rate on the morphology of the PbS product. The crystalline PbS products were characterized, and selected crystals were used to create a novel lead sulfide-based thermistor.

Received: November 29, 2017

Published: February 7, 2018



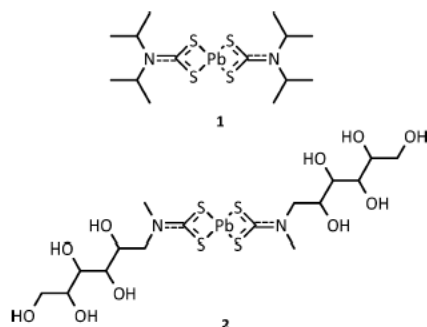


Figure 1. Chemical structures of 1 and 2.

## EXPERIMENTAL SECTION

**General.** *Caution!* Lead compounds are toxic, and appropriate precautions should be taken. All chemicals and solvents used in synthetic procedures were analytical grade, purchased from Sigma-Aldrich, and used as received. Sodium di(isopropyl)dithiocarbamate pentahydrate (NaDIPDTC) was prepared using the method of Angeloski et al.<sup>40</sup> Millipore water (18.4 MΩ cm<sup>-1</sup>) was used in synthetic procedures. High-resolution mass spectrometry was performed using an Agilent 6510 Q-TOF with a mobile phase of 70% acetonitrile, 30% water, and a flow rate of 0.5 mL min<sup>-1</sup>. Fourier transform infrared (FT-IR) spectra were acquired using a Nicolet 6700 FTIR spectrometer fitted with a diamond smart iTX ATR accessory, or using KBr pellets in transmission configuration. Each spectrum was collected using 64 scans, with a resolution of 2 cm<sup>-1</sup> over the range of 5000–450 cm<sup>-1</sup>.

Variable-temperature (VT) <sup>1</sup>H, <sup>13</sup>C, two-dimensional (2D) exchange spectroscopy (EXSY, with mixing time 100 ms), heteronuclear single quantum correlation (<sup>13</sup>C-HSQC), and heteronuclear multiple bond correlation (<sup>13</sup>C-HMBC and <sup>15</sup>N-HMBC) nuclear magnetic spectroscopy experiments using solutions were performed using a Bruker Avance III NMR spectrometer fitted with a BBFO Plus solution-state probe. The frequency was 600.1 MHz for <sup>1</sup>H, 150.9 MHz for <sup>13</sup>C, and 60.8 MHz for <sup>15</sup>N experiments. A Bruker BVT3000 VT unit was used in conjunction with a BCU-Xtreme cooler to accurately adjust the sample temperature between 293 and 225 K with acetonitrile-*d*<sub>3</sub> as the solvent. The temperature was calibrated using a Type K thermocouple within an NMR tube containing ethanol inserted into the probe. Instrument broadening was accounted for using the full width at half-maximum (fwhm) of acetonitrile-*d*<sub>3</sub> residual proton resonances. With these data, experimental rate constants were calculated at each temperature using the fwhm of the methine peak at 5.58 ppm. Arrhenius and Eyring activation parameters were obtained using generalized least-squares linear regressions of log *k* versus 1/*T* and log(*k*/*T*) versus 1/*T*, respectively.

Room-temperature <sup>1</sup>H, <sup>13</sup>C, and <sup>13</sup>C-HSQC correlation spectroscopy experiments using deuterated dimethyl sulfoxide (DMSO-*d*<sub>6</sub>) solutions were performed with an Agilent Technologies NMR instrument. The frequency was 500.3 MHz for <sup>1</sup>H and 125.7 MHz for <sup>13</sup>C experiments.

Solid-state <sup>13</sup>C NMR spectroscopy was performed using a Bruker Avance III 300 MHz spectrometer fitted with a 4 mm CPMAS probe. The frequency was 75.4 MHz for <sup>13</sup>C. Crystalline samples were loaded into a 4.0 mm zirconia rotor, and CPMAS-TOSS experiments were performed using a magic-angle spinning (MAS) rate of 6.5 kHz.

Variable-temperature polarized and isotropic light microscopy between −190 and 500 °C was performed using a modified Wild M21 microscope fitted with a Linkam THMS600 hot stage. Photomicrographs were acquired using QCapture Pro7 software and a QImaging MicroPublisher 3.3RTV CCD camera.

**Single-Crystal X-ray Diffraction.** Suitable crystals were selected under a Leica M165Z polarizing microscope and mounted on a MiTiGen MicroMount consisting of a thin polymer tip with a wicking

aperture. The X-ray diffraction measurements were performed on a Bruker Kappa-II CCD diffractometer at 150 K using a  $\mu$ S Incoatec Microfocus Source with Mo *K* $\alpha$  radiation ( $\lambda = 0.710\,723\,\text{\AA}$ ). The structure was solved using charge flipping, and the full matrix least-squares refinement was performed using ShelXL<sup>41</sup> in Olex2.<sup>42</sup> Heavy atoms were refined isotropically until *R*-factor convergence, and then an anisotropic model was applied. Where possible, hydrogen atoms were located using a difference Fourier plot and restrained to neutron diffraction distances where required. Hydrogen atoms and anisotropic refinement were omitted from disordered solvent molecules with partial occupancy in the structure of NaNMeGlu. CrystalExplorer<sup>43</sup> was used to generate Hirshfeld surfaces<sup>44–46</sup> representing *d*<sub>norm</sub>. Relevant crystallographic data can be found in the Supporting Information.

**Synthesis of PbS Crystal Precursors.** *Synthesis of Bis(κ²S,S'-di(isopropyl)dithiocarbamate)lead(II) (1).* An aqueous solution of NaDIPDTC (2.295 g, 8.0 mmol, in 50 mL of water) was added dropwise with stirring to an aqueous solution of lead acetate trihydrate (2.008 g, 5.3 mmol, in 50 mL of water). A pale yellow precipitate formed upon addition, and the resultant mixture was stirred for 5 min. The crude material was collected by vacuum filtration, and the filter cake was washed several times using hot water to produce a fluffy pale yellow agglomerate. The agglomerate was dried to completion in vacuo at 45 °C to yield 1.855 g of 1 (83%). Crystals suitable for X-ray analysis were obtained as clear colorless plates by recrystallization from diethyl ether. High-resolution mass spectrometry (HRMS) (*M*+*H*)<sup>+</sup> for PbN<sub>2</sub>S<sub>2</sub>C<sub>14</sub>H<sub>28</sub> Calculated: 561.0971; Observed: 561.0973; Difference: 0.4 ppm. <sup>1</sup>H NMR (600.1 MHz, CD<sub>3</sub>CN, 223 K):  $\delta$  5.58 (sept, <sup>3</sup>*J*<sub>HH</sub> = 6.7 Hz, 2H, H2, H12), 4.01 (sept, <sup>3</sup>*J*<sub>HH</sub> = 7.0 Hz, 2H, H5, H9), 1.67 (d, <sup>3</sup>*J*<sub>HH</sub> = 7.0 Hz, 12H, C6H<sub>3</sub>, C7H<sub>3</sub>, C10H<sub>3</sub>, C11H<sub>3</sub>), 1.24 (d, <sup>3</sup>*J*<sub>HH</sub> = 6.7 Hz, 12H, C3H<sub>3</sub>, C4H<sub>3</sub>, C13H<sub>3</sub>, C14H<sub>3</sub>). <sup>13</sup>C NMR (150.9 MHz, CD<sub>3</sub>CN, 223 K):  $\delta$  200.86 (C1, C8), 55.09 (C2, C12), 50.41 (C5, C9), 19.49 (C11, C10, C6, C7), 19.6 (C3, C4, C13, C14). <sup>15</sup>N NMR (60.8 MHz, CD<sub>3</sub>CN, 223 K):  $\delta$  197.4 (N1, N2).

*Synthesis of Sodium N-methyl-N-2,3,4,5,6-pentahydroxyhexyldithiocarbamate (NaNMeGlu).* NaNMeGlu was prepared using an adaptation of the method of Shinobu et al.<sup>47</sup> An aqueous solution of sodium hydroxide (4.00 g, 100 mmol, in 40 mL of water) was cooled to ~5 °C by adding ice. *N*-Methyl-D-glucamine (19.52 g, 100 mmol) was then added and dissolved with stirring. The resultant solution was maintained between 5 and 10 °C, while carbon disulfide (10 mL in 40 mL of ethanol, 170 mmol) was added dropwise. A white precipitate formed, and the mixture was stirred for a further 10 min. Methanol (100 mL) was added to the mixture, which was allowed to stand for 10 h at room temperature. The crude material was collected by vacuum filtration, and the filter cake was washed three times with 50 mL of cold methanol. The white solid was dried in vacuo in a desiccator charged with silica to yield 28.99 g of NaNMeGlu (80%). Crystals suitable for X-ray analysis were obtained as colorless blocks by solvent counterdiffusion of methanol into an aqueous solution of NaNMeGlu over 5 d. HRMS (*M*-Na)<sup>−</sup> for NaNS<sub>2</sub>C<sub>6</sub>O<sub>5</sub>H<sub>16</sub> Calculated: 270.0475; Observed: 270.0495; Difference: 7.5 ppm. <sup>1</sup>H NMR (500.3 MHz, DMSO-*d*<sub>6</sub>, 293 K):  $\delta$  5.14 (d, <sup>3</sup>*J*<sub>HH</sub> = 4.5 Hz, O4H, 1H), 4.78 (d, <sup>3</sup>*J*<sub>HH</sub> = 4.5 Hz, O3H, 1H), 4.52 (m, O1H, O2H 2H), 4.47 (m, C3H, 1H), 4.36 (t, <sup>3</sup>*J*<sub>HH</sub> = 5.5 Hz, O5H, 1H), 3.90 (m, C7H, 1H), 3.74 (m, C3H, 1H), 3.56 (m, C8H, 1H), 3.50 (m, C4H, C5H, C6H, 3H), 3.38 (m, C8H, 1H) 3.36 (s, C2H, 3H). <sup>13</sup>C NMR: (125.7 MHz, DMSO-*d*<sub>6</sub>, 293 K):  $\delta$  214.04 (C1), 73.27 (C6), 72.68 (C7), 71.74 (C5), 69.14 (C4), 63.67 (C8), 58.02 (C3), 43.36 (C2).

*Synthesis of Bis(κ²S,S'-N-methyl-N-2,3,4,5,6-pentahydroxyhexyldithiocarbamate)lead(II) (2).* An aqueous solution of NaNMeGlu (4.209 g, 11.7 mmol, in 45 mL of water) was added dropwise to an aqueous solution of lead acetate trihydrate (2.366 g, 6.2 mmol, in 50 mL of water). A yellow colored suspension immediately formed upon addition, which subsequently decolorized after ~3 s. The resultant mixture was subsequently stirred for 5 min and allowed to settle. The crude material was collected by vacuum filtration, and the filter cake was repeatedly triturated with water to produce a fluffy pale yellow agglomerate. The material was air-dried for 10 min and dried to completion in vacuo over P<sub>2</sub>O<sub>10</sub> at 45 °C to



produce 3.495 g of **2** (75%). Crystals suitable for X-ray analysis could not be obtained. HRMS ( $M+Na$ )<sup>+</sup> for  $PbN_2S_4C_{16}H_{32}O_{10}$ . Calculated: 771.0596; Observed: 771.0612; Difference: 2.1 ppm. <sup>1</sup>H NMR (500.3 MHz, DMSO-*d*<sub>6</sub>, 293 K):  $\delta$  4.92 (d, <sup>3</sup>*J*<sub>HH</sub> = 5.5 Hz, O4H, 1H), 4.54 (d, <sup>3</sup>*J*<sub>HH</sub> = 5.5 Hz, O3H, 1H), 4.41 (d, <sup>3</sup>*J*<sub>HH</sub> = 7 Hz, O2H, 1H), 4.39 (d, <sup>3</sup>*J*<sub>HH</sub> = 5.5 Hz, O1H, 1H), 4.35 (t, <sup>3</sup>*J*<sub>HH</sub> = 5.5 Hz, O5H, 1H), 4.14 (m, C7H, C3H, 2H), 3.56 (m, C4H, C3H, C8H, 3H), 3.46 (m, C5H, C6H, 2H), 3.35 (s, C2H, 3H), 3.34 (m, C8H, 1H). <sup>13</sup>C NMR (125.7 MHz, DMSO-*d*<sub>6</sub>, 293 K):  $\delta$  204.20 (C1), 72.69 (C6), 71.82 (C7), 71.65 (C5), 70.24 (C4), 63.69 (C8), 58.37 (C3), 43.23 (C2).

**Thermolysis of Precursors.** A Thermal Advantage SDT-Q600 thermal analyzer was used to obtain thermogravimetric (TG) and differential scanning calorimetry (DSC) data simultaneously using 90  $\mu$ L alumina crucibles. Experiments were conducted under an atmosphere of nitrogen gas (150 mL min<sup>-1</sup>) and a heating rate of 10 °C min<sup>-1</sup> over a temperature range of 30 to 500 °C. Large-scale (~1–5 g) thermolyses of SSPs **1** and **2** were conducted using a Labtec tube furnace in a 45 mm OD quartz tube. An alumina furnace boat was charged with vacuum-dried and pulverized SSPs, which were supported on a Si(111) wafer matrix to avoid direct contact with alumina. The quartz tube was purged with nitrogen gas for 10 min prior to insertion of SSPs under a constant flow of nitrogen. All SSPs were isothermally equilibrated at 50 °C for 10 min and then heated to 205 °C at a rate of 19 °C min<sup>-1</sup> (condition A) or to 550 °C at a rate of 28 °C min<sup>-1</sup> (condition B). Alternatively, SSPs were rapidly heated to 205 °C (condition C) or 550 °C (condition D) by immediate insertion at these temperatures. To conclude the thermolysis sequence, all SSPs were isothermally maintained at the final temperatures for 10 min followed by cooling under nitrogen to room temperature and storage in a desiccator. A type K thermocouple placed in proximity to the alumina furnace boat was used to measure the reaction temperature. Thermolysis experiments were performed in duplicate. The as-prepared microcrystalline material was detached from the silicon substrate and ground using an agate pestle and mortar for subsequent analysis.

**Microstructural Analysis.** Thermolysis products were imaged using a Zeiss Supra 55VP scanning electron microscope (SEM), using an Oxford Instruments INCA X-Sight 7558 for energy dispersive X-ray spectroscopy (EDX) microanalysis. Transmission electron microscope imaging was performed on an FEI Tecnai T20 TWIN microscope (LaB<sub>6</sub>) under an accelerating voltage of 200 kV. High-resolution transmission electron microscopy (HRTEM) was performed on a JEOL 2200FS operating at 200 kV. A Bruker Discover D8 Powder X-ray diffractometer with Cu K $\alpha$  ( $\lambda$  = 1.540 60 Å) was used to acquire powder diffraction (pXRD) patterns within the  $2\theta$  range from 10 to 80° and a step size of 0.02°. Key peaks in the powder diffraction pattern were indexed using a deposited PbS structure (PDF 04–004–4329). In situ pXRD measurements were performed on the Powder Diffraction beamline at the Australian Synchrotron. The X-ray wavelength was set at 0.589 348 Å (Confirmed by refinement on a LaB<sub>6</sub> standard). Scans were performed in two blocks of 30 s exposure, offset by 0.5° in the  $2\theta$  range between 2.5 and 60°. The diffraction results were merged using software developed in-house. Samples were placed within a 0.3 mm (internal diameter) open-ended quartz capillary, and a positive flow of 99.999% helium through the capillary was used in conjunction with a hot-air blower heating at ~3 °C min<sup>-1</sup>. Three-dimensional (3D) graphs were generated using MATLAB version 9.2.

**Fabrication of Thermistor Device.** A conductive substrate was prepared by coating a glass microscope slide with a 5 nm thick aluminum adhesion layer followed by 30 nm of gold using direct-current (DC) magnetron sputtering. A further 400 nm of gold was deposited by thermal evaporative deposition at a pressure of  $1 \times 10^{-6}$  mbar. The sensor microarchitecture was created using a New Wave Research NWR213 (Kennelec Scientific) laser operating at 2 J/cm<sup>2</sup> and 20 Hz with an 8  $\mu$ m spot size moving at a speed of 36  $\mu$ m/s. Thus, the continuous gold film was separated into two electrodes composed of 78 interdigitated fingers separated by a distance of 10  $\mu$ m. The area of the fabricated device was 2 mm  $\times$  2 mm.

PbS crystals were drop-cast onto the electrode area using a chlorobenzene suspension of PbS prepared by rapid thermolysis of **2** using condition C (PbS 2C), until a resistance of 117  $\Omega$  was obtained. Platinum wire contacts were attached to the gold electrodes using conductive epoxy.

**Characterization of Thermistor Device.** The resistivity of the PbS device (PbS,  $R$  = 117  $\Omega$  at 293 K) as a function of temperature was measured with a 1 mA source current within the 170–293 K temperature range using a Rigol DM3058E digital multimeter acquiring 250 readings per second. The device was adhered to a copper block using thermal adhesive within a glass-windowed chamber at a pressure of  $\sim 1.0 \times 10^{-2}$  mbar. The temperature was rapidly cooled to 170 K by injection of liquid nitrogen through the copper block, followed by passive heating to 293 K. The sensor temperature was calibrated using a Type K thermocouple physically imbedded within the device glass substrate measured by a separate Rigol DM3058E digital multimeter.

The thermal response time of PbS at 293 K,  $1.0 \times 10^{-2}$  mbar with a 1 mA bias current, with the device voltage drop was measured using a Stanford Research SR530 lock-in amplifier. A fiber-coupled xenon light source with mechanical chopper was used to produce pulses in temperature. The light was focused on the device using a lens, and the chopping rate was incrementally increased from 25 to 2230 Hz. Changes in amplifier response ( $\mu$ V) due to a changing resistance of the PbS detector were logged manually.

## RESULTS AND DISCUSSION

The lead(II) complexes **1** and **2** were synthesized in high yield by the addition of an aqueous solution of the corresponding ligand to a solution of lead(II) acetate. Recrystallization of **1** and NaNMeGlu gave crystals suitable for structural analysis by single-crystal X-ray diffraction. Relevant crystal data can be found in the Supporting Information (Tables S1–S3).

**Crystal Structure of NaNMeGlu.** The asymmetric unit of NaNMeGlu, Figure 2, contains one sodium cation coordinated

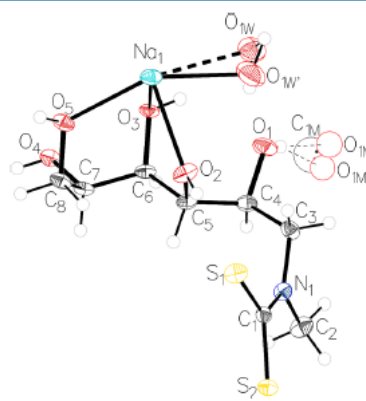


**Figure 2.** Structure of NaNMeGlu (asymmetric unit) showing the atom-labeling scheme and thermal displacement ellipsoids at 50% probability.

to one ligand molecule, one water of crystallization, and one methanol solvent molecule to give a distorted square antiprism coordination sphere with the Na–O distances ranging from 2.355 (7) to 2.668 (5) Å (Table S2). The methanol molecule occupies a special position on a crystallographic twofold rotation axis at (0.5, *y*, 1) and shows positional disorder for O1M and O1M'. The water of crystallization also exhibits positional disorder with an occupancy of 0.6 for O1W and 0.4

for O1W'. There is no direct S–Na bond, as Na is more than 4 Å from the NCS<sub>2</sub> moiety. The S1–C1 and S2–C1 bond lengths are equal within experimental error, and the NCS<sub>2</sub> moiety is approximately planar with a maximum deviation from the least-squares plane S1–S2–C2–C3 (with a root-mean-square (rms) deviation of 0.095 Å) of 0.102 Å for C3. There is an intramolecular O–H...S hydrogen bond of ~2.3 Å between S1...H2.

The crystal structure of **1** was redetermined<sup>48</sup> to obtain more precise data (significantly lower estimated standard deviations for bond lengths and angles) for comparison with NMR data (see below). The asymmetric unit is shown in Figure 3. The

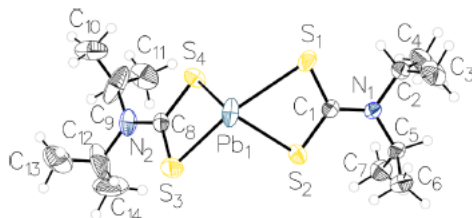


**Figure 3.** Structure of **1** (asymmetric unit) showing the atom-labeling scheme and thermal displacement ellipsoids at 50% probability.

molecule is  $\sim C_2$  symmetric. The coordination sphere about the metal center is distorted pyramidal, with Pb–S distances ranging from 2.6994 (2) to 2.8656 (2) Å. The NCS<sub>2</sub> moiety within the estimated standard deviations ligands is approximately planar, and there is no significant difference in the deviations from planarity of these groups between the two ligands. The maximum deviation from the least-squares plane C9–C12–S3–S4 (with an rms deviation of 0.025 Å) is 0.027 Å for C12, while the maximum deviation from the least-squares plane C2–C5–S1–S2 (with an rms deviation of 0.046 Å) is 0.050 Å for C2. There are two intramolecular C–H...S hydrogen bonds of ~2.3 Å between S3...H12 and ~2.4 Å between S1...H2, creating an electronic asymmetry about the two isopropyl groups within each dithiocarbamate ligand, which is in agreement with previous literature.<sup>40,49</sup> Detailed descriptions of the molecular packing motifs for both structures can be found in the Supporting Information, and all bond lengths are similar to those in other dithiocarbamate structures.<sup>40,49–55</sup>

**NMR Spectroscopy.** Variable-temperature solution-state <sup>1</sup>H NMR was used to obtain kinetic insights on the restricted rotation of isopropyl groups within **1** due to the intramolecular C–H...S interactions and steric effects.<sup>40,49</sup> From these VT experiments, values for the energy barrier ( $\Delta G^\ddagger$ ) to free rotation were determined to be 60 kJ mol<sup>−1</sup> (at 273 K) and 57 kJ mol<sup>−1</sup> (at 263 K). The latter value for  $\Delta G^\ddagger$  is in excellent agreement with our previously reported data for NaDIPDTC (56 kJ mol<sup>−1</sup>). The values for  $\Delta H^\ddagger$  (31 kJ mol<sup>−1</sup>),  $\Delta S$  (−99 J mol<sup>−1</sup> K<sup>−1</sup>) and an activation energy of 34 kJ mol<sup>−1</sup> are in agreement with those for NaDIPDTC indicating similar degrees of C–H...S and steric interactions.<sup>40</sup>

The solid-state (SS) <sup>13</sup>C NMR spectra for **1** and **2** and the ligands NaDIPDTC and NaNMeGlu are shown in Figure 4. The spectra of the ligands show signals for each of the carbon atoms, with no signals associated with any carbon-containing impurities in the solid state observed. The dithiocarbamate C1 signal appears at 200 and 207 ppm in NaDIPDTC and

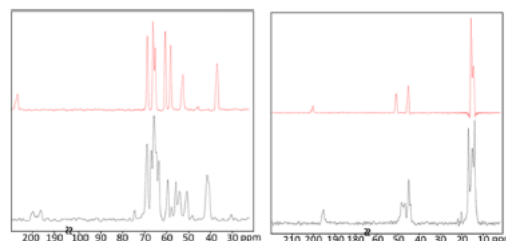


**Figure 4.** 6.5 kHz CP-MAS-SSNMR spectra for **1** (right) and **2** (left). Ligand spectra are shown in red.

NaNMeGlu, respectively. The inequivalence of the isopropyl environments in NaDIPDTC (see Supporting Information for discussion) is maintained in the solid state, as shown by the appearance of two separate methine carbon signals at 50.8 and 45.2 ppm. Upon complexation, all signals experience an upfield shift. The signals from C2/C12 and C5/C9 (48 and 45 ppm, respectively) exhibit a smaller separation in **1**, attributed to less electron delocalization about C2/C12 from the C–H...S interaction upon complexation. The slightly broader signals in **1** are attributed to disorder within the solid state. For **2**, there is an upfield shift in peaks upon complexation of NaNMeGlu, with the greatest deviation being for C1. There are no peaks in **2** attributed to unreacted ligand, but there are two sets of signals for each carbon, which indicates a magnetic inequivalence of the two ligand groups within the solid state.

**Infrared Spectroscopy.** The IR spectra for NaDIPDTC and NaNMeGlu contain bands assigned to the thioureide moiety at 1476 and 1470 cm<sup>−1</sup>, respectively. These frequencies are intermediate between that of a C–N single bond (1250–1350 cm<sup>−1</sup>) and a C=N double bond (1640–1690 cm<sup>−1</sup>), suggesting a partial double-bond character and thus delocalization of  $\pi$ -electron density about the dithiocarbamate group.<sup>25,49,56</sup> These findings are in agreement with the bond lengths measured in single crystals of NaNMeGlu and NaDIPDTC.<sup>40</sup> These bands appear at 1475 and 1467 cm<sup>−1</sup> in **1** and **2** indicating similar N...C bond distances, which is seen in the crystal structure data for **1**. The  $\nu$ (C...S) bands appear at 943 and 966 cm<sup>−1</sup> for NaDIPDTC and NaNMeGlu, respectively. Upon coordination to Pb(II), the corresponding bands are observed at 936 and 975 cm<sup>−1</sup>, respectively (Table S4 Supporting Information).

Thermogravimetric analysis (TGA) and differential scanning calorimetry (DSC) data for **1** (Figure 5) reveal no significant mass loss in the region of 25–230 °C indicating a lack of water (bound or otherwise), in agreement with the crystallographic data. An endothermic event at 187 °C with no accompanying mass loss was assigned to a solid-to-liquid phase change using variable-temperature polarization and isotropic optical microscopy, Figure S9. Decomposition of **1** in the region of 220–340 °C with an endothermic maximum at 324 °C is associated with a mass loss of 61%, which is reasonably consistent with the calculated mass loss of 57% to produce PbS. Importantly, these data reveal that formation of PbS occurs from the molten SSP.

TGA and DSC data for **2** (Figure 5) show a mass loss of 2% in the region of 50–150 °C with an endothermic maximum at 105 °C, which indicates the loss of unbound water. In contrast to **1**, there were no measurable phase changes prior to thermolysis. Decomposition occurred in two stages, first between 150–220 °C with an endothermic maximum at 205



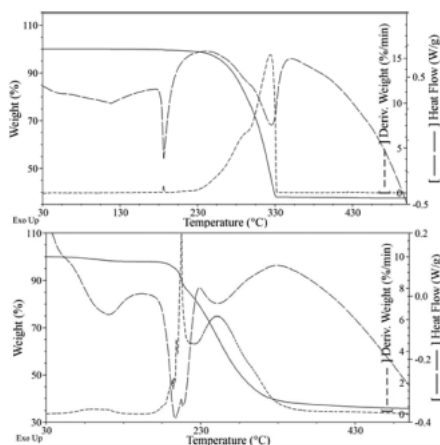


Figure 5. TGA and DSC data for 1 (upper) and 2 (lower).

°C, followed by a broad event between 220–350 °C with an endothermic maximum at 250 °C. Mass loss from these two events (67%) agrees closely with the calculated mass loss to yield PbS (68%). In contrast to the decomposition of 1, PbS was formed from 2 in the solid phase, which was supported by variable-temperature polarized and isotropic optical microscopy, Figure S10.

To further evaluate the thermal transformation/decomposition of 1 and 2 into PbS, in situ real-time synchrotron powder XRD experiments were performed. Diffraction patterns were collected while 1 and 2 were heated under an atmosphere of helium at 3 °C min<sup>-1</sup>, which revealed phase transformations and the nature of decomposition.

Diffraction data for 1 are presented in Figure 6. The first transformation occurred in the 150–180 °C region, where the diffraction peak intensities and areas decreased with respect to increased temperature, leading to a loss of all diffraction peaks from 1 by 200 °C. This transformation is associated with a first-

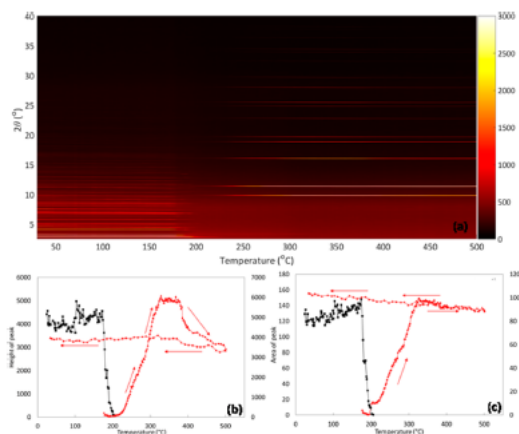


Figure 6. Color-coded heatmap showing powder diffraction data for 1 between 30 and 500 °C (a), peak height and area analysis for the (200) peak of PbS (red ▲) and peak at 3.1° for 1 (black ■) (b, c).

order phase transition from solid to liquid, which is in accordance with the thermogravimetric and optical microscopy data. As the peak areas diminished, peaks assigned to PbS (200) increased in height, and area from 190 °C and reached a maximum area at 325 °C, Figure 6b,c. These data show that growth of PbS occurs from molten 1 with no further decomposition of 1 by 325 °C, as shown by the steady state of peak area for PbS between 325 and 375 °C. An analysis of the PbS diffraction patterns using the Scherrer equation and the full Williamson–Hall technique, Figure S17, indicated that the nanoscale particles grew rapidly in the melt phase, then coarsened continuously reaching several hundred nanometers size by 350 °C. Between 375 and 500 °C there was a nonlinear decrease in the peak height of the PbS (200) diffraction peak without an associated decrease in peak area. No other diffraction peaks associated with other crystalline phases were observed. These observations are in agreement with the variable-temperature isotropic light microscopy, Figure S9, and thermogravimetric experiments, confirming that PbS is formed from the molten solution of 1, with no intermediate crystalline phases being present during thermolysis of 1.

The in situ diffraction data for 2 are presented in Figure 7. In contrast to the thermolysis of 1, there is no intermediate

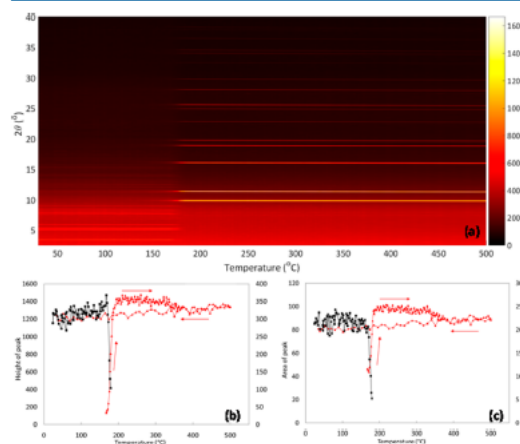


Figure 7. Color-coded heatmap showing powder diffraction data for 2 between 30 and 500 °C (a), peak height and area analysis for the (200) peak of PbS (red ▲) and peak at 3.3° for 2 (black ■) (b, c).

solution or amorphous phase, with decomposition of 2 and formation of PbS occurring in a single event. At 169 °C, diffraction peaks associated with 2 disappeared, and peaks associated with PbS appeared, Figure 7. The rate of PbS formation was orders of magnitude faster during the thermolysis of 2 compared to that of 1, as shown by the difference in the slope of the linear region between 170 and 183 °C in 1 and 2 (Figures 6c and 7c). Furthermore, there were no changes in peak height or area of the PbS diffraction patterns, indicating no changes in structure occurred after formation. Analysis using the Scherrer equation and Williamson–Hall technique, Figure S17, showed that PbS grew rapidly from the solid matrix and maintained a size of 60 nm (Scherrer) or 90 nm (Williamson–Hall analysis) thereafter.

**Characterization of PbS Crystals.** Compounds 1 and 2 were heated under a variety of thermal conditions, and the

resultant materials were characterized by powder XRD, FTIR, SEM, and TEM.

Powder XRD patterns for PbS, Figure 8, correspond to the standard pattern of face-centered cubic PbS (PDF 04–004–

#### Characterization of PbS crystals

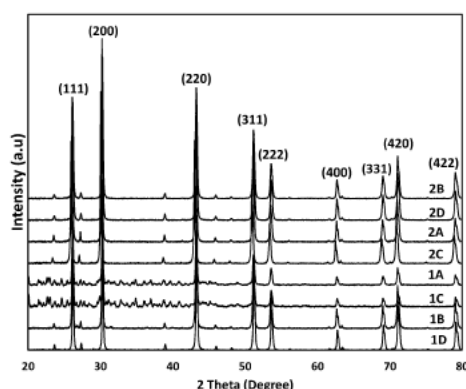


**Figure 8.** Powder diffraction patterns for PbS. Patterns are labeled based on the SSP (1 or 2) and thermolysis conditions (A–D).

4329). SEM revealed a variety of morphologies, Figure 5. Under heating conditions (A) and (C) (see Experimental) a number of low-intensity peaks attributed to unreacted 1 are evident, and IR absorbance bands at 2965, 1476, 1302, and 935  $\text{cm}^{-1}$  attributed to 1 were observed, Figure S11. No diffraction peaks or FTIR bands arising from impurities were detected in any other powders.

SEM images show that heating 1 to 205 °C, at either the slow or fast rate, Figure 9(1A and 1C), resulted in approximately cubic or rectangular prismatic PbS crystalline material coated by a layer (ca. 10–20 nm) of unreacted 1, consistent with the FTIR and XRD data. The crystals possess irregular edges, and none are independent, with noticeable contact of at least two of the edges. Partial penetration twinning is evident in some crystals.

Unreacted 1 (determined by XRD, SEM, and FTIR spectroscopy) is evident in the SEM images and surrounds

the crystals. Considering that the melting point of 1 is less than 205 °C, nucleation and crystallization of PbS occur within the molten SSP. Some periodicity is evident in the material surrounding the PbS crystals. Heating 1 for a total of 60 min at 205 °C resulted in clean PbS with no unreacted SSP, Figure S12.

Heating 1 to 550 °C gave approximately cubic crystals; however, the faces are somewhat textured and less smooth when compared to the other samples. The crystals formed upon slow heating to 550 °C are generally smaller than those formed under the other thermolysis conditions for 1. Rapid heating to 550 °C also gave pure cubic PbS crystals, as shown by TEM, Figure S13, and FTIR spectroscopy, Figure S11.

Heating 2 to 205 °C either slowly or rapidly, Figure 9(2A, 2C), gives submicron crystalline PbS. Crystals are mostly cubic with some being elongated rectangular prisms. Most have edges of length ~90–120 nm with a small number having edge lengths of 145–150 nm.

HRTEM and the corresponding FFT of a nanocrystal from residue 2C (Figure 10c,d) was indexed to the [001] zone axis of the FCC PbS, ( $Fm\bar{3}m$  space group). The {200} plane spacing was 0.3 nm, in agreement with the pXRD of PbS (0.2967 nm). The average size of the crystalline PbS 2C was 90 nm, Figure 10a. The transmission spectra of the PbS crystals at 293 K within KBr, Figure S14, reveal an absorption edge at ~0.43 eV for the PbS crystals, identical to that of bulk-phase PbS.<sup>1</sup>

Heating 2 slowly to 550 °C gave predominately sheetlike structures composed of stacked layers of PbS with an average thickness of ~30 nm, Figure S15. The crystals show characteristics of a terrace-ledge kink model for crystal growth, with flat, stepped, and kinked faces evident.<sup>57</sup> During crystal growth, new atoms preferentially add at the kink sites, so the layers grow to extend the flat face.

**Characterization of Thermistor Device.** PbS obtained by rapid heating of 2 to 205 °C (PbS 2C) was used as the resistance element in a thermistor device. This material was chosen for its phase and chemical purity, and contained single-crystalline and monodisperse PbS crystals. The electrode configuration containing 78 interdigitated fingers is shown in Figure S18a. There were no gold–gold contacts, and the resistance across the electrodes was greater than  $1 \times 10^6 \Omega$  prior to PbS deposition. A drop-cast layer of PbS 2C resulted in

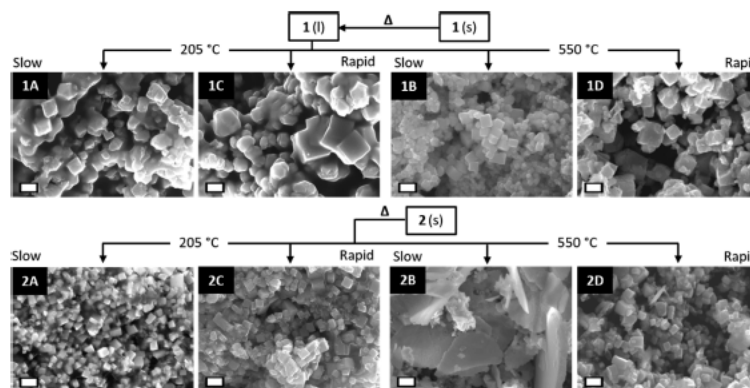


**Figure 9.** SEM micrographs of PbS crystals formed by thermolysis of 1 and 2 under different thermal regimes. Scale bars are 250 nm.

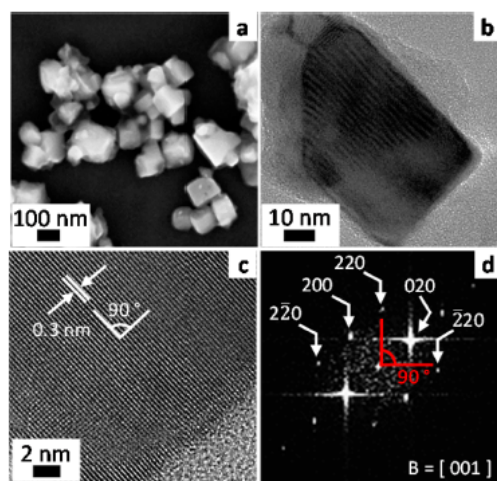


**Figure 10.** (a) SE-SEM micrograph of PbS 2C. (b) TEM micrograph of PbS 2C. (c) HRTEM micrograph of PbS 2C and (d) FFT of region shown in (c).

a resistance of 117  $\Omega$  at 293 K, attributed to the insertion of PbS between the gold electrodes. Backscatter SEM micrographs reveal a small number of Au-PbS-Au contacts, Figure S18b–d, where aggregates of PbS crystals span the 10  $\mu\text{m}$  electrode separation. Device electrical characterization data are shown in Figure 11.

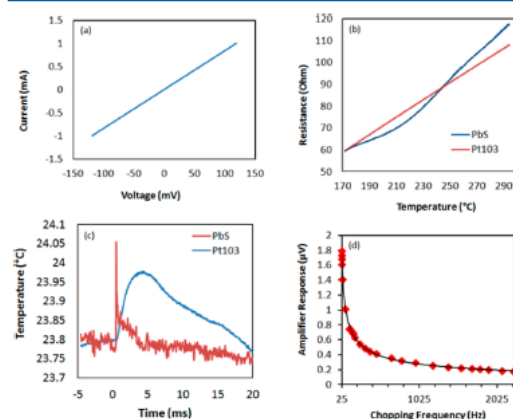


**Figure 11.** Device characterization: (a) room-temperature  $I$ – $V$  curve showing an ohmic response, (b) temperature-resistance comparison of PbS and a Pt-103 device, (c) response to pulse of hot air, (d) thermal-time response to chopped light.

A current–voltage scan at 293 K exhibited a linear ohmic response, Figure 11a. Resistance–temperature data were obtained using a liquid nitrogen-cooled cryogenic stage in a vacuum chamber. The calibration curve reveals a monotonic response with a positive temperature coefficient of resistivity between 170 and 293 K, Figure 11b. The response of a typical Pt103 resistance thermometer is included for reference. A least-

squares polynomial fit for the full temperature range (170–293 K) was found to be

$$R_{\text{PbS}} = 1 \times 10^{-8}T^5 + 2 \times 10^{-6}T^4 + 7 \times 10^{-5}T^3 - 0.0014T^2 + 0.5438T + 105.95$$

Two temperature response rate regimes are evident; 0.585  $\Omega \text{ K}^{-1}$  from 208 to 293 K and 0.260  $\Omega \text{ K}^{-1}$  from 173 to 208 K. The geometry-independent dimensionless sensitivity (DS) was determined by evaluating the slope of the resistance–temperature curve on a logarithmic scale giving a value of 1.41, which is superior to that of platinum resistance thermometers (DS = 1) in the range from 170 to 293 K.

The response of the device to a heat source was measured using a short pulse of hot air while sampling resistance. The acquired data indicate that the response of the PbS device ( $\sim 25 \mu\text{s}$ ) was orders of magnitude faster than the Pt103 reference device ( $\sim 5 \text{ ms}$ , Figure 11c). In a separate experiment, an optical fiber coupled to a variable-speed chopped xenon light source was used to heat the device. Temporal-thermal response data at 293 K are shown in Figure 11d. The lock-in amplifier response decreased with increased chopping frequency. The background voltage of the amplifier was 0.03  $\mu\text{V}$ , and the PbS device displayed sensitivity to the stimulus at frequencies upward of 2 kHz. This response rate is extremely fast due to the very low thermal mass of the active material. The amplifier response is directly proportional to the change in sensor resistance, and the PbS sensor device displayed a change of 1.27 m $\Omega$  at the 3 dB cutoff frequency of 48 Hz. Thus, the detectable change in temperature is 2.2 mK. We estimate from these data, Figure S16, that temperature changes in the order of 0.5  $\mu\text{K}$  should be detectable on a time scale of 13  $\mu\text{s}$ , which is consistent with the data obtained from the pulsed heat experiment, Figure 11c.

## CONCLUSIONS

The two SSPs examined here (1 and 2) exhibited markedly different decomposition properties; 1 decomposed at a temperature higher than its melting point, whereas decomposition of 2 occurred at a temperature at which the material was still in the solid state. The decomposition processes resulted in PbS crystals.

From 1, impure material was obtained when heated to  $\sim 200^\circ\text{C}$  for a short period of time, but pure PbS was obtained after longer thermolysis times or higher temperatures. In the case of 2, the purity of the resultant PbS was not influenced by the heating rate or temperature (beyond decomposition). In all but one thermolysis regime, the size and morphology of PbS crystals from 2 remained unchanged with crystals being smaller than those formed during equivalent treatment of 1.

Our results show that the relationship between melting point and decomposition temperature of the SSP (which in turn is influenced by the DTC ligand) affects the size and morphology of the resultant PbS crystals. Decomposition from the solid state gave smaller PbS crystals than those obtained by decomposition from the molten state.

Finally, crystalline PbS made using solid-state thermolysis can be used to create a novel PbS thermistor device capable of detecting very small (0.5  $\mu\text{K}$ ) and rapid (13  $\mu\text{s}$ ) changes in temperature in the range from 170 to 293 K.



## ■ ASSOCIATED CONTENT

## ■ Supporting Information

The Supporting Information is available free of charge on the ACS Publications website at DOI: 10.1021/acs.inorgchem.7b03009.

Crystallographic data, Hirshfeld surface analyses, discussion of crystal packing, FTIR and NMR spectra, TEM and SEM micrographs (PDF)

## ■ Accession Codes

CCDC 1554133–1554134 contain the supplementary crystallographic data for this paper. These data can be obtained free of charge via [www.ccdc.cam.ac.uk/data\\_request/cif](http://www.ccdc.cam.ac.uk/data_request/cif), or by emailing [data\\_request@ccdc.cam.ac.uk](mailto:data_request@ccdc.cam.ac.uk), or by contacting The Cambridge Crystallographic Data Centre, 12 Union Road, Cambridge CB2 1EZ, UK; fax: +44 1223 336033.

## ■ AUTHOR INFORMATION

## ■ Corresponding Author

\*E-mail: [Andrew.McDonagh@uts.edu.au](mailto:Andrew.McDonagh@uts.edu.au).

## ■ ORCID

Angus R. Gentle: 0000-0001-8964-0722

Michael B. Cortie: 0000-0003-3202-6398

Anthony T. Baker: 0000-0001-9700-0178

Andrew M. McDonagh: 0000-0002-9502-1175

## ■ Author Contributions

The manuscript was written through contributions from all authors.

## ■ Notes

The authors declare no competing financial interest.

## ■ ACKNOWLEDGMENTS

We acknowledge Mr. M. Berkahn for assistance with the laboratory powder diffractometer and Dr. R. Shimmon for laboratory assistance. We thank Mr. D. Totonjian for assistance with TEM image analysis. We are in gratitude to the Mark Wainwright Analytical Centre, UNSW, for access to single-crystal XRD and NMR spectrometers. We thank technical staff at the Australian Synchrotron for their assistance. This research is supported by an Australian Government Research Training Program Scholarship.

## ■ REFERENCES

- (1) Dalven, R. A review of the semiconductor properties of PbTe, PbSe, PbS and PbO. *Infrared Phys.* **1969**, *9* (4), 141–184.
- (2) Saran, R.; Curry, R. J. Lead sulphide nanocrystal photodetector technologies. *Nat. Photonics* **2016**, *10* (2), 81–92.
- (3) He, J.; Luo, M.; Hu, L.; Zhou, Y.; Jiang, S.; Song, H.; Ye, R.; Chen, J.; Gao, L.; Tang, J. Flexible lead sulfide colloidal quantum dot photodetector using pencil graphite electrodes on paper substrates. *J. Alloys Compd.* **2014**, *596*, 73–78.
- (4) Klimov, V. I. *Nanocrystal Quantum Dots*, 2nd ed.; CRC Press: 2010.
- (5) Moreels, I.; Lambert, K.; Smeets, D.; De Muynck, D.; Nollet, T.; Martins, J. C.; Vanhaecke, F.; Vantomme, A.; Delerue, C.; Allan, G.; Hens, Z. Size-Dependent Optical Properties of Colloidal PbS Quantum Dots. *ACS Nano* **2009**, *3* (10), 3023–3030.
- (6) Konstantatos, G.; Sargent, E. H. Nanostructured materials for photon detection. *Nat. Nanotechnol.* **2010**, *5* (6), 391–400.
- (7) Zhang, C.; Kang, Z. H.; Shen, E. H.; Wang, E. B.; Gao, L.; Luo, F.; Tian, C.; Wang, C.; Lan, Y.; Li, J.; Cao, X. Synthesis and evolution of PbS nanocrystals through a surfactant-assisted solvothermal route. *J. Phys. Chem. B* **2006**, *110*, 184–189.
- (8) Cao, Y.; Hu, P.; Jia, D. Solvothermal synthesis, growth mechanism, and photoluminescence property of sub-micrometer PbS anisotropic structures. *Nanoscale Res. Lett.* **2012**, *7* (1), 668.
- (9) Moreels, I.; Justo, Y.; De Geyter, B.; Hastraete, K.; Martins, J. C.; Hens, Z. Size-Tunable, Bright, and Stable PbS Quantum Dots: A Surface Chemistry Study. *ACS Nano* **2011**, *5* (3), 2004–2012.
- (10) Giansante, C.; Infante, I.; Fabiano, E.; Grisorio, R.; Suranna, G. P.; Gigli, G. Darker-than-Black PbS Quantum Dots: Enhancing Optical Absorption of Colloidal Semiconductor Nanocrystals via Short Conjugated Ligands. *J. Am. Chem. Soc.* **2015**, *137* (5), 1875–1886.
- (11) Zhang, Z. H.; Lee, S. H.; Vittal, J. J.; Chin, W. S. A simple way to prepare PbS nanocrystals with morphology tuning at room temperature. *J. Phys. Chem. B* **2006**, *110*, 6649–6654.
- (12) Zhang, J.; Crisp, R. W.; Gao, J.; Kroupa, D. M.; Beard, M. C.; Luther, J. M. Synthetic Conditions for High-Accuracy Size Control of PbS Quantum Dots. *J. Phys. Chem. Lett.* **2015**, *6* (10), 1830–1833.
- (13) Quan, Z.; Li, C.; Zhang, X.; Yang, J.; Yang, P.; Zhang, C.; Lin, J. Polyol-Mediated Synthesis of PbS Crystals: Shape Evolution and Growth Mechanism. *Cryst. Growth Des.* **2008**, *8* (7), 2384–2392.
- (14) Pradhan, N.; Katz, B.; Efrima, S. Synthesis of High-Quality Metal Sulfide Nanoparticles from Alkyl Xanthate Single Precursors in Alkylamine Solvents. *J. Phys. Chem. B* **2003**, *107* (50), 13843–13854.
- (15) McNaughton, P. D.; Saah, S. A.; Akhtar, M.; Abdulwahab, K.; Malik, M. A.; Raftery, J.; Awudza, J. A. M.; O'Brien, P. The effect of alkyl chain length on the structure of lead(II) xanthates and their decomposition to PbS in melt reactions. *Dalton Trans.* **2016**, *45* (41), 16345–16353.
- (16) Chen, J.; Chen, L.; Wu, L.-M. The Solventless Syntheses of Unique PbS Nanowires of X-Shaped Cross Sections and the Cooperative Effects of Ethylenediamine and a Second Salt. *Inorg. Chem.* **2007**, *46* (19), 8038–8043.
- (17) Lewis, E.; Haigh, S.; O'Brien, P. The synthesis of metallic and semiconducting nanoparticles from reactive melts of precursors. *J. Mater. Chem. A* **2014**, *2* (3), 570–580.
- (18) Clark, J. M.; Kociok-Kohn, G.; Hammett, N. J.; Hill, M. S.; Hill, R.; Molloy, K. C.; Saponia, H.; Stanton, D.; Sudlow, A. Formation of PbS materials from lead xanthate precursors. *Dalton Trans.* **2011**, *40* (26), 6893–6900.
- (19) Akhtar, J.; Afzaal, M.; Vincent, M. A.; Burton, N. A.; Hillier, I. H.; O'Brien, P. Low temperature CVD growth of PbS films on plastic substrates. *Chem. Commun.* **2011**, *47* (7), 1991–1993.
- (20) Sathiyaraj, E.; Thirumaran, S. Synthesis and spectral studies on Pb(II) dithiocarbamate complexes containing benzyl and furfuryl groups and their use as precursors for PbS nanoparticles. *Spectrochim. Acta, Part A* **2012**, *97*, 575–581.
- (21) Akhtar, J.; Malik, M. A.; O'Brien, P.; Helliwell, M. Controlled synthesis of PbS nanoparticles and the deposition of thin films by Aerosol-Assisted Chemical Vapour Deposition (AACVD). *J. Mater. Chem.* **2010**, *20* (29), 6116–6124.
- (22) Trindade, T.; O'Brien, P.; Zhang, X.-M.; Motevalli, M. Synthesis of PbS nanocrystallites using a novel single molecule precursors approach: X-ray single-crystal structure of Pb(S<sub>2</sub>CNEtPr)<sub>2</sub>. *J. Mater. Chem.* **1997**, *7* (6), 1011–1016.
- (23) Aly, A. A.; Brown, A. B.; Bedair, T. M. I.; Ishak, E. A. Dithiocarbamate salts: biological activity, preparation, and utility in organic synthesis. *J. Sulfur Chem.* **2012**, *33* (5), 605–617.
- (24) Steggerda, J. J.; Cras, J. A.; Willemse, J. Reactions of complexes of dithiocarbamate and related ligands. *Recl. Trav. Chim. Pays-Bas-J. R. Neth. Chem. Soc.* **1981**, *100* (2), 41–48.
- (25) Onwudiwe, D. C.; Strydom, C. A.; Oluwafemi, O. S.; Hosten, E.; Jordaan, A. Synthesis, spectral and thermal studies of pyridyl adducts of Zn(II) and Cd(II) dithiocarbamates, and their use as single source precursors for ZnS and CdS nanoparticles. *Dalton Trans.* **2014**, *43* (23), 8703–12.
- (26) Lazell, M.; Norager, S. J.; O'Brien, P.; Revaprasadu, N. The use of dithio- and diselenocarbamates as precursors to nanoscale materials. *Mater. Sci. Eng., C* **2001**, *16*, 129–133.
- (27) Mthethwa, T.; Pullabhotla, V. S. R. R.; Mdululi, P. S.; Wesley-Smith, J.; Revaprasadu, N. Synthesis of hexadecylamine capped CdS



- nanoparticles using heterocyclic cadmium dithiocarbamates as single source precursors. *Polyhedron* **2009**, *28* (14), 2977–2982.
- (28) Onwudiwe, D. C.; Ajibade, P. A.; Omondi, B. Synthesis, spectral and thermal studies of 2,2'-bipyridyl adducts of bis(N-alkyl-N-phenyldithiocarbamato)zinc(II). *J. Mol. Struct.* **2011**, *987* (1–3), 58–66.
- (29) Hogarth, G. Transition-Metal Dithiocarbamates: 1978–2003. In *Progress in Inorganic Chemistry*; John Wiley & Sons, Inc., 2005; pp 71–561.
- (30) Cookson, J.; Beer, P. D. Exploiting the dithiocarbamate ligand in metal-directed self-assembly. *Dalton Trans.* **2007**, *15*, 1459–1472.
- (31) Benson, R. E.; Ellis, C. A.; Lewis, C. E.; Tiekink, E. R. T. 3D-, 2D- and 1D-supramolecular structures of  $\{Zn[S_2CN(CH_2CH_2OH)R]_2\}$  and their  $\{Zn[S_2CN(CH_2CH_2OH)R]_2\}$ (4,4'-bipyridine) adducts for R =  $CH_2CH_2OH$ , Me or Et: polymorphism and pseudo-polymorphism. *CrystEngComm* **2007**, *9* (10), 930–940.
- (32) Wong, W. W. H.; Phipps, D. E.; Beer, P. D. Acyclic and macrocyclic transition metal dithiocarbamate complexes containing imidazolium moieties for anion binding. *Polyhedron* **2004**, *23* (17), 2821–2829.
- (33) Prasad, R.; Yadav, R.; Trivedi, M.; Kociok-Köhn, G.; Kumar, A. The interplay of thiophilic and hydrogen bonding interactions in the supramolecular architecture of phenylmercury 4-hydroxypiperidine dithiocarbamate. *J. Mol. Struct.* **2016**, *1103*, 265–270.
- (34) Boadi, N. O.; Malik, M. A.; O'Brien, P.; Awudza, J. A. M. Single source molecular precursor routes to lead chalcogenides. *Dalton Trans.* **2012**, *41* (35), 10497–10506.
- (35) Paca, A. M.; Ajibade, P. A. Synthesis and structural studies of iron sulphide nanocomposites prepared from Fe(III) dithiocarbamates single source precursors. *Mater. Chem. Phys.* **2017**, *202*, 143–150.
- (36) Ramasamy, K.; Kuznetsov, V. L.; Gopal, K.; Malik, M. A.; Raftery, J.; Edwards, P. P.; O'Brien, P. Organotin Dithiocarbamates: Single-Source Precursors for Tin Sulfide Thin Films by Aerosol-Assisted Chemical Vapor Deposition (AACVD). *Chem. Mater.* **2013**, *25* (3), 266–276.
- (37) Kevin, P.; Lewis, D. J.; Raftery, J.; Azad Malik, M.; O'Brien, P. Thin films of tin(II) sulphide (SnS) by aerosol-assisted chemical vapour deposition (AACVD) using tin(II) dithiocarbamates as single-source precursors. *J. Cryst. Growth* **2015**, *415*, 93–99.
- (38) Arul Prakasam, B.; Lahtinen, B.; Peuronen, M.; Muruganandham, A.; Kolehmainen, M.; Haapaniemi, E.; Sillanpää, M. Spectral and structural studies on Ni(II) dithiocarbamates: Nickel sulfide nanoparticles from a dithiocarbamate precursor. *Inorg. Chim. Acta* **2015**, *425*, 239–246.
- (39) Lee, S.-M.; Jun, Y.-w.; Cho, S.-N.; Cheon, J. Single-Crystalline Star-Shaped Nanocrystals and Their Evolution: Programming the Geometry of Nano-Building Blocks. *J. Am. Chem. Soc.* **2002**, *124* (38), 11244–11245.
- (40) Angeloski, A.; Hook, J. M.; Bhadbhade, M.; Baker, A. T.; McDonagh, A. M. Intramolecular H...S interactions in metal di-(isopropyl)dithiocarbamate complexes. *CrystEngComm* **2016**, *18* (37), 7070–7077.
- (41) Sheldrick, G. M. *Acta Crystallogr., Sect. A: Found. Crystallogr.* **2008**, *64*, 112–122.
- (42) Dolomanov, O. V.; Bourhis, L. J.; Gildea, R. J.; Howard, J. A. K.; Puschmann, H. *J. Appl. Crystallogr.* **2009**, *42*, 339–341.
- (43) Wolff, S. K.; Grimwood, D. J.; McKinnon, J. J.; Turner, M. J.; Jayatilaka, D.; Spackman, M. A. *CrystalExplorer (Version 3.1)*; University of Western Australia, 2012.
- (44) McKinnon, J. J.; Spackman, M. A.; Mitchell, A. S. Novel tools for visualizing and exploring intermolecular interactions in molecular crystals. *Acta Crystallogr., Sect. B: Struct. Sci.* **2004**, *60* (6), 627–668.
- (45) Spackman, M. A.; McKinnon, J. J. Fingerprinting intermolecular interactions in molecular crystals. *CrystEngComm* **2002**, *4* (66), 378–392.
- (46) McKinnon, J. J.; Jayatilaka, D.; Spackman, M. A. Towards quantitative analysis of intermolecular interactions with Hirshfeld surfaces. *Chem. Commun.* **2007**, *37*, 3814–3816.
- (47) Shinobu, L. A.; Jones, S. G.; Jones, M. M. Sodium N-methyl-D-glucamine dithiocarbamate and cadmium intoxication. *Acta Pharmacol. Toxicol.* **1984**, *54* (3), 189–194.
- (48) Ito, M.; Iwasaki, H. Structure of Lead(II) N,N-Diisopropylidithiocarbamate [Bis(N,N-diisopropylidithiocarbamato)lead(II)]. *Acta Crystallogr., Sect. B: Struct. Crystallogr. Cryst. Chem.* **1980**, *36*, 443–444.
- (49) Angeloski, A.; Baker, A. T.; Bhadbhade, M.; McDonagh, A. M. Bis( $\kappa^2S,S'$ -di(isopropyl)dithiocarbamato)nickel(II): Anagostic C–H...Ni interactions and physical properties. *J. Mol. Struct.* **2016**, *1113*, 127–132.
- (50) Healy, P. C.; Connor, J. W.; Skelton, B. W.; White, A. H. Alkyl Substituent Effects in Diamagnetic Dithiocarbamate Cobalt and Nickel Complexes. *Aust. J. Chem.* **1990**, *43* (6), 1083–1095.
- (51) Ma, J.; Feng, B.; Li, J.; Yang, X.; Lu, L.; Wang, X. Solid Phase Synthesis at Room Temperature, Characterization and Crystal Structure of bis(diiso-propylcarbamodithioato-S,S') Molybdenum. *J. Nanjing Univ. Sci. Technol.* **2004**, *28*, 648–652.
- (52) Ito, M.; Iwasaki, H. The Structure of the Monomeric Form of Mercury(II) N,N-Diisopropylidithiocarbamate [Bis(N,N-diisopropylidithiocarbamato)mercury(II)]. *Acta Crystallogr., Sect. B: Struct. Crystallogr. Cryst. Chem.* **1979**, *35*, 2720–2721.
- (53) Newman, P. W. G.; White, A. H. Crystal Structure of Bis(NN-di-isopropylidithiocarbamato)nickel(II). *J. Chem. Soc., Dalton Trans.* **1972**, *20*, 2239–2243.
- (54) Iwasaki, H.; Kobayashi, K. Structure of bis(N,N-diisopropylidithiocarbamato)copper(II). *Acta Crystallogr., Sect. B: Struct. Crystallogr. Cryst. Chem.* **1980**, *36* (7), 1655–1657.
- (55) Xu, L. Z.; Zhao, P. S.; Zhang, S. S. Crystal Structure and Characterization of Pd(II) Bis(diiso-propylidithiocarbamate) Complex. *Chin. J. Chem.* **2001**, *19* (4), 436–440.
- (56) Sovilj, S. P.; Vučković, G.; Babić, K.; Sabo, T. J.; Macura, S.; Juranić, N. Mixed-ligand complexes of cobalt(III) with dithiocarbamates and a cyclic tetradentate secondary amine. *J. Coord. Chem.* **1997**, *41* (1–2), 19–25.
- (57) De Yoreo, J. J.; Zepeda-Ruiz, L. A.; Friddle, R. W.; Qiu, S. R.; Wasylenki, L. E.; Chemov, A. A.; Gilmer, G. H.; Dove, P. M. Rethinking Classical Crystal Growth Models through Molecular Scale Insights: Consequences of Kink-Limited Kinetics. *Cryst. Growth Des.* **2009**, *9* (12), S135–S144.

## Author Contributions and Copyright Information: Conversion of single-crystals of a nickel(II) dithiocarbamate complex to nickel sulfide crystals

- A. Angeloski performed synthesis, isolation, all measurements (excluding TEM, solid state NMR spectroscopy and single crystal X-ray diffraction), data analysis, and wrote the manuscript
- A. R. Gentle provided assistance with electrical characterisation of the PbS device
- J. Scott performed and analysed the electron microscopies
- M.B. Cortie provided assistance with X-ray powder diffraction, and conceptual advice
- J.M. Hook provided assistance with the NMR spectroscopies
- M. Westerhausen provided assistance with fabrication of the sensor substrate
- M. Bhadbhade acquired single-crystal X-ray diffraction data
- A.T. Baker edited the manuscript
- A.M. McDonagh provided conceptual advice and revised the manuscript
- All authors have reviewed the manuscript, and all persons providing assistance have been acknowledged within the manuscript.

The article was reprinted (adapted) with permission from *Inorganic Chemistry*. Copyright (2018) American Chemical Society.



[Home](#) [Create Account](#) [Help](#)

 **ACS Publications**  
Most Trusted. Most Cited. Most Read.

**Title:** From Lead(II) Dithiocarbamate Precursors to a Fast Response PbS Positive Temperature Coefficient Thermistor

**Author:** Alexander Angeloski, Angus R. Gentle, John A. Scott, et al

**Publication:** *Inorganic Chemistry*

**Publisher:** American Chemical Society

**Date:** Feb 1, 2018

Copyright © 2018, American Chemical Society

**LOGIN**

If you're a [copyright.com](#) user, you can login to RightsLink using your copyright.com credentials. Already a RightsLink user or want to [learn more?](#)

### PERMISSION/LICENSE IS GRANTED FOR YOUR ORDER AT NO CHARGE

This type of permission/license, instead of the standard Terms & Conditions, is sent to you because no fee is being charged for your order. Please note the following:

- Permission is granted for your request in both print and electronic formats, and translations.
- If figures and/or tables were requested, they may be adapted or used in part.
- Please print this page for your records and send a copy of it to your publisher/graduate school.
- Appropriate credit for the requested material should be given as follows: "Reprinted (adapted) with permission from (COMPLETE REFERENCE CITATION). Copyright (YEAR) American Chemical Society." Insert appropriate information in place of the capitalized words.
- One-time permission is granted only for the use specified in your request. No additional uses are granted (such as derivative works or other editions). For any other uses, please submit a new request.

Permission for reuse of the article within this dissertation has been obtained prior to use

## **Chapter 5:**

Intramolecular H $\cdots$ S interactions in  
metal di(isopropyl)dithiocarbamate  
complexes



Cite this: *CrystEngComm*, 2016, 18, 7070

## Intramolecular H $\cdots$ S interactions in metal di-(isopropyl)dithiocarbamate complexes†

Alexander Angeloski,<sup>a</sup> James M. Hook,<sup>b</sup> Mohan Bhadbhade,<sup>c</sup> Anthony T. Baker<sup>d</sup> and Andrew M. McDonagh<sup>\*a</sup>

Networks of C–H $\cdots$ S interactions have been discovered within the molecular structure of sodium di-(isopropyl)dithiocarbamate pentahydrate with the formula Na(C<sub>7</sub>H<sub>14</sub>NS<sub>2</sub>) $\cdot$ 5H<sub>2</sub>O, revealed by single crystal X-ray diffraction. These interactions have also been investigated by *ab initio* and Hirshfeld surface analyses which show that the electron density is not symmetrical about the molecule. NMR spectroscopy in solution and solid the state showed temperature dependent restricted rotation of the isopropyl groups, which is attributed to the intramolecular C–H $\cdots$ S intramolecular interactions in this class of compound is evident in the structures of other di-(isopropyl)dithiocarbamate complexes deposited in the CSD. In general, the restricted rotation in di-(isopropyl)dithiocarbamate complexes can be directly attributed to intramolecular C–H $\cdots$ S interactions, which subsequently influence the geometry in association with steric repulsion factors.

Received 1st July 2016,  
Accepted 16th August 2016

DOI: 10.1039/c6ce01475e

www.rsc.org/crystengcomm

### 1. Introduction

Noncovalent interactions can exert significant influence on the geometry of molecules and their associated crystal structures.<sup>1</sup> Hydrogen bonding is an important noncovalent interaction where the focus has traditionally been on strong acceptors such as oxygen and nitrogen.<sup>2–7</sup> In contrast, sulfur is considered a weak acceptor, and the influence of H $\cdots$ S hydrogen bonds on molecular structure has received considerably less attention.<sup>8–11</sup> Such interactions can influence side chain geometries and secondary structure in biological systems (such as those involving the amino acid cysteine).<sup>12–16</sup> Thus, an understanding of the nature of H $\cdots$ S interactions is of fundamental importance. Here, we examine a low molecular weight compound to illustrate the influence of H $\cdots$ S interactions upon both solid and solution phase geometries. We demonstrate that the H $\cdots$ S interaction has a profound effect in both regimes that effectively breaks the symmetry of the

molecule and creates a restricted rotation about several of the covalent bonds within the molecule.

Dithiocarbamate complexes have been studied extensively for their ability to coordinate a range of transition and main block elements, and for their interesting and useful properties.<sup>17,18</sup> In particular, there is a significant amount of data pertaining to di-(isopropyl)dithiocarbamate (dipdte) compounds. The structure of the dipdte ligand is such that the C<sub>2</sub>NCS<sub>2</sub> atoms lie within a plane. It has been known for some time that there is a disruption to the symmetry of dipdte complexes whereby the methine hydrogens are oriented in different directions relative to the C<sub>2</sub>NCS<sub>2</sub> plane (Fig. 1). This orientation results in the inequivalence of the two isopropyl

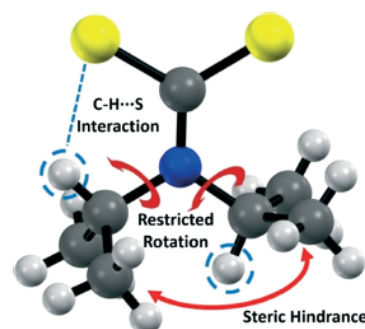


Fig. 1 Structure of the dipdte anion showing the important interactions.

<sup>a</sup> School of Mathematical and Physical Sciences, University of Technology Sydney, Ultimo, 2007, Australia. E-mail: andrew.mcdonagh@uts.edu.au

<sup>b</sup> NMR Facility, Mark Wainwright Analytical Centre, The University of New South Wales, Sydney, 2052, Australia

<sup>c</sup> School of Chemistry, The University of New South Wales, Sydney, 2052, Australia

<sup>d</sup> College of Science, Health and Engineering, La Trobe University, Melbourne, 3086, Australia

† Electronic supplementary information (ESI) available: Kinetic data, data obtained from CSD database survey of metal dipdte complexes, fingerprint plots for the Hirshfeld surface of Na(dipdte) $\cdot$ 5H<sub>2</sub>O, and relevant NMR spectra. CCDC 1488005. For ESI and crystallographic data in CIF or other electronic format see DOI: 10.1039/c6ce01475e



groups, which has been ascribed to a steric interaction hindering rotation about the N–C<sub>isopropyl</sub> bonds based on NMR experiments in solution.<sup>19–23</sup> The NMR data reveal thermodynamic parameters associated with this restricted rotation but in isolation, these studies do not elucidate the origin of the inequivalence of the two isopropyl groups.

In this work, we have redetermined<sup>24</sup> the crystal structure of sodium di(isopropyl)dithiocarbamate pentahydrate, Na(dipdte)·5H<sub>2</sub>O, with greater accuracy to allow a detailed examination of intramolecular C–H···S interactions. The compound was also analysed using variable temperature solution state NMR spectroscopy, which shows features associated with restricted rotation about the N–C<sub>isopropyl</sub> bonds. Using a combination of theoretical calculations and experimental observations, we elucidate the origin of the inequivalence of the two isopropyl groups and restricted rotation. Furthermore, we show that these C–H···S interactions are ubiquitous throughout metal dipdte complexes for which structural determinations have been deposited.

## 2. Experimental

### Reagents and instruments

Chemicals and solvents used in synthetic procedures were analytical grade and purchased from Sigma Aldrich and used as received. Millipore water (18.4 MΩ cm<sup>−1</sup>) was used in synthetic procedures. A high resolution mass spectrum was acquired using an Agilent 6510 Q-TOF with a mobile phase of 70% acetonitrile, 30% water.

### Synthesis

Sodium di(isopropyl)dithiocarbamate was prepared as described by Angeloski *et al.*<sup>25</sup> An aqueous solution of sodium hydroxide (10.00 g in 40 mL) was cooled with stirring to 5 °C. Diisopropylamine (25 mL) was added followed by diethyl ether (75 mL). The solution was maintained between 5–10 °C whilst carbon disulfide (25 mL) was added dropwise. A precipitate formed upon addition and the resultant mixture was stirred for 20 minutes. The crude material was collected by vacuum filtration, and the filter cake purified by recrystallization using layer diffusion of ether into a methanolic solution of the crude material. The colourless crystals were collected by vacuum filtration, washed with warm diethyl ether and dried *in vacuo* to produce 15.34 g of sodium di(isopropyl)dithiocarbamate (31%). HRMS (M + H)<sup>+</sup> for NaNS<sub>2</sub>C<sub>7</sub>H<sub>14</sub> calculated: 200.0538; found: 200.0549. <sup>1</sup>H NMR (600.1 MHz, CD<sub>3</sub>CN, 258 K): δ 6.21 (sept, *J* = 6.8 Hz, 1H, H2), 3.79 (sept, *J* = 6.9 Hz, 1H, H5), 1.63 (d, *J* = 6.8 Hz, 6H, C6H<sub>3</sub>, C7H<sub>3</sub>), 1.06 (d, *J* = 6.9 Hz, 6H, C3H<sub>3</sub>, C4H<sub>3</sub>). <sup>13</sup>C NMR (150.9 MHz, CD<sub>3</sub>CN, 258 K): δ 212.4 (C1), 56.1 (C2), 50.0 (C5), 20.9 (C6, C7), 19.6 (C3, C4).

### NMR spectroscopy and kinetic analysis

Variable temperature proton (<sup>1</sup>H), carbon (<sup>13</sup>C), 2D exchange spectroscopy (EXSY, with mixing time 100 ms), heteronuclear

single quantum correlation (HSQC) and heteronuclear multiple bond correlation (HMBC) nuclear magnetic spectroscopy of solutions was performed using a Bruker Avance III NMR spectrometer fitted with a BBFO Plus solution state probe. The frequency was 600.1 MHz for <sup>1</sup>H, 150.9 MHz for <sup>13</sup>C and 60.8 MHz for <sup>15</sup>N experiments. A Bruker BVT3000 VT unit was used in conjunction with a BCU-Xtreme cooler to accurately adjust the sample temperature between 293 and 258 K with deuterated acetonitrile as the solvent. Instrument broadening was accounted for using acetonitrile residual proton resonances. Using this data, experimental rate constants were calculated at each temperature using the signal FWHM for the methyl peak at 1.63 ppm. Arrhenius and Eyring activation parameters were obtained using generalized least squares linear regressions of log *k* vs. 1/*T* and log(*k*/*T*) vs. 1/*T* respectively. A solid state <sup>1</sup>H NMR spectrum was acquired using a Bruker Avance III 700 MHz solid state NMR spectrometer. Samples were loaded into a 1.3 mm zirconia rotor and a MAS rate of 60 kHz was adopted using a Bruker MAS 2 unit.

### Crystallographic analysis

Crystals of Na(dipdte)·5H<sub>2</sub>O suitable for analysis were prepared by layer diffusion of ether into a methanolic solution. A suitable crystal was selected under a polarising microscope (Leica M165Z), mounted on a MicroMount (MiTiGen) consisting of a thin polymer tip with a wicking aperture. The X-ray diffraction measurements were carried out on a Bruker Kappa-II CCD diffractometer at 150 K by using IμS Incoatec Microfocus Source with Mo-Kα radiation (λ = 0.710723 Å). The structure was solved using charge flipping and the full matrix least squares refinement was performed using ShelXL<sup>26</sup> in Olex2.<sup>27</sup> Heavy atoms were refined isotropically until *R*-factor convergence, and then an anisotropic model was applied. Hydrogen atoms were located using a difference Fourier plot, and restrained to neutron diffraction distances where required for water molecules.

CrystalExplorer<sup>28</sup> was used to generate Hirshfeld surfaces<sup>29–31</sup> representing *d*<sub>norm</sub> and electron deformation density. The latter surface was calculated using TONTO<sup>32</sup> which is integrated into CrystalExplorer, and the experimental geometry was used as the input. The electron deformation density was mapped on the Hirshfeld surface using the 6-311G(*d,p*) basis set with the Density Functional Theory.

### Crystal structure retrieval

Previous determinations of metal dipdte crystal structures were retrieved from the Cambridge Structural Database (CSD)<sup>33</sup> with the following specifications: *R* ≤ 5%, no disorder, no errors, no powder structures and complete 3D coordinates. This produced a total of 32 crystal structures, which were sorted by hand to remove duplicates and non-relevant structures. A final number of 28 crystal structures were retrieved. Lists of the crystal structure CSD reference codes are available in the ESI†

## Evaluation of intramolecular contacts

Atoms from the retrieved structures were relabelled to be in accordance with the labelling scheme in Fig. 2. The presence of an intramolecular C–H...S interaction was preliminarily assessed by calculation of the S1...H2 distance. Quantitative measurements were performed using the heavy atom structural parameters to avoid uncertainty due to hydrogen atom treatment. The structures were sorted by hand to retrieve the following parameters: C1–N1–C2 and C1–N1–C5 bond angles. The C1–N1, C2–S1 and C5–S2 (Fig. 2) distances were also extracted. Bond angles were kept to two decimal places, and bond lengths to three. All statistical analyses were conducted using the statistical analysis software, R 3.2.5.<sup>34</sup>

## 3. Results and discussion

## X-Ray structure determination

Relevant crystal data, selected bond lengths and angles are given in Tables 1 and 2 (see ESI† for complete data). These values are in good agreement with the previously reported structure (CSD-Refcode BUNPIJ), with bond lengths falling in the ranges expected on the analysis of the literature.<sup>24,36</sup> The asymmetric unit, Fig. 2, contains one molecular anion together with one sodium cation (Na1) co-ordinated to five water molecules (O1–O5) (the sixth octahedral site is occupied by O3 on the symmetry related water molecule O3 (1 – x, 1 – y, 1 – z)). The co-ordination sphere of sodium is distorted octahedral with deviations from ideal octahedral geometry of less than 5°. The Na–O distances range from 2.3859(15) Å to 2.4492(14) Å. There is no direct S2–Na1 bond; Na1 is located more than 4 Å from S2. Within the dipdtc anion, the maximum deviations from the least-squares plane through C2–C5–S2–S1 (with a r.m.s. deviation of 0.008 Å) are 0.009 Å for C2 and C5, and 0.008 Å for S1 and S2. The S2–C1 and S1–C1 bond lengths are inequivalent with S1–C1 [1.7484(16) Å] elongated compared to S2–C1 [1.7145(17) Å]. The N1–C2 and N1–C5 bond lengths are equal within experimental error and all

Table 1 Crystal data and structure refinement parameters for Na(dipdtc)·5H<sub>2</sub>O

Chemical formula	2(C <sub>7</sub> H <sub>14</sub> NS <sub>2</sub> )·H <sub>2</sub> O·Na <sub>2</sub> O <sub>10</sub>
<i>M<sub>r</sub></i>	578.76
Crystal system, space group	Triclinic, <i>P</i> 1
Temperature (K)	150
<i>a</i> , <i>b</i> , <i>c</i> (Å)	5.9472(11), 7.7189(16), 17.425(3)
$\alpha$ , $\beta$ , $\gamma$ (°)	92.183(8), 95.095(8), 106.851(8)
<i>V</i> (Å <sup>3</sup> )	760.8(3)
<i>Z</i>	1
Radiation type	Mo K $\alpha$
$\mu$ (mm <sup>−1</sup> )	0.38
Crystal size (mm)	0.41 × 0.09 × 0.04
Absorption correction	Multi-scan <i>SADABS</i> 2014/5 (ref. 35) was used for absorption correction. <i>wR<sub>2</sub></i> (int) was 0.1663 before and 0.0594 after correction. The ratio of minimum to maximum transmission is 0.9019. The $\lambda/2$ correction factor is 0.00150
Diffractionmeter	Bruker APEX-II CCD
<i>T<sub>min</sub></i> , <i>T<sub>max</sub></i>	0.672, 0.746
No. of measured, independent and observed [ <i>I</i> > 2 $\sigma$ ( <i>I</i> )] reflections	18 709, 3304, 2666
<i>R<sub>int</sub></i>	0.060
( $\sin \theta/\lambda$ ) <sub>max</sub> (Å <sup>−1</sup> )	0.639
<i>R</i> [ <i>F</i> <sup>2</sup> > 2 $\sigma$ ( <i>F</i> <sup>2</sup> )], <i>wR</i> [ <i>F</i> <sup>2</sup> ], <i>S</i>	0.032, 0.070, 1.04
No. of reflections	3304
No. of parameters	241
No. of restraints	11
H-atom treatment	All H-atom parameters refined
$\Delta\rho_{\text{max}}$ , $\Delta\rho_{\text{min}}$ (e Å <sup>−3</sup> )	0.30, −0.25

bond lengths are similar to those in other M(dipdtc) structures, where M = Pb, Hg, Ni, In, Co, Be, Cu and Au.<sup>37–44</sup>

From the molecular assembly diagram, Fig. 3, a layered supramolecular motif is evident parallel to the crystallographic *b* direction (see ESI† for images showing packing

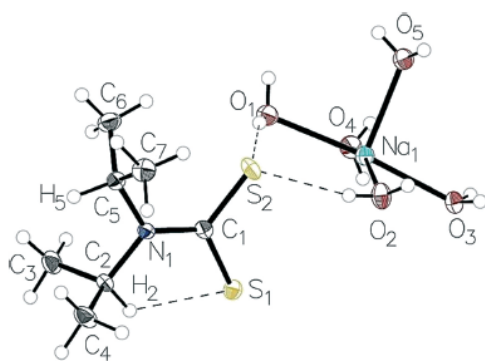


Fig. 2 The structure the Na(dipdtc)·5H<sub>2</sub>O asymmetric unit showing the atom-labelling scheme and thermal displacement ellipsoids at 50% probability.

Table 2 Selected bond lengths (Å) and angles (°) for Na(dipdtc)·5H<sub>2</sub>O

S1–C1	1.7484(16)	Na1–O4	2.3891(13)
S2–C1	1.7145(17)	Na1–O1	2.4492(14)
N1–C2	1.492(2)	Na1–O2	2.4207(13)
N1–C1	1.345(2)	Na1–O5	2.3859(15)
C2–C3	1.524(2)	Na1–O3 <sup>i</sup>	2.4278(14)
C5–C6	1.522(2)	Na1–O3	2.3879(14)
C2–N1–C5	113.38(12)	O4–Na1–O1	92.33(5)
C1–N1–C2	122.01(13)	O4–Na1–O2	162.67(5)
C1–N1–C5	124.59(14)	O4–Na1–O3 <sup>i</sup>	84.60(5)
N1–C2–C3	111.51(13)	O2–Na1–O1	95.54(5)
N1–C2–C4	111.23(13)	O2–Na1–O3 <sup>i</sup>	80.40(5)
C4–C2–C3	112.74(15)	O5–Na1–O4	96.85(5)
S2–C1–S1	118.11(9)	O5–Na1–O1	88.03(5)
N1–C1–S1	120.25(12)	O5–Na1–O2	98.83(5)
N1–C1–S2	121.63(12)	O5–Na1–O3	97.38(5)
N1–C5–C7	113.60(13)	O5–Na1–O3 <sup>i</sup>	175.04(5)
N1–C5–C6	113.02(13)	O3–Na1–O4	85.89(5)
C6–C5–C7	113.36(15)	O3–Na1–O1	174.47(5)
O3–Na1–O2	84.83(5)	O3 <sup>i</sup> –Na1–O1	87.17(5)
Na1–O3–Na1 <sup>i</sup>	92.55(5)	O3–Na1–O3 <sup>i</sup>	87.45(5)

Symmetry code: (i) −x + 1, −y + 1, −z + 1.



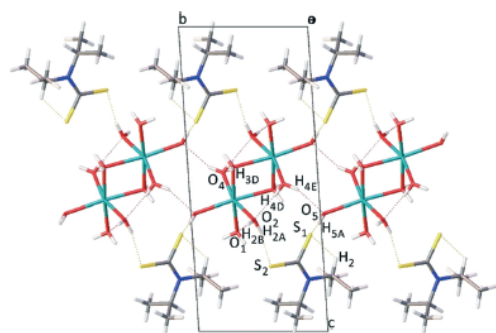


Fig. 3 Molecular packing diagram as viewed along the *a* axis, showing layered morphology of Na(dipdte)·5H<sub>2</sub>O.

diagrams viewed along *b* and *c* directions). The layered structure is stabilised by van der Waals interactions between the alkyl groups on the anion.

Sodium ions are positioned between layers of symmetrically equivalent ligand anions, forming a two dimensional Na–Na array oriented parallel to the crystallographic *b* direction. The sodium ions are separated by a distance of 3.4804(12) Å, significantly longer than the sum of ionic radii of 2.32 Å. Alternating sodium ions are linked by bridging water molecules at O3, forming a four membered Na1–O3–Na1–O3 ring with vertices of 92.55(5)° for Na1–O3–Na1 and 87.45(5)° for O3–Na1–O3. That is, dinuclear entities [Na<sub>2</sub>(OH<sub>2</sub>)<sub>10</sub>] exist in which the distorted NaO<sub>6</sub> octahedra share an edge. The array of Na cations is stabilised by a network of hydrogen bonding<sup>45</sup> between alternate and neighbouring water molecules where distances and angles are in agreement with literature values for O–H···O hydrogen bonds.<sup>46–48</sup> The ligand anions are linked by O–H···S hydrogen bonds<sup>2,49</sup> to the water molecules associated with the array of sodium cations. These hydrogen bonding contacts are summarised in Table 3.

Contacts involving intermolecular H···S, H···O and H···H interactions were examined using Hirshfeld surface analysis.<sup>29–31,50,51</sup> The majority of interactions within the structure are dominated by van der Waals H···H interactions

(~65%) followed by O–H···S (~17%) and O–H···O (~13%) interactions. The intermolecular contacts are highlighted in the map of  $d_{\text{norm}}$  on the Hirshfeld surface, Fig. 4. The dark red regions are due to hydrogen bonding whilst the blue and white regions reflect H···H interactions. C–H···S interactions are also evident.

Of significance to the current work are the intramolecular non-bonding interactions involving sulfur. The S1···H2 intramolecular interaction has a distance of ~2.4 Å (Table 3), which as we show here, exerts influence throughout the entire molecular structure. The C1–N1–C2 angle is 2.58 (13)° smaller than the C1–N1–C5 angle and the C2–S1 distance is 0.034 Å shorter than the C5–S2 distance (Table 4). The S1···H2 interaction also results in a pair of interactions between S2 and the methyl hydrogens attached to C6 and C7 of ~2.7 Å (Table 3). That is, the S1···H2 interaction creates an inequivalence of the two isopropyl groups within the dipdte anion. The intramolecular C–H···S dihedral angles and lengths are similar to those involving cysteine (117.4° and 2.51 Å) and methionine (119.0° and 2.74 Å) residues interacting within proteins.<sup>12</sup>

Electrostatic deformation density and topological features of the intramolecular C–S···H interaction.

A 3D electrostatic deformation density map (Fig. 5) shows the electron density about the dipdte anion. The lone pair electron density (LPED) about S1 and S2 is of particular interest as this may influence hydrogen bond directionality and the capacity of S1 and S2 to form multiple H bonds.<sup>2</sup> Our calculations show that the S atom LPED adopts a toroidal geometry, in agreement with previous analyses of sulfur-containing compounds.<sup>2</sup> Upon closer examination (Fig. 6), the LPED about S1 and S2 is somewhat distorted as a result of S···H interactions. In addition to intermolecular interactions with H<sub>2</sub>O, electron density is directed from S1 towards H2 while S2 directs electron density towards H6 and H7. A region of charge depletion (shown in red) about H2 is oriented toward the LPED about S1. This attractive behaviour between

Table 3 Selected hydrogen bond parameters

<i>D</i> –H··· <i>A</i>	<i>D</i> –H (Å)	H··· <i>A</i> (Å)	<i>D</i> ··· <i>A</i> (Å)	<i>D</i> –H··· <i>A</i> (°)
C2–H2···S1	0.998(16)	2.392(16)	3.0264(17)	120.8(12)
C7–H7A···S2	0.921(19)	2.714(17)	3.270(2)	119.7(13)
C6–H6A···S2	0.938(19)	2.741(17)	3.280(2)	117.4(13)
O2–H2A···S2	0.85(2)	2.41(2)	3.2336(15)	165(2)
O5–H5A···S1 <sup>i</sup>	0.83(2)	2.53(2)	3.2831(14)	151(2)
O3–H3D···O4 <sup>ii</sup>	0.83(2)	2.02(2)	2.8407(18)	171(2)
O2–H2B···O1 <sup>ii</sup>	0.84(2)	1.97(2)	2.8123(18)	175(2)
O4–H4D···O2 <sup>iii</sup>	0.83(2)	1.95(2)	2.7796(19)	176(2)
O4–H4E···O5 <sup>iv</sup>	0.83(2)	2.08(2)	2.8751(19)	160(2)

Symmetry codes: (i) *x*, *y* + 1, *z*; (ii) *x* + 1, *y*, *z*; (iii) *−x* + 1, *−y* + 1, *−z* + 1; (iv) *−x* + 1, *−y* + 2, *−z* + 1.

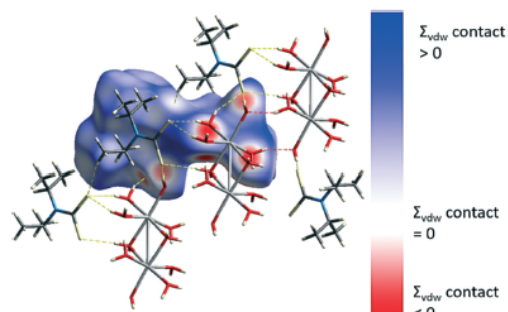


Fig. 4 Hirshfeld surface and O–H···S hydrogen bonds (yellow) and O–H···O hydrogen bonds (red).

Table 4 Summary of CSD structural parameters

Parameter	Mean $\pm$ standard error	Current study
C2–S1 distance	3.024(6) Å	3.0264(17) Å
C5–S2 distance	3.147(8) Å	3.1014(18) Å
S2–C1–S1 angle	111.81(71)°	118.11(9)°
C1–N1 distance	1.321(2) Å	1.345(2) Å
C1–N1–C5 angle	123.78(11)°	124.59(13)°
C1–N1–C2 angle	120.11(22)°	122.01(13)°

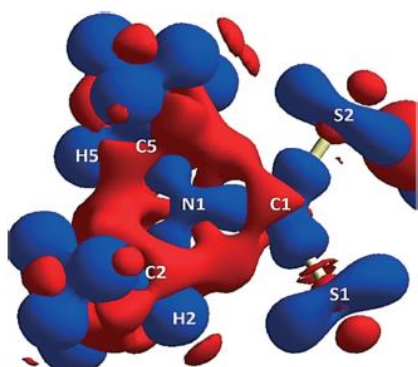
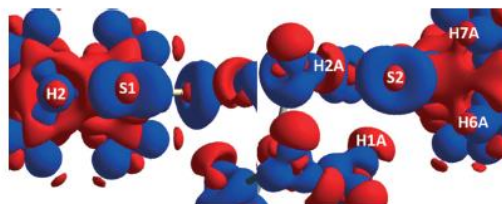
Fig. 5 Theoretical 3D electrostatic densities of the Na(dipdte)·5H<sub>2</sub>O anion at the B3LYP 6-311G(d,p) level. Areas of lower density are shown in red, and areas of higher density are shown in blue.

Fig. 6 3D static deformation densities of the sulfur tori (viewed down the C–S bond).

S1 and H2 is the origin of the unsymmetrical geometry of the isopropyl groups about N1.

#### NMR Spectroscopy

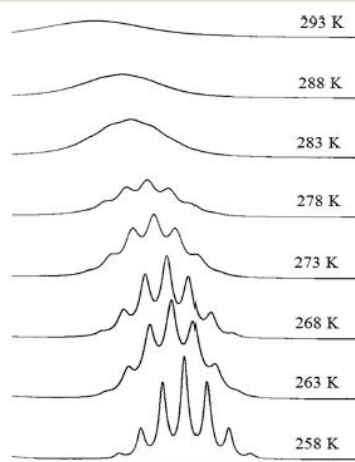
The crystallographic intramolecular C–H $\cdots$ S interactions yield two inequivalent isopropyl groups which are also manifested in solution, evidenced by two sets of signals in solution state NMR spectra. <sup>1</sup>H and <sup>13</sup>C NMR spectra of Na(dipdte)·5H<sub>2</sub>O recorded using deuterated acetonitrile at room temperature revealed broad proton and carbon resonances associated with the methyl and methine groups. Two broad signals for the methyl protons and two broad signals for the methine protons were observed, consistent with two inequivalent environments (ESI†). That is, H2 is maintained in synchronous gear-

like arrangement relative to H5 such that the steric repulsion between the associated methyl groups is minimised, Fig. 1. A DOSY experiment confirmed that the signals arose from only a single molecular species (ESI†).

The methine protons, H2 and H5, exhibit chemical shifts of 6.2 and 3.8 ppm, respectively. We attribute the large difference in chemical shifts to the influence of the C–H $\cdots$ S interaction upon the local electron density about H2, whereby H2 is significantly more deshielded than H5. Similarly, the signal assigned to the methyl protons associated with C6 and C7 appears at 1.6 ppm while the signal assigned to protons on C3 and C4 appears at 1.1 ppm. Thus, while the influence of the C–H $\cdots$ S interaction is still apparent, the difference in chemical shifts between the methyl protons on the two inequivalent isopropyl groups is less than that between H2 and H5 due to the greater distance between the methyl protons and sulfur. In the <sup>13</sup>C NMR spectrum recorded at 293 K, two sets of signals are also observed, which are significantly broadened. 2D-EXSY spectra recorded at 293 K contain H2/H5 cross peaks with intensity equal to the source peaks indicating a chemical exchange process at room temperature (ESI†).

Similarly, the high speed MAS solid state <sup>1</sup>H NMR spectrum (ESI†) contains methyl resonances in the range of 0–2 ppm and a signal assigned to the methine C–H $\cdots$ S proton H2 at 6.1 ppm. A signal at ~3.7 ppm is assigned to the methine proton H5, which is partially obscured by a broad peak associated with water molecules.

Variable temperature <sup>1</sup>H NMR (Fig. 7) data also provide kinetic insights into the rotation about the C2–N1 and C5–N1 bonds. A 2D-EXSY spectrum recorded at 258 K exhibits H2/H5 cross peaks of lower intensity than those recorded at 293 K, characteristic of reduced exchange between H2 and H5, and consistent with a greater restriction of rotation of the

Fig. 7 Selected portion of the 600 MHz <sup>1</sup>H spectra for Na(dipdte)·5H<sub>2</sub>O in CD<sub>3</sub>CN, showing the change in H2 resonance as a function of temperature.



isopropyl groups at this temperature. Upon cooling from 293 K to 258 K, the broad signals observed in the 1D  $^1\text{H}$  NMR spectrum resolve into their respective splitting patterns (septets for H2/H5 and doublets for the methyl protons), which is also consistent with the slowing rate of concerted rotation of the isopropyl groups. From the VT NMR data recorded using acetonitrile as solvent, a value of  $63\text{ kJ mol}^{-1}$  for  $\Delta G^\ddagger$  was calculated at 283 K and at 263 K, a value of  $56\text{ kJ mol}^{-1}$  was obtained. While the latter value for  $\Delta G^\ddagger$  agrees with data reported by others<sup>20</sup> using dichloromethane as solvent, our values for  $\Delta H^\ddagger$  ( $27\text{ kJ mol}^{-1}$ ),  $\Delta S$  (and  $-117\text{ J mol}^{-1}\text{ K}^{-1}$ ) and activation energy ( $30\text{ kJ mol}^{-1}$ ) are all somewhat smaller than those reported.<sup>20</sup> This indicates that the barrier to rotation may be lower in acetonitrile although quantitative comparison to the literature data<sup>20</sup> is problematic as the exact composition of the previously reported compound was uncertain.

#### Database survey of intramolecular C–H $\cdots$ S interactions in metal di(isopropyl)dithiocarbamate complexes

Having examined the CH $\cdots$ S interactions in Na(dipdte) $\cdot$ 5H $_2$ O, we sought to find crystallographic evidence for this interaction in other dipdte complexes. A survey of the Cambridge Structural Database was undertaken. A total of 28 suitable structure determinations were selected. All structures were planar about the S $_2$ CNC $_2$  moiety and importantly, showed evidence of intramolecular S1 $\cdots$ H2 interactions that induce differences between the two isopropyl groups. Table 4 summarises some relevant structural parameters.

The C2 to S1 distances,  $x$  (Fig. 8), were chosen for comparison in preference to H2 to S1 distances as the former are more accurate data. Values for  $x$  are tightly clustered about the mean of  $3.024\text{ \AA}$ . The shortest distance is  $2.941\text{ \AA}$  (Nd(dipdte) $_3$ phen) and the longest is  $3.117\text{ \AA}$  (Co(dipdte) $_3$ ). With the exception of Co(dipdte) $_3$ , all values of  $x$  fall within the  $2.941\text{--}3.054\text{ \AA}$  (a range of  $0.113\text{ \AA}$ ). In comparison, the C5–S2 distances ( $y$ ) varied more, and ranged from  $3.072$  to  $3.219\text{ \AA}$  (a range of  $0.147\text{ \AA}$ ) as shown in Fig. 9. The mean  $x$  distance for the 28 structures is significantly shorter (by  $0.123 \pm 0.01\text{ \AA}$ ) than that of  $y$  ( $t = -12.233$ ,  $\text{df} = 49.412$ ,  $p < 2.2 \times 10^{-16}$ ).

Unsurprisingly, the S1–C1–S2 angles ( $\psi$ ) are dependent on the coordinated metal<sup>24</sup> and span the range  $106.47$  to  $117.31^\circ$ . The angle C1–N1–C2 ( $\sigma$ ) ranges from  $117.0$  to  $122.3^\circ$  while the angle C1–N1–C5 ( $\varphi$ ) has a range of  $122.1$  to  $124.9^\circ$

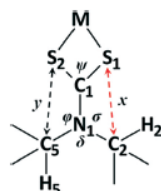


Fig. 8 Depiction of the important distances and angles discussed in the text.

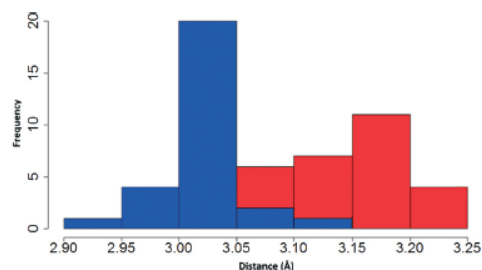


Fig. 9 Stacked histogram showing distribution of distances  $x$  (blue) and  $y$  (red).

and for any structure,  $\sigma < \varphi$  ( $t = -5.058$ ,  $\text{df} = 40.716$ ,  $p < 2.2 \times 10^{-16}$ ). As planarity is maintained across the S $_2$ CNC $_2$  moiety for all structures,  $\varphi + \delta + \sigma = 360^\circ$  and  $\delta > 114^\circ$  in all cases.

Our interpretation of these data is as follows. The angle  $\psi$  is dependent upon the coordinated metal while the distance  $x$  is a consequence of the C–H $\cdots$ S interaction. There were no statistically significant pairwise correlations between  $x$  and  $\psi$ , nor between  $x$  and any other structural parameter. Thus, the relationships  $\sigma \neq \varphi$  and  $x \neq y$  are a consequence of the C–H $\cdots$ S interaction. The C–H $\cdots$ S interaction restricts the rotation of the corresponding isopropyl group about the C2–N1 bond. This, in turn, influences the rotation of the isopropyl group about the C5–N1 bond (through steric effects). Previously published VT NMR-based analysis of the unusual geometry of metal dipdte complexes attributed the cause of restricted rotation to purely steric effects<sup>19–23</sup> but here we have shown that the underlying cause of the restricted rotation is the intramolecular C–H $\cdots$ S interaction, an electronic effect.

## Conclusions

We have shown that C–H $\cdots$ S intramolecular interactions are present within the molecular structure of Na(dipdte) $\cdot$ 5H $_2$ O. Theoretical calculations constrained by the experimentally derived structural data indicate that these interactions arise from the interaction between the lone pair electron density on sulfur and regions of electron depletion about a methine hydrogen.

Inequivalent chemical environments about the methine protons produced by the C–H $\cdots$ S intramolecular interaction were observed using NMR spectroscopy in solution and solid samples. Variable temperature solution state NMR spectroscopy was used to probe the restricted rotation of the isopropyl groups about the N–C single bonds revealing an energy barrier for this rotation of  $30\text{ kJ mol}^{-1}$ . The Gibbs free energy of the transition state ( $63\text{ kJ mol}^{-1}$ ) is in agreement with previous studies of restricted rotation in dipdte structures.

An analysis of 28 similar structures using the CSD revealed the presence of intramolecular C–H $\cdots$ S interactions. In all of the analysed structures, the heavy atom geometries supported the presence of these interactions. In all cases, the relevant intramolecular C–S distances were shorter and less

variable where intramolecular C–H⋯S interactions were present. There are no significant correlations between the steric factors of the structure and the C–H⋯S intramolecular interaction.

Thus, the restricted rotation in metal dipdte structures is directly attributable to the intramolecular C–H⋯S interaction, which subsequently influences the geometry in association with steric repulsion factors between methyl groups. We propose that these interactions are worthy of further examination in a wider range of compounds such as those found in biological systems (proteins, peptides) where bonds are subject to restricted rotation in proximity to sulfur atoms.

## Acknowledgements

We acknowledge Mr Leinad Diaz and Dr Ronald Shimmon for laboratory assistance and the Mark Wainwright Analytical Centre, UNSW, for access to single crystal XRD, solid and solution state NMR spectrometers. We also acknowledge Dr Parthapratim Munshi for assistance with CrystalExplorer software.

## References

- M. Nishio, Y. Umezawa, K. Honda, S. Tsuboyama and H. Suezawa, *CrystEngComm*, 2009, 11, 1757–1788.
- B. M. Francuski, S. B. Novaković and G. A. Bogdanović, *CrystEngComm*, 2011, 13, 3580.
- P. Schuster, G. Zundel and C. Sander, *The Hydrogen Bond—Recent Developments in Theory and Experiment*, North-Holland Pub. Co., 1976.
- G. C. Pimental and A. L. McClellan, *The Hydrogen Bond*, W. H. Freeman and Co., San Francisco, 1960.
- G. A. Jeffrey and W. Saenger, *Hydrogen Bonding in Biological Structures*, Springer-Verlag, Berlin, 1991.
- P. A. Hunt, C. R. Ashworth and R. P. Matthews, *Chem. Soc. Rev.*, 2015, 44, 1257–1288.
- A. Gavezzotti and L. L. Presti, *Cryst. Growth Des.*, 2016, 16, 2952–2962.
- T. Steiner, *Crystallogr. Rev.*, 2003, 9, 177–228.
- G. A. Jeffrey, *Crystallogr. Rev.*, 2003, 9, 135–176.
- J. Perlstein, *J. Am. Chem. Soc.*, 2001, 123, 191–192.
- G. R. Desiraju and T. Steiner, *The Weak Hydrogen Bond: In Structural Chemistry and Biology*, Oxford University Press, 2001.
- P. Zhou, F. Tian, F. Lv and Z. Shang, *Proteins: Struct., Funct., Bioinf.*, 2009, 76, 151–163.
- D. Pal and P. Chakrabarti, *J. Biomol. Struct. Dyn.*, 2001, 19, 115–128.
- L. M. Gregoret, S. D. Rader, R. J. Fletterick and F. E. Cohen, *Proteins: Struct., Funct., Bioinf.*, 1991, 9, 99–107.
- M. Iwaoka and N. Isozumi, *Molecules*, 2012, 17, 7266.
- S. Horowitz and R. C. Trievel, *J. Biol. Chem.*, 2012, 287, 41576–41582.
- A. A. Aly, A. B. Brown, T. M. I. Bedair and E. A. Ishak, *J. Sulfur Chem.*, 2012, 33, 605–617.
- J. J. Steggerda, J. A. Cras and J. Willemse, *Recl. Trav. Chim. Pays-Bas*, 1981, 100, 41–48.
- R. M. Golding, P. C. Healy, P. W. G. Newman, A. H. White and E. Sinn, *Inorg. Chem.*, 1972, 11, 2435–2440.
- A. F. Lindmark and R. C. Fay, *Inorg. Chem.*, 1983, 22, 2000–2006.
- Y. I. Takeda, N. Watanabe and T. Tanaka, *Spectrochim. Acta, Part A*, 1976, 32, 1553–1556.
- S. Bhattacharya, B. K. Kanungo and S. Sahoo, *J. Coord. Chem.*, 2006, 59, 371–378.
- A. N. Bhat, R. C. Fay, D. F. Lewis, A. F. Lindmark and S. H. Strauss, *Inorg. Chem.*, 1974, 13, 886–892.
- I. Ymen, *Acta Crystallogr., Sect. C: Cryst. Struct. Commun.*, 1983, 39, 874–877.
- A. Angeloski, A. T. Baker, M. Bhadbhade and A. M. McDonagh, *J. Mol. Struct.*, 2016, 1113, 127–132.
- G. M. Sheldrick, *Acta Crystallogr., Sect. A: Found. Crystallogr.*, 2008, 64, 112–122.
- O. V. Dolomanov, L. J. Bourhis, R. J. Gildea, J. A. K. Howard and H. Puschmann, *J. Appl. Crystallogr.*, 2009, 42, 339–341.
- S. K. Wolff, D. J. Grimwood, J. J. McKinnon, M. J. Turner, D. Jayatilaka and M. A. Spackman, *CrystalExplorer (Version 3.1)*, University of Western Australia, 2012.
- M. A. Spackman and J. J. McKinnon, *CrystEngComm*, 2002, 4, 378–392.
- J. J. McKinnon, M. A. Spackman and A. S. Mitchell, *Acta Crystallogr., Sect. B: Struct. Sci.*, 2004, 60, 627–668.
- J. J. McKinnon, D. Jayatilaka and M. A. Spackman, *Chem. Commun.*, 2007, 3814–3816.
- D. Jayatilaka, D. J. Grimwood, A. Lee, A. Lemay, A. J. Russell, C. Taylor, S. K. Wolff, P. Cassam-Chenai and A. Whetton, *TONTOL*, Available at: <http://Hirshfieldsurface.net/>, 2005.
- F. Allen, *Acta Crystallogr., Sect. B: Struct. Sci.*, 2002, 58, 380–388.
- R. D. C. Team, *R: A Language and Environment for Statistical Computing*, Vienna, Austria, 2008.
- Bruker, *SADABS*, Bruker AXS Inc, Wisconsin USA, Madison, 2001.
- F. H. Allen, D. G. Watson, L. Brammer, A. G. Orpen and R. Taylor, in *International Tables for Crystallography*, John Wiley & Sons, Ltd, 2006, DOI: 10.1107/97809553602060000621.
- T. A. Rodina, A. V. Ivanov, A. V. Gerasimenko, O. V. Loseva, O. N. Antzutkin and V. I. Sergienko, *Polyhedron*, 2012, 40, 53–64.
- M. Ito and H. Iwasaki, *Acta Crystallogr., Sect. B: Struct. Crystallogr. Cryst. Chem.*, 1979, 35, 2720–2721.
- M. Ito and H. Iwasaki, *Acta Crystallogr., Sect. B: Struct. Crystallogr. Cryst. Chem.*, 1980, 36, 443–444.
- P. C. Healy, J. W. Connor, B. W. Skelton and A. H. White, *Aust. J. Chem.*, 1990, 43, 1083–1095.
- S. Bhattacharya, N. Seth Miss, V. D. Gupta, H. Nöth and M. Thomann, *Z. Naturforsch., B: J. Chem. Sci.*, 1994, 49, 193.
- F. Jian, F. Bei, P. Zhao, X. Wang, H. Fun and K. Chinnakali, *J. Coord. Chem.*, 2002, 55, 429–437.
- H. Nöth and D. Schlosser, *Chem. Ber.*, 1988, 121, 1711–1713.
- F. Jian, Z. Wang, Z. Bai, X. You, H.-K. Fun, K. Chinnakali and I. A. Razak, *Polyhedron*, 1999, 18, 3401–3406.

- 45 I. A. Baburin and V. A. Blatov, *Acta Crystallogr., Sect. B: Struct. Sci.*, 2007, 63, 791–802.
- 46 X.-Z. Li, B. Walker and A. Michaelides, *Proc. Natl. Acad. Sci. U. S. A.*, 2011, 108, 6369–6373.
- 47 R. Kumar, J. R. Schmidt and J. L. Skinner, *J. Chem. Phys.*, 2007, 126, 204107.
- 48 I. D. Brown, *Acta Crystallogr., Sect. A: Cryst. Phys., Diffraction, Theor. Gen. Crystallogr.*, 1976, 32, 24–31.
- 49 E. Arunan, G. R. Desiraju, R. A. Klein, J. Sadlej, S. Scheiner, I. Alkorta, D. C. Clary, R. H. Crabtree, J. J. Dannenberg, P. Hobza, H. G. Kjaergaard, A. C. Legon, B. Mennucci and D. J. Nesbitt, *Pure Appl. Chem.*, 2011, 83, 1637–1641.
- 50 E. N. M. Yusof, M. M. Jotani, E. R. T. Tiekink and T. B. S. A. Ravoo, *Acta Crystallogr., Sect. E: Crystallogr. Commun.*, 2016, 72, 516–521.
- 51 C. Jelsch, K. Eijssmont and L. Huder, *IUCr*, 2014, 1, 119–128.



## Author Contributions and Copyright Information: Intramolecular H...S interactions in metal di-(isopropyl)dithiocarbamate complexes

- A. Angeloski performed the synthesis, isolation, all measurements (excluding single crystal X-ray diffraction, and solid state NMR spectroscopy), data analysis, and wrote the manuscript
- J.M. Hook performed solid state NMR spectroscopy
- M. Bhadbhade acquired single-crystal X-ray diffraction data
- A.T. Baker edited the manuscript
- A.M. McDonagh provided conceptual advice and revised the manuscript
- All authors have reviewed the manuscript, and all persons providing assistance have been acknowledged within the manuscript.

The article was reprinted (adapted) with permission from *CrystEngComm* – Published by the Royal Society of Chemistry.

### Intramolecular H...S interactions in metal di-(isopropyl)dithiocarbamate complexes

A. Angeloski, J. M. Hook, M. Bhadbhade, A. T. Baker and A. M. McDonagh,  
*CrystEngComm*, 2016, **18**, 7070  
DOI: 10.1039/C6CE01475E

This article is licensed under a [Creative Commons Attribution 3.0 Unported Licence](#). Material from this article can be used in other publications provided that the correct acknowledgement is given with the reproduced material.

Reproduced material should be attributed as follows:

- For reproduction of material from NJC:  
[Original citation] - Published by The Royal Society of Chemistry (RSC) on behalf of the Centre National de la Recherche Scientifique (CNRS) and the RSC.
- For reproduction of material from PCCP:  
[Original citation] - Published by the PCCP Owner Societies.
- For reproduction of material from PPS:  
[Original citation] - Published by The Royal Society of Chemistry (RSC) on behalf of the European Society for Photobiology, the European Photochemistry Association, and RSC.
- For reproduction of material from all other RSC journals:  
[Original citation] - Published by The Royal Society of Chemistry.

Information about reproducing material from RSC articles with different licences is available on our [Permission Requests page](#).

# **Chapter 6:**

An Unusual Mercury(II)  
Di(isopropyl)dithiocarbamate  
Coordination Polymer

## Chapter 6: An Unusual Mercury(II) Diisopropylthiocarbamate Coordination Polymer



Cite This: *Cryst. Growth Des.* 2019, 19, 1125–1133

Article

pubs.acs.org/crystal

### An Unusual Mercury(II) Diisopropylthiocarbamate Coordination Polymer

Alexander Angeloski,<sup>†</sup> Aditya Rawal,<sup>‡</sup> Mohan Bhadbhade,<sup>§</sup> James M. Hook,<sup>‡,§</sup> Robert W. Schurko,<sup>||</sup> and Andrew M. McDonagh<sup>\*,†</sup>

<sup>†</sup>School of Mathematical and Physical Sciences, University of Technology Sydney, Ultimo 2007, Australia

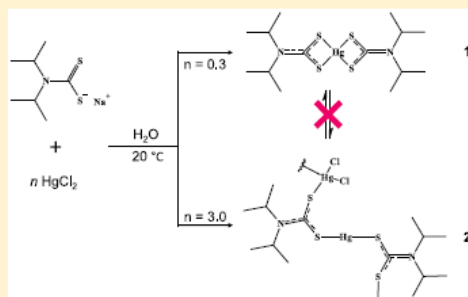
<sup>‡</sup>NMR Facility, Mark Wainwright Analytical Centre, The University of New South Wales, Sydney 2052, Australia

<sup>§</sup>School of Chemistry, The University of New South Wales, Sydney 2052, Australia

<sup>||</sup>Department of Chemistry and Biochemistry, University of Windsor, Windsor, Ontario, Canada N9B 3P4

#### Supporting Information

**ABSTRACT:** A new polymeric mercury(II) diisopropylthiocarbamate complex was synthesized by the reaction of sodium diisopropylthiocarbamate with excess  $\text{HgCl}_2$  in water. The precise structure of the new compound was determined by single-crystal X-ray diffraction. A similar reaction, using a stoichiometric excess of the ligand, yielded the known monomeric bis-(diisopropylthiocarbamato)mercury(II) complex. The complexes could not be distinguished from each other by their solution-phase NMR spectra or their FTIR spectra. Solid-state NMR spectroscopy ( $^{199}\text{Hg}$  and  $^{13}\text{C}$ ) provided unambiguous data and showed that the monomeric complex and polymeric complex do not interconvert in solution or during crystal growth. Thermogravimetric experiments revealed quite different thermal decomposition behavior between the two compounds.



#### 1. INTRODUCTION

Metal dithiocarbamate complexes are renowned for their ease of synthesis, useful properties, and coordination chemistry.<sup>1–16</sup> The flexibility to readily engineer and alter the dithiocarbamate ligand allows a range of coordination complexes to be generated. Thus, metal dithiocarbamate complexes have been extensively studied in the area of crystal growth and design and as single-source precursors for metal sulfide crystal synthesis.<sup>1,4,7,9,17–33</sup>

Of particular relevance to the current work, mercury(II) dithiocarbamate complexes produce a diverse range of molecular architectures and isomers; generating at least five distinct structural motifs in systems bearing two dithiocarbamate ligands.<sup>1</sup> The reaction of  $\text{HgCl}_2$  with diethyldithiocarbamate has been reported to produce three unique crystals (two polymorphs and an isomer) during crystal growth.<sup>34–37</sup> In this case, the isomer was identified as a polymeric dithiocarbamate complex consisting of bridging mercury chloride and dithiocarbamate moieties. Subsequently, the products of reactions of  $\text{HgCl}_2$  with diethyldithiocarbamate were found to be dependent on the ratio of ligand to metal.<sup>38</sup>

Reactions of  $\text{HgCl}_2$  with S-donor ligands have a propensity to form coordination polymers by interaction with sulfur-containing species,<sup>39–41</sup> although detailed studies of the formation of mercury coordination polymers are scarce, especially in the case of dithiocarbamates.<sup>36,42–47</sup> Furthermore,

the question of whether the mercury dithiocarbamate structures (i.e., monomer, dimer, or polymer) are formed during the initial reaction between metal and ligand or during crystal growth experiments remains unanswered. We therefore investigated the formation of mercury(II) diisopropylthiocarbamate complexes, which can exist in multiple structural forms.<sup>48–50</sup> We employed solid- and solution-state techniques to track the formation of monomeric, dimeric, and polymeric mercury(II) diisopropylthiocarbamate complexes from the initial reaction between metal and ligand to the isolation of individual crystals. Solid-state NMR ( $^{13}\text{C}$  and  $^{199}\text{Hg}$ ) spectroscopy and single-crystal X-ray diffraction were definitive in demonstrating the structural differences.

#### 2. RESULTS AND DISCUSSION

Reaction of sodium diisopropylthiocarbamate ( $\text{NaDIPDTC}$ ) with  $\text{HgCl}_2$  in a 3:1 molar ratio in water (Scheme 1) gave the known complex **1**<sup>48</sup> (as determined by solid-state  $^{199}\text{Hg}$  NMR spectroscopy, see below) in 82% yield. In contrast, reaction of  $\text{NaDIPDTC}$  with  $\text{HgCl}_2$  in a 1:3 molar ratio produced a new complex, **2**, in 75% yield. Reactions using a 2:1 molar ratio of  $\text{NaDIPDTC}$  to  $\text{HgCl}_2$  produced a mixture of **1** and **2**.

Received: October 29, 2018

Revised: December 18, 2018

Published: January 2, 2019

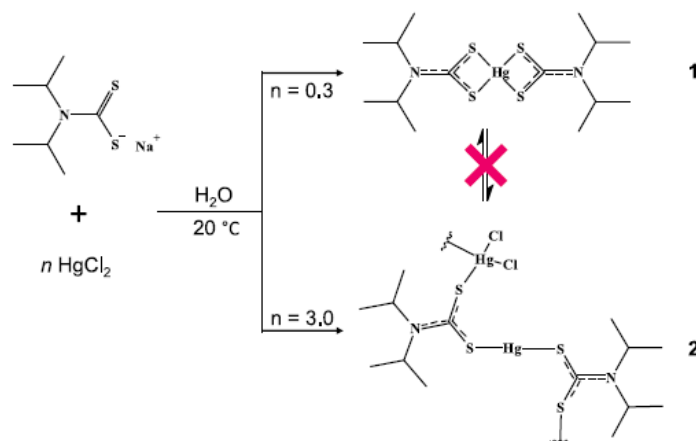


© 2019 American Chemical Society

1125

DOI: 10.1021/acs.cgd.8b01619  
*Cryst. Growth Des.* 2019, 19, 1125–1133

Scheme 1. Synthesis of 1 and 2



The molecular structure of **1** was redetermined<sup>48</sup> to obtain more precise data (significantly lower estimated standard deviations for bond lengths and angles) for comparison with solid-state NMR data (see below). The structure is shown in Figure 1. The coordination sphere of mercury is approximated

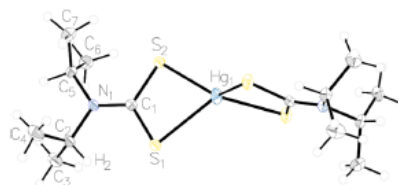


**Figure 1.** Structure of **1** showing the atom-labeling scheme and thermal displacement ellipsoids at 50% probability.

as distorted tetrahedral, with two short (2.4428(6) Å, Hg1–S2) and two long (2.6523(6) Å, Hg1–S1) mercury–sulfur bonds. The –C1S2Hg and –C1N1C2 moieties are planar. There is one intramolecular C–H⋯S hydrogen bond of ~2.4 Å between S1 and H2, creating an electronic asymmetry about the two isopropyl groups within each ligand, in agreement with previous reports.<sup>9–11</sup> All ligand bond lengths are similar to those in other DIPDTC complexes.<sup>9–11,48,51–55</sup>

The structure of polymeric **2** contains a bonding motif that is new for mercury dithiocarbamate complexes.<sup>1</sup> The asymmetric unit (Figure 2) contains two monodentate, bridging dithiocarbamate ligands, two inequivalent mercury environments, and a disordered diethyl ether molecule that occupies a special position on a crystallographic inversion center. One mercury atom (Hg1) is coordinated by two monodentate dithiocarbamate ligands with equivalent Hg–S bond lengths of 2.3686(14) Å to produce an approximately linear environment with a S1–Hg1–S4 angle of 171.65(5)°. The S–C–S bond angles are the same within each dithiocarbamate ligand. Both ligands are approximately planar with deviations of no greater than 0.06 Å from their S–C–S least planes and torsion angles of 174.7(5)° for S1–C1–N1–C9 and 178.6(4)° for S4–C8–N2–C12. The two –CS<sub>2</sub> moieties are rotated relative to each other about the S1–Hg1–S4 bond by 96.6(3)°. A second mercury atom (Hg2) is

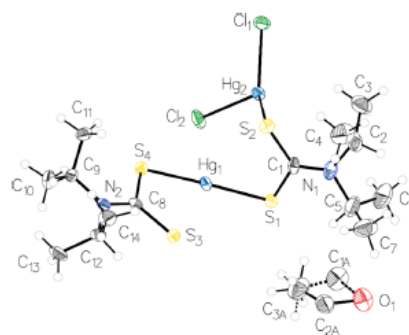


**Figure 2.** Structure of **2** (asymmetric unit) showing the atom-labeling scheme and thermal displacement ellipsoids at 50% probability.

coordinated to two chlorine atoms (Cl1 and Cl2), and the remaining sulfur atoms (S2 and S3) are coordinated in a monodentate fashion. The coordination geometry about Hg2 is approximately tetrahedral; however, all four bonds are inequivalent and range from 2.4526(14) Å (for Hg2–Cl1) to 2.5691(14) Å (for Hg2–S3). The Hg2–S bonds are similar in length to those found in **1**, but the Hg–Cl bonds are at least 0.2 Å longer than those found in HgCl<sub>2</sub>.<sup>39,56</sup>

The structure contains chains of **2** that align parallel to the *c* axis and arise from Hg2–S bonds between neighboring asymmetric units (Figure 3). The individual parallel ribbons of polymeric Hg(DIPDTC)<sub>2</sub> maintain contact with each other through intermolecular Hg–Cl⋯H–C and C–S⋯H–C interactions. There is an intramolecular C–S⋯H–C interaction between S4 and H10A of ~2.7 Å. The disordered ether molecule resides in solvent-accessible voids within the structure and has no interactions with distances <3 Å. Relevant crystal data for **1** and **2** can be found in Tables S1–S6 in the Supporting Information.

Crystal growth experiments using solutions containing a mixture of **1** and **2** (~1:1 ratio) yielded independent crystals of **1** and **2** (Figure 4), which could be physically separated on the basis of morphology. Interestingly, a previously described dimeric disappearing isomer of **1**<sup>50</sup> was obtained during crystallization experiments and characterized by X-ray



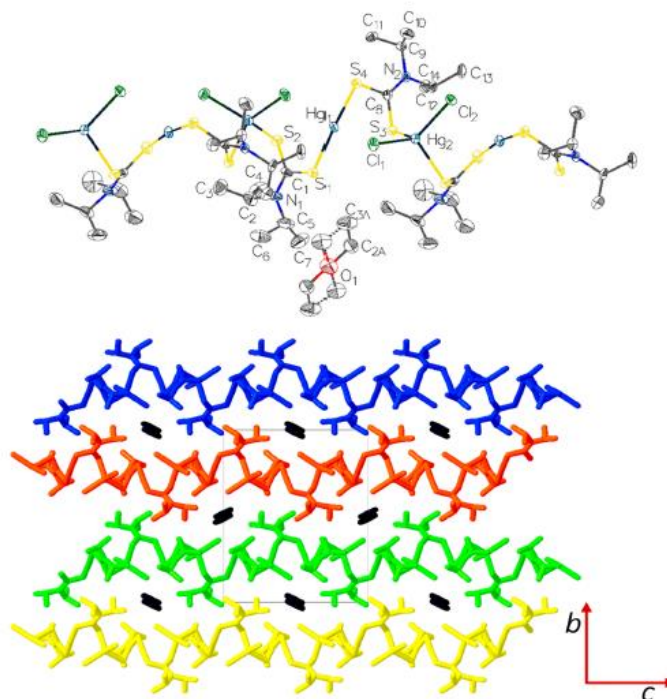


**Figure 3.** (top) Extended structure of 2 with thermal displacement ellipsoids at 50% probability. (bottom) Crystal packing showing 1-D chains of 2 along the *c* axis. Disordered ether molecules are shown in black, and hydrogen atoms are omitted for clarity.

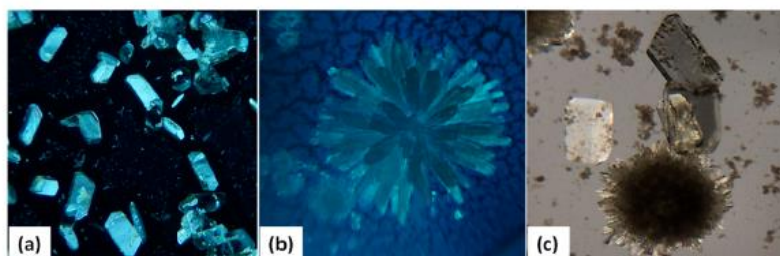


**Figure 4.** Photomicrographs showing the morphology of 1 (a) and 2 (b) and crystallization of 1 and 2 from a mixture of 1 and 2 (c).

diffraction (see the Supporting Information). Attempts to reproduce the material were unsuccessful after several months of trials.

Time-lapsed cross-polarized photomicroscopy (Video 1 in the Supporting Information) during ether counterdiffusion into a chloroform solution of 1 was used to probe the crystallization process. The onset of crystal growth occurs at  $T = 80$  min, with active expansion of the crystal facets occurring until  $T = 220$  min. Only a single morphology of crystals is produced, with no appearance of 2, indicating that there is no solution equilibrium between 1 and 2 during crystal growth. Further counterdiffusion of solvent occurs without any change in the morphology of crystallized 1, and total evaporation of the crystallization solvent did not produce any further crystalline products (albeit at a cost of crystal destruction) (Figure S1).

Solution-state  $^1\text{H}$  and  $^{13}\text{C}$  NMR spectra of 1 and 2 were indistinguishable. Spectra obtained using a mixture of 1 and 2 (determined using solid-state  $^{199}\text{Hg}$  NMR spectroscopy) contained a single set of signals that remained indistinguishable even at lower temperatures (238 K). In addition, DOSY-NMR at room temperature (Figure S2) revealed a single set of signals with a single diffusion constant. However, the variable-temperature solution-state NMR data (Figures S3–S5) revealed kinetic insights into the restricted rotation of the isopropyl groups (due to intramolecular C–H $\cdots$ S interactions and steric effects).<sup>9,11</sup> Examination of the variable-temperature experimental data yielded an energy barrier ( $\Delta G^\ddagger$ ) to free rotation at coalescence (268 K) of  $59 \text{ kJ mol}^{-1}$ , which is in excellent agreement with our previously reported data for NaDIPDTC ( $56 \text{ kJ mol}^{-1}$ )<sup>11</sup> and PbDIPDTC ( $57 \text{ kJ mol}^{-1}$ ),<sup>9</sup> indicating an equivalent transition state during isopropyl bond rotation (despite the fact that experiments were performed in



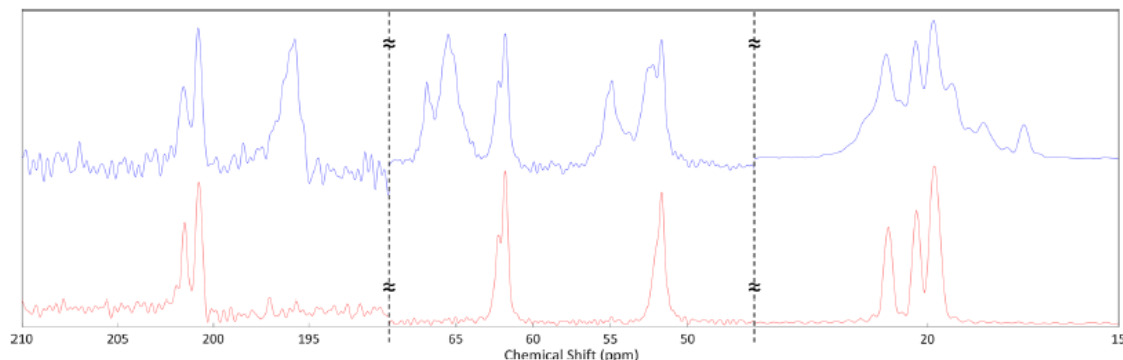


**Figure 5.** Solid-state  $^{13}\text{C}\{^1\text{H}\}$  CPTOSS NMR spectra for **1** (bottom) and **2** (top) acquired with a MAS rate of 3 kHz. Regions devoid of signals are omitted for clarity.

different solvents). The values for  $\Delta H^\ddagger$  ( $37 \text{ kJ mol}^{-1}$ ),  $\Delta S^\ddagger$  ( $-75 \text{ J mol}^{-1} \text{ K}^{-1}$ ), and the activation energy ( $40 \text{ kJ mol}^{-1}$ ) are somewhat similar to those for NaDIPDTC and PbDIPDTC, indicating comparable degrees of C–H $\cdots$ S and steric interactions. Detailed comparisons of these kinetic data were not obtained because of the limited solubility of **1** and **2** in acetonitrile.

In contrast to the solution-state spectra, the solid-state  $^{13}\text{C}$  CPMAS-TOSS NMR spectra for **1** and **2** are distinct (Figure 5). The spectra contain signals for each of the carbon atom environments with no impurities detected.

In the spectrum of **1**, a single set of peaks corresponding to each of the carbon atoms indicates equivalent DIPDTC moieties. As with other DIPDTC complexes,<sup>9,57</sup> the non-equivalence of the isopropyl environments (due to intra-molecular C–H $\cdots$ S hydrogen bonding)<sup>11</sup> gives rise to two separate methine carbon signals at  $\delta_{\text{C}}$  51.7 and 61.8 ppm. The dithiocarbamate carbon signal appears at  $\delta_{\text{C}}$  200.8 ppm and has a slightly higher chemical shift in comparison to the corresponding signal in the spectrum of Pb(DIPDTC)<sub>2</sub>,<sup>9</sup> likely arising from differential contributions from the Pb and Hg bonding orbitals. Three signals appearing between  $\delta_{\text{C}}$  19.8 to 21.0 ppm are assigned to nonequivalent methyl groups arising from the presence of intra- and intermolecular C–H $\cdots$ S interactions in the solid state, a phenomenon that has been previously observed.<sup>9,11</sup>

In the spectrum of **2**, C2, C5, C9, and C12 are all nonequivalent and give rise to four sets of peaks. Similarly, C1 and C8 (196 to 202 ppm) are also nonequivalent and show different  $J$  couplings to the  $^{14}\text{N}$  sites; however, an extra set of signals for each carbon atom is present, indicating that both ligands are not equivalent. In addition to the extra peaks, signals due to disordered diethyl ether within the matrix are present at  $\delta_{\text{C}}$  17.5 and 66.9 ppm.

In both cases, all peaks for carbon atoms bonded to nitrogen (C1, C8, C4, C5, C9, and C12) are partially split and broadened, which we attribute to residual dipolar coupling between  $^{14}\text{N}$  and  $^{13}\text{C}$ .<sup>58–60</sup> In **1**, the splitting is more pronounced and is likely attributed to a longer longitudinal relaxation time constant ( $T_1$ ) for  $^{14}\text{N}$  or the higher visual crystallinity of **1** in comparison to **2**. These observations in the solid-state  $^{13}\text{C}$  NMR acquired using individually isolated (on the basis of morphology) single crystals of **1** and **2** are supported by comparison to the crystallographic data.

$^{199}\text{Hg}$  solid-state NMR experiments were performed using nonspinning crystalline **1** and **2**. The spectra are shown in Figure 6. The chemical shift tensor parameters obtained by analytical simulation of the spikelet patterns for **1** and **2** are shown in Table 1.

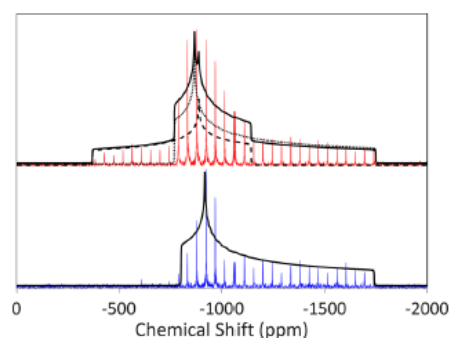


**Figure 6.** Solid-state  $^1\text{H}\text{--}^{199}\text{Hg}\{^1\text{H}\}$  BRAIN-CP static NMR spectra of crystalline **1** (bottom) and **2** (top). The solid traces show the analytical simulations of the  $^{199}\text{Hg}$  spectra for **1** and **2**. Simulations for the two Hg environments in **2** are represented by a dotted line (site A) and a dashed line (site B).

For **1**, the simulation revealed a single Hg site with an isotopic shift  $\delta_{\text{Hg}}$  of  $-1155 \text{ ppm}$ , in agreement with the crystal structure, where the coordination of Hg is approximated as a highly distorted tetrahedron. The principal components of the chemical shift tensor ( $\delta_{11}$ ,  $\delta_{22}$ , and  $\delta_{33}$ ) deviate from ideal tetrahedral geometry ( $\delta_{11} = \delta_{22} = \delta_{33}$ ),<sup>61</sup> and the value of the skew ( $\kappa$ ) indicates a distorted-tetrahedral geometry at the Hg site, consistent with  $^{199}\text{Hg}$  chemical shift tensors measured for distorted-tetrahedral Hg environments with multiple Hg–S bonds.<sup>46,62</sup> In addition, the positive value of  $\kappa$  near unity and the local symmetry dictates that the distinct principal component (which also represents the direction of highest shielding),  $\delta_{33}$ , is oriented along or near the 2-fold rotational axis away from the directions of the Hg–S bonds (Figure S6); accordingly, the  $\delta_{11}$  and  $\delta_{22}$  components are likely directed into similar environments approximately perpendicular to the 2-fold rotational axis.

In the case of **2**, the  $^{199}\text{Hg}$  NMR clearly shows the presence of two patterns corresponding to two distinct sites: Hg1 (site

Table 1.  $^{199}\text{Hg}$  NMR Parameters (ppm) for 1 and 2

	$\delta_{11}$	$\delta_{22}$	$\delta_{33}$	$\delta_{\text{iso}}^a$	$\Omega^b$	$\kappa^c$
1	−802.5(26)	−920(27)	−1742.5(33)	−1155(20)	940(40)	0.75(0.05)
2 <sup>d</sup>	−770.7(43)	−868.7(45)	−1750.7(48)	−1130(40)	980(40)	0.80(0.05)
	−370.1(48)	−889.8(48)	−1140(46)	−800(40)	770(40)	−0.35(0.1)

<sup>a</sup> $\delta_{\text{iso}} = (\delta_{11} + \delta_{22} + \delta_{33})/3$ . <sup>b</sup> $\Omega = |\delta_{33} - \delta_{11}|$ . <sup>c</sup> $\kappa = 3(\delta_{22} - \delta_{\text{iso}})/\Omega$ . <sup>d</sup>Multiple signals due to site nonequivalence. The experimental uncertainty in the last digit(s) for each value is indicated in parentheses.

A) and Hg2 (site B). One pattern has  $^{199}\text{Hg}$  chemical shift tensor parameters that are equal (within experimental error) to those of the Hg site in 1, with a high, positive value for  $\kappa$  near unity (Table 1). This pattern is assigned to site A, which has a  $\text{HgS}_2$  environment, with two sets of longer range, secondary Hg–S and Hg–Cl interactions. As in the case of 1, the direction of the  $\delta_{33}$  component is very likely along the pseudo 2-fold rotational axis, which points in a direction away from the Hg–S bonds and between the positions of two nearby chloride ions (Figure S6). The second pattern has a different  $\delta_{\text{iso}}$  value and a dissimilar set of chemical shift tensor parameters; the negative skew indicates that  $\delta_{11}$  is the distinct parameter. This pattern is assigned to site B, which features a unique four-coordinate  $\text{HgS}_2\text{Cl}_2$  environment; unfortunately, since each of the Hg–S and Hg–Cl bond lengths are distinct, and there are no local symmetry elements, there is no straightforward way to assign the chemical shift tensor orientation on the basis of symmetry (ab initio computations of chemical shift tensors would be useful in this case but are beyond the scope of the current work).

These assignments on the basis of local symmetry are consistent with the similarity in the mercury sites of 1 and 2, evidenced in the single-crystal X-ray structures (Figures 1 and 3). Having established the patterns of 1 and 2 using isolated microcrystalline samples, solid-state  $^{199}\text{Hg}$  NMR experiments confirmed that 1 and 2 did not interconvert during crystal growth (Video 1) of isolated 1 (on the basis of  $^{199}\text{Hg}$  SSNMR).

The solid-state  $^{199}\text{Hg}$  NMR spectra of 1 and 2 prior to crystal growth experiments show significant differences between the powders (Figure 7), indicating different numbers and types of mercury environments, which were formed on the basis of ligand to metal reaction stoichiometry. Previous studies using a small excess of ligand (2.1:1 ligand to metal ratio) produced a monomer and dimer without any 2 being detected.<sup>50</sup> Differences in relative spikelet intensities before and after crystallization are attributed to changes in the physical sample morphology (though it is noted that these spectra cannot be used for quantitative interpretation without careful calibration of known standards). In the case of 2, the spectra before and after are noticeably different, which we attribute to differences in the molecular conformation and different physical sample morphology instigated by the incorporation of ether, which occurs during the crystal growth (indicated by disordered ether molecules within the crystal structure of 2).

The FTIR spectra of 1 and 2 are shown in Figure S8 and are similar to each other. The spectra show the typical thioureide band at  $1495\text{ cm}^{-1}$ , which is at an energy intermediate between that of a C–N single bond ( $1250\text{--}1350\text{ cm}^{-1}$ ) and a C=N double bond ( $1640\text{--}1690\text{ cm}^{-1}$ ). The  $\nu(\text{C}=\text{S})$  band appears at  $922\text{ cm}^{-1}$ . These bands are within  $\sim 15\text{ cm}^{-1}$  of the corresponding bands for  $\text{Pb}(\text{DIPDTC})_2$ ,<sup>9</sup>  $\text{NaDIPDTC}$ ,<sup>9</sup> and  $\text{Ni}(\text{DIPDTC})_2$ .<sup>10</sup>

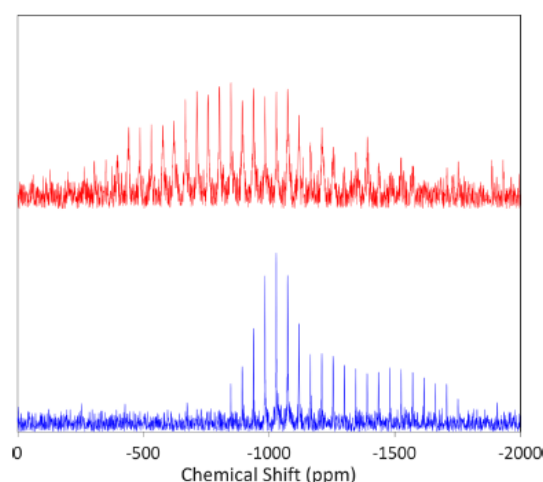


Figure 7. Solid-state  $^1\text{H}$ – $^{199}\text{Hg}$  BRAIN-CP NMR spectra of powdered 1 (bottom) and 2 (top) prior to crystal growth.

Thermogravimetric analysis data are shown in Figure 8 and reveal distinct pathways for thermal decomposition. Analysis of

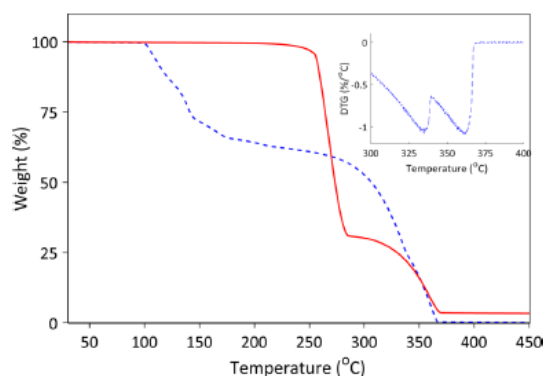


Figure 8. Thermogravimetric data for 1 (red solid line) and 2 (blue dashed line). The inset shows the first derivative of mass loss between 300 and 400 °C.

1 reveals no significant mass loss in the region of  $30\text{--}100\text{ }^\circ\text{C}$ , indicating a lack of water (bound or otherwise), in agreement with the crystallographic data. Thermal decomposition occurs in two endothermic events. The first event occurs between  $230$  and  $285\text{ }^\circ\text{C}$  with a  $\text{DTG}_{\text{max}}$  value of  $268\text{ }^\circ\text{C}$  and a mass loss of 69%, which we assign to the formation of  $\text{HgS}$  (calculated mass loss 58%). The second event occurs between  $285$  and  $370\text{ }^\circ\text{C}$  with a  $\text{DTG}_{\text{max}}$  value of  $360\text{ }^\circ\text{C}$  and a mass loss of 28%



corresponding to the thermolysis of HgS into mercury vapor and sulfur (calculated mass loss 42%). The significant discrepancies between observed and calculated mass losses are due to the overlap of complex decomposition and the onset of HgS decomposition.<sup>50,63</sup>

Thermogravimetric analysis of **2** shows no significant mass loss below 100 °C, again indicating a lack of water (bound or otherwise). Thermal decomposition occurs in six well-defined endothermic events, with the first four occurring between 96 and 218 °C with an associated mass loss of 38.3%, in excellent agreement with the calculated loss of all ligands to produce HgS and HgCl<sub>2</sub> (38.2%). There are two overlapping mass loss events between 240 and 340 °C attributed to the thermal decomposition of HgS into mercury vapor and sulfur<sup>63</sup> and the sublimation of HgCl<sub>2</sub> at ~280 °C.<sup>64</sup>

The marked difference in thermal behavior between **1** and **2** is attributed to the different coordination environments about each mercury atom. In **1**, Hg is chelated by the DIPDTC ligands, forming HgS<sub>4</sub> moieties, whereas in **2** there is a mixture of HgS<sub>2</sub> and HgS<sub>2</sub>Cl<sub>2</sub> centers. Moreover, these results show that neither **1** nor **2** is a suitable single-source precursor for the synthesis of HgS nanocrystals, as the decomposition of **1** occurs simultaneously with that of HgS and, in the case of **2**, HgS is obtained as a mixture with HgCl<sub>2</sub>. Comparison of these data with thermal data for other mercury(II) dithiocarbamate complexes<sup>19,32</sup> suggests that further investigation of **1** under conditions that utilize a chemical passivating agent (e.g., hexadecylamine) is warranted.

### 3. CONCLUSIONS

The product obtained from the reaction of sodium diisopropylidithiocarbamate with HgCl<sub>2</sub> in water is dependent upon the reaction stoichiometry. The known monomeric Hg(DIPDTC)<sub>2</sub> complex was formed when the ligand was present in excess, as distinct from when the metal was in excess, and a new polymeric mercury(II) dithiocarbamate was discovered. Surprisingly, the solution-phase NMR spectra and FTIR spectra provided no basis upon which the two complexes could be distinguished from each other. Solid-state NMR spectroscopy (<sup>199</sup>Hg and <sup>13</sup>C) and single-crystal diffraction provided data that enabled the two complexes to be differentiated. These data were vital to establish that the monomeric (**1**) and polymeric (**2**) complexes do not interconvert in solution or during crystal growth.

Thermogravimetric experiments revealed different thermal decomposition behavior between the two compounds, with neither deemed to be suitable as a single-source precursor for HgS formation.

### 4. EXPERIMENTAL SECTION

**4.1. General Considerations.** *Caution!* Mercury compounds are toxic, and appropriate precautions should be taken.

Deionized water was used in synthetic procedures. All chemicals and solvents used in synthetic procedures were analytical grade and were purchased from Sigma-Aldrich and used as received. Sodium diisopropylidithiocarbamate pentahydrate was prepared as previously described.<sup>10</sup> Product yields were calculated with respect to the limiting reagent, which was HgCl<sub>2</sub> in the case of **1** and sodium diisopropylidithiocarbamate in the case of **2**. FTIR spectra were acquired using a Nicolet 6700 FTIR spectrometer with a diamond iTX ATR accessory. A Thermal Advantage SDT-Q600 thermal analyzer was used to simultaneously obtain thermogravimetric (TG) and differential scanning calorimetry (DSC) data using 90 μL alumina crucibles. Experiments were conducted under an atmosphere of

nitrogen gas (150 mL min<sup>-1</sup>) and a heating rate of 10 °C min<sup>-1</sup> over a temperature range of 30–450 °C. High-resolution mass spectrometry was performed using an Agilent 6510 Q-TOF instrument with a mobile phase of 70% acetonitrile and 30% water (with 0.01% formic acid) and a flow rate of 0.5 mL min<sup>-1</sup>. Variable-temperature NMR spectroscopy using a mixture of **1** and **2** in chloroform-*d* was performed using a Bruker Avance III NMR spectrometer fitted with a BBFO Plus solution-state probe and a BCU-Xtreme cooler. The frequency was 600.1 MHz for <sup>1</sup>H and 150.9 MHz for <sup>13</sup>C. The sample temperature was calibrated using a Type K thermocouple in an NMR tube containing ethanol that was inserted into the probe. Instrument broadening was accounted for using the full width at half-maximum (fwhm) of chloroform-*d* residual proton resonances. With these data, experimental rate constants were calculated at each temperature using the fwhm of the methyl peak at 1.63 ppm. Arrhenius and Eyring activation parameters were obtained using generalized least-squares linear regressions of log *k* versus 1/*T* and log(*k*/*T*) versus 1/*T*, respectively. Solid-state <sup>199</sup>Hg and <sup>13</sup>C NMR spectra were acquired using a Bruker Avance III solid-state NMR spectrometer with a 7 T superconducting magnet operating at frequencies of 53.62, 75.37, and 299.75 MHz for the <sup>199</sup>Hg, <sup>13</sup>C, and <sup>1</sup>H nuclei, respectively. The crystalline samples were acquired by manual separation of crystals produced from crystal growth experiments. Candidate crystals of **1** and **2** were separated on the basis of their morphology and periodically checked using unit cell analysis by single-crystal X-ray diffraction. Specimens were loaded into 4 mm zirconia rotors fitted with Kel-F caps and packed with Teflon tape. The solid-state <sup>13</sup>C NMR spectra were acquired with the CP-TOSS pulse program at a spinning speed of 3 kHz MAS, and cross-polarization contact time of 1 ms, and SPINAL-64 <sup>1</sup>H decoupling with a 80 kHz decoupling field strength during acquisition. The <sup>199</sup>Hg NMR spectra were acquired under static conditions, using the BRAIN-CP<sup>65</sup> method, with a 25 ms broad-band adiabatic pulse for polarization transfer, coupled with the WURST-CPMG<sup>66</sup> pulse sequence during detection for signal enhancement. The envelope of the resulting “spikelet” pattern yields the anisotropic line shape of the <sup>199</sup>Hg NMR spectrum and was modeled by Sola using Bruker’s Topspin software. The experimental uncertainties in the principal components of the chemical shift tensor were estimated using WSOLIDS software,<sup>67</sup> using bidirectional variation of each parameter and visual comparison of the experimental and simulated spectra; uncertainties in δ<sub>iso</sub>, Ω, and κ were then calculated using standard propagation of error methods.

**4.2. Single-Crystal X-ray Diffraction.** Suitable single crystals were selected using a Leica M165Z polarizing microscope and mounted on a MiTiGen MicroMount. X-ray diffraction measurements were made using a Bruker Kappa-II CCD diffractometer at 150 K using a IμS Incoatec Microfocus Source and Mo Kα radiation (λ = 1.710723 Å). The structures were solved using charge flipping, and the full-matrix least-squares refinement was performed using ShelXL<sup>68</sup> in Olex2.<sup>69</sup> Heavy atoms were refined isotropically until *R* factor convergence, and then an anisotropic model was applied. Where possible, hydrogen atoms were located using a difference Fourier plot or restrained to neutron diffraction distances when required. Bond angles were kept to two decimal places and bond lengths to three.

**4.3. Optical Photomicroscopy.** Optical photomicroscopy was performed using a Zeiss Stemi-305 stereomicroscope operating in a cross-polarized light configuration. Photomicrographs were acquired using a Q-Imaging MicroPublisher 3.3RTV CCD camera. Time lapse of crystal growth was performed using an in situ chamber made in house with photomicrographs acquired in 10 min intervals.

**4.4. Synthesis.** **4.4.1. Synthesis of Bis(κ<sup>2</sup>S,S′-diisopropylidithiocarbamato)mercury(II) (**1**).** An aqueous solution of sodium diisopropylidithiocarbamate (1.012 g, 3.50 mmol, in 100 mL of water) was added dropwise to an aqueous solution of mercury(II) chloride (0.312 g, 1.15 mmol, in 100 mL of water). A white precipitate formed upon addition, and the suspension was stirred for 2 min. The crude product was collected by vacuum filtration, and the filter cake was repeatedly triturated with water to produce a white paste which was dried in vacuo at 45 °C to yield 0.522 g of **1** (82%). Crystals suitable for X-ray analysis were obtained

as pale yellow tabular plates by solvent counterdiffusion of ether into a solution of **1** in chloroform.  $^1\text{H}$  NMR (600.1 MHz,  $\text{CDCl}_3$ , 238 K):  $\delta$  5.15 (sept,  $^3J_{\text{HH}} = 6.6$  Hz,  $^1J_{\text{CH}} = 140$  Hz, 2H, C2H, C2H'), 3.88 (sept,  $^3J_{\text{HH}} = 6.8$  Hz,  $^1J_{\text{CH}} = 136$  Hz, 2H, C5H, C5H'), 1.63 (d,  $^3J_{\text{HH}} = 6.8$  Hz,  $^1J_{\text{CH}} = 128$  Hz, 12H, C6H3, C6H3', C7H3, C7H3'), 1.27 (d,  $^3J_{\text{HH}} = 6.6$  Hz,  $^1J_{\text{CH}} = 128$  Hz, 12H, C3H3, C3H3', C4H3, C4H3').  $^{13}\text{C}$  NMR (150.9 MHz,  $\text{CDCl}_3$ , 238 K):  $\delta$  202.0 (C1, C1'), 62.3 (C2, C2'), 51.4 (C5, C5'), 19.8 (C6, C7, C6', C7'), 19.5 (C3, C4, C3', C4').  $^{15}\text{N}$  NMR (60.8 MHz,  $\text{CDCl}_3$ , 238 K):  $\delta$  190.3 (N1, N1').  $^{13}\text{C}\{^1\text{H}\}$  NMR (3.0 kHz, 293 K):  $\delta$  202–200 (C1, C1'), 63–61 (C2, C2'), 53–51 (C5, C5'), 22–19 (C3, C3', C4, C4', C6, C6', C7, C7').  $^{199}\text{Hg}\{^1\text{H}\}$  NMR (static, 293 K):  $\delta$  –1170 (Hg1). HRMS:  $(\text{M} + \text{H})^+$  for  $\text{HgN}_2\text{S}_4\text{C}_{14}\text{H}_{28}$  calculated 555.0908, observed 555.0888, difference 3.6 ppm.

**4.4.2. Synthesis of Bis( $\kappa^2\text{S},\text{S}'$ -diisopropylthiocarbamate)-mercury(II)- $\text{HgCl}_2$  (**2**).** An aqueous solution of sodium diisopropylthiocarbamate (0.110 g, 0.38 mmol, in 100 mL of water) was added with stirring to a solution of mercury(II) chloride (0.313 g, 1.15 mmol, in 100 mL of water). A pale yellow precipitate formed, and the mixture was stirred vigorously for 2 min. The crude product was collected by vacuum filtration, and the filter cake was repeatedly washed with water and then dried at 45 °C in vacuo to produce 0.236 g of **2** (75%) as a pale yellow powder. Crystals suitable for X-ray analysis were acquired as radial prismatic clusters by solvent counterdiffusion of ether into a solution of **2** in chloroform.  $^{13}\text{C}\{^1\text{H}\}$  NMR (3.0 kHz, 293 K):  $\delta$  202–196 (C1, C8), 68–60 (C5, C12), 56–51 (C2, C9), 23–17 (C3, C4, C6, C7, C10, C11, C13, C14).  $^{199}\text{Hg}\{^1\text{H}\}$  NMR (static, 293 K):  $\delta$  –1129 (Hg1), –799 (Hg2).

## ■ ASSOCIATED CONTENT

### Supporting Information

The Supporting Information is available free of charge on the ACS Publications website at DOI: 10.1021/acs.cgd.8b01619.

Relevant crystallographic and NMR data (PDF)

Video showing counterdiffusion (AVI)

### Accession Codes

CCDC 1858161, 1858163, and 1858175 contain the supplementary crystallographic data for this paper. These data can be obtained free of charge via [www.ccdc.cam.ac.uk/data\\_request/cif](http://www.ccdc.cam.ac.uk/data_request/cif), or by emailing [data\\_request@ccdc.cam.ac.uk](mailto:data_request@ccdc.cam.ac.uk), or by contacting The Cambridge Crystallographic Data Centre, 12 Union Road, Cambridge CB2 1EZ, UK; fax: +44 1223 336033.

## ■ AUTHOR INFORMATION

### Corresponding Author

\*E-mail for A.M.M.: [andrew.mcdonagh@uts.edu.au](mailto:andrew.mcdonagh@uts.edu.au).

### ORCID

Aditya Rawal: 0000-0002-5396-1265

Andrew M. McDonagh: 0000-0002-9502-1175

### Notes

The authors declare no competing financial interest.

## ■ ACKNOWLEDGMENTS

We gratefully acknowledge Dr. Ronald Shimmon for laboratory assistance. We express our gratitude to the Mark Wainwright Analytical Center, UNSW, for access to single crystal XRD, and NMR spectrometers supported by ARC funding LE0989541, for NMR equipment. This research was supported by an Australian Government Research Training Program Scholarship and the Natural Sciences and Engineering Research Council (NSERC, Canada).

## ■ REFERENCES

- (1) Howie, R. A.; Tiekink, E. R. T.; Wardell, J. L.; Wardell, S. M. S. V. Complementary Supramolecular Aggregation via O–H...O Hydrogen-bonding and Hg...S Interactions in Bis[N,N'-di(2-hydroxyethyl)-dithiocarbamate-S,S']mercury(II):  $\text{Hg}[\text{S}_2\text{CN}(\text{CH}_2\text{CH}_2\text{OH})_2]_2$ . *J. Chem. Crystallogr.* **2009**, *39*, 293–298.
- (2) Hogarth, G. Metal-dithiocarbamate complexes: chemistry and biological activity. *Mini-Rev. Med. Chem.* **2012**, *12*, 1202–15.
- (3) Andrew, F. P.; Ajibade, P. A. Metal complexes of alkyl-aryl dithiocarbamates: Structural studies, anticancer potentials and applications as precursors for semiconductor nanocrystals. *J. Mol. Struct.* **2018**, *1155*, 843–855.
- (4) Cookson, J.; Beer, P. D. Exploiting the dithiocarbamate ligand in metal-directed self-assembly. *Dalton Trans.* **2007**, 1459–72.
- (5) Hogarth, G., Transition Metal Dithiocarbamates: 1978–2003. In *Progress in Inorganic Chemistry*; Karlin, K. D., Ed.; Wiley: 2005; Vol. 53.
- (6) Tiekink, E. R. Influence of crystal structure on molecular structure: Syntactic structural chemistry. *Rigaku J.* **2002**, *19*, 14–24.
- (7) Liu, Y.; Tiekink, E. R. Supramolecular associations in binary antimony (III) dithiocarbamates: Influence of ligand steric bulk, influence on coordination geometry, and competition with hydrogen bonding. *CrystEngComm* **2005**, *7*, 20–27.
- (8) Tiekink, E. R. Molecular architecture and supramolecular association in the zinc-triad 1, 1-dithiolates. Steric control as a design element in crystal engineering? *CrystEngComm* **2003**, *5*, 101–113.
- (9) Angeloski, A.; Gentle, A. R.; Scott, J. A.; Cortie, M. B.; Hook, J. M.; Westerhausen, M. T.; Bhadbhade, M.; Baker, A. T.; McDonagh, A. M. From Lead(II) Dithiocarbamate Precursors to a Fast Response PbS Positive Temperature Coefficient Thermistor. *Inorg. Chem.* **2018**, *57*, 2132–2140.
- (10) Angeloski, A.; Baker, A. T.; Bhadbhade, M.; McDonagh, A. M. Bis( $\kappa^2\text{S},\text{S}'$ -di(isopropyl)dithiocarbamate)nickel(II): Anagostic C–H...Ni interactions and physical properties. *J. Mol. Struct.* **2016**, *1113*, 127–132.
- (11) Angeloski, A.; Hook, J. M.; Bhadbhade, M.; Baker, A. T.; McDonagh, A. M. Intramolecular H...S interactions in metal di-(isopropyl)dithiocarbamate complexes. *CrystEngComm* **2016**, *18*, 7070–7077.
- (12) Golding, R. M.; Healy, P. C.; Newman, P. W. G.; Sinn, E.; White, A. H. Temperature dependence of the proton nuclear magnetic resonance spectra of some diamagnetic N,N-dialkylthiocarbamate complexes of transition metals. *Inorg. Chem.* **1972**, *11*, 2435–2440.
- (13) Lindmark, A. F.; Fay, R. C. Kinetics of hindered Rotation about Carbon-Nitrogen Single Bonds in Some N,N-diisopropylthiocarbamates. *Inorg. Chem.* **1983**, *22*, 2000–2006.
- (14) Takeda, Y.-I.; Watanabe, N.; Tanaka, T. Barrier to internal rotation around isopropyl–nitrogen bond of some N,N-diisopropylthio- and -diselenocarbamate complexes of tin (IV),  $\text{X}_2\text{Sn}[\text{Y}_2\text{CN}(\text{Pr}-i)_2]_2$  (X = Cl, Me; Y = S, Se). *Spectrochim. Acta, Part A* **1976**, *32*, 1553–1556.
- (15) Bhattacharya, S.; Kanungo, B. K.; Sahoo, S. Synthesis, characterization and dynamic stereochemistry of thermochromic tris(dithiocarbamate)vanadium(III) complexes. *J. Coord. Chem.* **2006**, *59*, 371–378.
- (16) Bhat, A. N.; Fay, R. C.; Lewis, D. F.; Lindmark, A. F.; Strauss, S. H. Preparation and characterization of some six-, seven-, and eight-coordinate titanium(IV) N, N-dialkylthiocarbamates. *Inorg. Chem.* **1974**, *13*, 886–892.
- (17) Benson, R. E.; Ellis, C. A.; Lewis, C. E.; Tiekink, E. R. T. 3D-, 2D- and 1D-supramolecular structures of  $\{\text{Zn}[\text{S}_2\text{CN}(\text{CH}_2\text{CH}_2\text{OH})-\text{R}]_2\}_2$  and their  $\{\text{Zn}[\text{S}_2\text{CN}(\text{CH}_2\text{CH}_2\text{OH})\text{R}]_2\}_2(4,4'$ -bipyridine) adducts for R =  $\text{CH}_2\text{CH}_2\text{OH}$ , Me or Et: polymorphism and pseudo-polymorphism. *CrystEngComm* **2007**, *9*, 930–940.
- (18) Roffey, A.; Hollingsworth, N.; Islam, H. U.; Mercy, M.; Sankar, G.; Catlow, C. R.; Hogarth, G.; de Leeuw, N. H. Phase control during the synthesis of nickel sulfide nanoparticles from dithiocarbamate precursors. *Nanoscale* **2016**, *8*, 11067–11075.



- (19) Ajibade, P. A.; Mbese, J. Z.; Omondi, B. Group 12 dithiocarbamate complexes: Synthesis, characterization, and X-ray crystal structures of Zn(II) and Hg(II) complexes and their use as precursors for metal sulfide nanoparticles. *Inorg. Nano-Met. Chem.* **2017**, *47*, 202–212.
- (20) Arul Prakasam, B.; Lahtinen, M.; Peuronen, A.; Muruganandham, M.; Kolehmainen, E.; Haapaniemi, E.; Sillanpää, M. Spectral and structural studies on Ni(II) dithiocarbamates: Nickel sulfide nanoparticles from a dithiocarbamate precursor. *Inorg. Chim. Acta* **2015**, *425*, 239–246.
- (21) Gomathi, G.; Dar, S. H.; Thirumaran, S.; Ciattini, S.; Selvanayagam, S. Bis(N-benzyl-N-furfuryldithiocarbamate-S,S')-mercury(II) as a precursor for the preparation of mercury sulfide nanoparticles. *C. R. Chim.* **2015**, *18*, 499–510.
- (22) Chintso, T.; Ajibade, P. A. Synthesis and structural studies of hexadecylamine capped lead sulfide nanoparticles from dithiocarbamate complexes single source precursors. *Mater. Lett.* **2015**, *141*, 1–6.
- (23) Sathiyaraj, E.; Gurumoorthy, G.; Thirumaran, S. Nickel(II) dithiocarbamate complexes containing the pyrrole moiety for sensing anions and synthesis of nickel sulfide and nickel oxide nanoparticles. *New J. Chem.* **2015**, *39*, 5336–5349.
- (24) Hollingsworth, N.; Roffey, A.; Islam, H.-U.; Mercy, M.; Roldan, A.; Bras, W.; Wolthers, M.; Catlow, C. R. A.; Sankar, G.; Hogarth, G.; de Leeuw, N. H. Active Nature of Primary Amines during Thermal Decomposition of Nickel Dithiocarbamates to Nickel Sulfide Nanoparticles. *Chem. Mater.* **2014**, *26*, 6281–6292.
- (25) Nemati, F.; Ghorbani Gharjeh Ghiaei, A.; Notash, B.; Shayegan, M. H.; Amani, V. A rapid and convenient synthesis of gem-bis(dithiocarbamate) derivatives from primary aliphatic amines, carbon disulfide, and aromatic aldehydes using boron trifluoride-diethyl etherate. *Tetrahedron Lett.* **2014**, *55*, 3572–3575.
- (26) Ehsan, M. A.; Peiris, T. A.; Wijayantha, K. G.; Olmstead, M. M.; Arifin, Z.; Mazhar, M.; Lo, K. M.; McKee, V. Development of molecular precursors for deposition of indium sulphide thin film electrodes for photoelectrochemical applications. *Dalton Trans* **2013**, *42*, 10919–28.
- (27) Sivagurunathan, G. S.; Ramalingam, K.; Rizzoli, C. Nanohallium(III) sulfide from dithiocarbamate precursors: Synthesis, single crystal X-ray structures and characterization. *Polyhedron* **2013**, *65*, 316–321.
- (28) Ramasamy, K.; Kuznetsov, V. L.; Gopal, K.; Malik, M. A.; Raftery, J.; Edwards, P. P.; O'Brien, P. Organotin Dithiocarbamates: Single-Source Precursors for Tin Sulfide Thin Films by Aerosol-Assisted Chemical Vapor Deposition (AACVD). *Chem. Mater.* **2013**, *25*, 266–276.
- (29) Li, P.; Li, H.; Jie, W. Preparation of lanthanum sulfide nanoparticles by thermal decomposition of lanthanum complex. *J. Rare Earths* **2011**, *29*, 317–320.
- (30) Jen-La Plante, I.; Zeid, T. W.; Yang, P.; Mokari, T. Synthesis of metal sulfide nanomaterials via thermal decomposition of single-source precursors. *J. Mater. Chem.* **2010**, *20*, 6612.
- (31) An, G.; Chenguang, L.; Hou, Y.; Zhang, X.; Liu, Y. Transition metal dichalcogenide materials: Solid-state reaction synthesis of nanocrystalline nickel disulfide. *Mater. Lett.* **2008**, *62*, 2643–2646.
- (32) Gurumoorthy, G.; Thirumaran, S.; Ciattini, S. Unusual octahedral Hg(II) dithiocarbamate: Synthesis, spectral and structural studies on Hg(II) complexes with pyrrole based dithiocarbamates and their utility for the preparation of  $\alpha$ - and  $\beta$ -HgS. *Polyhedron* **2016**, *118*, 143–153.
- (33) Cookson, J.; Beer, P. D. Exploiting the dithiocarbamate ligand in metal-directed self-assembly. *Dalton Trans.* **2007**, 1459–1472.
- (34) Book, L.; Chieh, C. The structure of catena-[di- $\mu$ ]-chlorotetrakis[[ $\mu$ ]-{N,N-diethyldithiocarbamate-S,S'}]trimercury(II)}, [Hg<sub>3</sub>(C<sub>5</sub>H<sub>10</sub>NS<sub>2</sub>)<sub>4</sub>Cl<sub>2</sub>]. *Acta Crystallogr., Sect. B: Struct. Crystallogr. Cryst. Chem.* **1980**, *36*, 300–303.
- (35) Iwasaki, H. Crystal structure of dichloro-tetrakis-(diethyldithiocarbamate)trimercury, Hg<sub>3</sub>Cl<sub>2</sub>(S<sub>2</sub>CNEt<sub>2</sub>)<sub>4</sub>. *Chem. Lett.* **1972**, *1*, 1105–1106.
- (36) Bond, A. M.; Colton, R.; Hollenkamp, A. F.; Hoskins, B. F.; McGregor, K.; Tiekink, E. R. T. An unexpected stoichiometric effect in both solution and solid state in mercury-rich dithiocarbamate cation chemistry: crystal and molecular structure of polymeric tris(piperidinecarbodithioato)dimercury(II) perchlorate. *Inorg. Chem.* **1991**, *30*, 192–197.
- (37) Healy, P. C.; White, A. H. Crystal structure of bis(NN-diethyldithiocarbamate)mercury(II). *J. Chem. Soc., Dalton Trans.* **1973**, 284–287.
- (38) Kobayashi, N.; Fujisawa, T. The Reactions of Sodium Diethyldithiocarbamate and Tetraethylthiuram Disulfide with Mercury(II) Chloride. *Bull. Chem. Soc. Jpn.* **1976**, *49*, 2780–2783.
- (39) House, D. A.; Robinson, W. T.; McKee, V. Chloromercury(II) anions. *Coord. Chem. Rev.* **1994**, *135–136*, 533–586.
- (40) Okuniewski, A.; Rosiak, D.; Chojnacki, J.; Becker, B. Coordination polymers and molecular structures among complexes of mercury(II) halides with selected 1-benzoylthioureas. *Polyhedron* **2015**, *90*, 47–57.
- (41) Englert, U. Halide-bridged polymers of divalent metals with donor ligands – structures and properties. *Coord. Chem. Rev.* **2010**, *254*, 537–554.
- (42) Guzmán-Percástegui, E.; Zakharov, L. N.; Alvarado-Rodríguez, J. G.; Carnes, M. E.; Johnson, D. W. Synthesis of a Self-Assembled Hg(II)-Dithiocarbamate Metallomacrocyclic. *Cryst. Growth Des.* **2014**, *14*, 2087–2091.
- (43) Morsali, A.; Masoomi, M. Y. Structures and properties of mercury(II) coordination polymers. *Coord. Chem. Rev.* **2009**, *253*, 1882–1905.
- (44) Levason, W.; McAuliffe, C. *The Chemistry of Mercury*, 1st ed.; Palgrave Macmillan UK: 1977.
- (45) Sahebzaamani, H.; Ghammamy, S.; Mehrani, K.; Salimi, F. Synthesis, characterization and thermal analysis of Hg (II) complexes with hydrazide ligands. *Der Chemica Sinica* **2010**, *1*, 67.
- (46) Sañ, D. A.; Holmberg, R. J.; Burgess, K. M. N.; Robeyns, K.; Bryce, D. L.; Munugesu, M. Hybrid Material Constructed from Hg(NCS)<sub>2</sub> and 2,4,6-Tris(2-pyrimidyl)-1,3,5-triazine (TPyMT): Coordination of TPyMT in a 2,2'-Bipyridine-Like Mode. *Eur. J. Inorg. Chem.* **2015**, *2015*, 441–446.
- (47) Khavasi, H. R.; Mohammad Sadegh, B. M. Temperature-Dependent Supramolecular Motif in Coordination Compounds. *Inorg. Chem.* **2010**, *49*, 5356–5358.
- (48) Ito, M.; Iwasaki, H. The Structure of the Monomeric Form of Mercury(II) N,N-Diisopropylthiocarbamate [Bis(N,N-diisopropylthiocarbamate)mercury(II)]. *Acta Crystallogr., Sect. B: Struct. Crystallogr. Cryst. Chem.* **1979**, *35*, 2720–2721.
- (49) Iwasaki, H.; Ito, M.; Kobayashi, K. Coexistence of monomeric and dimeric complex molecules in a crystal: The crystal structure of the  $\beta$ -form of mercury(II) N,N-diisopropylthiocarbamate. *Chem. Lett.* **1978**, *7*, 1399–1402.
- (50) Loseva, O. V.; Rodina, T. A.; Smolentsev, A. I.; Ivanov, A. V. A new polymorphic modification and chemisorption activity of mercury(II) N,N-di-isopropylthiocarbamate: Synthesis and characterisation of the heteronuclear double complex of ([Au{S<sub>2</sub>CN(iso-C<sub>3</sub>H<sub>7</sub>)<sub>2</sub>}]<sub>2</sub>[Hg<sub>2</sub>Cl<sub>6</sub>]-OC(CH<sub>3</sub>)<sub>2</sub>)<sub>n</sub>. *Polyhedron* **2017**, *134*, 238–245.
- (51) Healy, P. C.; Connor, J. W.; Skelton, B. W.; White, A. H. Alkyl Substituent Effects in Diamagnetic Dithiocarbamate Cobalt and Nickel Complexes. *Aust. J. Chem.* **1990**, *43*, 1083–1095.
- (52) Ma, J.; F, B.; Li, J.; Yang, X.; Lu, L.; Wang, X. Solid Phase Synthesis at Room Temperature, Characterization and Crystal Structure of bis(diiso-propylcarbomodithioato-S,S') Molybdenum. *J. Nanjing University of Science and Technology* **2004**, *28*, 648–652.
- (53) Newman, P. W. G.; White, A. H. Crystal Structure of Bis(NN-diisopropylthiocarbamate)nickel(II). *J. Chem. Soc., Dalton Trans.* **1972**, 2239–2243.
- (54) Iwasaki, H.; Kobayashi, K. Structure of bis(N,N-diisopropylthiocarbamate)copper(II). *Acta Crystallogr., Sect. B: Struct. Crystallogr. Cryst. Chem.* **1980**, *36*, 1655–1657.





- (55) Xu, L.-Z.; Zhao, P.-S.; Zhang, S.-S. Crystal Structure and Characterization of Pd(II) Bis(diiso-propyldithiocarbamate) Complex. *Chin. J. Chem.* **2001**, *19*, 436–440.
- (56) *Tables of interatomic distances and configuration in molecules and ions*; The Chemical Society: London, 1958.
- (57) Ivanov, A. V.; Korneeva, E. V.; Bukvetskii, B. V.; Goryan, A. S.; Antzutkin, O. N.; Forsling, W. Structural organization of mercury(II) and copper(II) dithiocarbamates from EPR and  $^{13}\text{C}$  and  $^{15}\text{N}$  MAS NMR spectra and X-ray diffraction analysis. *Russ. J. Coord. Chem.* **2008**, *34*, 59–69.
- (58) Harris, R. K.; Jonsen, P.; Packer, K. J. Residual ( $^{13}\text{C}$ ,  $^{14}\text{N}$ ) dipolar coupling in  $^{13}\text{C}$  NMR of solid nitrogen-containing aromatic compounds. *Magn. Reson. Chem.* **1985**, *23*, 565–577.
- (59) Wi, S.; Frydman, L. Residual dipolar couplings between quadrupolar nuclei in high resolution solid state NMR: Description and observations in the high-field limit. *J. Chem. Phys.* **2000**, *112*, 3248–3261.
- (60) Olivieri, A. C.; Frydman, L.; Grasselli, M.; Diaz, L. E. Microcomputer simulation of solid-state  $^{13}\text{C}$  NMR line shapes affected by quadrupolar nuclei. *Magn. Reson. Chem.* **1988**, *26*, 615.
- (61) Bowmaker, G. A.; Churakov, A. V.; Harris, R. K.; Howard, J. A. K.; Apperley, D. C. Solid-State  $^{199}\text{Hg}$  MAS NMR Studies of Mercury(II) Thiocyanate Complexes and Related Compounds. Crystal Structure of  $\text{Hg}(\text{SeCN})_2$ . *Inorg. Chem.* **1998**, *37*, 1734–1743.
- (62) Natan, M. J.; Millikan, C. F.; Wright, J. G.; O'Halloran, T. V. Solid-state mercury-199 nuclear magnetic resonance as a probe of coordination number and geometry in Hg(II) complexes. *J. Am. Chem. Soc.* **1990**, *112*, 3255–3257.
- (63) Leckey, J. H.; Nulf, L. E. *Thermal decomposition of mercuric sulfide*; Report Y/DZ-1124; Oak Ridge Y-12 Plant, Oak Ridge, TN (United States): 1994.
- (64) Loseva, O. V.; Rodina, T. A.; Smolentsev, A. I.; Ivanov, A. V. Syntheses, supramolecular structures, and thermal behavior of heteronuclear gold(III)–mercury(II) dithiocarbamatechloride complexes  $[\text{Au}\{\text{S}_2\text{CN}(\text{CH}_3)_2\}_2]_2[\text{HgCl}_4]$  and  $[\text{Au}\{\text{S}_2\text{CN}(\text{C}_2\text{H}_5)_2\}_2]_2[\text{Hg}_2\text{Cl}_6] \cdot \text{OC}(\text{CH}_3)_2\text{n}$  by  $^{13}\text{C}$  MAS NMR, X-ray diffraction, and simultaneous thermal analysis data. *Russ. J. Coord. Chem.* **2016**, *42*, 719–729.
- (65) Harris, K. J.; Lupulescu, A.; Lucier, B. E. G.; Frydman, L.; Schurko, R. W. Broadband adiabatic inversion pulses for cross polarization in wideband solid-state NMR spectroscopy. *J. Magn. Reson.* **2012**, *224*, 38–47.
- (66) MacGregor, A. W.; O'Dell, L. A.; Schurko, R. W. New methods for the acquisition of ultra-wideband solid-state NMR spectra of spin-1/2 nuclides. *J. Magn. Reson.* **2011**, *208*, 103–113.
- (67) Eichele, K. *WSolids1*, 1.21.3; Universität Tübingen, 2015.
- (68) Sheldrick, G. M. A Short History of SHELX. *Acta Crystallogr., Sect. A: Found. Crystallogr.* **2008**, *64*, 112–122.
- (69) Dolomanov, O. V.; Bourhis, L. J.; Gildea, R. J.; Howard, J. A. K.; Puschmann, H. OLEX2: a complete structure solution, refinement and analysis program. *J. Appl. Crystallogr.* **2009**, *42*, 339–341.


## Author Contributions and Copyright Information: An Unusual Mercury(II) Diisopropylthiocarbamate Coordination Polymer

- A. Angeloski performed synthesis, isolation, all measurements (excluding solid state NMR spectroscopy and single crystal X-ray diffraction), data analysis, and wrote the manuscript
- A. Rawal and J.M.Hook acquired solid state NMR spectra
- M. Bhadbhade acquired single-crystal X-ray diffraction data
- A.M. McDonagh provided conceptual advice and revised the manuscript
- R. W. Schurko provided assistance in interpretation of solid state  $^{199}\text{Hg}$  NMR
- All authors have reviewed the manuscript, and all persons providing assistance have been acknowledged within the manuscript.

The article was reprinted (adapted) with permission from *CrystGrowthDes.* Copyright (2019) American Chemical Society.



[Home](#) [Create Account](#) [Help](#)



**Title:** An Unusual Mercury(II) Diisopropylthiocarbamate Coordination Polymer  
**Author:** Alexander Angeloski, Aditya Rawal, Mohan Bhadbhade, et al  
**Publication:** Crystal Growth and Design  
**Publisher:** American Chemical Society  
**Date:** Jan 1, 2019  
Copyright © 2019, American Chemical Society

**LOGIN**  
If you're a copyright.com user, you can login to RightsLink using your copyright.com credentials. Already a RightsLink user or want to [learn more?](#)

**PERMISSION/LICENSE IS GRANTED FOR YOUR ORDER AT NO CHARGE**

This type of permission/license, instead of the standard Terms & Conditions, is sent to you because no fee is being charged for your order. Please note the following:

- Permission is granted for your request in both print and electronic formats, and translations.
- If figures and/or tables were requested, they may be adapted or used in part.
- Please print this page for your records and send a copy of it to your publisher/graduate school.
- Appropriate credit for the requested material should be given as follows: "Reprinted (adapted) with permission from (COMPLETE REFERENCE CITATION). Copyright (YEAR) American Chemical Society." Insert appropriate information in place of the capitalized words.
- One-time permission is granted only for the use specified in your request. No additional uses are granted (such as derivative works or other editions). For any other uses, please submit a new request.

# **Chapter 7:**

## Discussion

## Chapter 7: Discussion

DTC anions have proven to be excellent ligands in the realm of coordination chemistry. The resultant metal DTC complexes have stimulated a great deal of interest due to their ease of synthesis, the ability to coordinate to a range of transition and main block elements, and their interesting and useful properties.<sup>21-23</sup> Clearly there is great scope for the synthesis of many new structures due to the ability to manipulate both the central metal and DTC ligand. In this work, the synthesis, properties and applications of a range of metal DTC complexes (where the metal = Hg, Pb, Ni, Na) have been investigated. During the course of the research the metal DTC structures were carefully selected with the intention of investigating the complexes as single source precursors to metal sulfide materials. Thus, complexes containing Pb, Hg and Ni were synthesised to investigate their capability to produce industrially and academically relevant PbS, HgS and NiS.

The di(isopropyl)dithiocarbamate ligand was chosen for many of the target complexes on the basis of ease of synthesis and favourable properties such as solubility in a range of organic solvents. There also exist a number of studies investigating metal di(isopropyl)dithiocarbamate complexes within the literature which provide useful comparisons with the current work.<sup>170-177</sup>

Characterisation of bis( $\kappa^2$ S,S'-di(isopropyl)dithiocarbamato) nickel(II) using XRD analysis of single-crystals revealed a previously undescribed polymorph (Chapter 2, page 10). Importantly, the single-crystal X-ray structure revealed the presence of a seldom discussed class of intermolecular interactions known as anagostic interactions.<sup>178, 179</sup> Anagostic (and agostic) interactions belong to a class of C-H...M interactions (where M is often a  $d^6$  or  $d^8$  metal) and are characterised by short H...M distances ( $\sim 1.8$  to  $2.2$  Å) with C-H...M angles of  $90$ - $130^\circ$  (for agostic), or long H...M ( $\sim 2.3$  to  $3.0$  Å) with C-H...M angles of  $110$ - $170^\circ$  for anagostic interactions.<sup>180, 181</sup> Whilst these interactions are known for nickel(II) complexes, including another nickel(II) DTC, the current work is unique in that it revealed the influence of the Ni...H interaction on the vibrational frequencies of methyl groups involved in the interaction. The complex was subsequently used to generate nickel(II) sulfide by solid-state decomposition of the complex, which provided the basis for further investigation into the mechanisms involved during thermal decomposition of metal DTC complexes. Importantly, this work provided the initial indication that metal DTC complexes utilising di(isopropyl)dithiocarbamate ligands are suitable as SSPs to metal sulfide materials.

SSPs provide all of the necessary atoms to generate the resultant materials within a single compound.<sup>182</sup> In the case of metal sulfides, these precursors generally contain a metal-sulfur bond. The presence of the required atoms within the same molecule is important because it



allows for the intimate control of reactant stoichiometry and the potential to tune the precursors thermal properties through ligand design, and thus control the resultant metal sulfide phase and morphology. There has been considerable interest in the development of single source precursors, such as DTCs<sup>25-27, 88, 126-133, 135</sup> and xanthates<sup>89, 106, 114, 119, 122-124, 183</sup> for the synthesis of metal sulfides such as Ni<sub>x</sub>S<sub>y</sub> and PbS.

An understanding of the mechanism for thermal decomposition of an SSP is quite important as this will guide the SSP design to achieve suitable properties such as low decomposition temperatures and/or selective metal sulfide generation. Mechanistic studies on the role of solution-state decomposition of nickel(II) DTC complexes are extant,<sup>129, 131, 134</sup> however studies focussing on the processes involved in the solid state decomposition of nickel(II) DTC complexes were absent from the literature. The current work (Chapter 3, page 18) addressed this gap in knowledge. The sophisticated capabilities of the Australian Synchrotron were especially useful together with specialised instruments available within UTS (commercial and self-assembled). A plethora of *in-situ* techniques provided detailed data throughout the solid-state thermal decomposition of single-crystals of bis( $\kappa^2$ S,S'-di(isopropyl)dithiocarbamato)-nickel(II). Variable temperature powder X-ray diffraction experiments performed at the Australian Synchrotron (Proposal M12485) provided powder diffraction patterns at 30 second intervals during the decomposition process. These data showed that decomposition occurred with no intermediate phases and produced phase-pure nickel(II) sulfide. These insights could not have been obtained using regular laboratory X-ray equipment, which are incapable of providing the necessary time-resolved data for such studies due to low source intensity (and thus integration times longer than the time-scale of decomposition processes).

Having established that decomposition occurred in a single event, attention was given to the volatile species produced during decomposition, which were examined using thermogravimetric analysis coupled to gas chromatography mass spectrometry (TGA-GC-MS). The precursor complex was heated at a known rate whilst measuring the change in mass. A significant difference between the current work and thermogravimetry experiments typically reported in the literature is the use of a furnace directly coupled to a gas chromatography mass spectrometer, allowing for the real-time detection and identification of volatile species emitted during mass loss. This technique is extremely powerful and was the first study to examine the decomposition of metal DTC complexes. The major volatile by-products were fragments associated with the cleavage of the di-isopropyl N-C and dithiocarbamato C=N bonds. Time-resolved evolved gas analysis showed that the species co-existed in the gas phase with no temporal dispersion of the fragments (i.e. the dithiocarbamato backbone decomposed

in a single step), in accordance with the synchrotron data. Synchrotron and TGA-GC-MS experiments indicated that decomposition occurred in a single step, but there was no direct observation of decomposition proceeding directly from the solid state or *via* an intermediate solution state. It could be inferred by inspection of the synchrotron data that no such solution state existed (i.e. precursor diffraction peaks remained until observation of product peaks) however a great deal of care must be applied as retention of diffraction peaks does unambiguously exclude the existence of a non diffracting state. To address this, a home-built variable-temperature optical microscope was constructed to obtain direct visual observation of the decomposition process. The experiment showed that decomposition occurred in the solid state, as no melting of the SSP was observed.

Thus, a combination of three *in situ* experimental techniques produced the first detailed observation and description of solid-state decomposition of a DTC SSP in the literature. Not only are these findings novel, they also have widespread applications in the study of SSP decomposition because the complex can be utilised as a readily accessible SSP that generates only volatile by-products with no intermediate liquid phase, to synthesize a single phase of nickel sulfide without the need for solvents.

Lead(II) dithiocarbamate complexes were found to be useful SSPs to PbS materials. Two lead(II) DTC complexes were synthesised and their thermal decomposition properties were compared (Chapter 4, page 26). One complex utilised the di(isopropyl)dithiocarbamate ligand and the other had oxygen-containing ligands. N-methyl-D-glucamine was chosen as the precursor amine for the synthesis of the 'oxygenated' lead(II) dithiocarbamate complex, as the ligand (sodium N-methyl-D-glucamine dithiocarbamate) was known, thus providing a convenient synthetic route.<sup>12</sup>

Oxygen can affect thermolysis regimes; thermal decomposition of lead(II) DTC complexes in a partial atmosphere of oxygen is detrimental to the formation of metal sulfides but the effect of oxygen within the SPP was unknown prior to the work presented in this dissertation.

Variable temperature powder X-ray diffraction at the Australian Synchrotron, and variable temperature optical microscopy were utilised to examine the key differences in the thermal behaviours of the two complexes. The complex containing intramolecular oxygen decomposed in the solid state, whilst the complex lacking intramolecular oxygen decomposed from an intermediate non-diffracting state. The loss of X-ray diffraction peaks, in isolation, is insufficient evidence to conclude whether decomposition occurs within the solution state or *via* an amorphous material. Variable-temperature optical microscopy showed that the alkyl precursor melted, followed by decomposition some time later from the solution. Investigations

of the resultant metal sulfide materials revealed differences in the morphology of the resultant materials, as alluded to in similar studies.<sup>123, 184, 185</sup> Electron microscope data showed significant differences in the resultant lead sulfide materials. Decomposition from the solid state gave smaller PbS crystals than those obtained by decomposition from the molten state. The resultant PbS (from the oxygen containing precursor) was utilised without need for any further purification or treatment, to manufacture a positive-temperature coefficient thermal resistor. The device had thermal-response properties superior to current industry standard materials. Thus, this study has widespread implications in areas that utilize PbS as the active material for sensing applications, as it shows the ease of which high purity PbS can be easily produced in a single step, with no processing required for use in electronic devices.

This work also showed that metal DTC complexes are useful materials for investigation of solid-state phenomena. Whilst characterising sodium di(isopropyl)dithiocarbamate, unusually broad proton nuclear magnetic resonance (NMR) signals were noticed, prompting investigations to determine the reasons for this broadening (Chapter 5, page 37). At the time of the work, a disruption of the symmetry of some di(isopropyl)dithiocarbamate complexes was reported in the literature. The nature of this disruption was described as arising from the orientation of the methine hydrogens in different directions relative to the  $C_2NCS_2$  plane, determined using variable temperature NMR spectroscopy.<sup>186-190</sup> However, the origin of this reduction in symmetry was not presented. In the work presented in this dissertation, a study of restricted rotation within di(isopropyl)dithiocarbamate compounds began with a redetermined single-crystal X-ray structure of sodium di(isopropyl)dithiocarbamate, variable temperature NMR spectroscopy, and examination of the Cambridge structural database.

Single-crystal X-ray data revealed an intramolecular C-H $\cdots$ S hydrogen bond, which is significant in its own right as the influence of H $\cdots$ S hydrogen bonds on molecular structure is scarce.<sup>147-150</sup> Variable temperature NMR experiments were used to probe the broad NMR signals and to determine kinetic parameters for the restricted rotation. An energy barrier for the restricted rotation of 30 kJ mol<sup>-1</sup> was obtained. Two sets of signals for each hydrogen environment indicated an inequivalence of the two isopropyl groups in the solution state. However, the role of C-H $\cdots$ S hydrogen bonding could not be elucidated as the experiment was performed in the solution state, making comparisons to the single-crystal structure not straightforward. This shortcoming was addressed using solid-state <sup>1</sup>H NMR spectroscopy, which was in agreement with the solution state spectroscopy, and showed inequivalent isopropyl groups. As the isopropyl groups are inequivalent in both the solution and solid state, this work provided direct experimental evidence that the restricted rotation within sodium

di(isopropyl)dithiocarbamate is attributable to an intramolecular C-H...S hydrogen bond. The study was the first to provide the origin of peak broadening, and restricted rotation, in di(isopropyl)dithiocarbamate complexes.

Further insights towards the structural chemistry of DTC's were provided by the detailed study of mercury(II) di(isopropyl)dithiocarbamate complexes (Chapter 6, page 47). Whilst obtaining crystals suitable for single-crystal X-ray analysis, three morphologically distinct single-crystals were obtained, which yielded three unique structures (two of which were previously reported).<sup>171, 191</sup> It became evident that further investigation into the cause of this phenomenon was warranted. Examination of the literature revealed that whilst uncommon, mercury(II) DTC complexes can produce a diverse range of molecular architectures and isomers.<sup>37</sup> Further, it is known that reaction of HgCl<sub>2</sub> with sodium diethyldithiocarbamate produces three unique crystals during crystal growth of the product.<sup>159, 160, 192, 193</sup> Despite this, no studies focussing on the cause of isomerisation within mercury(II) DTC structures were extant.

Careful examination of the processes before, during, and after crystal growth using solid state <sup>199</sup>Hg NMR spectroscopy was critical to providing an understanding of these processes. During the initial stages of investigation, concerns were raised due to the inability to reproduce crystal growth experiments, which were addressed by resynthesis of the complex. Crystals obtained from the new material were isolated as a single form, and reproducible across many batches.

The metal to ligand ratio in the initial reaction was found to affect the reaction outcome. Standard <sup>199</sup>Hg NMR spectra (of the individual isomers) obtained from isolated single-crystals was used to track the formation of mercury complexes. Material obtained from reactions deficient in mercury showed different proportions of the isomers when compared to products obtained from reactions with an excess of mercury. This provided evidence that the initial reaction between ligand and metal ions determined the form of the resultant mercury(II) DTC complexes, and is dependent on the relative stoichiometry of the starting materials.



## Chapter 8: Conclusions and Future Directions

### Conclusions

The studies within this dissertation focussed on the synthesis, properties and applications for a range of metal DTC complexes. The research aims as stated in Chapter 1 have been addressed, and in doing so, some areas for future study have become apparent. In addition to the individual conclusions shown within Chapters 2-6, some more general insights are presented. Through investigation of the spectroscopic properties of the complexes synthesised, all of the di-(isopropyl)dithiocarbamate complexes contain intramolecular C-H $\cdots$ S interactions. Investigation of the thermal decomposition behaviours of these DTC complexes revealed that all (with the exception of the mercury(II) complexes) were suitable as SSPs for the synthesis of metal sulfide materials. The relative ease of decomposition to metal sulfides show that DTCs can be used in settings requiring high purity metal sulfide materials for fabrication of electronic devices (as shown in Chapter 4). The ability to reach these conclusions was greatly enhanced through the use of sophisticated *in-situ* techniques.

### Future Directions

The studies in this dissertation clearly show the conversion of metal DTC complexes to their respective metal sulfides. A natural progression of this, and thus an area for future study, would be to investigate the possibility of forming mixed metal sulfide species, which have interesting semiconductor properties with possible applications in new sensor technologies. For example, an intimate mixture of two metal DTC complexes may be thermalised to yield bimetallic sulfide species. Keeping with this theme, another avenue for future study might investigate the synthesis of mixed metal DTCs for use as SSPs. An example of a mixed metal DTC SSP could be a bis DTC with a 1:1 ratio of metals X and Y, or even co-crystals of more than one metal complex. Studies such as these are scarce in the literature, and would be somewhat difficult to achieve due to the complexity involved with understanding the relationship between formation of the resultant metal sulfide material from the precursor structure.

An alternative area of future study concerns the manipulation of the DTC structure for molecular sensor applications. For example, it is known that di-(isopropyl)dithiocarbamate complexes exhibit a temperature-dependent restricted rotation about the N-C bond within the ligand; it may be possible to tune the structure in such a way that a macroscopic observation of this rotation (e.g. a change in absorbance) is possible.

For the spectroscopically inclined, there is opportunity and potential for detailed investigations on the relationship between molecular structure and spectroscopic properties.

Such studies might focus on the relationship between crystallographic orientation and UV-VIS-NIR absorbance, synthesis of DTCs with fluorophores for fluorescence applications, or if a significant challenge is required, the synthesis of chiral DTC's for access to the properties of non-centrosymmetric crystals. All of these would require an investment in the development and/or modification of R groups within the DTC ligand structures.

## Appendices:

### A1: Supporting information associated with Chapter 3

#### Conversion Of Single Crystals of a Nickel(II) Dithiocarbamate Complex to Nickel Sulfide Crystals

Alexander Angeloski,<sup>a</sup> Michael B. Cortie,<sup>a</sup> John A. Scott,<sup>a</sup> Dayanne M. Bordin,<sup>a</sup> and Andrew M. McDonagh<sup>a\*</sup>

<sup>a</sup> School of Mathematical and Physical Sciences, University of Technology Sydney, Ultimo 2007, Australia

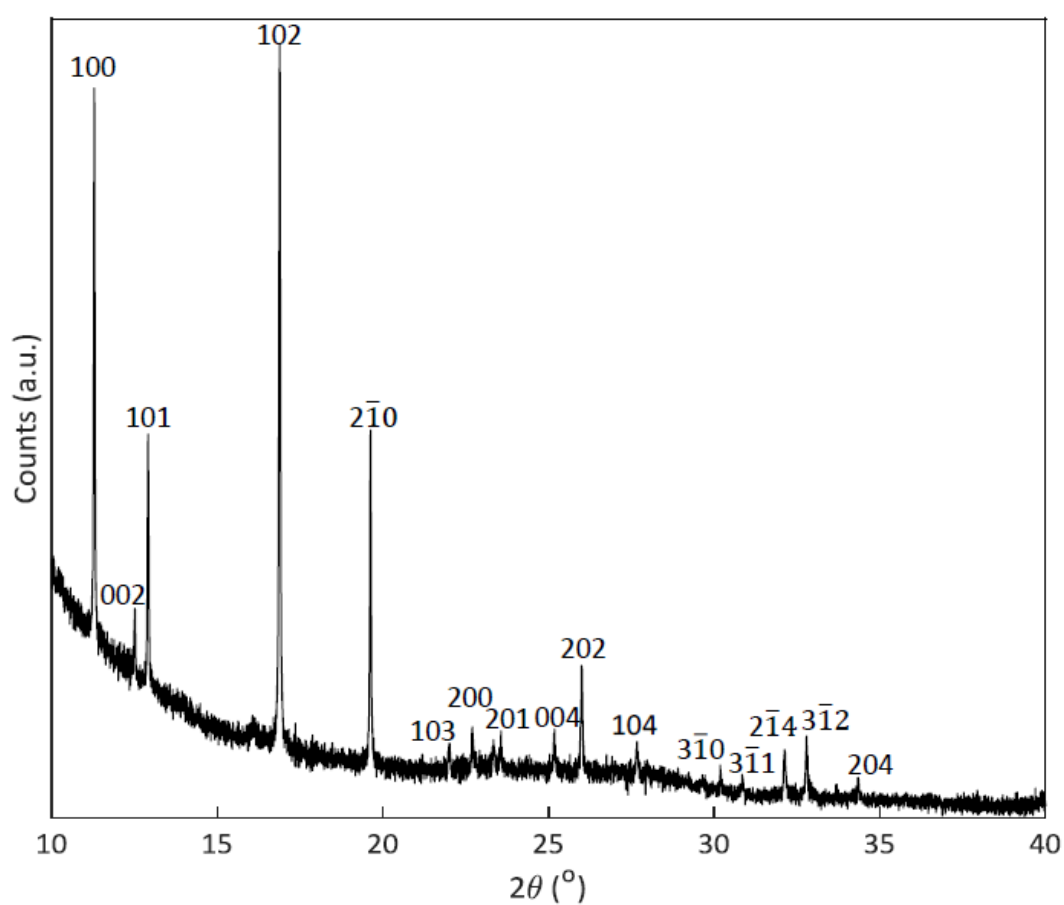


Figure S1: pXRD pattern of  $\alpha$ -NiS obtained by heating  $\text{Ni}(\text{DIPDTC})_2$  to 460  $^{\circ}\text{C}$ .

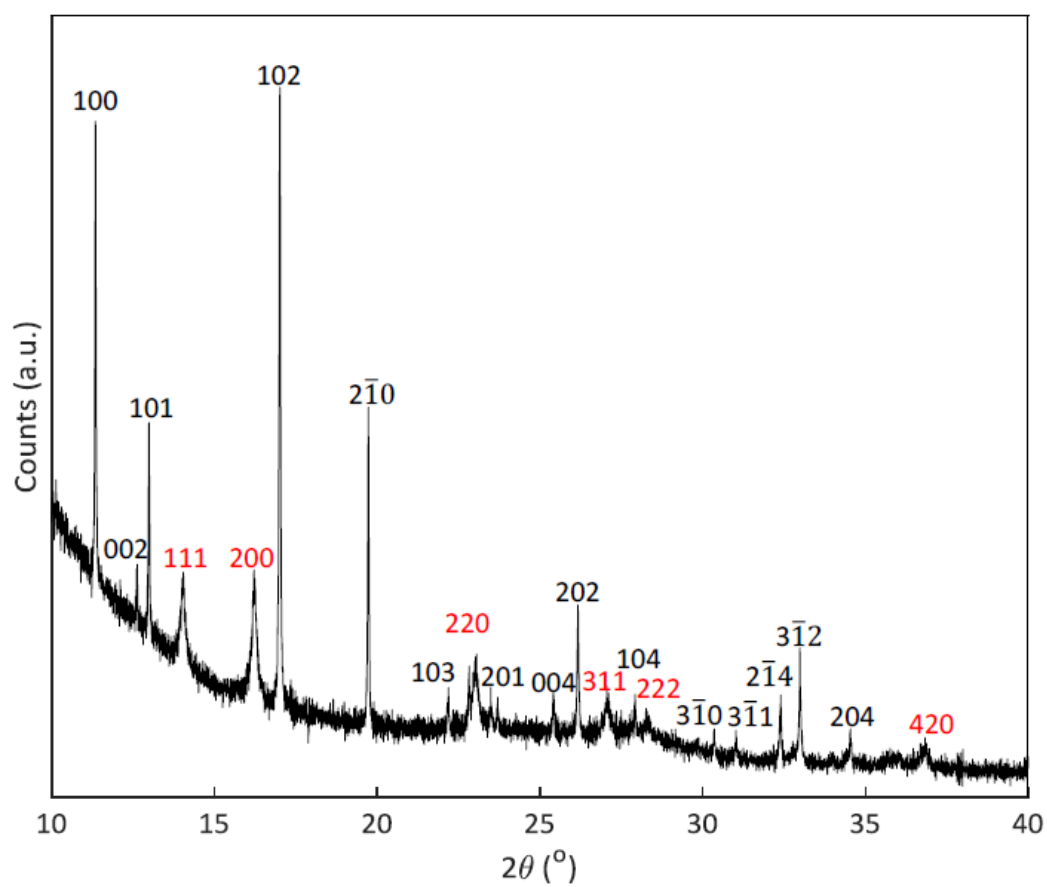


Figure S2: pXRD pattern of the thermolysis residue after heating to 500°C showing peaks assigned to  $\alpha$ -NiS and NiO (shown in red)



## Supporting Information

### From Lead(II) Dithiocarbamate Precursors to a Fast Response PbS Positive Temperature Coefficient Thermistor

Alexander Angeloski, Angus R. Gentle, John A. Scott, Michael B. Cortie, James M. Hook, Mika T. Westerhausen, Mohan Bhadbhade, Anthony T. Baker and Andrew M. McDonagh

**Table S1:** Crystal data and structure refinement parameters for NaNMeGlu and 1.

Chemical formula	C <sub>8</sub> H <sub>18</sub> NNaO <sub>6</sub> .4S <sub>2</sub> (NANMeGlu)	C <sub>14</sub> H <sub>28</sub> N <sub>2</sub> PbS <sub>4</sub> (1)
Mr	320.35	563.81
Crystal system, space group	Monoclinic, C2	Monoclinic, P2 <sub>1</sub> /c
Temperature (K)	151.56	150.0
a, b, c (Å)	18.5921(10), 5.9777(3), 14.4326(10)	11.7703 (12), 8.3978 (9), 20.916 (2)
$\beta$ (°)	120.156(4)	90.657 (4)
V (Å <sup>3</sup> )	1386.92(15)	2053.5 (4)
Z	4	4
Radiation type	MoK $\alpha$ ( $\lambda$ = 0.71073)	MoK $\alpha$ ( $\lambda$ = 0.71073)
$\mu$ (mm <sup>-1</sup> )	0.435	8.62
Crystal size (mm)	0.589, 0.357, 0.149	0.347, 0.170, 0.104
Absorption correction	SADABS-2014/5 was used for absorption correction. $wR^2(\text{int})$ was 0.1212 before and 0.0501 after correction. The Ratio of minimum to maximum transmission is 0.8852. The $\lambda/2$ correction factor is 0.00150.	SADABS-2014/5 was used for absorption correction. $wR^2(\text{int})$ was 0.1582 before and 0.0991 after correction. The Ratio of minimum to maximum transmission is 0.4971. The $\lambda/2$ correction factor is 0.00150.
Tmin, Tmax	0.6599, 0.7455	0.3706, 0.7455
No. of measured, independent and observed [ $I > 2\sigma(I)$ ] reflections	11061, 2989, 2943	31758, 4462, 3968
Rint	0.041	0.071
( $\sin \theta/\lambda$ ) <sub>max</sub> (Å <sup>-1</sup> )	0.638	0.640
R[F <sup>2</sup> > 2 $\sigma$ (F <sup>2</sup> )], wR(F <sup>2</sup> ), S	0.029, 0.079, 1.08	0.039, 0.093, 1.04
No. of reflections	2989	4462
No. of parameters	206	198
H-atom treatment	Independent and Constrained Refinement	Constrained Refinement
$\Delta\rho_{\text{max}}$ , $\Delta\rho_{\text{min}}$ (e Å <sup>-3</sup> )	0.69, -0.24	2.62, -3.01
Absolute structure parameter	-0.04 (2)	N/A

**Table S2:** Crystallographic bond lengths and angles for NaNMeGlu.

S1—C1	1.718 (3)	Na1—O2	2.417 (2)
S2—C1	1.720 (2)	Na1—Na1 <sup>ii</sup>	3.4739 (11)
N1—C1	1.341 (3)	Na1—Na1 <sup>i</sup>	3.4739 (11)
N1—C2	1.466 (3)	Na1—O3	2.563 (2)
N1—C3	1.468 (3)	Na1—O3 <sup>i</sup>	2.642 (2)
C3—C4	1.535 (4)	Na1—O4 <sup>iii</sup>	2.521 (2)
C4—C5	1.523 (3)	Na1—O4 <sup>i</sup>	2.495 (2)
C5—C6	1.540 (3)	Na1—O5 <sup>i</sup>	2.500 (2)
C6—C7	1.522 (3)	C1M—O1M	1.399 (16)
C7—C8	1.518 (4)	C1M—O1M <sup>iv</sup>	1.311 (14)
O1—C4	1.426 (3)	C1M—O1M'	1.311 (14)
O2—C5	1.424 (3)	O1M'—O1M <sup>iv</sup>	1.07 (2)
O3—C6	1.433 (3)	O5—C8	1.425 (3)
Na1—O5	2.382 (2)	O4—Na1 <sup>ii</sup>	2.495 (2)
Na1—O1W	2.668 (5)	O4—Na1 <sup>iv</sup>	2.521 (2)
O3—Na1 <sup>ii</sup>	2.642 (2)	O4—C7	1.426 (3)
Na1—O1W'	2.355 (7)	O5—Na1 <sup>ii</sup>	2.500 (2)
Na1 <sup>i</sup> —Na1—Na1 <sup>ii</sup>	118.72 (6)	C1—N1—C2	121.6 (2)
O2—Na1—Na1 <sup>i</sup>	125.55 (6)	C1—N1—C3	123.5 (2)
O2—Na1—Na1 <sup>ii</sup>	104.38 (6)	C2—N1—C3	114.8 (2)
O2—Na1—O3	65.18 (6)	S1—C1—S2	119.39 (15)
O2—Na1—O3 <sup>i</sup>	144.67 (8)	N1—C1—S1	121.49 (18)
O2—Na1—O4 <sup>iii</sup>	83.22 (7)	N1—C1—S2	119.11 (19)
O2—Na1—O4 <sup>i</sup>	138.72 (8)	N1—C3—C4	113.7 (2)
O2—Na1—O5 <sup>i</sup>	139.18 (8)	O1—C4—C3	108.2 (2)
O2—Na1—O1W	82.63 (11)	O1—C4—C5	109.7 (2)
O3 <sup>i</sup> —Na1—Na1 <sup>i</sup>	47.16 (5)	C5—C4—C3	113.5 (2)
O3 <sup>i</sup> —Na1—Na1 <sup>ii</sup>	71.60 (6)	O2—C5—C4	111.2 (2)
O3—Na1—Na1 <sup>ii</sup>	49.10 (4)	O2—C5—C6	108.4 (2)
O3—Na1—Na1 <sup>i</sup>	167.59 (6)	C4—C5—C6	111.5 (2)
O3—Na1—O3 <sup>i</sup>	120.70 (7)	O3—C6—C5	111.3 (2)
O3—Na1—O1W	73.58 (11)	O3—C6—C7	108.34 (19)
O3 <sup>i</sup> —Na1—O1W	132.60 (11)	C7—C6—C5	112.9 (2)
C8—O5—Na1	122.61 (16)	O4—C7—C6	107.15 (19)
C8—O5—Na1 <sup>ii</sup>	112.12 (16)	O4—C7—C8	110.6 (2)
O4 <sup>iii</sup> —Na1—Na1 <sup>i</sup>	45.85 (5)	C8—C7—C6	116.4 (2)
O4 <sup>i</sup> —Na1—Na1 <sup>i</sup>	95.73 (6)	O5—C8—C7	110.2 (2)
O4 <sup>iii</sup> —Na1—Na1 <sup>ii</sup>	124.28 (7)	C6—O3—Na1 <sup>ii</sup>	114.58 (14)
O4 <sup>i</sup> —Na1—Na1 <sup>ii</sup>	46.49 (5)	C6—O3—Na1	113.02 (14)
O4 <sup>iii</sup> —Na1—O3 <sup>i</sup>	72.11 (6)	Na1 <sup>ii</sup> —O4—Na1 <sup>iv</sup>	87.66 (6)
O4 <sup>i</sup> —Na1—O3	73.88 (6)	C7—O4—Na1 <sup>iv</sup>	131.57 (15)

O4 <sup>i</sup> —Na1—O3 <sup>i</sup>	63.75 (6)	C7—O4—Na1 <sup>ii</sup>	105.83 (14)
O4 <sup>iii</sup> —Na1—O3	139.53 (7)	Na1—O5—Na1 <sup>ii</sup>	90.70 (7)
O4 <sup>i</sup> —Na1—O4 <sup>iii</sup>	135.37 (6)	O5 <sup>i</sup> —Na1—Na1 <sup>ii</sup>	114.10 (6)
O4 <sup>i</sup> —Na1—O5 <sup>i</sup>	70.15 (6)	O5 <sup>i</sup> —Na1—Na1 <sup>i</sup>	43.28 (5)
O4 <sup>i</sup> —Na1—O1W	81.04 (12)	O5—Na1—Na1 <sup>ii</sup>	46.03 (5)
O4 <sup>iii</sup> —Na1—O1W	128.83 (13)	O5—Na1—Na1 <sup>i</sup>	105.79 (7)
O5—Na1—O4 <sup>iii</sup>	83.01 (7)	O5—Na1—O2	80.57 (7)
O5—Na1—O4 <sup>i</sup>	89.28 (7)	O5—Na1—O3 <sup>i</sup>	71.82 (7)
O5 <sup>i</sup> —Na1—O4 <sup>iii</sup>	86.08 (7)	O5—Na1—O3	68.01 (7)
O5—Na1—O5 <sup>i</sup>	136.86 (5)	O5 <sup>i</sup> —Na1—O3	134.37 (7)
O5 <sup>i</sup> —Na1—O1W	73.92 (11)	O5 <sup>i</sup> —Na1—O3 <sup>i</sup>	65.10 (7)
O5—Na1—O1W	141.57 (12)	O1W—Na1—Na1 <sup>ii</sup>	106.85 (12)
O1W—Na1—Na1 <sup>i</sup>	112.11 (11)	O1M <sup>v</sup> —C1M—O1M <sup>v</sup>	48.3 (10)
O1W <sup>v</sup> —Na1—Na1 <sup>ii</sup>	127.9 (2)	O1M <sup>v</sup> —O1M <sup>v</sup> —C1M	65.9 (5)
O1W <sup>v</sup> —Na1—Na1 <sup>i</sup>	102.1 (2)	O3—C6—C7—C8	-68.0 (3)
O1W <sup>v</sup> —Na1—O2	71.59 (18)	O4—C7—C8—O5	-62.7 (3)
O1W <sup>v</sup> —Na1—O3 <sup>i</sup>	139.37 (19)	N1—C3—C4—O1	-168.7 (2)
O1W <sup>v</sup> —Na1—O3	87.0 (2)	N1—C3—C4—C5	69.3 (3)
O1W <sup>v</sup> —Na1—O4 <sup>iii</sup>	107.2 (2)	C1—N1—C3—C4	-108.7 (3)
O1W <sup>v</sup> —Na1—O4 <sup>i</sup>	102.1 (2)	C2—N1—C1—S1	-174.1 (2)
O1W <sup>v</sup> —Na1—O5	148.64 (19)	C2—N1—C1—S2	6.8 (3)
O1W <sup>v</sup> —Na1—O5 <sup>i</sup>	74.28 (18)	C2—N1—C3—C4	74.9 (3)
C5—O2—Na1	125.14 (15)	C3—N1—C1—S1	9.7 (3)
Na1—O3—Na1 <sup>ii</sup>	83.74 (6)	C3—N1—C1—S2	-169.39 (19)
Na1—O2—C5—C4	103.4 (2)	C3—C4—C5—O2	55.4 (3)
Na1—O2—C5—C6	-19.5 (3)	C3—C4—C5—C6	176.5 (2)
Na1 <sup>ii</sup> —O3—C6—C5	-139.10 (16)	C4—C5—C6—O3	-80.9 (3)
Na1—O3—C6—C5	-45.4 (2)	C4—C5—C6—C7	157.0 (2)
Na1—O3—C6—C7	79.3 (2)	C5—C6—C7—O4	179.98 (19)
Na1 <sup>ii</sup> —O3—C6—C7	-14.4 (2)	C5—C6—C7—C8	55.7 (3)
Na1 <sup>iv</sup> —O4—C7—C6	29.8 (3)	C6—C7—C8—O5	59.9 (3)
Na1 <sup>ii</sup> —O4—C7—C6	-71.41 (19)	O1—C4—C5—C6	55.4 (3)
Na1 <sup>iv</sup> —O4—C7—C8	157.55 (16)	O2—C5—C6—O3	41.8 (3)
Na1 <sup>ii</sup> —O4—C7—C8	56.3 (2)	O2—C5—C6—C7	-80.3 (2)
Na1—O5—C8—C7	-73.4 (3)	O3—C6—C7—O4	56.2 (2)
Na1 <sup>ii</sup> —O5—C8—C7	32.6 (2)	O1—C4—C5—O2	-65.7 (3)

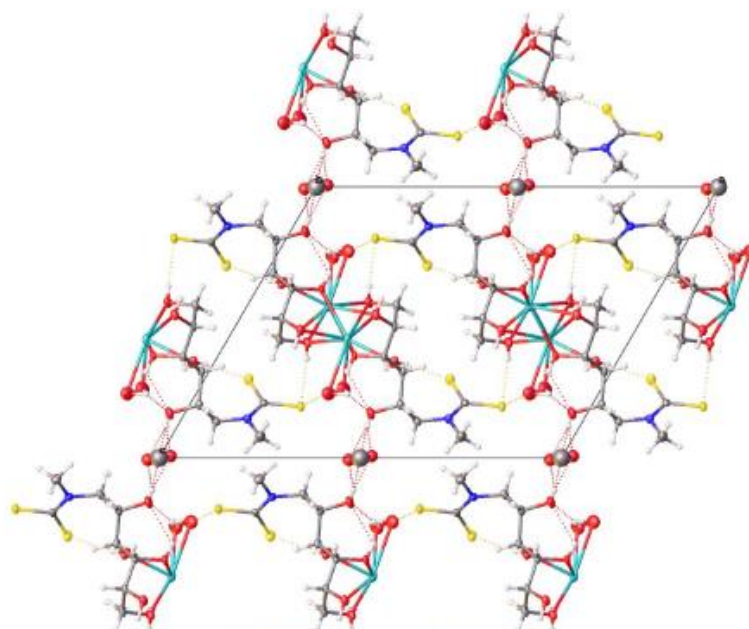
Symmetry codes: (i)  $-x+1/2, y-1/2, -z+1$ ; (ii)  $-x+1/2, y+1/2, -z+1$ ; (iii)  $x, y-1, z$ ; (iv)  $x, y+1, z$ ; (v)  $-x+1, y, -z+2$ .

Table S3: Crystallographic bond lengths and angles for 1\*.

Pb1—S1	2.8656 (18)	N1—C2	1.490 (7)
Pb1—S3	2.853 (2)	N2—C9	1.466 (9)
Pb1—S2	2.6994 (14)	N2—C12	1.486 (10)
Pb1—S4	2.7027 (16)	C5—C7	1.520 (8)
S1—C1	1.719 (5)	C5—C6	1.522 (8)
S3—C8	1.710 (6)	C11—C9	1.474 (9)
S2—C1	1.727 (5)	C9—C10	1.445 (11)
S4—C8	1.728 (6)	C12—C14	1.448 (14)
C8—N2	1.339 (7)	C12—C13	1.426 (12)
C1—N1	1.334 (6)	C2—C4	1.522 (9)
N1—C5	1.492 (6)	C2—C3	1.522 (10)
S3—Pb1—S1	138.63 (5)	C1—N1—C2	121.0 (4)
S2—Pb1—S1	64.01 (4)	C2—N1—C5	113.8 (4)
S2—Pb1—S3	88.32 (5)	C8—N2—C9	124.4 (6)
S2—Pb1—S4	97.19 (5)	C8—N2—C12	121.6 (6)
S4—Pb1—S1	88.54 (5)	C9—N2—C12	114.0 (7)
S4—Pb1—S3	63.81 (4)	N1—C5—C7	114.2 (5)
C1—S1—Pb1	86.06 (18)	N1—C5—C6	112.3 (4)
C8—S3—Pb1	86.26 (19)	C7—C5—C6	114.2 (5)
C1—S2—Pb1	91.35 (17)	N2—C9—C11	116.5 (6)
C8—S4—Pb1	90.82 (19)	C10—C9—N2	117.2 (6)
S3—C8—S4	117.5 (3)	C10—C9—C11	121.5 (8)
N2—C8—S3	121.5 (4)	C14—C12—N2	113.7 (8)
N2—C8—S4	121.0 (4)	C13—C12—N2	115.5 (8)
S1—C1—S2	117.9 (3)	C13—C12—C14	124.7 (8)
N1—C1—S1	121.0 (4)	N1—C2—C4	112.2 (5)
N1—C1—S2	121.1 (4)	N1—C2—C3	110.5 (5)
C1—N1—C5	125.2 (4)	C4—C2—C3	113.1 (6)

\* There are no significant differences in bond lengths and angles between the current data and the previous structural determination,<sup>2</sup> however, the ESDs and R factor are substantially lower in the data presented here.





**Figure S1:** Molecular packing diagram of NaNMeGlu viewed along the *b* axis, showing layered morphology.

From the molecular assembly diagram of NaNMeGlu (Figure S1), a layered supramolecular motif is evident parallel to the crystallographic *b* direction. The layered structure is stabilized by hydrogen bonding interactions. Sodium ions are positioned between layers of symmetrically equivalent ligand anions, forming a two dimensional array oriented parallel to the crystallographic *b* direction. The sodium ions are separated by a distance of 3.4739 (11) Å, significantly longer than the sum of Na<sup>+</sup> ionic radii of 2.32 Å. Alternating sodium ions are linked by bridging hydroxyl groups O3, O4 and O5 on symmetrically equivalent anionic ligand molecules. The array of Na cations is stabilized by a network of hydrogen bonding between alternate and neighbouring hydroxyl groups. The ligand anions are linked *via* intermolecular O-H...S hydrogen bonds to the water molecules associated with the array of sodium cations.

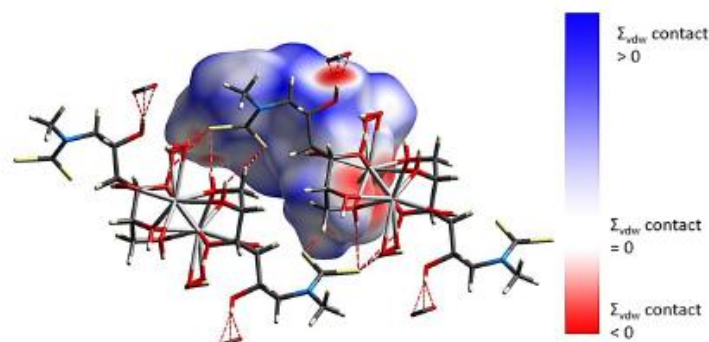


**Figure S2:** Hirshfeld surface highlighting O-H...S hydrogen bonds (red).

Contacts involving intermolecular H...S, H...O, H...H and Na...O were examined using Hirshfeld surface analysis. The majority of interactions within the structure are dominated by van der Waals H...H interactions (~38%), followed by H...S hydrogen bonds (~24%) and O...H hydrogen bonds (~16%). The

intermolecular contacts are highlighted in the map of  $d_{\text{norm}}$  on the Hirshfeld surface (Figure S2). The dark red regions are due to hydrogen bonding whilst the blue and white regions reflect van der Waals type interactions.

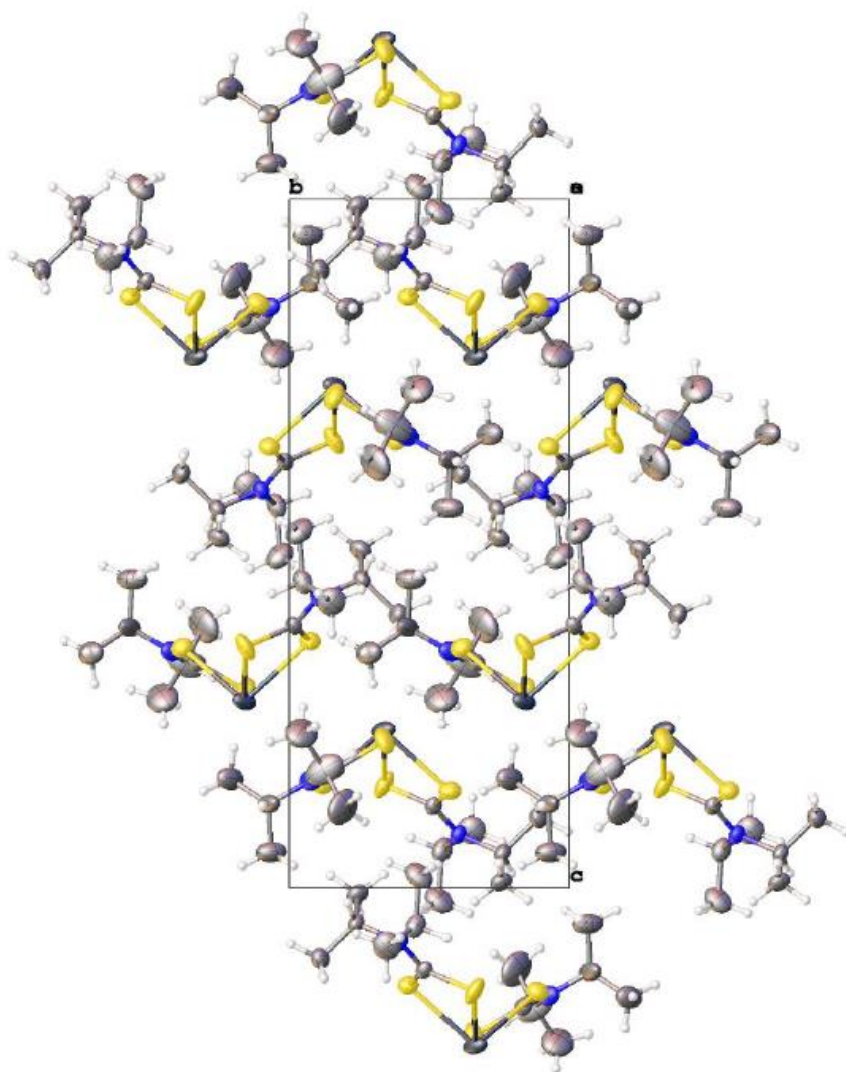


**Figure S3:** Molecular packing diagram as viewed along the  $a$  axis, showing layered morphology of **1** parallel to the  $b$  axis.

From the molecular assembly diagram of **1** (Figure S3), when viewed along the  $a$  axis, a layered supramolecular motif is evident parallel to the crystallographic  $b$  axis along a two-fold screw axis at  $(0, y, 1/4)$ . The lead ions are separated by a distance of 4.2887 (5) Å, significantly longer than the sum of Pb ionic radii of approximately 2.7 Å. A pair of inequivalent Pb $\cdots$ S interactions of 3.5325 (16) Å (Pb1 $\cdots$ S4) and 3.9463 (13) Å (Pb $\cdots$ S4) complete a distorted octahedral environment about each lead ion. The distorted octahedral environment about Pb1 is such that the Pb-S distances opposite to the Pb $\cdots$ S contacts are equal

and shorter than those that are perpendicular to the Pb $\cdots$ S interactions. In addition, there are a pair of C-H $\cdots$ S interactions of  $\sim 3.0$  Å for S4 $\cdots$ H6 and  $\sim 2.9$  Å for S2 $\cdots$ H10B. Lastly, there are two intramolecular C-H $\cdots$ S interactions of  $\sim 2.3$  Å between S3 $\cdots$ H12 and  $\sim 2.4$  Å between S1 $\cdots$ H2.

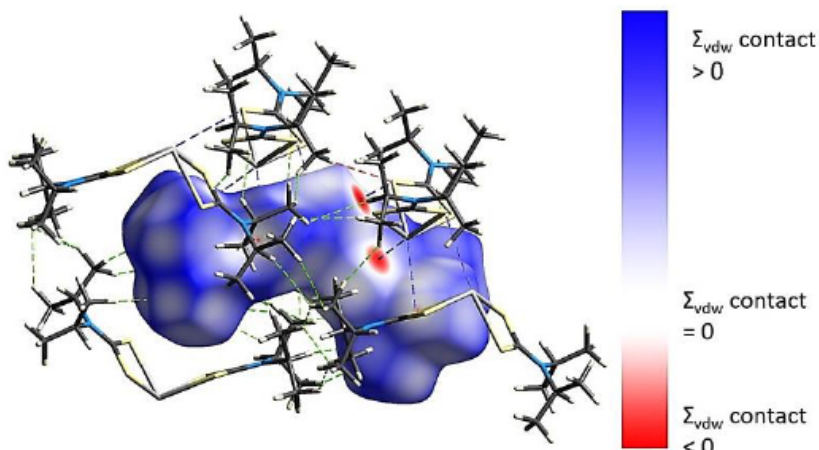


**Figure S4:** Hirshfeld surface of **1** highlighting Pb $\cdots$ S (blue), H $\cdots$ S (red) and H $\cdots$ H (green) interactions.

An examination of the intermolecular forces responsible for the layered morphology was performed using Hirshfeld surface analysis. The majority of interactions are dominated by weak intermolecular attractions such as van der Waals H $\cdots$ H (61%), C-H $\cdots$ S (26%) and Pb $\cdots$ S (4%) interactions. The intermolecular contacts are highlighted in the map of  $d_{\text{norm}}$  on the Hirshfeld surface (Figure S4). The dark red regions are due to Pb $\cdots$ S interactions whilst the blue and white regions reflect van der Waals type interactions.

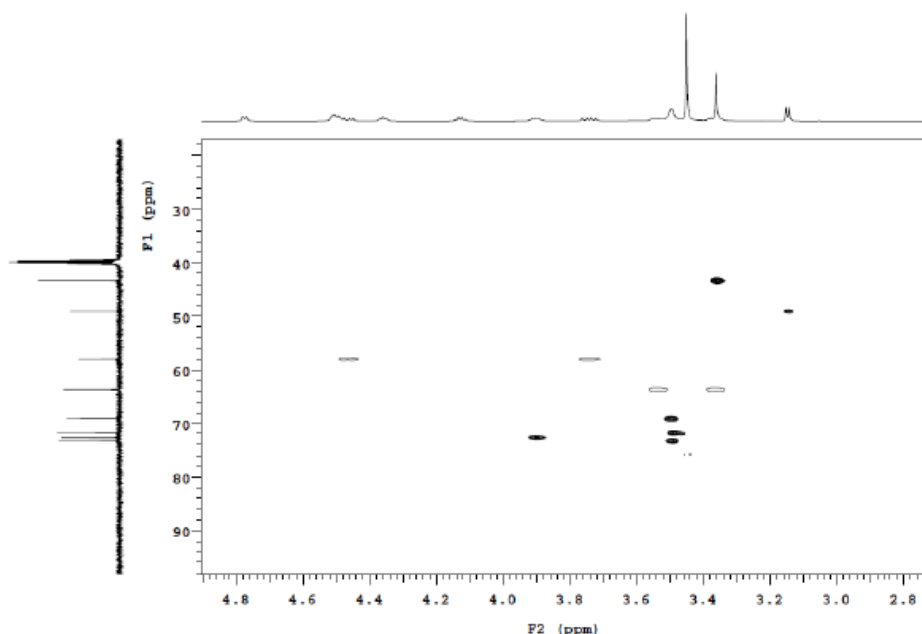


**Figure S5:** 500.3 MHz  $^{13}\text{C}$ - $^1\text{H}$  HSQC spectrum of NaNMeGlu in dimethylsulfoxide- $d_6$  acquired at 293 K. Regions without cross-peaks have been omitted for clarity.



The solubility of compounds was tested in a range of deuterated solvents (chloroform, dichloromethane, methanol, ethanol, acetone, acetonitrile, pyridine, DMF, DMSO). The choice of solvent was informed by (i) solubility and (ii) (for VT experiments) an ability to remain liquid at 223 K.  $^1\text{H}$  and  $^{13}\text{C}$  solution state NMR spectra of NaNMeGlu and **2** recorded at room temperature in  $\text{DMSO}-d_6$  contain sharp signals associated with the methine, methyl and hydroxyl groups. Remarkably, signals assigned to the hydroxyl protons O1H-O5H (assigned using  $^{13}\text{C}$ - $^1\text{H}$  HSQC experiments, Figure S5) appear as well defined doublets with vicinal coupling to their associated methine protons in the order of 4.5 to 7.0 Hz.

Resonances assigned to methylene protons associated with C3 and C8 appeared as two sets of signals for each methylene group as a result of their position adjacent to the C4 and C7 chiral centres. The chemical shifts of the protons on C3 are separated by  $\sim 0.7$  ppm while those of the C8 protons are separated by  $\sim 0.2$  ppm. The larger difference in chemical shift for methylene protons on C3 is likely due to the interaction between one of the methylene protons with the  $\text{NCS}_2$  moiety, with the other being in proximity to the C2 methyl group, as shown in the crystal structure of NaNMeGlu (Figure 2, main text).

The  $^1\text{H}$  NMR spectrum of **2** is remarkably similar to that of NaNMeGlu; the only significant differences (in chemical shifts) are associated with the hydroxyl protons O1H-O5H that we attribute to slight differences in concentration.

The  $^{13}\text{C}$  NMR spectra show signals arising from each of the carbon atoms of NaNMeGlu and **2**. Resonances assigned to the dithiocarbamate C1 appear at 214 ppm in NaNMeGlu and 204 ppm in **2**. The upfield shift of  $\sim 10$  ppm upon moving from NaNMeGlu to **2** can be attributed to an increased electron density within the  $\text{NCS}_2$  moiety that arises upon coordination.

In **1**, the intramolecular C-H $\cdots$ S interactions produce two inequivalent isopropyl groups in the solid state and in solution. Notably,  $^1\text{H}$  and  $^{13}\text{C}$  spectra at 223 K reveal two signals for the methyl groups and two signals for the methine groups consistent with two inequivalent isopropyl environments. The methine protons, H2/H12 and H5/H9 exhibit chemical shifts of 5.58 and 4.01 ppm, respectively. This difference in chemical shifts is not as pronounced as that seen in the spectrum of NaDIPDTC, with signals being  $\sim 0.8$  ppm closer to each other in **1**.<sup>1</sup> Nevertheless, these differences are attributed to the influence of the C-H $\cdots$ S interactions upon the local electron density about H2/H12.<sup>1</sup> Similarly, the signal assigned to the methyl protons of C6,C7,C10 and C11 appears at 1.67 ppm whilst that assigned to protons on C3,C4,C13 and C14 appears at 1.24 ppm.

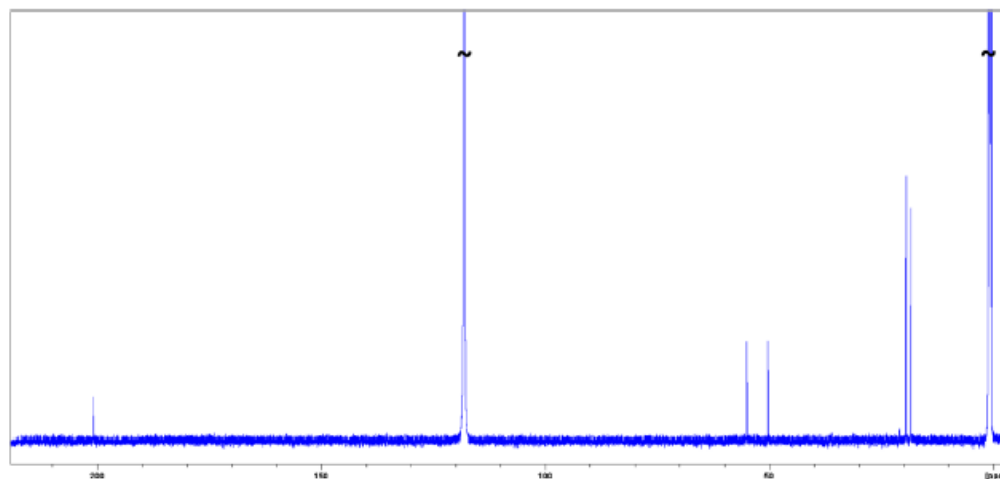
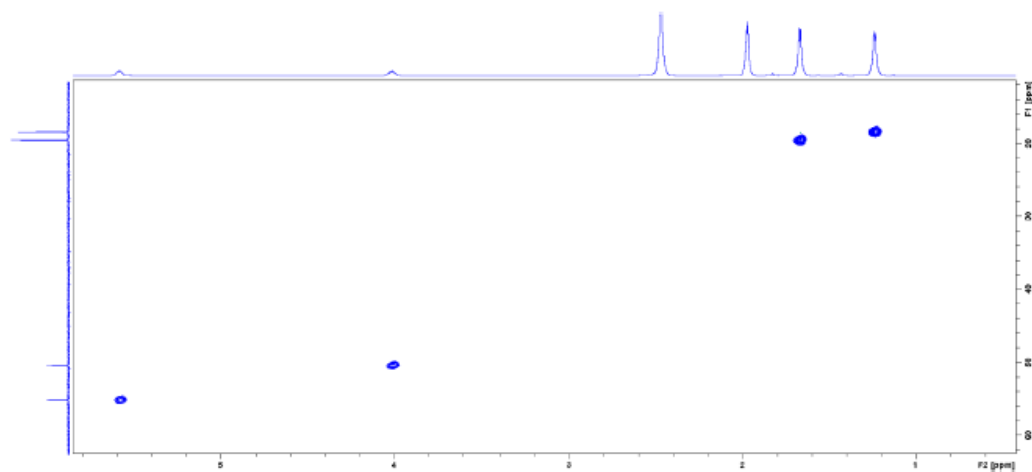
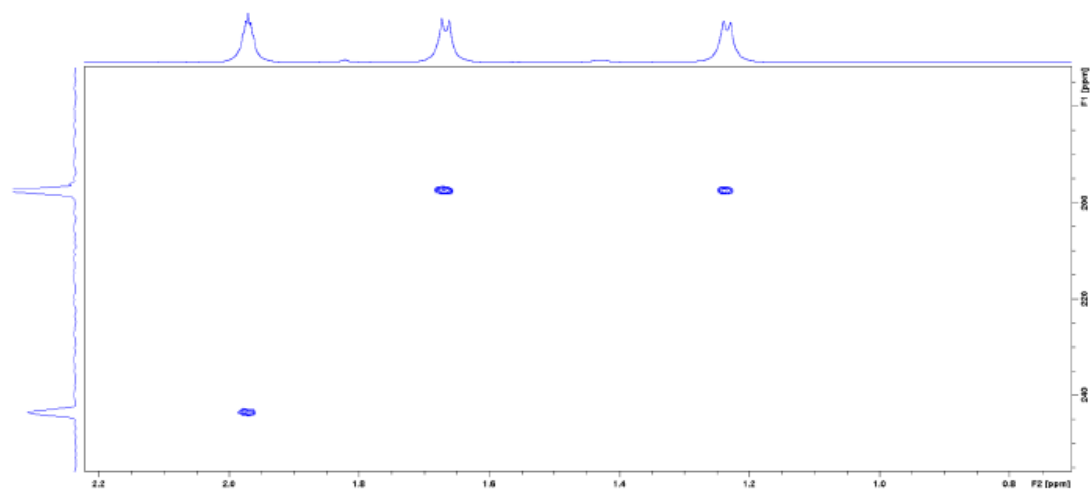


Figure S6: 150.9 MHz  $^{13}\text{C}$  NMR spectrum of **1** in acetonitrile- $d_3$  acquired at 225 K.





**Figure S7:**  $^{13}\text{C}$ - $^1\text{H}$  HSQC spectrum of **1** in acetonitrile- $d_3$  acquired at 225 K.



**Figure S8:**  $^{15}\text{N}$ - $^1\text{H}$  HMBC spectrum of **1** in acetonitrile- $d_3$  acquired at 225 K.

**Table S4:** Selected IR frequencies and assignments for NaNMeGlu, **2**, NaDIPDTC and **1**.

	NaNMeGlu	<b>2</b>	NaDIPDTC	<b>1</b>
$\nu(\text{O-H})$	3245	3249	3343	N/A
$\nu(\text{C-H})$	2913	2912	3012	2999
$\delta(\text{O-H})$	1637	1638	1665	N/A
$\nu_s(\text{C}\cdots\text{N})$	1470	1467	1476	1475
$\nu_{as}(\text{CH}_3)$	1425	1438	1433	1436
$\nu_{sy}(\text{CH}_3)$	1330	1331	1354	1363
$\nu(\text{N-C})$	1365	1378	1295	1305
$\rho(\text{CH}_3)$	1186	1188	1141	1133
$\nu(\text{C-O})$	1089	1079	N/A	N/A
$\nu_s(\text{C}\cdots\text{S})$	966	975	943	936

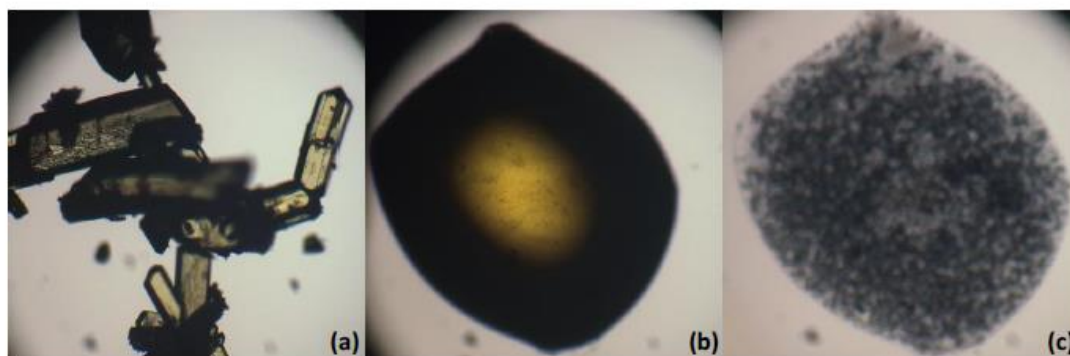


**Figure S9:** Isotropic variable temperature photomicrographs depicting the decomposition of **1** before (a), during (b) and after (c) heating to 500 °C. The intermediate molten **1** is clearly visible in (b).

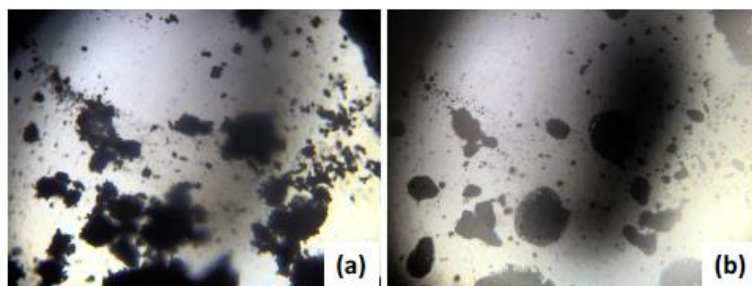


**Figure S10:** Isotropic variable temperature photomicrographs depicting the decomposition of **2** before (a) and after (b) heating to 500 °C. There was no intermediate molten **2** visible.

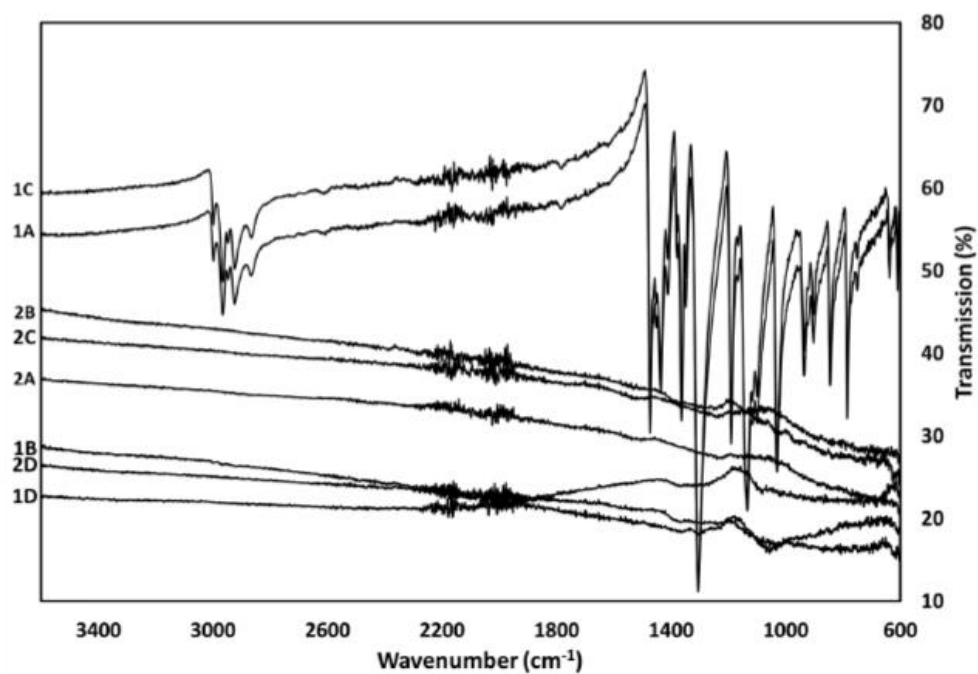


Figure S11: FTIR spectra of crystalline PbS formed by thermolysis of **1** and **2** under conditions A to D.

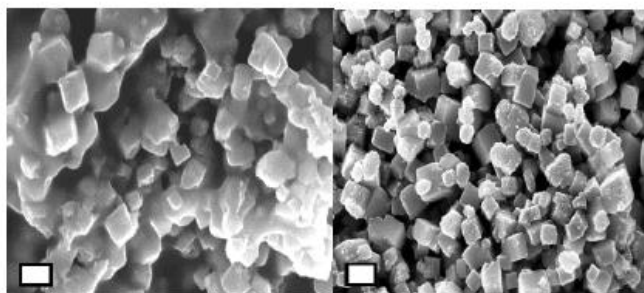


Figure S12: PbS formed by thermolysis of **1** under condition A, with residue heated for 10 minutes (left) and 60 minutes (right). Scale bar is 250 nm.

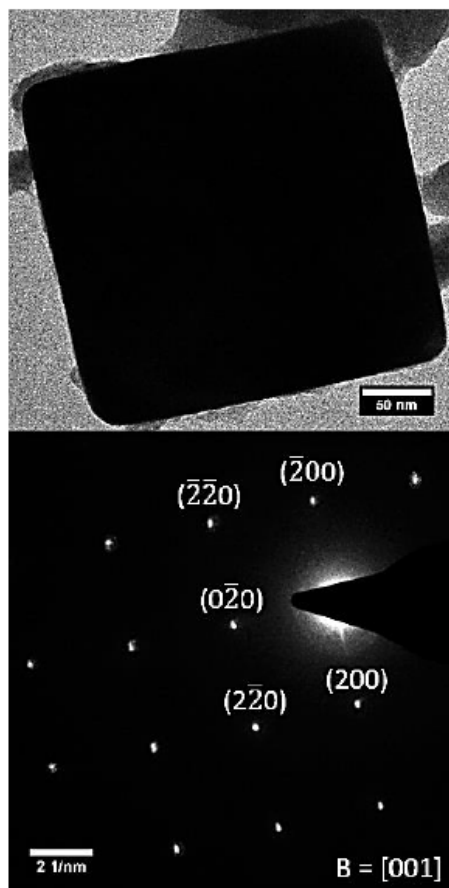


Figure S13: Low Resolution TEM image of single crystal PbS formed by thermolysis of **1** under condition D (upper), with SAED pattern (lower).

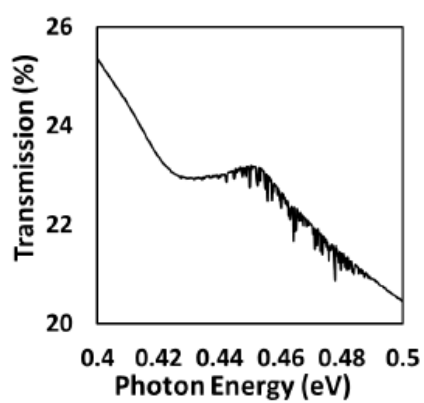
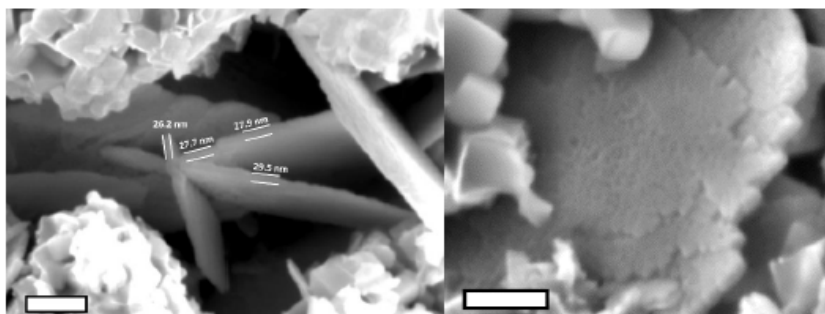
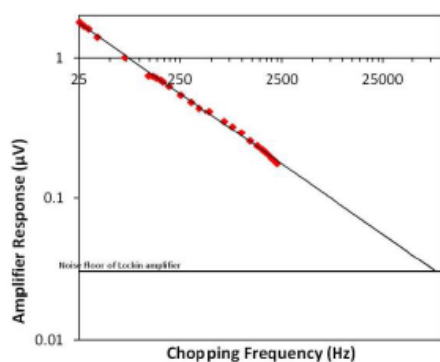


Figure S14: Transmission curve of the PbS nanocubes (**2C**) at 293 K in KBr.





**Figure S15:** SEM image showing selected thicknesses and morphology of PbS nanosheets formed by thermolysis of **2** under condition B. Scale bar is 200 nm (left) and 150 nm (right).



**Figure S16:** Extrapolated thermal-time response to chopped light source for the PbS device. The intersect between lock-in amplifier noise and extrapolated response is the maximum response rate and minimum temperature change of the device.

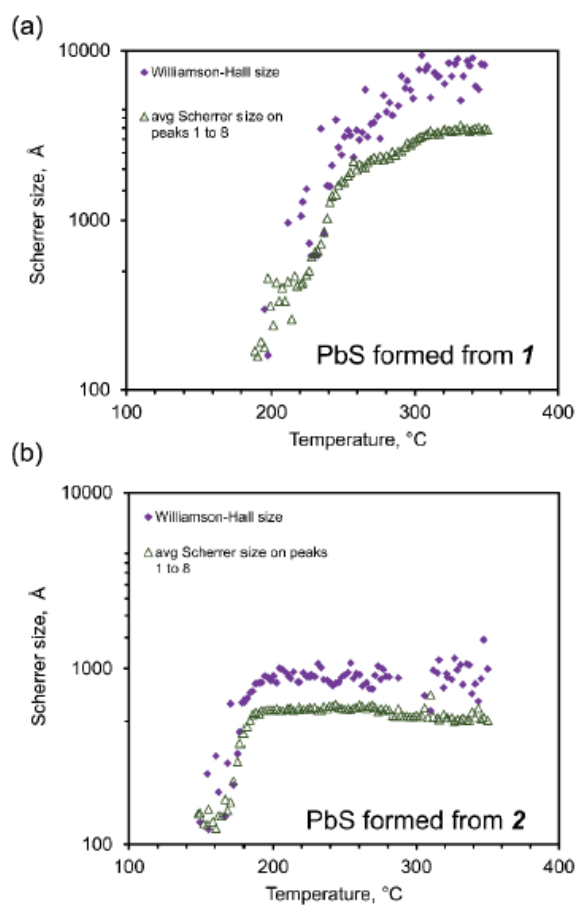


**Figure S17.** Estimation of the crystallite size using the Scherrer equation and the Williamson-Hall technique (after correcting for instrumental broadening). Most data points were obtained from between six and eight diffraction peaks. The Scherrer values plotted are the averages of the values obtained for the individual peaks. The samples had some microstrain (about  $5 \times 10^{-4}$  strain units).

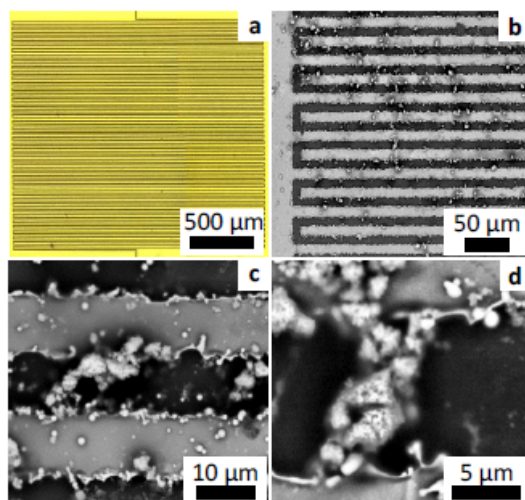


**Figure S18:** Optical photomicrograph of device prior to PbS 2C addition (a) BS-SEM micrograph of device after addition of PbS (b) and BS-SEM micrograph showing Au-PbS-Au contacts (c and d).

#### References:

1. Angeloski, A.; Hook,.; Bhadbhade, M.; Baker, A.T.; McDonagh, A.M., Intramolecular H $\cdots$ S interactions in metal di-(isopropyl)dithiocarbamate complexes. *CrystEngComm*, 2016, **18**, 7070-7077.
2. Ito, M.; Iwasaki, H., Structure of Lead(II) N,N-Diisopropylthiocarbamate [Bis(N,N-diisopropylthiocarbamato)lead(II)]. *Acta Crystallogr. Sect. B* 1980, 36, 443-444.

## **Intramolecular H...S interactions in metal di-(isopropyl)dithiocarbamate complexes**

Alexander Angeloski<sup>a</sup>, James M. Hook<sup>b</sup>, Mohan Bhadbhade<sup>c</sup>, Anthony T. Baker<sup>d</sup> and Andrew M. McDonagh<sup>a\*</sup>

<sup>a</sup> School of Mathematical and Physical Sciences, University of Technology Sydney, Ultimo, 2007, Australia.

<sup>b</sup> NMR Facility, Mark Wainwright Analytical Centre, The University of New South Wales, Sydney, 2052, Australia.

<sup>c</sup> School of Chemistry, The University of New South Wales, Sydney, 2052, Australia.

<sup>d</sup> College of Science, Health and Engineering, La Trobe University, Melbourne, 3086, Australia.

## **Electronic Supplementary Information**

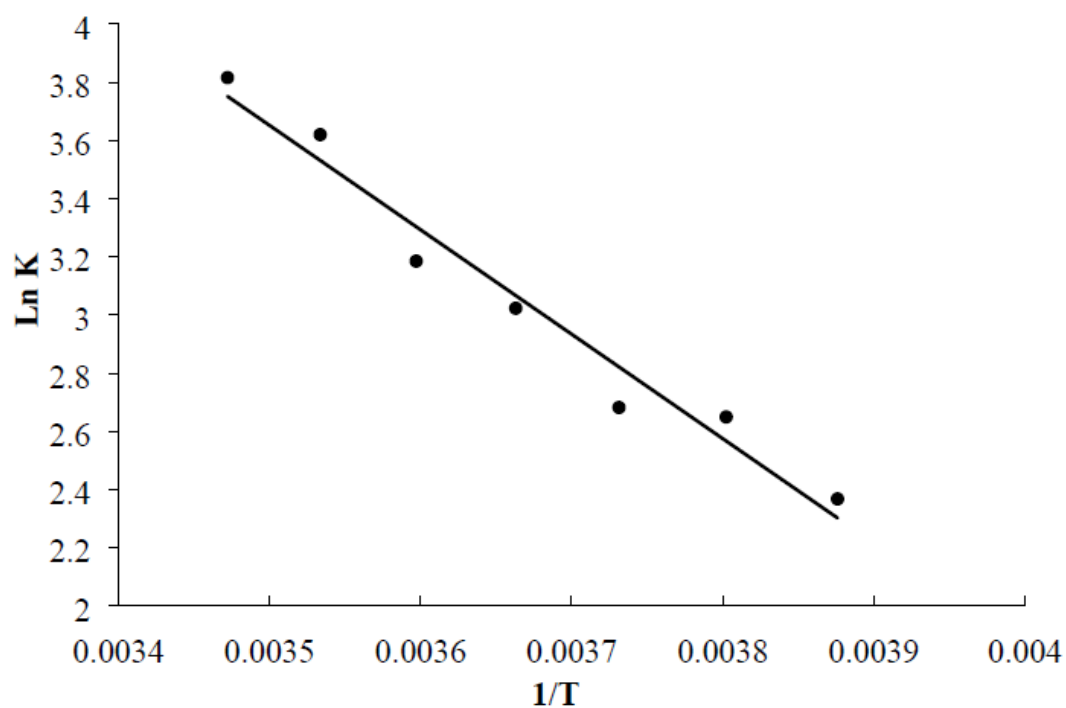


Figure S1: Arrhenius plot for exchange of isopropyl methyl groups in Na(dipdte)-5H<sub>2</sub>O.

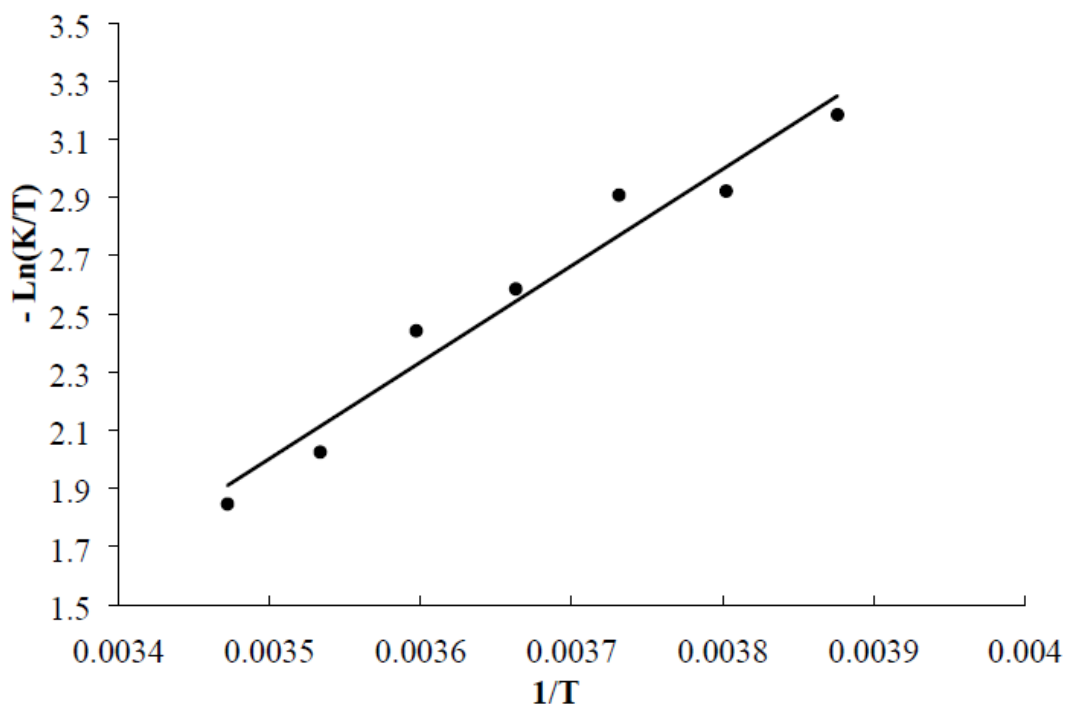


Figure S2: Eyring plot for exchange of isopropyl methyl groups in Na(dipdte)-5H<sub>2</sub>O.



Table S1: Selected data obtained from CSD database survey of metal dipdte complexes.

CSD Refcode	CSD number	Metal	C1-N1-C2	C1-N1-C5	C2-S1	C5-S2	C1-N1	S1-C1-S2
AFELEE	908263	Au	119.4	123.5	2.998	3.195	1.305	109.46
CEXZEM	924188	In	120.88	124.07	3.008	3.101	1.329	116.15
DUHPEC	754186	Zn	119.9	124.9	3.006	3.126	1.34	115.69
FERROJ	1154897	Mo	119.2	123.6	3.006	3.201	1.323	109.2
GOPRIM	1170146	Nd	120.1	123.5	2.941	3.098	1.324	116.5
IPTCMO	1180752	Mo	120.8	123.113	3.042	3.116	1.309	109.95
IPTCNI10	1180754	Ni	119.5	124.2	3.037	3.174	1.311	108.38
IPTCZN	1180758	Zn	121.38	124.19	3.017	3.096	1.326	115.99
JAKNEO	1182236	Be	120.32	123.91	3.042	3.152	1.324	111.73
JERDUF	1184894	Co	117	123	3.117	3.121	1.322	108.7
LITJUT	144058	Zn	122.2	123.3	3.046	3.072	1.34	115.6
LITKAA01	118972	Zn	121.1	123.7	3.027	3.099	1.342	115.7
MIFDEK	162242	Sn	121.1	123.8	3.005	3.139	1.329	115
NDTCU02	111990	Cu	120.1	124.1	3.018	3.162	1.321	111.3
PRCBFE	1237953	Fe	119.07	123.32	3.046	3.166	1.315	108.1
QIWMAK	145420	W	120.1	122.1	3.018	3.17	1.327	109.3
QIYTIK	638242	Cd	121.01	124.59	2.995	3.128	1.336	117.25
QUKCII	139236	Ni	118.8	124.8	3.04	3.219	1.314	107.2
RAHKUI	833598	Au	119.5	123.4	3.027	3.153	1.293	109
RAZBEB	827580	Au	119.8	123.9	3.03	3.174	1.3	109.37
SUVTUY	131014	Cd	122.3	123.5	3.018	3.084	1.327	117.31
TISFIK	1271462	In	120.4	124.4	2.994	3.098	1.317	116.5
UFEWEH01	135544	Pd	120.8	123.5	3.029	3.173	1.307	109.9
XAJWOU	139090	Ni	120.87	123.53	3.077	3.177	1.312	108.12
XUJHEP	196553	Cr	118.48	123.73	3.017	3.217	1.335	108.11
YECXAF	1300618	In	120.7	123.9	2.991	3.117	1.33	116.5
YEFIQ	856056	Ni	119.2	123.7	3.054	3.21	1.324	106.47
YEFVUC	868305	Pd	119.1	124.7	3.037	3.185	1.31	108.2

Table S2. Complete set of bond lengths (Å) and angles (°) for Na(dipdtc)·5H<sub>2</sub>O.

S1-C1	1.7484(16)	C5-C6	1.522(2)
S2-C1	1.7145(17)	Na1-O4	2.3891(13)
N1-C2	1.492(2)	Na1-O1	2.4492(14)
N1-C1	1.345(2)	Na1-O2	2.4207(13)
N1-C5	1.496(2)	Na1-O5	2.3859(15)
C2-C3	1.524(2)	Na1-O3	2.3879(14)
C2-C4	1.519(2)	Na1-O3 <sup>1</sup>	2.4278(14)
C5-C7	1.525(2)	O3-Na1 <sup>1</sup>	2.4278(14)
C2-N1-C5	113.38(12)	O4-Na1-O3 <sup>1</sup>	84.60(5)
C2-N1-C5	113.38(12)	O4-Na1-O3 <sup>1</sup>	84.60(5)
C1-N1-C2	122.01(13)	O2-Na1-O1	95.54(5)
C1-N1-C5	124.59(14)	O2-Na1-O3 <sup>1</sup>	80.40(5)
N1-C2-C3	111.51(13)	O5-Na1-O4	96.85(5)
N1-C2-C4	111.23(13)	O5-Na1-O1	88.03(5)
C4-C2-C3	112.74(15)	O5-Na1-O2	98.83(5)
S2-C1-S1	118.11(9)	O5-Na1-O3	97.38(5)
N1-C1-S1	120.25(12)	O5-Na1-O3 <sup>1</sup>	175.04(5)
N1-C1-S2	121.63(12)	O3-Na1-O4	85.89(5)
N1-C5-C7	113.60(13)	O3 <sup>1</sup> -Na1-O1	87.17(5)
N1-C5-C6	113.02(13)	O3-Na1-O1	174.47(5)
C6-C5-C7	113.36(15)	O3-Na1-O2	84.83(5)
O4-Na1-O1	92.33(5)	O3-Na1-O3 <sup>1</sup>	87.45(5)
O4-Na1-O2	162.67(5)	Na1-O3-Na1 <sup>1</sup>	92.55(5)
C2-N1-C1-S1	-2.19(18)	C1-N1-C5-C7	-65.41(19)
C2-N1-C1-S2	179.00(10)	C1-N1-C5-C6	65.6(2)
C2-N1-C5-C7	116.30(15)	C5-N1-C2-C3	61.13(17)
C2-N1-C5-C6	-112.71(16)	C5-N1-C2-C4	-65.66(17)
C1-N1-C2-C3	-117.20(16)	C5-N1-C1-S1	179.67(10)
C1-N1-C2-C4	116.01(16)	C5-N1-C1-S2	0.9(2)

Symmetry Code: <sup>1</sup>1-X,1-Y,1-Z

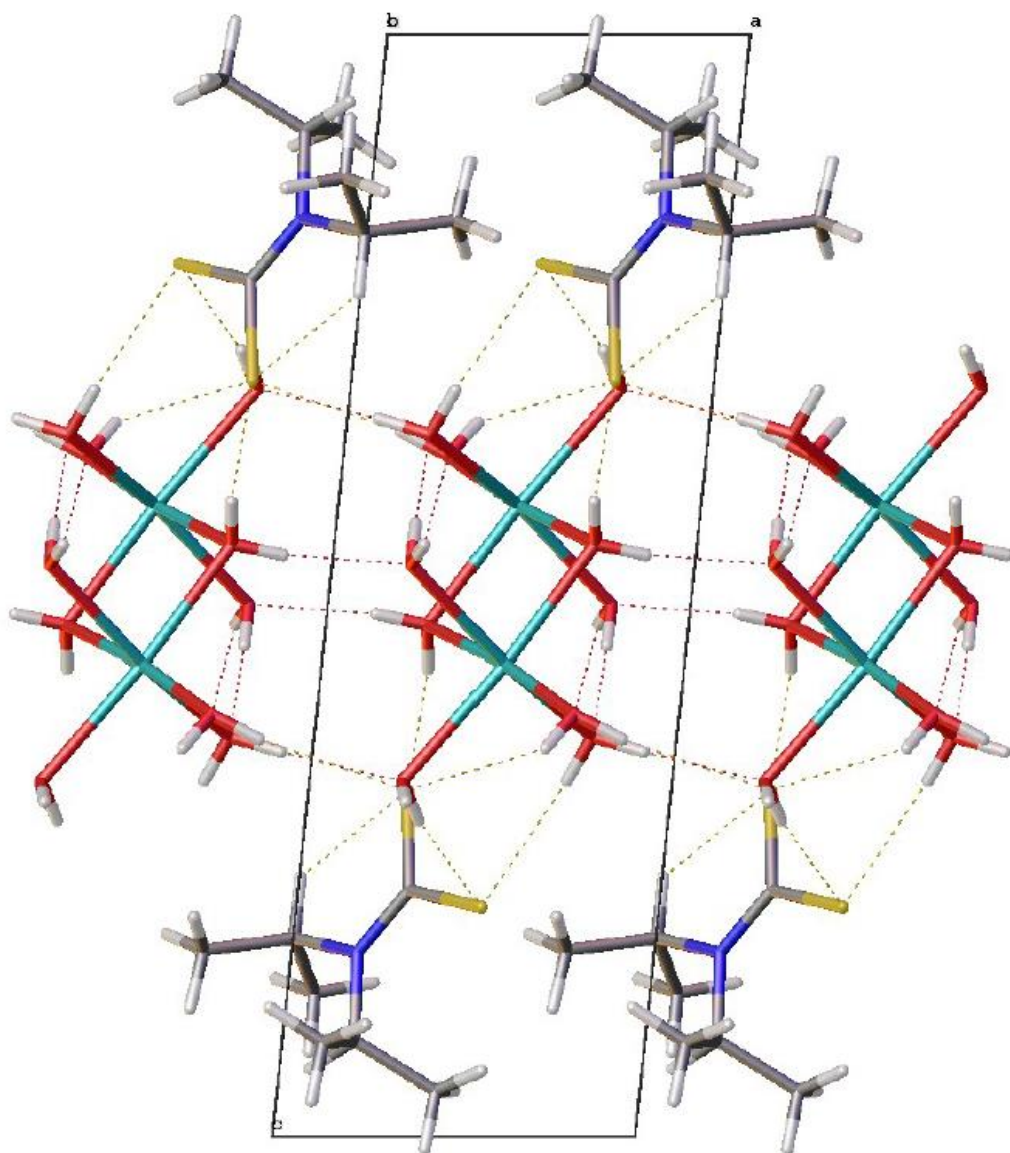


Figure S3. Molecular packing diagram as viewed along the *b* axis, showing layered morphology of Na(dipdte)·5H<sub>2</sub>O.

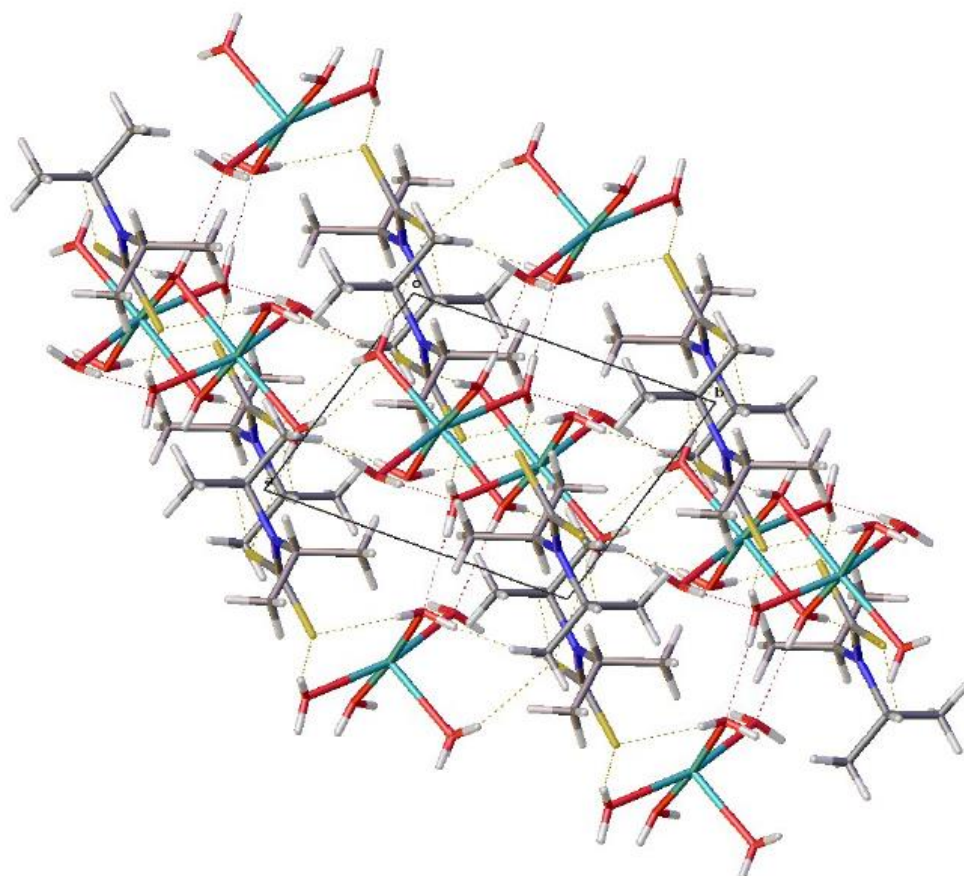


Figure S4. Molecular packing diagram as viewed along the *c* axis, showing layered morphology of Na(dipdte)-5H<sub>2</sub>O.

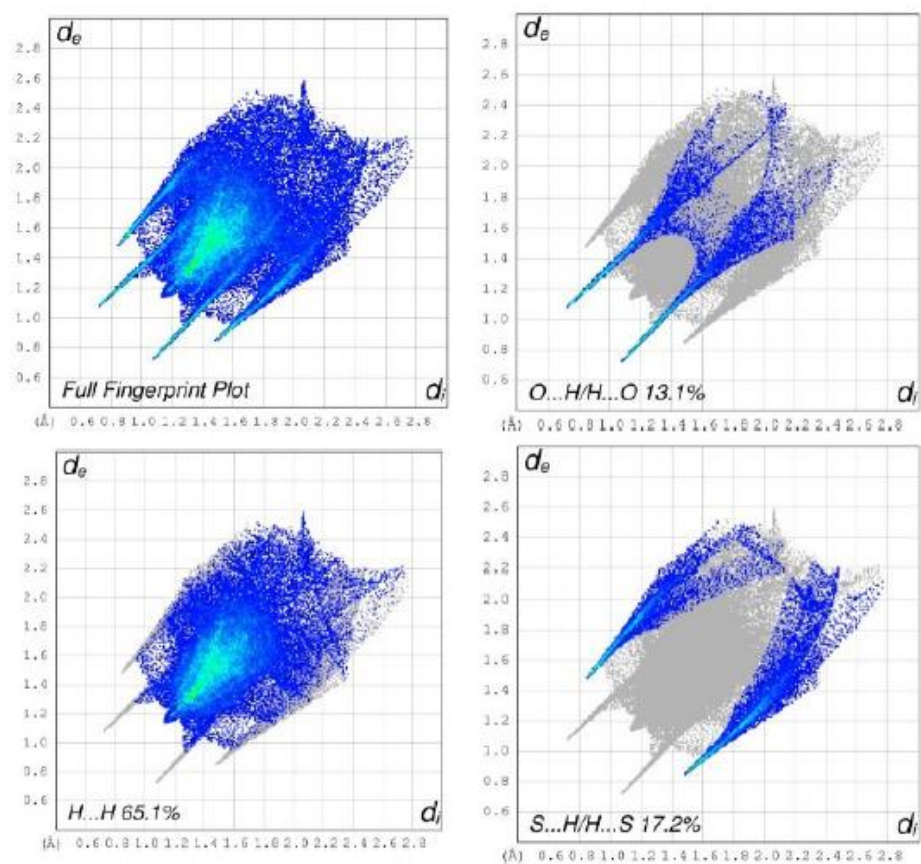


Figure S5: Two-dimensional fingerprint plots for the Hirshfeld surface of  $\text{Na}(\text{dipdte}) \cdot 5\text{H}_2\text{O}$ .



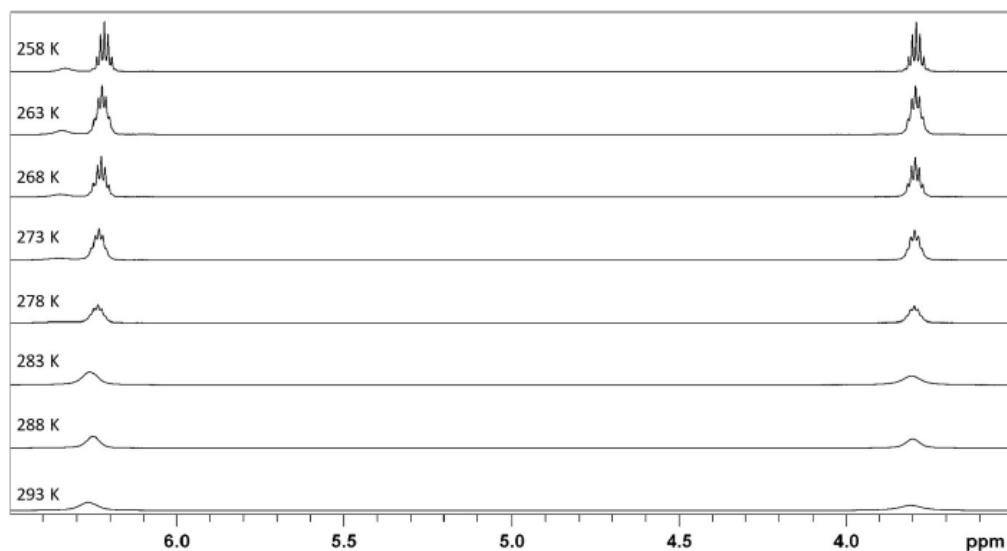


Figure S6: Overlaid variable temperature <sup>1</sup>H NMR spectra acquired at 600 MHz for an acetonitrile-*d*<sub>3</sub> solution of Na(dipdte)-5H<sub>2</sub>O in the region of 6.5 to 3.5 ppm.

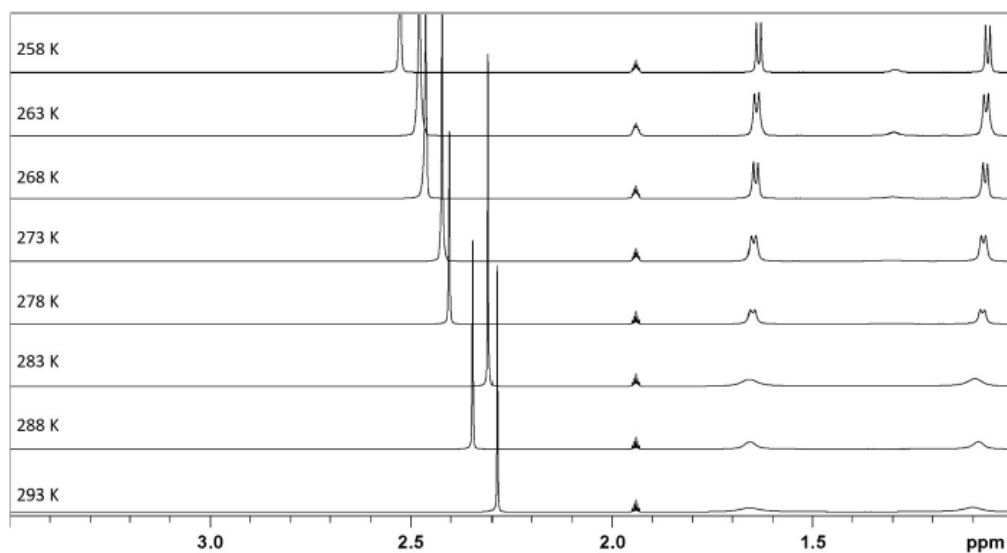


Figure S7: Overlaid variable temperature <sup>1</sup>H NMR spectra acquired at 600 MHz for an acetonitrile-*d*<sub>3</sub> solution of Na(dipdte)-5H<sub>2</sub>O in the region of 3.5 to 1.0 ppm.

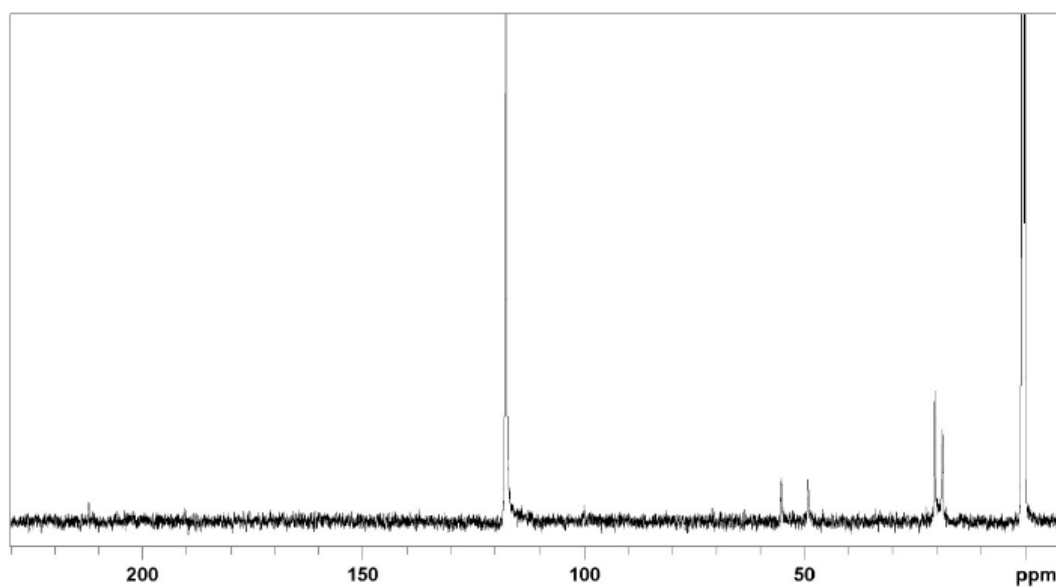


Figure S8: 150 MHz  $^{13}\text{C}$  NMR spectrum of  $\text{Na}(\text{dipdte})\cdot 5\text{H}_2\text{O}$  in acetonitrile- $d_3$  acquired at 293 K.

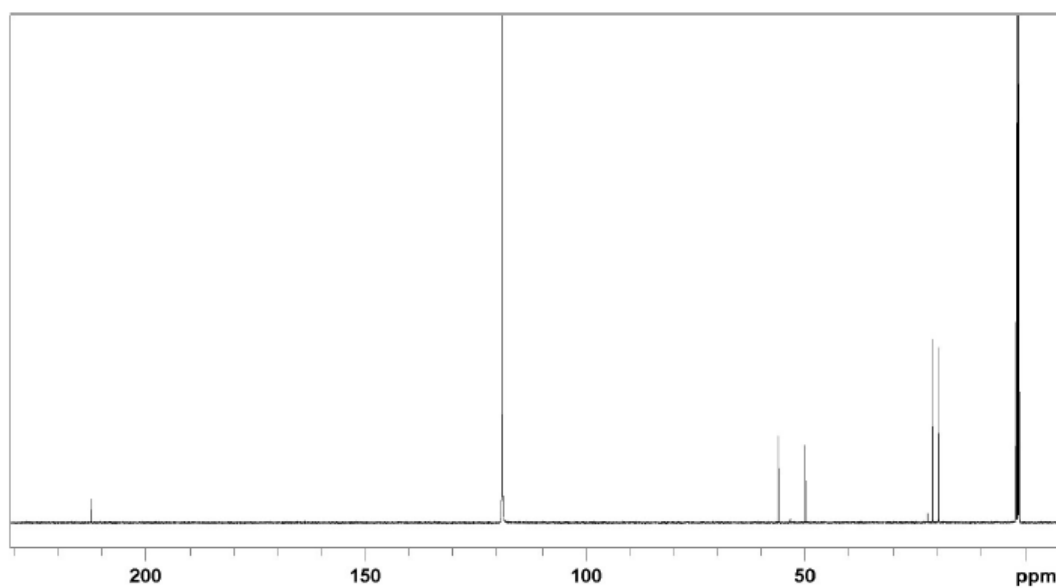


Figure S9: 150 MHz  $^{13}\text{C}$  NMR spectrum of  $\text{Na}(\text{dipdte})\cdot 5\text{H}_2\text{O}$  in acetonitrile- $d_3$  acquired at 258 K.

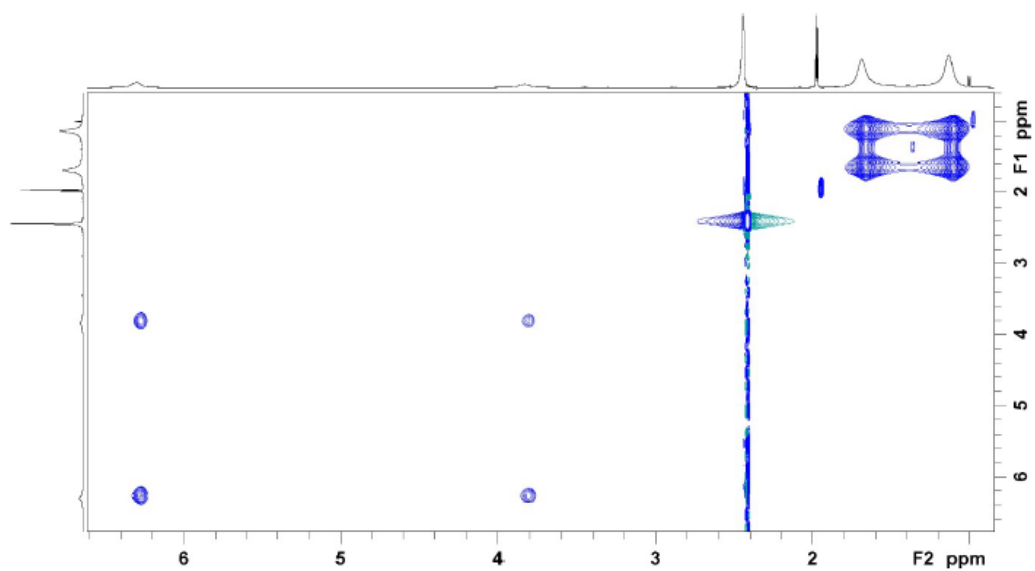


Figure S10: 600 MHz <sup>1</sup>H 2D-NOESY spectrum of Na(dipdte)·5H<sub>2</sub>O in acetonitrile-*d*<sub>3</sub> acquired at 293 K with a mixing time of 100 ms.

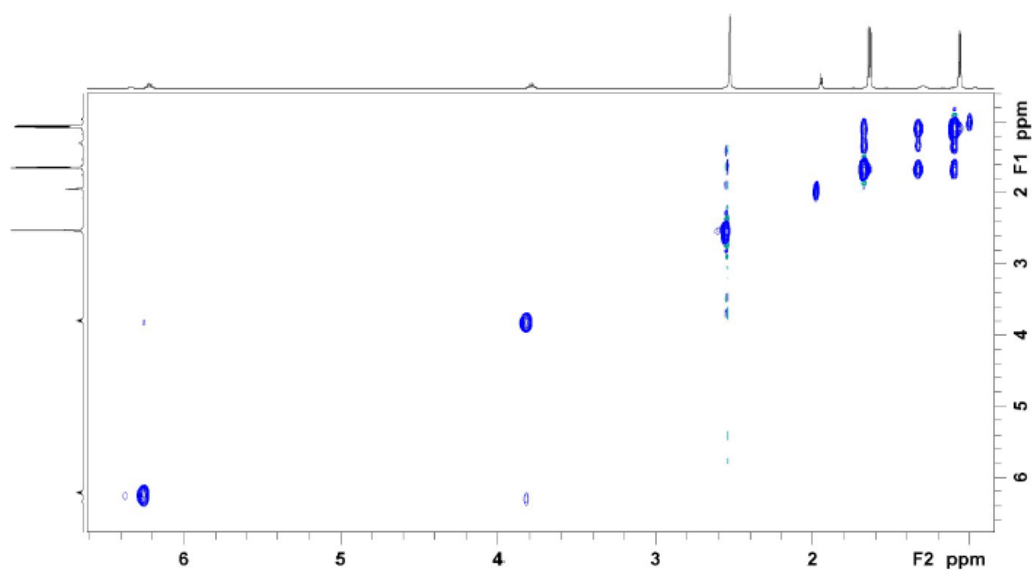


Figure S11: 600 MHz <sup>1</sup>H 2D-NOESY spectrum of Na(dipdte)·5H<sub>2</sub>O in acetonitrile-*d*<sub>3</sub> acquired at 258 K with a mixing time of 100 ms.

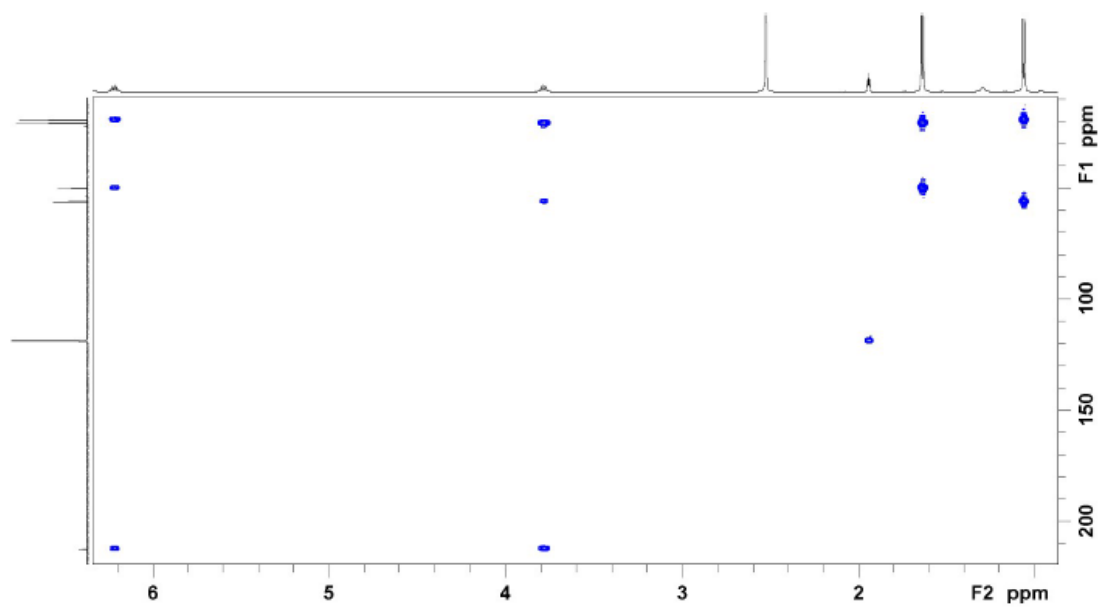


Figure S12: 600 MHz  $^1\text{H}$ - $^{13}\text{C}$  HMBC spectrum of  $\text{Na}(\text{dipdte})\cdot 5\text{H}_2\text{O}$  in acetonitrile- $d_3$  acquired at 258 K.

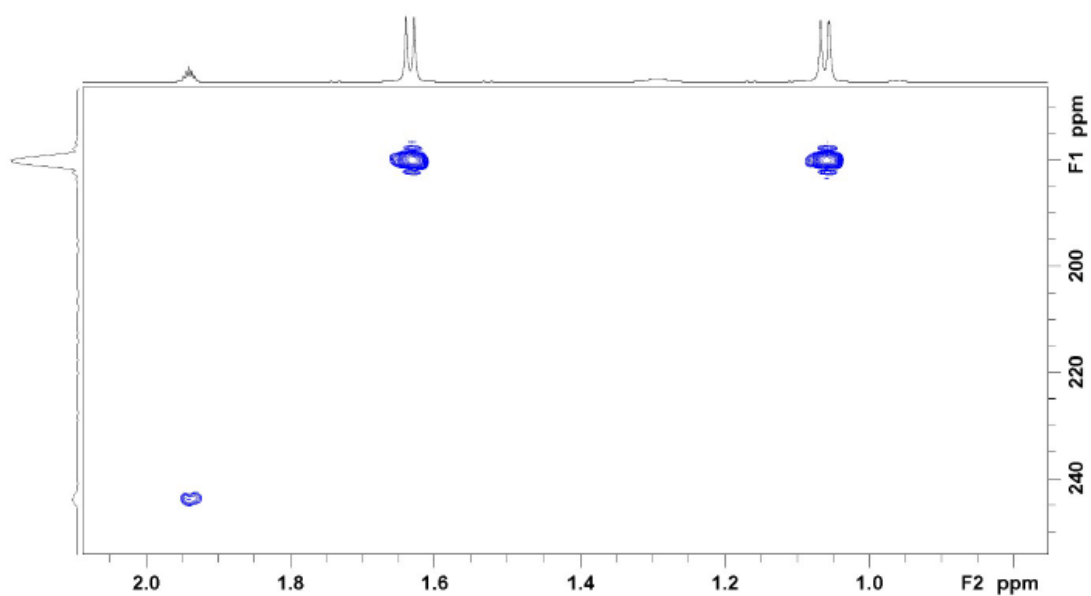


Figure S13. 600 MHz  $^1\text{H}$ - $^{15}\text{N}$  HMBC spectrum of  $\text{Na}(\text{dipdte})\cdot 5\text{H}_2\text{O}$  in acetonitrile- $d_3$  acquired at 258 K.

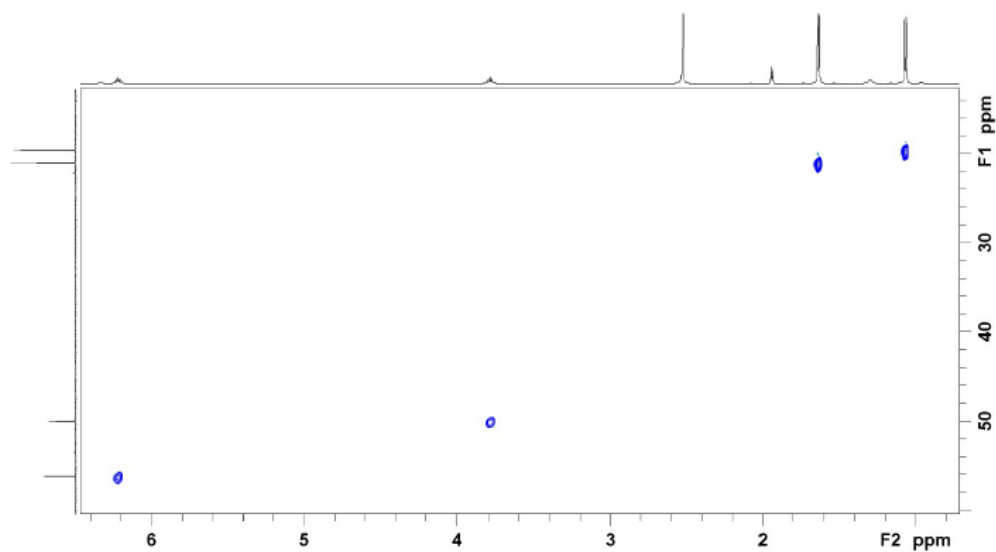


Figure S14: 600 MHz  $^{13}\text{C}/^1\text{H}$  HSQC spectrum of  $\text{Na}(\text{dipdte})\cdot 5\text{H}_2\text{O}$  in acetonitrile- $d_3$  acquired at 258 K.

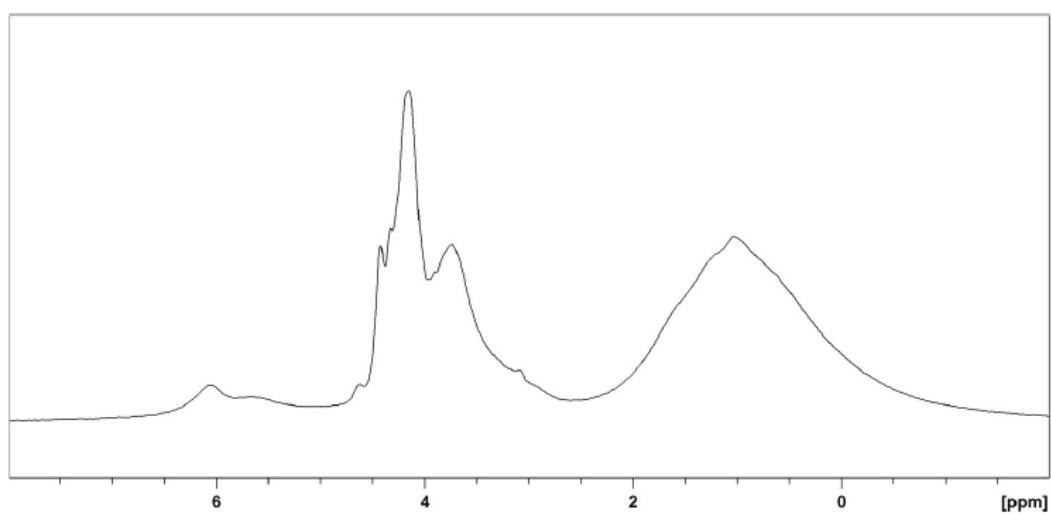


Figure S15: 700 MHz solid state  $^1\text{H}$  NMR spectrum of  $\text{Na}(\text{dipdte})\cdot 5\text{H}_2\text{O}$  acquired at 60 KHz MAS.



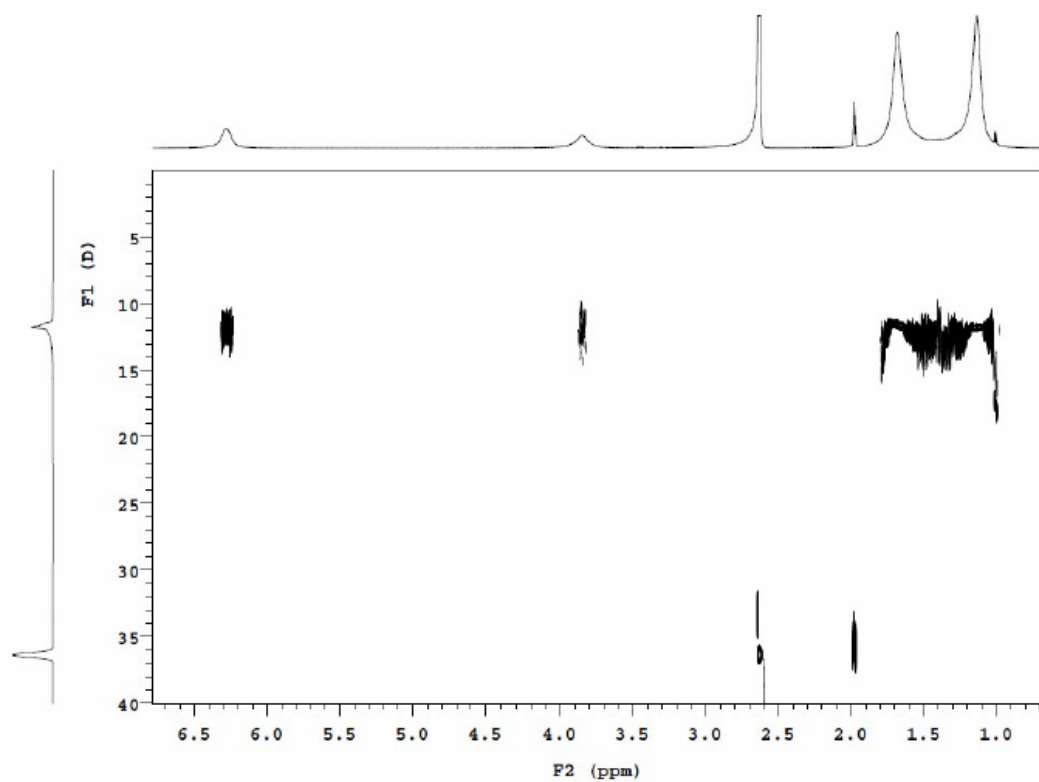
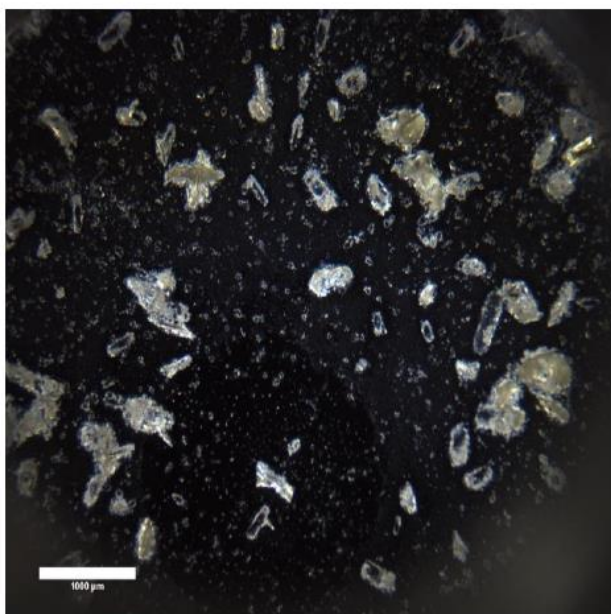


Figure S16: 500 MHz 2D-DOSY spectrum of Na(dipdte)·5H<sub>2</sub>O in acetonitrile-*d*<sub>3</sub> at 293 K.

## Supporting Information

### An unusual mercury(II) di-isopropyldithiocarbamate coordination polymer

Alexander Angeloski, Aditya Rawal, Mohan Bhadbhade, James M. Hook, Robert W. Schurko and Andrew M. McDonagh



**Figure S1:** Photomicrograph showing crystal destruction following complete evaporation of mother liquor.

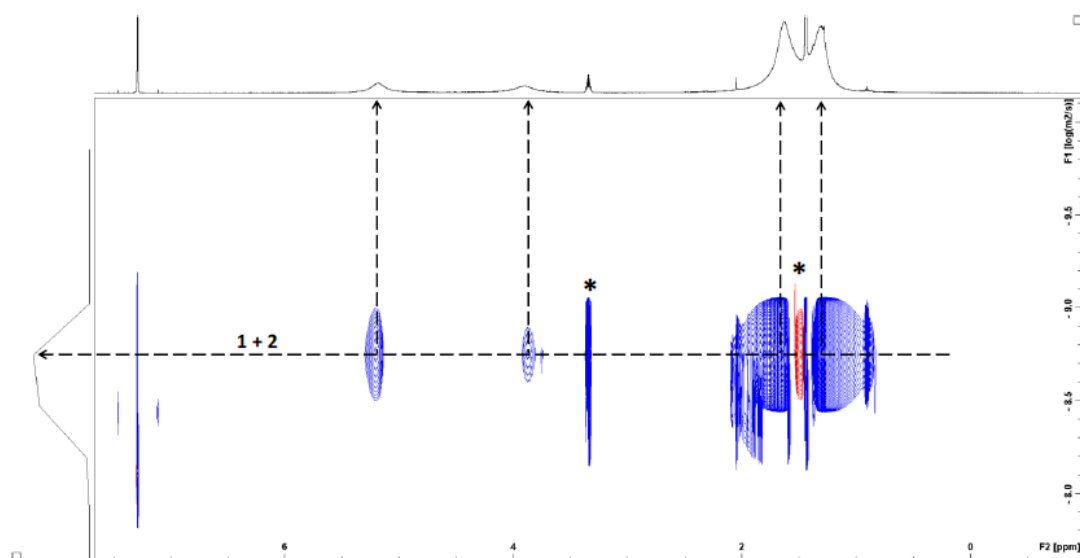


**Figure S2:** 600 MHz 2D-DOSY spectrum of a mixture of **1** and **2** in chloroform-d at 298 K. Residual di-isopropylamine formed by decomposition of **1** and **2** in chloroform (due to traces of HCl) indicated by an asterisk.

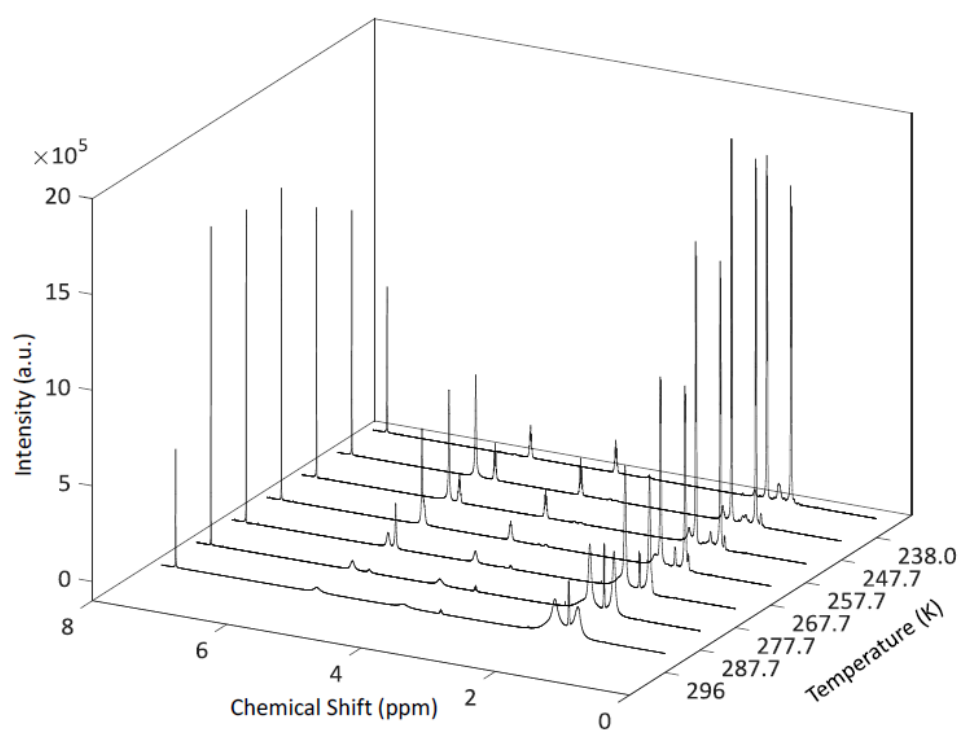


**Figure S3:** Variable temperature 600 MHz  $^1\text{H}$  NMR of a mixture of **1** and **2** in  $\text{CDCl}_3$  between 296 to 238 K.

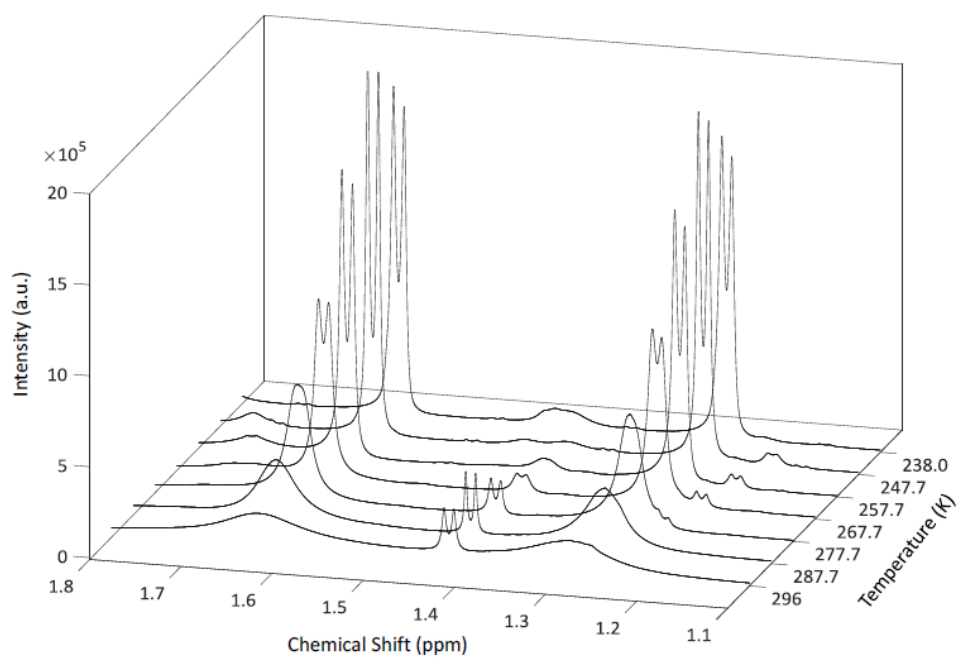


Figure S4: Magnified region of Figure S3 showing sharpening of methyl proton signals between 296 to 238 K.

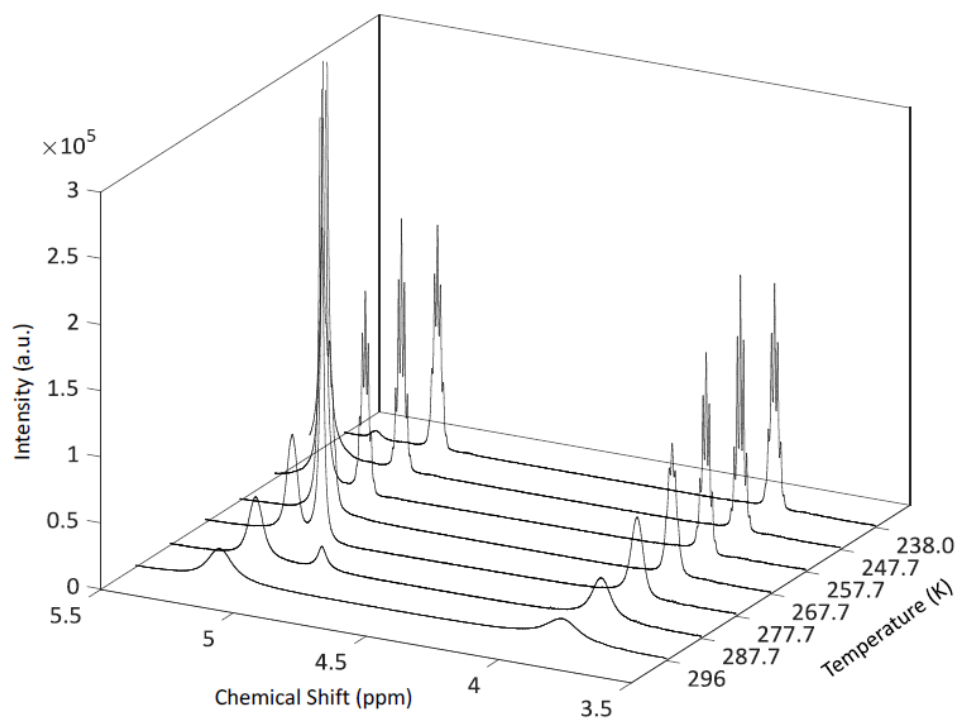
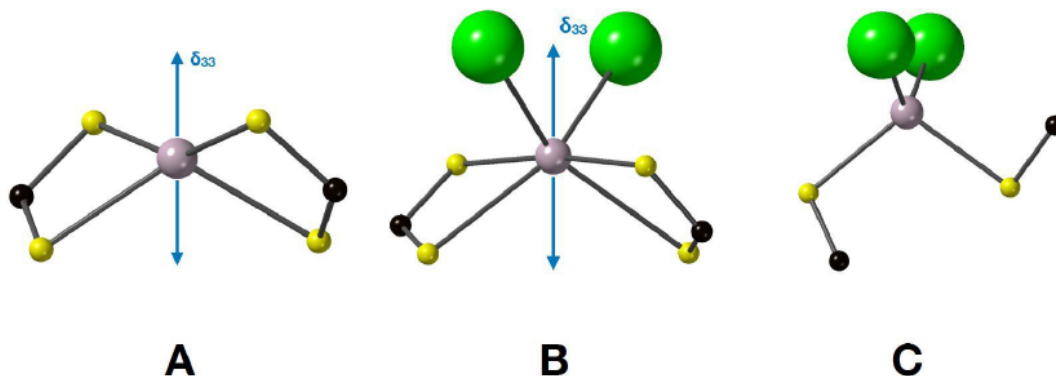
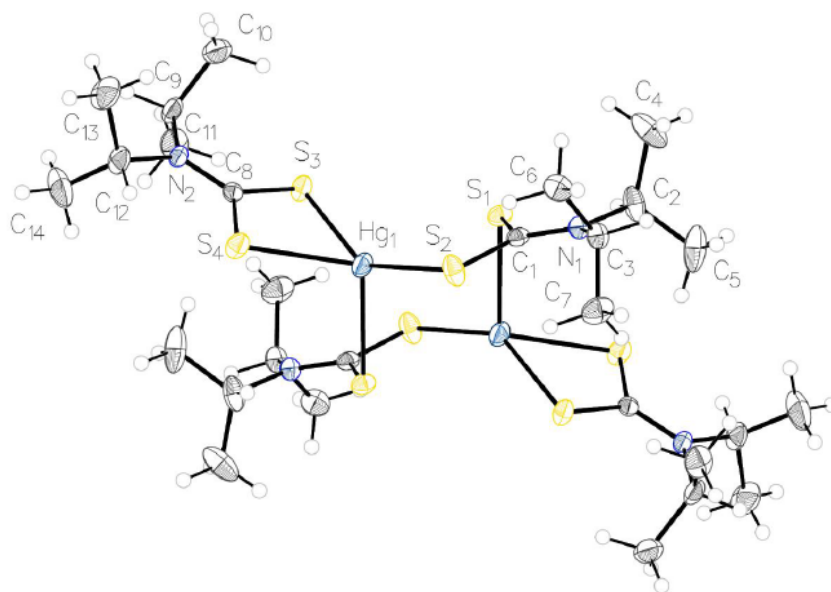


Figure S5: Magnified region of Figure S3 showing sharpening of methine proton signals between 296 to 238 K.



**Figure S6:** Local Hg environments in **1** (A: Site Hg) and **2** (B: Hg site A, C: Hg site B). Proposed  $^{199}\text{Hg}$  chemical shift tensor orientations for  $\delta_{33}$  are shown for the HgS4 sites in **1** and **2**. The chemical shift tensor orientation for Hg2 in **2** is not straightforward to assign without the aid of first principles calculations.



**Figure S7:** Molecular structure of **1A** showing atom labelling scheme. Thermal ellipsoids are drawn at the 50% probability level.

While attempting to isolate single crystals of **1** and **2** for solid state NMR experiments, a previously described dimeric disappearing isomer of **1** (**1A**) was isolated.<sup>1</sup> Complex **1A** (Figure S7) contains two chelating and two bridging dithiocarbamate ligands. The central eight membered  $[\text{Hg-S-C-S}]_2$  ring adopts a chair configuration, with all four Hg-S bond lengths being inequivalent and ranging from 2.4453 (6) Å between Hg1-S2 to 2.6604 (6) Å between Hg1-S4. The co-ordination geometry



about Hg is strongly distorted tetrahedral due to the restricted bite distance associated with the chelating ligand and the close approach of S1.<sup>2</sup> The chelating ligand is planar with a maximum deviation from the least squares plane C9-C12-S4-S3 (With a r.m.s. of 0.004 Å) of 0.005 Å, in contrast to the bridging ligand which has a maximum deviation of 0.08 Å from the C2-C3-S2-S1 least squares plane. This difference in planarity is shown as an 8° torsion angle (twist of the C-N) about S2-C1-N1-C3 in the bridging ligand. The structure possess a range of intramolecular C-H...S intramolecular interactions with distances of ~ 2.6 Å between methyl protons H10C and H11A to chelating S3, and H6C to bridging S2. There is also an intramolecular hydrogen bond between H12 and S4 of approximately 2.4 Å, which is not evident in the bridging position (Between H2 and S1) due to the twisted C=N bond producing a lack of coplanarity between S1 and H2. These interactions and their distances are in excellent agreement with other di-isopropylthiocarbamate structures.<sup>3-5</sup> The crystal packing is unremarkable and can be loosely approximated as layered, and stacked along the *c* direction by intermolecular C-H...S bonds of ~ 2.9 Å between H11C-S2 and H11B-S4.

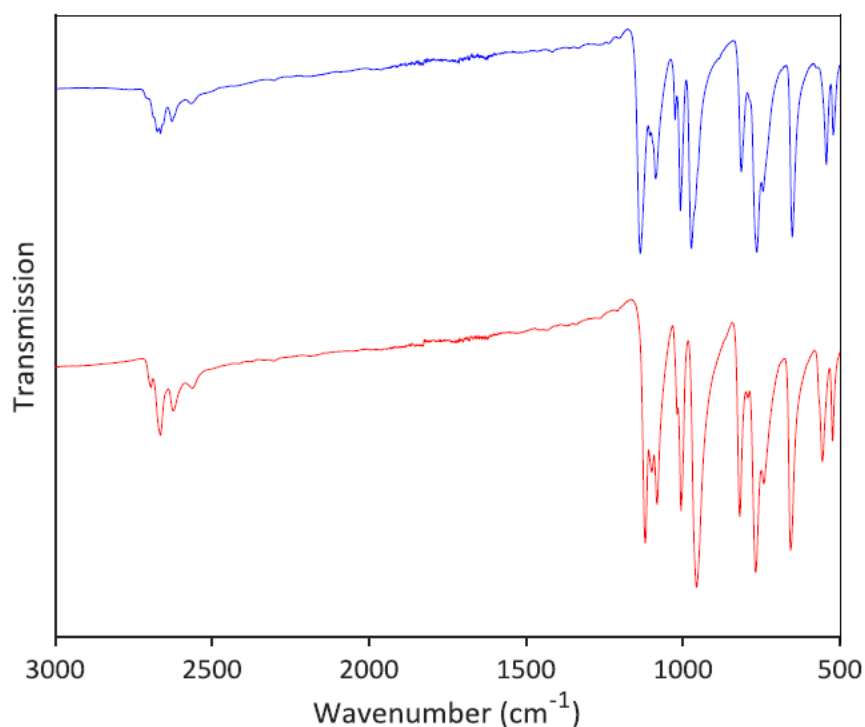


Figure S8: FTIR spectra of 1 (bottom, red) and 2 (top, blue).

Table S1: Crystal data and structure refinement parameters for **1**.

Chemical formula	C <sub>14</sub> H <sub>28</sub> HgN <sub>2</sub> S <sub>4</sub> ( <b>1</b> )
M <sub>r</sub>	553.21
Crystal system, space group	Monoclinic, C2/c
Temperature (K)	155
a, b, c (Å)	19.3948(18), 7.9304(7), 14.6804(14)
β (°)	119.428(6)
V (Å <sup>3</sup> )	1966.6(3)
D <sub>x</sub> (Mg m <sup>-3</sup> )	1.868
Z	4
Radiation type	MoKα (λ = 0.71073)
μ (mm <sup>-1</sup> )	8.25
Crystal size (mm)	0.187 × 0.138 × 0.116
Absorption correction	SADABS-2014/5 was used for absorption correction. wR <sub>2</sub> (int) was 0.0912 before and 0.0546 after correction. The Ratio of minimum to maximum transmission is 0.6820. The λ/2 correction factor is 0.00150.
T <sub>min</sub> , T <sub>max</sub>	0.508, 0.746
No. of measured, independent and observed [I > 2σ(I)] reflections	22426, 2139, 2000
R <sub>int</sub>	0.044
(sin θ/λ) <sub>max</sub> (Å <sup>-1</sup> )	0.638
R[F <sup>2</sup> > 2σ(F <sup>2</sup> )], wR(F <sup>2</sup> ), S	0.017, 0.038, 0.59
No. of reflections	2139
No. of parameters	95
H-atom treatment	Constrained
Δρ <sub>max</sub> , Δρ <sub>min</sub> (e Å <sup>-3</sup> )	1.37, -1.26

Table S2: Crystal data and structure refinement parameters for **2**.

Chemical formula	0.25(C <sub>28</sub> H <sub>56</sub> Cl <sub>4</sub> Hg <sub>4</sub> N <sub>4</sub> S <sub>8</sub> )-0.25(C <sub>4</sub> H <sub>6</sub> O) ( <b>2</b> )
M <sub>r</sub>	429.87
Crystal system, space group	Monoclinic, P2 <sub>1</sub> /c
Temperature (K)	150
a, b, c (Å)	10.1380 (7), 18.6015 (12), 14.5723 (10)
β (°)	102.732(2)
V (Å <sup>3</sup> )	2680.5(3)
D <sub>x</sub> (Mg m <sup>-3</sup> )	2.130
Z	8
Radiation type	MoKα (λ = 0.71073)
μ (mm <sup>-1</sup> )	11.96
Crystal size (mm)	0.103 × 0.047 × 0.022
Absorption correction	SADABS-2016/2 was used for absorption correction. wR <sub>2</sub> (int) was 0.1068 before and 0.0587 after correction. The Ratio of minimum to maximum transmission is 0.7061.
T <sub>min</sub> , T <sub>max</sub>	0.526, 0.746
No. of measured, independent and observed [I > 2σ(I)] reflections	54504, 5904, 4684
R <sub>int</sub>	0.065
(sin θ/λ) <sub>max</sub> (Å <sup>-1</sup> )	0.641
R[F <sup>2</sup> > 2σ(F <sup>2</sup> )], wR(F <sup>2</sup> ), S	0.030, 0.054, 1.05
No. of reflections	5904
No. of parameters	259
H-atom treatment	Constrained
Δρ <sub>max</sub> , Δρ <sub>min</sub> (e Å <sup>-3</sup> )	1.53, -1.20

**Table S3:** Crystal data and structure refinement parameters for **1A** (a disappearing polymorph of **1**).

Chemical formula	C <sub>14</sub> H <sub>28</sub> HgN <sub>2</sub> S <sub>4</sub>
M <sub>r</sub>	553.21
Crystal system, space group	Monoclinic, P2 <sub>1</sub> /n
Temperature (K)	151
a, b, c (Å)	11.3767 (7), 11.1786 (6), 16.6172 (10)
β (°)	108.630(3)
V (Å <sup>3</sup> )	2002.6(15)
D <sub>x</sub> (Mg m <sup>-3</sup> )	1.835
Z	4
Radiation type	MoKα (λ = 0.71073)
μ (mm <sup>-1</sup> )	8.10
Crystal size (mm)	0.143, 0.069, 0.035
Absorption correction	SADABS-2014/5 was used for absorption correction. wR <sub>2</sub> (int) was 0.1009 before and 0.0457 after correction. The Ratio of minimum to maximum transmission is 0.7948. The λ/2 correction factor is 0.00150.
T <sub>min</sub> , T <sub>max</sub>	0.593, 0.746
No. of measured, independent and observed [I > 2σ(I)] reflections	23195, 4408, 3827
R <sub>int</sub>	0.035
(sin θ/λ) <sub>max</sub> (Å <sup>-1</sup> )	0.641
R[F <sup>2</sup> > 2σ(F <sup>2</sup> ), wR(F <sup>2</sup> ), S	0.022, 0.043, 1.08
No. of reflections	4408
No. of parameters	192
H-atom treatment	Constrained
Δρ <sub>max</sub> , Δρ <sub>min</sub> (e Å <sup>-3</sup> )	1.72, -1.21

**Table S4:** Crystallographic bond lengths and angles for **1**.

Hg1—S1 <sup>1</sup>	2.6529 (6)	N1—C1	1.326 (3)
Hg1—S1	2.6529 (6)	N1—C2	1.493 (3)
Hg1—S2 <sup>1</sup>	2.4429 (6)	N1—C5	1.496 (3)
Hg1—S2	2.4429 (6)	C5—C7	1.527 (4)
S1—C1	1.724 (2)	C5—C6	1.521 (3)
S2—C1	1.743 (2)	C2—C4	1.519 (4)
C2—C3	1.517 (3)	S1 <sup>1</sup> —Hg1—S1	116.09 (3)
S2—Hg1—S1	70.61 (2)	S2 <sup>1</sup> —Hg1—S1 <sup>1</sup>	70.61 (2)
S2 <sup>1</sup> —Hg1—S1	126.02 (2)	S2—Hg1—S1 <sup>1</sup>	126.01 (2)
S2 <sup>1</sup> —Hg1—S2	152.01 (3)	C1—S1—Hg1	83.23 (8)
C1—S2—Hg1	89.52 (8)	C5—N1—C2	114.90 (18)
C1—N1—C5	124.8 (2)	C1—N1—C2	120.3 (2)
N1—C5—C7	113.2 (2)	N1—C5—C6	112.3 (2)
C6—C5—C7	113.9 (2)	S1—C1—S2	116.61 (13)
N1—C1—S1	122.65 (18)	N1—C1—S2	120.73 (18)
N1—C2—C4	111.1 (2)	N1—C2—C3	111.0 (2)
C3—C2—C4	113.1 (2)	Hg1—S1—C1—S2	1.63 (12)
Hg1—S1—C1—N1	-178.4 (2)	Hg1—S2—C1—S1	-1.76 (13)
Hg1—S2—C1—N1	178.29 (19)	C5—N1—C1—S1	-178.41 (17)
C5—N1—C1—S2	1.5 (3)	C5—N1—C2—C4	-61.2 (3)
C5—N1—C2—C3	65.6 (3)	C1—N1—C5—C7	-64.7 (3)
C1—N1—C5—C6	66.0 (3)	C1—N1—C2—C4	118.4 (2)
C1—N1—C2—C3	-114.9 (2)	C2—N1—C5—C7	114.9 (2)
C2—N1—C5—C6	-114.4 (2)	C2—N1—C1—S1	2.1 (3)
C2—N1—C1—S2	-177.98(17)		

Symmetry codes: (1) 1-X, +Y, 1/2-Z.



Table S5: Crystallographic bond lengths and angles for 2.

Hg1—S4	2.3772 (14)	N1—C5	1.516 (8)
Hg1—S1	2.3686 (14)	C9—C11	1.519 (7)
Hg2—S3 <sup>1</sup>	2.5690 (14)	C9—C10	1.519 (8)
Hg2—C11	2.4526 (14)	C12—C14	1.511 (8)
Hg2—S2	2.5347 (14)	C12—C13	1.521 (8)
Hg2—C12	2.4860 (15)	C2—C3	1.501 (10)
S3—C8	1.743 (6)	C2—C4	1.520 (10)
S4—C8	1.749 (5)	C5—C6	1.493 (11)
S2—C1	1.739 (6)	C5—C7	1.504 (10)
S1—C1	1.751 (6)	O1—C2A	1.384 (14)
N2—C9	1.494 (7)	O1—C2A <sup>2</sup>	1.384 (14)
N2—C12	1.510 (7)	O1—C1A <sup>2</sup>	1.488 (15)
N2—C8	1.325 (6)	O1—C1A	1.488 (15)
N1—C1	1.307 (7)	C3A—C2A	1.501 (17)
N1—C2	1.497 (8)	C3A—C1A	1.408 (17)
S1—Hg1—S4	171.65 (5)	N1—C1—S2	122.9 (5)
C11—Hg2—S3 <sup>1</sup>	107.89 (5)	N1—C1—S1	118.2 (4)
C11—Hg2—S2	110.09 (5)	N2—C12—C14	109.1 (4)
C11—Hg2—C12	116.05 (5)	N2—C12—C13	111.9 (5)
S2—Hg2—S3 <sup>1</sup>	106.06 (4)	C14—C12—C13	113.1 (5)
C12—Hg2—S3 <sup>1</sup>	108.08 (5)	N1—C2—C3	113.3 (6)
C12—Hg2—S2	108.21 (5)	N1—C2—C4	115.1 (6)
C8—S3—Hg2 <sup>2</sup>	95.65 (17)	C3—C2—C4	113.3 (6)
C8—S4—Hg1	98.67 (18)	S3—C8—S4	118.1 (3)
C1—S2—Hg2	97.57 (18)	N2—C8—S3	121.8 (4)
C1—S1—Hg1	100.16 (19)	N2—C8—S4	120.0 (4)
C9—N2—C12	115.6 (4)	C6—C5—N1	109.9 (6)
C8—N2—C9	124.5 (5)	C6—C5—C7	116.2 (7)
C8—N2—C12	119.9 (5)	C7—C5—N1	109.8 (6)
C1—N1—C2	124.7 (5)	C2A—O1—C2A <sup>3</sup>	180.0
C1—N1—C5	121.4 (5)	C2A—O1—C1A <sup>3</sup>	109.6 (9)
C2—N1—C5	113.9 (5)	C2A <sup>3</sup> —O1—C1A <sup>3</sup>	70.4 (9)
N2—C9—C11	114.1 (5)	C1A <sup>3</sup> —O1—C1A	180.0
N2—C9—C10	112.4 (5)	O1—C2A—C3A	109.7 (11)
C10—C9—C11	113.8 (5)	C3A—C1A—O1	109.1 (11)
S2—C1—S1	118.8 (3)		

Symmetry codes: (1) +X, 1/2 - Y, -1/2 + Z (2) +X, 1/2 - Y, 1/2 + Z (3) 2-X, -Y, 1-Z

**Table S6:** Crystallographic bond lengths and angles for 1A.

Hg1—S1 <sup>1</sup>	2.6227 (7)	N1—C1	1.321 (3)
Hg1—S3	2.5053 (7)	N1—C3	1.499 (3)
Hg1—S4	2.6607 (7)	N1—C2	1.481 (4)
Hg1—S2	2.4454 (7)	C12—C13	1.508 (4)
S1—C1	1.741 (3)	C12—C14	1.512 (5)
S3—C8	1.735 (3)	C9—C10	1.510 (4)
S4—C8	1.721 (3)	C9—C11	1.515 (4)
S2—C1	1.724 (3)	C6—C3	1.517 (4)
N2—C8	1.330 (3)	C3—C7	1.516 (4)
N2—C12	1.488 (4)	C2—C5	1.511 (5)
N2—C9	1.490 (4)	C2—C4	1.515 (5)
S1 <sup>1</sup> —Hg1—S4	105.80 (2)	N2—C8—S3	121.8 (2)
S3—Hg1—S1 <sup>1</sup>	109.27 (2)	N2—C8—S4	121.2 (2)
S3—Hg1—S4	69.49 (2)	N2—C12—C13	111.0 (3)
S2—Hg1—S1 <sup>1</sup>	103.04 (3)	N2—C12—C14	111.3 (3)
S2—Hg1—S3	143.14 (3)	C14—C12—C13	113.2 (3)
S2—Hg1—S4	118.15 (3)	S2—C1—S1	118.44 (16)
C1—S1—Hg1 <sup>1</sup>	98.53 (9)	N1—C1—S1	121.1 (2)
C8—S3—Hg1	89.01 (9)	N1—C1—S2	120.4 (2)
C8—S4—Hg1	84.33 (9)	N2—C9—C10	112.6 (2)
C1—S2—Hg1	99.83 (9)	N2—C9—C11	113.0 (2)
C8—N2—C12	121.0 (2)	C10—C9—C11	114.4 (3)
C8—N2—C9	124.2 (2)	N1—C3—C6	113.2 (2)
C12—N2—C9	114.8 (2)	N1—C3—C7	112.6 (2)
C1—N1—C3	124.5 (2)	C7—C3—C6	113.8 (3)
C1—N1—C2	121.0 (2)	N1—C2—C5	112.1 (3)
C2—N1—C3	114.4 (2)	N1—C2—C4	110.0 (3)
S4—C8—S3	116.99 (15)	C5—C2—C4	113.6 (3)

Symmetry codes: (1) 1-X, 1-Y, 1-Z.

## References

1. O. V. Loseva, T. A. Rodina, A. I. Smolentsev and A. V. Ivanov, *Polyhedron*, 2017, **134**, 238-245.
2. R. E. Benson, C. A. Ellis, C. E. Lewis and E. R. T. Tiekink, *CrystEngComm*, 2007, **9**, 930-940.
3. A. Angeloski, A. R. Gentle, J. A. Scott, M. B. Cortie, J. M. Hook, M. T. Westerhausen, M. Bhadbhade, A. T. Baker and A. M. McDonagh, *Inorg. Chem.*, 2018, **57**, 2132-2140.
4. A. Angeloski, A. T. Baker, M. Bhadbhade and A. M. McDonagh, *J. Mol. Struct.*, 2016, **1113**, 127-132.
5. A. Angeloski, J. M. Hook, M. Bhadbhade, A. T. Baker and A. M. McDonagh, *CrystEngComm*, 2016, **18**, 7070-7077.

## References:

1. H. Debus, *Justus Liebigs Annalen der Chemie*, 1850, **73**, 26-34.
2. A.K. Eaton, Patent US24695A, 1859.
3. M. Delepine, *Comptes rendus de l'Academie des Sciences*, 1907, **144**, 1125-1127.
4. H. F. Dietz and H. G. Guy, *Journal of Economic Entomology*, 1939, **32**, 248-252.
5. J. W. Roberts, *Botanical Review*, 1946, **12**, 538-547.
6. G. E. Harrington, *Science*, 1941, **93**, 311-311.
7. R. D. McMullen, *Nature*, 1959, **184**, 1338-1338.
8. B. B. Till and L. G. Fish, *Plant Pathology*, 1964, **13**, 10-14.
9. L.D. Goodhue, Patent US2862850, 1958.
10. W.F. Hester, Patent US2317765, 1943.
11. P. Padungros and A. Wei, *Synthetic Communications*, 2014, **44**, 2336-2343.
12. L. A. Shinobo, S. G. Jones and M. M. Jones, *Acta Pharmacologica et Toxicologica*, 1984, **54**, 189-194.
13. P. Giboreau and C. Morin, *Journal of Organic Chemistry*, 1994, **59**, 1205-1207.
14. A. Hulanicki, *Talanta*, 1967, **14**, 1371-1392.
15. E. R. Tiekink, *CrystEngComm*, 2003, **5**, 101-113.
16. R. A. Howie, E. R. T. Tiekink, J. L. Wardell and S. M. S. V. Wardell, *Journal of Chemical Crystallography*, 2008, **39**, 293-298.
17. M. J. Cox and E. R. T. Tiekink, *Reviews in Inorganic Chemistry*, 1997, **17**, 1-24.
18. A. Angeloski, A. Rawal, M. Bhadbhade, J. M. Hook, R. W. Schurko and A. M. McDonagh, *Crystal Growth and Design*, 2019, **19**, 1125-1133.
19. A. Angeloski, A. R. Gentle, J. A. Scott, M. B. Cortie, J. M. Hook, M. T. Westerhausen, M. Bhadbhade, A. T. Baker and A. M. McDonagh, *Inorganic Chemistry*, 2018, **57**, 2132-2140.
20. E. R. T. Tiekink, *Applied Organometallic Chemistry*, 2008, **22**, 533-550.
21. A. A. Aly, A. B. Brown, T. M. I. Bedair and E. A. Ishak, *Journal of Sulfur Chemistry*, 2012, **33**, 605-617.
22. Y. K. T. Yoshimura, *Antioxidants and Redox Signalling*, 2004, **6**, 639-647.
23. J. J. Steggerda, J. A. Cras and J. Willemse, *Recueil des Travaux Chimiques des Pays-Bas*, 1981, **100**, 41-48.
24. D. C. Onwudiwe, C. A. Strydom, O. S. Oluwafemi, E. Hosten and A. Jordaan, *Dalton Transactions*, 2014, **43**, 8703-8712.
25. M. Lazell, S. K. Norager, P. O'Brien and N. Revaprasadu, *Materials Science and Engineering: C*, 2001, **16**, 129-133.
26. T. Mthethwa, V. S. R. R. Pullabhotla, P. S. Mdluli, J. W. Smith and N. Revaprasadu, *Polyhedron*, 2009, **28**, 2977-2982.
27. D. C. Onwudiwe, P. A. Ajibade and B. Omondi, *Journal of Molecular Structure*, 2011, **987**, 58-66.
28. G. Hogarth, in *Progress in Inorganic Chemistry*, John Wiley & Sons, Inc., 2005, pp. 71-561.
29. J. Cookson and P. D. Beer, *Dalton Transactions*, 2007, 1459-1472.
30. R. E. Benson, C. A. Ellis, C. E. Lewis and E. R. T. Tiekink, *CrystEngComm*, 2007, **9**, 930-940.
31. W. W. H. Wong, D. E. Phipps and P. D. Beer, *Polyhedron*, 2004, **23**, 2821-2829.
32. R. Prasad, R. Yadav, M. Trivedi, G. Kociok-Köhn and A. Kumar, *Journal of Molecular Structure*, 2016, **1103**, 265-270.
33. M. N. Kouodom, G. Boscutti, M. Celegato, M. Crisma, S. Sitran, D. Aldinucci, F. Formaggio, L. Ronconi and D. Fregona, *Journal of Inorganic Biochemistry*, 2012, **117**, 248-260.

34. R. F. Borch, J. C. Katz, P. H. Lieder and M. E. Pleasants, *Proceedings of the National Academy of Sciences of the United States of America*, 1980, **77**, 5441-5444.
35. K. Saito and M. Kohno, *Analytical Biochemistry*, 2006, **349**, 16-24.
36. G. S. Sivagurunathan, K. Ramalingam and C. Rizzoli, *Polyhedron*, 2013, **65**, 316-321.
37. R. A. Howie, E. R. T. Tiekink, J. L. Wardell and S. M. S. V. Wardell, *Journal of Chemical Crystallography*, 2009, **39**, 293-298.
38. Y. Liu and E. R. T. Tiekink, *CrystEngComm*, 2005, **7**, 20-27.
39. A. Roffey, N. Hollingsworth, H. U. Islam, M. Mercy, G. Sankar, C. R. Catlow, G. Hogarth and N. H. de Leeuw, *Nanoscale*, 2016, **8**, 11067-11075.
40. P. A. Ajibade, J. Z. Mbese and B. Omondi, *Inorganic and Nano-Metal Chemistry*, 2016, **47**, 202-212.
41. B. A. Prakasam, M. Lahtinen, A. Peuronen, M. Muruganandham, E. Kolehmainen, E. Haapaniemi and M. Sillanpää, *Inorganica Chimica Acta*, 2015, **425**, 239-246.
42. G. Gomathi, S. H. Dar, S. Thirumaran, S. Ciattini and S. Selvanayagam, *Comptes Rendus Chimie*, 2015, **18**, 499-510.
43. T. Chintso and P. A. Ajibade, *Materials Letters*, 2015, **141**, 1-6.
44. E. Sathiyaraj, G. Gurumoorthy and S. Thirumaran, *New Journal of Chemistry*, 2015, **39**, 5336-5349.
45. N. Hollingsworth, A. Roffey, H. U. Islam, M. Mercy, A. Roldan, W. Bras, M. Wolthers, C. R. A. Catlow, G. Sankar, G. Hogarth and N. H. de Leeuw, *Chemistry of Materials*, 2014, **26**, 6281-6292.
46. F. Nemati, A. Ghorbani Gharjeh Ghiyaei, B. Notash, M. H. Shayegan and V. Amani, *Tetrahedron Letters*, 2014, **55**, 3572-3575.
47. M. A. Ehsan, T. A. Peiris, K. G. Wijayantha, M. M. Olmstead, Z. Arifin, M. Mazhar, K. M. Lo and V. McKee, *Dalton Transactions*, 2013, **42**, 10919-10928.
48. K. Ramasamy, V. L. Kuznetsov, K. Gopal, M. A. Malik, J. Raftery, P. P. Edwards and P. O'Brien, *Chemistry of Materials*, 2013, **25**, 266-276.
49. P. Li, H. Li and W. Jie, *Journal of Rare Earths*, 2011, **29**, 317-320.
50. I. Jen-La Plante, T. W. Zeid, P. Yang and T. Mokari, *Journal of Materials Chemistry*, 2010, **20**, 6612-6617.
51. G. An, L. Chenguang, Y. Hou, X. Zhang and Y. Liu, *Materials Letters*, 2008, **62**, 2643-2646.
52. G. Gurumoorthy, S. Thirumaran and S. Ciattini, *Polyhedron*, 2016, **118**, 143-153.
53. J. Cookson and P. D. Beer, *Dalton Transactions*, 2007, 1459-1472.
54. R. S. Mane and C. D. Lockhande, *Materials Chemistry and Physics*, 2000, **65**, 1-31.
55. R. Saran and R. J. Curry, *Nature Photonics*, 2016, **10**, 81-92.
56. G. Konstantatos and E. H. Sargent, *Nature Nanotechnology*, 2010, **5**, 391-400.
57. R. Dalven, *Infrared Physics*, 1969, **9**, 141-184.
58. J. He, M. Luo, L. Hu, Y. Zhou, S. Jiang, H. Song, R. Ye, J. Chen, L. Gao and J. Tang, *Journal of Alloys and Compounds*, 2014, **596**, 73-78.
59. V.I. Klimov, *Nanocrystal Quantum Dots, Second Edition*, CRC Press, 2010.
60. I. Moreels, K. Lambert, D. Smeets, D. De Muynck, T. Nolle, J. C. Martins, F. Vanhaecke, A. Vantomme, C. Delerue, G. Allan and Z. Hens, *ACS Nano*, 2009, **3**, 3023-3030.
61. L. L. Feng, G. Yu, Y. Wu, G.-D. Li, H. Li, Y. Sun, T. Asefa, W. Chen and X. Zou, *Journal of the American Chemical Society*, 2015, **137**, 14023-14026.
62. P. Luo, H. Zhang, L. Liu, Y. Zhang, J. Deng, C. Xu, N. Hu and Y. Wang, *ACS Applied Materials and Interfaces*, 2017, **9**, 2500-2508.
63. W. Zhang, Y. Wang, Z. Wang, Z. Zhong and R. Xu, *Chemical Communications*, 2010, **46**, 7631-7633.
64. L. Zhang, B. Tian, F. Chen and J. Zhang, *International Journal of Hydrogen Energy*, 2012, **37**, 17060-17067.

65. Y. Pan, Y. Chen, X. Li, Y. Liu and C. Liu, *RSC Advances*, 2015, **5**, 104740-104749.
66. X. L. Wu, B. Yang, Z. J. Li, L. C. Lei and X. W. Zhang, *RSC Advances*, 2015, **5**, 32976.
67. C. Kong, S. Min and G. Lu, *ACS Catalysis*, 2014, **4**, 2763-2769.
68. T. Zhu, H. B. Wu, Y. Wang, R. Xu and X. W. D. Lou, *Advanced Energy Materials*, 2012, **2**, 1497-1502.
69. A. Olivas, J. Cruz-Reyes, V. Petranovskii, M. Avalos and S. Fuentes, *Journal of Vacuum Science & Technology A*, 1998, **16**, 3515-3520.
70. J. Yang, X. Duan, Q. Qin and W. Zheng, *Journal of Materials Chemistry A*, 2013, **1**, 7880-7884.
71. H. Pang, C. Wei, X. Li, G. Li, Y. Ma, S. Li, J. Chen and J. Zhang, *Scientific Reports*, 2014, **4**, 3577.
72. Y. Zhang, W. Sun, X. Rui, B. Li, H. T. Tan, G. Guo, S. Madhavi, Y. Zong and Q. Yan, *Small*, 2015, **11**, 3694-3702.
73. W. Zhou, X. Cao, Z. Zeng, W. Shi, Y. Zhu, Q. Yan, H. Liu, J. Wang and H. Zhang, *Energy & Environmental Science*, 2013, **6**, 2216-2221.
74. S. B. Ni, X. L. Yang and T. Li, *Journal of Materials Chemistry*, 2012, **22**, 2395-2397.
75. S. Ji, L. Zhang, L. Yu, X. Xu and J. Liu, *RSC Advances*, 2016, **6**, 101752-101759.
76. S.-C. Han, K.-W. Kim, H.-J. Ahn, J.-H. Ahn and J.-Y. Lee, *Journal of Alloys and Compounds*, 2003, **361**, 247-251.
77. N. H. Idris, M. M. Rahman, S.-L. Chou, J.-Z. Wang, D. Wexler and H.-K. Liu, *Electrochimica Acta*, 2011, **58**, 456-462.
78. Z. Liu, X. Zheng, S.-L. Luo, S.-Q. Xu, N.-Y. Yuan and J.-N. Ding, *Journal of Materials Chemistry A*, 2016, **4**, 13395-13399.
79. N. Mahmood, C. Zhang and Y. Hou, *Small*, 2013, **9**, 1321-1328.
80. K. Aso, A. Hayashi and M. Tatsumisago, *Electrochimica Acta*, 2012, **83**, 448-453.
81. X. Sun, J. Dou, F. Y. Xie, Y. F. Li and M. D. Wei, *Chemical Communications*, 2014, **50**, 9869-9871.
82. J. Yang, C. Bao, K. Zhu, T. Yu, F. Li, J. Liu, Z. Li and Z. Zou, *Chemical Communications*, 2014, **50**, 4824-4826.
83. H. K. Mulmudi, S. K. Batabyal, M. Rao, R. R. Prabhakar, N. Mathews, Y. M. Lam and S. G. Mhaisalkar, *Physical Chemistry Chemical Physics*, 2011, **13**, 19307-19309.
84. X. Wang, B. Batter, Y. Xie, K. Pan, Y. Liao, C. Lv, M. Li, S. Sui and H. Fu, *Journal of Materials Chemistry A*, 2015, **3**, 15905-15912.
85. S. Peng, L. Li, H. Tan, R. Cai, W. Shi, C. Li, S. G. Mhaisalkar, M. Srinivasan, S. Ramakrishna and Q. Yan, *Advanced Functional Materials*, 2014, **24**, 2155-2162.
86. Y. Liao, K. Pan, Q. Pan, G. Wang, W. Zhou and H. Fu, *Nanoscale*, 2015, **7**, 1623-1626.
87. H. Sun, D. Qin, S. Huang, X. Guo, D. Li, Y. Luo and Q. Meng, *Energy & Environmental Science*, 2011, **4**, 2630-2637.
88. C. Gervas, S. Mlowe, M. P. Akerman, I. Ezekiel, T. Moyo and N. Revaprasadu, *Polyhedron*, 2017, **122**, 16-24.
89. C. Buchmaier, M. Glänzer, A. Torvisco, P. Poelt, K. Wewerka, B. Kunert, K. Gatterer, G. Trimmel and T. Rath, *Journal of Materials Science*, 2017, **52**, 10898-10914.
90. G. Kullerud and R. A. Yund, *Journal of Petrology*, 1962, **3**, 126-175.
91. J. C. Barry and S. Ford, *Journal of Materials Science*, 2001, **36**, 3721-3730.
92. K. Ramasamy, M. A. Malik, P. O'Brien, J. Raftery and M. Helliwell, *Chemistry of Materials*, 2010, **22**, 6328-6340.
93. M. V. Swain, *Journal of Materials Science*, 1981, **16**, 151-158.
94. A. Ghezelbash and B. A. Korgel, *Langmuir*, 2005, **21**, 9451-9456.
95. Y. Zhou, D. Yan, H. Xu, J. Feng, X. Jiang, J. Yue, J. Yang and Y. Qian, *Nano Energy*, 2015, **12**, 528-537.
96. Q. Liu, A. Diaz, A. Prosvirin, Z. Luo and J. D. Batteas, *Nanoscale*, 2014, **6**, 8935-8942.



97. L. Shen, J. Wang, G. Xu, H. Li, H. Dou and X. Zhang, *Advanced Energy Materials*, 2015, **5**, 1400977.
98. J. Xiao, L. Wan, S. Yang, F. Xiao and S. Wang, *Nano Letters*, 2014, **14**, 831-838.
99. X. Y. Yu, L. Yu, L. Shen, X. Song, H. Chen and X. W. D. Lou, *Advanced Functional Materials*, 2014, **24**, 7440-7446.
100. H. Li, Y. Shao, Y. Su, Y. Gao and X. Wang, *Chemistry of Materials*, 2016, **28**, 1155-1164.
101. I. Moreels, Y. Justo, B. De Geyter, K. Haestraete, J. C. Martins and Z. Hens, *ACS Nano*, 2011, **5**, 2004-2012.
102. C. Giansante, I. Infante, E. Fabiano, R. Grisorio, G. P. Suranna and G. Gigli, *Journal of the American Chemical Society*, 2015, **137**, 1875-1886.
103. Z. H. Zhang, S. H. Lee, J. J. Vittal and W. S. Chin, *Journal of Physical Chemistry B*, 2006, **110**, 6649-6654.
104. J. Zhang, R. W. Crisp, J. Gao, D. M. Kroupa, M. C. Beard and J. M. Luther, *The Journal of Physical Chemistry Letters*, 2015, **6**, 1830-1833.
105. Z. Quan, C. Li, X. Zhang, J. Yang, P. Yang, C. Zhang and J. Lin, *Crystal Growth and Design*, 2008, **8**, 2384-2392.
106. N. Pradhan, B. Katz and S. Efrima, *The Journal of Physical Chemistry B*, 2003, **107**, 13843-13854.
107. M. Liu, G. Lv, G. Chen, Y. Qin, P. Sun, K. Zhou, X. Xing and C. He, *RSC Advances*, 2016, **6**, 102472-102481.
108. P. Gaikar, S. P. Pawar, R. S. Mane, M. Nuashad and D. Shinde, *RSC Advances*, 2016, **6**, 112589-112593.
109. A. Molla, M. Sahu and S. Hussain, *Scientific Reports*, 2016, **6**, 26034.
110. C. Wei, C. Cheng, J. Zhao, Y. Wang, Y. Cheng, Y. Xu, W. Du and H. Pang, *Chemistry – An Asian Journal*, 2015, **10**, 679-686.
111. S. He, C. Lu, G.-S. Wang, J.-W. Wang, H.-Y. Guo and L. Guo, *ChemPlusChem*, 2014, **79**, 569-576.
112. X. Jiang, Y. Xie, J. Lu, L. Zhu, W. He and Y. Qian, *Advanced Materials*, 2001, **13**, 1278-1281.
113. J. Wang, D. Cao, G. Yang, Y. Yang and H. Wang, *Journal of Solid State Electrochemistry*, 2017, **21**, 3047-3055.
114. N. Alam, M. S. Hill, G. Kociok-Köhn, M. Zeller, M. Mazhar and K. C. Molloy, *Chemistry of Materials*, 2008, **20**, 6157-6162.
115. P. R. Bonneau, R. K. Shibao and R. B. Kaner, *Inorganic Chemistry*, 1990, **29**, 2511-2514.
116. D. Mondal, G. Villemure, G. Li, C. Song, J. Zhang, R. Hui, J. Chen and C. Fairbridge, *Applied Catalysis A*, 2013, **450**, 230-236.
117. R. Boughalmi, R. Rahmani, A. Boukhachem, B. Amrani, K. Driss-Khodja and M. Amlouk, *Materials Chemistry and Physics*, 2015, **163**, 99-106.
118. Y. Fazli, S. Pourmortazavi, I. Kohsari, M. Karimi and M. Tajdari, *Journal of Materials Science - Materials in Electronics*, 2016, **27**, 7192-7199.
119. J. Cheon, D. S. Talaga and J. I. Zink, *Chemistry of Materials*, 1997, **9**, 1208-1212.
120. N. Pradhan, B. Katz and S. Efrima, *Journal of Physical Chemistry B*, 2003, **107**, 13843-13854.
121. L. Barry, J. D. Holmes, D. J. Otway, M. P. Copley, O. Kazakova and M. A. Morris, *Journal of Physics: Condensed Matter*, 2010, **22**, 076001.
122. L. K. Macreadie, H. E. Maynard-Casely, S. R. Batten, D. R. Turner and A. S. R. Chesman, *ChemPlusChem*, 2015, **80**, 107-118.
123. P. D. McNaughten, S. A. Saah, M. Akhtar, K. Abdulwahab, M. A. Malik, J. Raftery, J. A. M. Awudza and P. O'Brien, *Dalton Transactions*, 2016, **45**, 16345-16353.
124. J. M. Clark, G. Kociok-Kohn, N. J. Harnett, M. S. Hill, R. Hill, K. C. Molloy, H. Saponia, D. Stanton and A. Sudlow, *Dalton Transactions*, 2011, **40**, 6893-6900.

125. J. Akhtar, M. Afzaal, M. A. Vincent, N. A. Burton, I. H. Hillier and P. O'Brien, *Chemical Communications*, 2011, **47**, 1991-1993.
126. T. Trindade, P. O'Brien, X.-m. Zhang and M. Motevalli, *Journal of Materials Chemistry*, 1997, **7**, 1011-1016.
127. S.-M. Lee, Y.-w. Jun, S.-N. Cho and J. Cheon, *Journal of the American Chemical Society*, 2002, **124**, 11244-11245.
128. P. O'Brien, J. H. Park and J. Waters, *Thin Solid Films*, 2003, **431-432**, 502-505.
129. A. Roffey, N. Hollingsworth, H. U. Islam, M. Mercy, G. Sankar, C. R. Catlow, G. Hogarth and N. H. de Leeuw, *Nanoscale*, 2016, **8**, 11067-11075.
130. C. Xiangying, W. Zhenghua, W. Xiong, W. Junxi, L. Jianwei and Q. Yitai, *Chemistry Letters*, 2004, **33**, 1294-1295.
131. N. Hollingsworth, A. Roffey, H.-U. Islam, M. Mercy, A. Roldan, W. Bras, M. Wolthers, C. R. A. Catlow, G. Sankar, G. Hogarth and N. H. de Leeuw, *Chemistry of Materials*, 2014, **26**, 6281-6292.
132. B. Arul Prakasam, M. Lahtinen, A. Peuronen, M. Muruganandham, E. Kolehmainen, E. Haapaniemi and M. Sillanpää, *Inorganica Chimica Acta*, 2015, **425**, 239-246.
133. E. Sathiyaraj, G. Gurumoorthy and S. Thirumaran, *New Journal of Chemistry*, 2015, **39**, 5336-5349.
134. Y. K. Jung, J. I. Kim and J. K. Lee, *Journal of the American Chemical Society*, 2010, **132**, 178-184.
135. B. F. Ali, W. S. Al-Akramawi, K. H. Al-Obaidi and A. H. Al-Karboli, *Thermochimica Acta*, 2004, **419**, 39-43.
136. A. Angeloski, A. T. Baker, M. Bhadbhade and A. M. McDonagh, *Journal of Molecular Structure*, 2016, **1113**, 127-132.
137. E. Sathiyaraj and S. Thirumaran, *Spectrochim Acta A Mol Biomol Spectrosc*, 2012, **97**, 575-581.
138. J. Akhtar, M. A. Malik, P. O'Brien and M. Helliwell, *Journal of Materials Chemistry*, 2010, **20**, 6116-6124.
139. N. O. Boadi, M. A. Malik, P. O'Brien and J. A. M. Awudza, *Dalton Transactions*, 2012, **41**, 10497-10506.
140. M. Nishio, Y. Umezawa, K. Honda, S. Tsuboyama and H. Suezawa, *CrystEngComm*, 2009, **11**, 1757-1788.
141. B. M. Francuski, S. B. Novaković and G. A. Bogdanović, *CrystEngComm*, 2011, **13**, 3580-3591.
142. P. Schuster, G. Zundel and C. Sandorfy, *The Hydrogen Bond-Recent Developments in Theory and Experiment*, North-Holland Pub. Co, 1976.
143. G. C. Pimental and A. L. McClellan, *The Hydrogen Bond*, W. H. Freeman and Co., San Francisco, 1960.
144. G. A. Jeffrey and W. Saenger, *Hydrogen Bonding in Biological Structures*, Springer-Verlag, Berlin, 1991.
145. P. A. Hunt, C. R. Ashworth and R. P. Matthews, *Chemical Society Reviews*, 2015, **44**, 1257-1288.
146. A. Gavezzotti and L. L. Presti, *Crystal Growth and Design*, 2016, **16**, 2952-2962.
147. T. Steiner, *Crystallography Reviews*, 2003, **9**, 177-228.
148. G. A. Jeffrey, *Crystallography Reviews*, 2003, **9**, 135-176.
149. J. Perlstein, *Journal of the American Chemical Society*, 2001, **123**, 191-192.
150. G. R. Desiraju and T. Steiner, *The Weak Hydrogen Bond: In Structural Chemistry and Biology*, Oxford University Press, 2001.
151. P. Zhou, F. Tian, F. Lv and Z. Shang, *Proteins: Structure, Function, and Bioinformatics*, 2009, **76**, 151-163.

152. D. Pal and P. Chakrabarti, *Journal of Biomolecular Structure and Dynamics*, 2001, **19**, 115-128.
153. L. M. Gregoret, S. D. Rader, R. J. Fletterick and F. E. Cohen, *Proteins: Structure, Function, and Bioinformatics*, 1991, **9**, 99-107.
154. M. Iwaoka and N. Isozumi, *Molecules*, 2012, **17**, 7266-7283.
155. S. Horowitz and R. C. Trievel, *Journal of Biological Chemistry*, 2012, **287**, 41576-41582.
156. I. Ymen, *Acta Crystallographica Section C*, 1983, **39**, 874-877.
157. L. Book and C. Chieh, *Acta Crystallographica Section B*, 1980, **36**, 300-303.
158. H. Iwasaki, *Chemistry Letters*, 1972, **1**, 1105-1106.
159. A. M. Bond, R. Colton, A. F. Hollenkamp, B. F. Hoskins, K. McGregor and E. R. T. Tiekink, *Inorganic Chemistry*, 1991, **30**, 192-197.
160. P. C. Healy and A. H. White, *Journal of the Chemical Society, Dalton Transactions*, 1973, 284-287.
161. D. A. House, W. T. Robinson and V. McKee, *Coordination Chemistry Reviews*, 1994, **135-136**, 533-586.
162. A. Okuniewski, D. Rosiak, J. Chojnacki and B. Becker, *Polyhedron*, 2015, **90**, 47-57.
163. U. Englert, *Coordination Chemistry Reviews*, 2010, **254**, 537-554.
164. E. Guzmán-Percástegui, L. N. Zakharov, J. G. Alvarado-Rodríguez, M. E. Carnes and D. W. Johnson, *Crystal Growth and Design*, 2014, **14**, 2087-2091.
165. A. Morsali and M. Y. Masoomi, *Coordination Chemistry Reviews*, 2009, **253**, 1882-1905.
166. W. Levason and C. McAuliffe, *The Chemistry of Mercury*, Palgrave Macmillan UK, 1st edn., 1977.
167. H. Sahebalzamani, S. Ghammamy, K. Mehrani and F. Salimi, *Der Chemica Sinica*, 2010, **1**, 67-72.
168. D. A. Safin, R. J. Holmberg, K. M. N. Burgess, K. Robeyns, D. L. Bryce and M. Murugesu, *European Journal of Inorganic Chemistry*, 2015, **2015**, 441-446.
169. H. R. Khavasi and B. M. Mohammad Sadegh, *Inorganic Chemistry*, 2010, **49**, 5356-5358.
170. T. A. Rodina, A. V. Ivanov, A. V. Gerasimenko, O. V. Loseva, O. N. Antzutkin and V. I. Sergienko, *Polyhedron*, 2012, **40**, 53-64.
171. M. Ito and H. Iwasaki, *Acta Crystallographica Section B*, 1979, **35**, 2720-2721.
172. M. Ito and H. Iwasaki, *Acta Crystallographica Section B*, 1980, **36**, 443-444.
173. P. C. Healy, J. W. Connor, B. W. Skelton and A. H. White, *Australian Journal of Chemistry*, 1990, **43**, 1083-1095.
174. S. Bhattacharya, N. Seth Miss, V. D. Gupta, H. Nöth and M. Thomann, *Zeitschrift für Naturforschung B*, 1994, **49**, 193-198.
175. F. Jian, F. Bei, P. Zhao, X. Wang, H. Fun and K. Chinnakali, *Journal of Coordination Chemistry*, 2002, **55**, 429-437.
176. H. Nöth and D. Schlosser, *Chemische Berichte*, 1988, **121**, 1711-1713.
177. F. Jian, Z. Wang, Z. Bai, X. You, H.-K. Fun, K. Chinnakali and I. A. Razak, *Polyhedron*, 1999, **18**, 3401-3406.
178. M. Brookheart, M. L. H. Green and G. Parkin, *Proceedings of the National Academy of Sciences of the United States of America*, 2007, **104**, 6908-6914.
179. J. Ruiz, J. Lorenzo, C. Vicente, G. Lopez, J. M. L. de Luzuriaga, M. Monge, F. X. Aviles, D. Bautista, V. Moreno and A. Laguna, *Inorganic Chemistry*, 2008, **47**, 6990-7001.
180. A. Husain, S. A. A. Nami, S. P. Singh, M. Oves and K. S. Siddiqi, *Polyhedron*, 2011, **30**, 33-40.
181. N. Ding, J. Zhang and T. S. Andy-Hor, *Dalton Transactions*, 2009, 1853-1858.
182. P. S. Nair and G. D. Scholes, *Journal of Materials Chemistry*, 2006, **16**, 467-473.
183. B. Louise, D. H. Justin, J. O. David, P. C. Mark, K. Olga and A. M. Michael, *Journal of Physics: Condensed Matter*, 2010, **22**, 076001.
184. J. Chen, L. Chen and L.-M. Wu, *Inorganic Chemistry*, 2007, **46**, 8038-8043.

- 185. E. Lewis, S. Haigh and P. O'Brien, *Journal of Materials Chemistry A*, 2014, **2**, 570-580.
- 186. R. M. Golding, P. C. Healy, P. W. G. Newman, E. Sinn and A. H. White, *Inorganic Chemistry*, 1972, **11**, 2435-2440.
- 187. A. F. Lindmark and R. C. Fay, *Inorganic Chemistry*, 1983, **22**, 2000-2006.
- 188. Y.-i. Takeda, N. Watanabe and T. Tanaka, *Spectrochimica Acta Part A: Molecular Spectroscopy*, 1976, **32**, 1553-1556.
- 189. S. Bhattacharya, B. K. Kanungo and S. Sahoo, *Journal of Coordination Chemistry*, 2006, **59**, 371-378.
- 190. A. N. Bhat, R. C. Fay, D. F. Lewis, A. F. Lindmark and S. H. Strauss, *Inorganic Chemistry*, 1974, **13**, 886-892.
- 191. O. V. Loseva, T. A. Rodina, A. I. Smolentsev and A. V. Ivanov, *Polyhedron*, 2017, **134**, 238-245.
- 192. L. Book and C. Chieh, *Acta Crystallographica Section B*, 1980, **36**, 300-303.
- 193. H. Iwasaki, *Chemistry Letters*, 1972, **1**, 1105-1106.